JANUARY-MARCH 2019 VOL. 11 № 1 (40)

ISSN 2075-8251

ActaNaturae

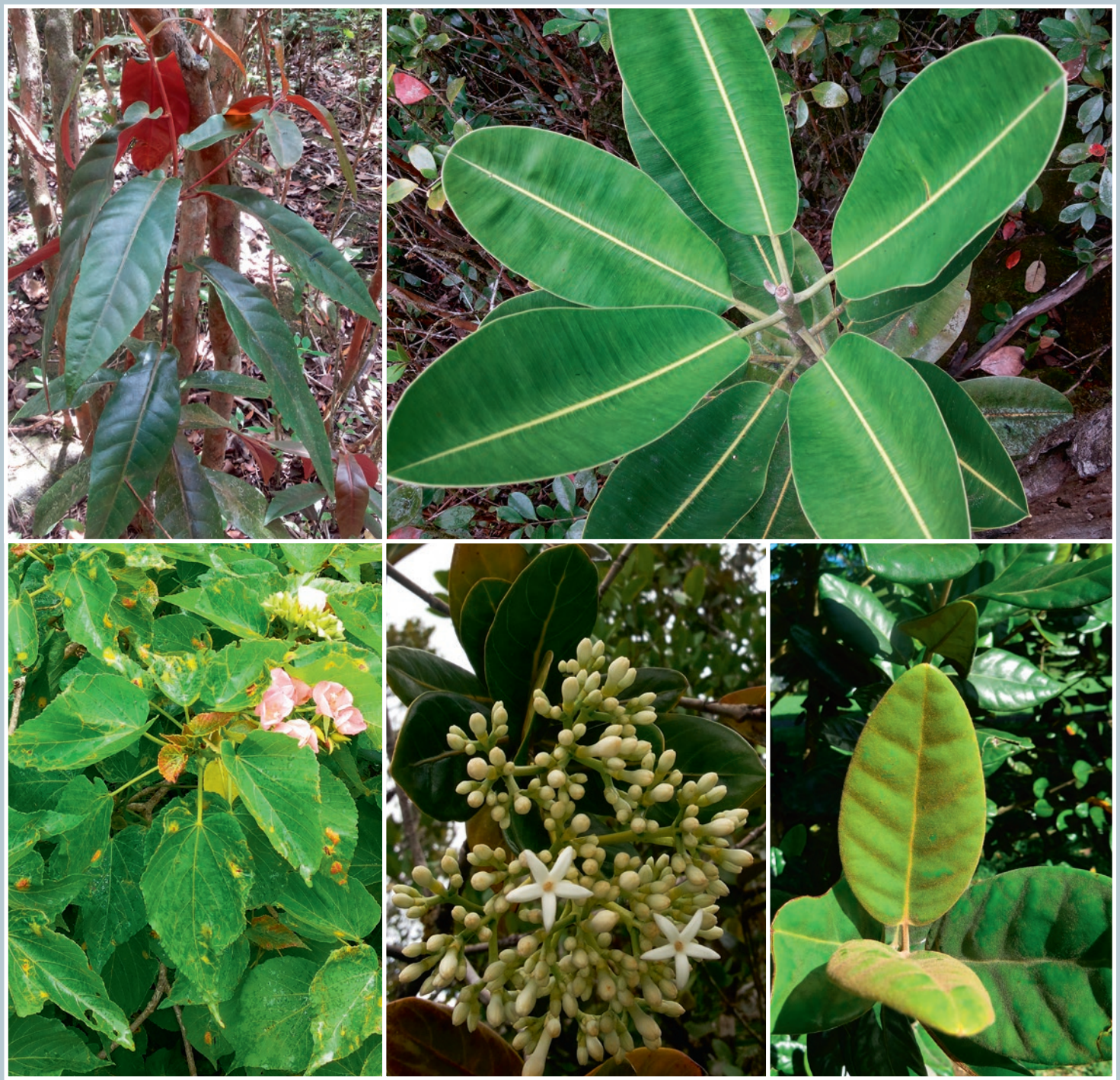

MERCK

Comprehensive solutions for cell analysis

- Cell lines and primary cells
- Traditional and specialized culture media
- Sterilizing filtration
- Biochemical reagents
- Water purification systems
- Cell counting and analysis
- Cryopreservation

An extensive range and top quality of cell lines from our partner, the European Collection of Authenticated Cell Cultures (ECACC):

- 4000 animal and human cell lines;
- Cells of 45 animal species and 50 tissue types;
- 370 B-lymphoblastoid cell lines for which human leukocyte antigen (HLA) typing data are available;
- 480 hybridoma cell lines secreting monoclonal antibodies;
- DNA, RNA, and cDNA extracted from the cell lines from our collection;

SIGMAaldrich.com/ECACC

LLC Merck
Valovaya Str., 35, Moscow, 115054, Russia;
Tel. +7 (495) 937-33-04
E-mail: mm.russia@merckgroup.com, ruorder@sial.com

SIGMAaldrich.com/cellculture
MERCKmillipore.com/cellculture

SIGMA-ALDRICH® is now MERCK

Thermodynamics of the DNA Repair Process by Endonuclease VIII

O. A. Kladova, N. A. Kuznetsov, O. S. Fedorova

In the present work, a thermodynamic analysis of the interaction between endonuclease VIII (Endo VIII) and model DNA substrates containing damaged nucleotides was performed. The changes in the fluorescence intensity of the 1,3-diaza-2-oxophenoxazine (tC^O) residue located in the complementary chain opposite the specific site were recorded in the course of the enzyme-substrate interaction. The kinetics of the enzyme-substrate interaction was analyzed by the stopped-flow method at different temperatures. The comparison of the kinetic and thermodynamic data characterizing the conformational transitions of enzyme and DNA in the course of their interaction made it possible to specify the nature of the molecular processes occurring at the stages of substrate binding, recognition of the damaged base, and its removal from DNA.

The structure of Endo VIII complexed with DNA containing an AP-site

Structure of the Anti-C_{60} Fullerene Antibody Fab Fragment: Structural Determinants of Fullerene Binding

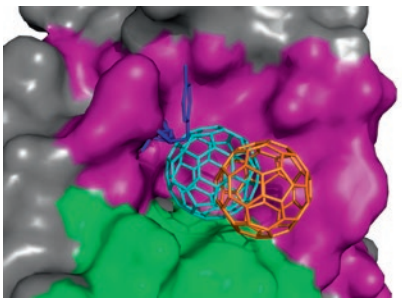

Docking of C_{60} to the unmodified and modified antigen-binding pockets of $FabC_{60}$

E. M. Osipov, O. D. Hendrickson, T. V. Tikhonova, A. V. Zherdev, O. N. Solopova, P. G. Sveshnikov, B. B. Dzantiev, V. O. Popov

The structure of the anti-C_{60} fullerene antibody Fab fragment ($FabC_{60}$) was solved by X-ray crystallography. The computer-aided docking of C_{60} into the antigen-binding pocket of $FabC_{60}$ showed that binding of C_{60} to $FabC_{60}$ is governed by the enthalpy and entropy; namely, by π-π stacking interactions with aromatic residues of the antigen-binding site and reduction of the solvent-accessible area of the hydrophobic surface of C_{60}. A fragment of the mobile CDR H3 loop located on the surface of $FabC_{60}$ interferes with C_{60} binding in the antigen-binding site, thereby resulting in low antibody affinity for C_{60}. The structure of apo-$FabC_{60}$ has been deposited with pdbid 6H3H.

Adaptation of the Newcastle Disease Virus to Cell Cultures for Enhancing Its Oncolytic Properties

K. S. Yurchenko, Yi. Jing, A. M. Shestopalov

This study focuses on the adaptation of natural Newcastle disease virus strains isolated from wild birds to human tumor cells. This study demonstrates that serial passaging increases the viral infectious titer in cancer cells. Moreover, the viability of tumor cells decreases post-infection when Newcastle disease virus strains are adapted to these cell cultures. The findings of this study complement the well-known data on the adaptation of the Newcastle disease virus to human cancer cells. Hence, it is possible to obtain a NDV strain with a more pronounced oncolytic potential during adaptation.

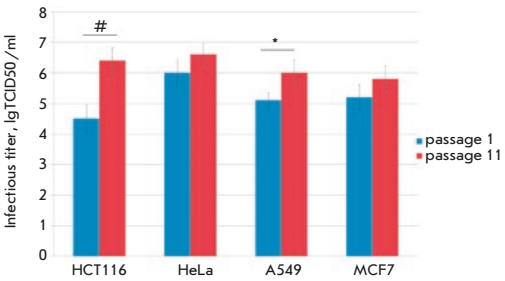

The increasing infectious titers of Newcastle disease virus strains during adaptation to human tumor cell cultures

ActaNaturae
JANUARY-MARCH 2019 VOL. 11 № 1 (40)
since april 2009, 4 times a year

Indexed in Pubmed, Web of Science, Scopus, and RISC

Founders
Acta Naturae, Ltd,
National Research University
Higher School of Economics

Phone/Fax: +7 (495) 727 38 60
E-mail: vera.knorre@gmail.com, actanaturae@gmail.com

Номер подписан в печать 29 марта 2019 г.
Тираж 100 экз. Цена свободная.
Отпечатано в типографии «МИГ ПРИНТ»

CONTENTS

REVIEWS

RESEARCH ARTICLES

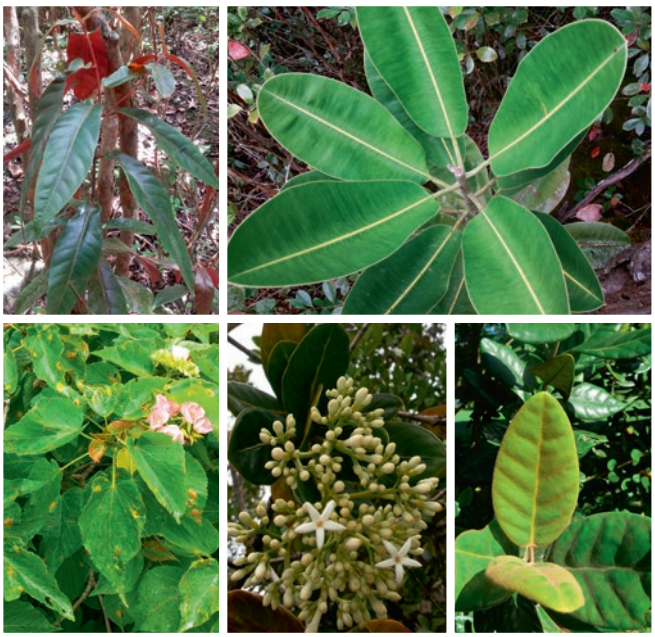

IMAGE ON THE COVER PAGE
(see the article by *N. Rummun et al.*)

Ligands of Acid-Sensing Ion Channel 1a: Mechanisms of Action and Binding Sites

D. B. Tikhonov*, L. G. Magazanik, E. I. Nagaeva
I.M. Sechenov Institute of Evolutinary Physiology and Biochemistry Russian Academy of Sciences, Thorez pr. 44, 194223, St.Petersburg, Russia
*E-mail: denistikhonov2002@ yahoo.com
Received April 16, 2018; in final form November 28, 2018

ABSTRACT **The proton-gated cationic channels belonging to the ASIC family are widely distributed in the central nervous system of vertebrates and play an important role in several physiological and pathological processes. ASIC1a are most sensitive to acidification of the external medium, which is the reason for the current interest in their function and pharmacology. Recently, the list of ASIC1a ligands has been rapidly expanding. It includes inorganic cations, a large number of synthetic and endogenous small molecules, and peptide toxins. The information on the mechanisms of action and the binding sites of the ligands comes from electrophysiological, mutational and structural studies. In the present review, we attempt to present a systematic view of the complex pattern of interactions between ligands and ASIC1a.**
KEYWORDS **CNS, ASIC, potentiation, inhibition, mechanisms of ligand-receptor interactions, binding sites.**

LOCALIZATION AND FUNCTION OF ASIC IN THE CENTRAL NERVOUS SYSTEM

Proton-induced ionic currents were discovered in 1980 by Krishtal and Pidoplichko [1], who suggested that reduced pH in an extracellular medium would trigger a population of proton-gated ion channels. Cloning of proton-gated ion channels in the mid-1990s classified them as a new family (ASICs – acid-sensing ion channels) belonging to the superfamily of degenerin/epithelial sodium channels (DEG/ENaC) [2]. The genes encoding ASICs have been identified in many vertebrate species, starting with *cyclostomata*. Four mammalian *accn1-4* genes encoding at least six different subunits (ASIC1a, ASIC1b, ASIC2a, ASIC2b, ASIC3, and ASIC4) are currently known. These subunits can form both homo- and heterotrimeric complexes.

Proton-induced currents can be found in almost all types of neurons. The levels of expression of different ASIC subunits differ markedly depending on localization. Thus, ASIC1a, ASIC2a, and ASIC2b subunits are mainly found in the brain [3–5], while ASIC1b and ASIC3 subunits are more common in sensory neurons of the spinal cord and spinal ganglia [6, 7]. Ca^{2+}-permeable ASIC1a, which are similar to the ASIC1a receptors of hippocampal neurons in terms of their functional and pharmacological properties, were found on the surface of NG2 hippocampal glial cells at a high density [8]. In the hippocampus, ASICs predominantly reside in interneurons, while the proton-induced currents in CA1 pyramidal cells are negligible [9]. In the central nervous system, ASICs are putatively involved in the mechanisms of synaptic transmission and synaptic plasticity, as well as many other systemic functions, such as memory and learning [10], fear and depression [3]. Their role can be determined by analyzing the mechanisms of drug addiction [11] and the pathogenesis of a number of mental disorders [12].

Taste, auditory, and photosensitive receptor cells [13–15], as well as smooth muscle cells lining the vessel walls [16], express ASICs on their surface, although to a much lesser extent than neurons. In the peripheral nervous system, ASICs are responsible for the perception of the pain stimuli accompanying inflammation, fractures, tumors, hematomas and postoperative wounds. Furthermore, they participate in mechanoreception [17]. Tumor growth also stimulates ASIC expression [18].

Most of the data pertaining to the physiological role of proton-gated ion channels are indirect, since they are based on the experimental findings obtained from knockout animals. Elimination of particular ASIC subunits allowed researchers to trace their role in the occurrence of certain behavioral phenotypes, as well as the involvement of ASICs in the development of various pathological processes in the nervous system [19].

It was not until recently that direct evidence of ASIC involvement in synaptic transmission was obtained.

The content of synaptic vesicles has pH ~ 5.2–5.7 [20]. Accordingly, as the vesicle content is released, pH of the synaptic cleft may transiently decrease by 0.2–0.6 pH units and lead to activation of both pre- and postsynaptic ASICs [21–23]. However, the contribution of ASIC-mediated postsynaptic currents is 15–20 times lower than that of glutamate-mediated postsynaptic currents [11, 24, 25].

Among the proton-gated channels expressed in the CNS, ASIC1a is the one most sensitive to acidification of the medium [26]. In addition, PcTx1, a specific inhibitor of ASIC1a homomers, eliminates most of the proton-induced currents in hippocampal and cerebral cortex cell cultures [27, 28]. Thus, most proton-induced currents in the brain are likely to be mediated by ASIC1a and ASIC1a-containing heteromers. These facts explain the keen interest in the properties of ASIC1a and their ligands.

The main challenge faced by neurophysiologists studying ASICs consists in resolving the contradiction between the obvious role of these channels in physiological and pathological processes and the small values of ASIC-mediated currents observed experimentally upon synaptic transmission. Meanwhile, the *in vitro* experiments involving CNS neurons demonstrate that the currents caused by acidification of the extracellular medium and application of glutamate, the major excitatory neurotransmitter, have similar amplitudes. The second problem is that ASICs expressed in the central nervous system desensitize (i.e., lose their ability to conduct current) rapidly in response even to minor acidification. Thus, acidification to pH 7.0 causes about 80% desensitization of ASIC1a and actually turns off their function [26].

The existence of endogenous compounds that modulate the function of ASICs under physiological conditions could be a solution to these problems. The NMDA-type ionotropic glutamate receptor is the classic example of such modulation. These channels can be efficiently activated only in the presence of a co-agonist, glycine [29]. That is why it is of great interest to search and study new ASIC ligands (and potentiators of ASICs in particular) in the context of both the fundamental problems of pharmacology and neurophysiology.

ASIC1A LIGANDS

Studies focused on the relationship between the structures and molecular mechanisms of action of ASIC1a modulators are important for determining the physiological role of ASICs and designing a novel class of medications. Among ASIC1a modulators, there are synthetic compounds, endogenous organic substances and ions, as well as a number of peptide toxins from the components of natural venoms. The structures of some low-molecular-weight ligands are shown in *Fig. 1*.

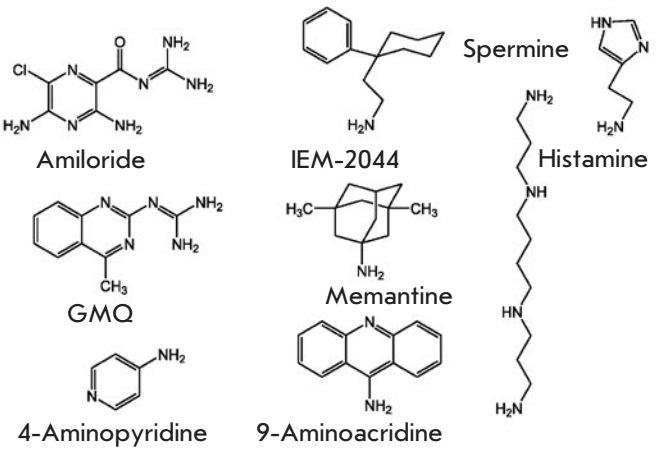

Fig. 1. The chemical structures of some ASIC1a ligands

Amiloride

Amiloride, a diuretic prescribed to patients with hypertension and heart failure, was the first discovered blocker of proton-gated ion channels [30, 31]. Amiloride acts as a nonselective ASIC blocker with low affinity to the binding site (IC_{50}= 5–100 μM), which is also capable of blocking other ion channels and exchangers [32]. Interestingly, at higher amiloride concentrations its inhibitory effect is inverted to a potentiating or even activating action. Application of amiloride (EC_{50} = 560 μM) under neutral conditions (pH 7.4) activates homomeric ASIC3 and heteromeric ASIC3/ASIC1b-channels and synergistically increases the currents through these channels in response to moderate acidification of the extracellular medium [33]. Hence, it is obvious that amiloride has a dual multidirectional effect on proton-gated ion channels.

2-Guanidine-4-methylquinazoline (GMQ)

The discovery of the unusual effect of amiloride on proton-gated ion channels has inspired researchers to synthesize a number of its analogs carrying the guanidine moiety and a heterocyclic ring [34, 35]. Among all these compounds, GMQ stands out for the specificity of its activating effect. It was the first synthetic non-proton activator of ASIC3; this fact suggests that there can be other synthetic/endogenous ASIC activators. At high concentrations (EC_{50} = 1 mM), GMQ can induce a stationary non-desensitizing current through the ASIC3 channels which is many times greater than the nondesensitizing current evoked by saturating concentration of the natural agonists (protons). The action

of GMQ depends on extracellular Ca^{2+}, being enhanced as the Ca^{2+} concentration in the medium decreases [36, 37]. In addition to its activating effect on ASIC3, GMQ also specifically interacts with ASIC1a. The effect involves a shift in the pH dependences of activation and steady-state desensitization towards more acidic values by approximately 0.2 pH units. Both effects have a competitive-like nature; i.e., both steady-state desensitization and activation develop completely, although at lower pH values [38].

4-Aminopyridine (4AP)

The well-known potassium channel blocker 4AP is another small molecule that can block ASIC1a homomers (IC_{50} ~ 760 μM) and heteromers containing ASIC1a, ASIC1b and ASIC2a subunits. As is the case for potassium channels, the binding site of 4AP in ASICs and other degenerin/epithelial channels resides within the pore, since its effect is significantly voltage-gated [39].

Metal ions

ASICs are inhibited by various metal ions [40–42]. It was shown that the affinity of protons to the channel directly depends on calcium concentration in the medium [43, 44]: the lower the Ca^{2+} concentration, the higher the affinity of protons is and, accordingly, the greater the ASIC responses are.

Spermine

Spermine is an endogenous polyamine that amplifies the proton-gated currents through ASIC1a and ASIC1a/2a channels [45]. The mechanism of ASIC1a channel potentiation consists of several components and involves a slowdown of inactivation (in other words, the activated channel remains open for a longer time); reduction of proton affinity to the receptor and, consequently, an increase in their responses at low background pH; and quicker channel recovery under repeated stimulation. All these effects enhance Ca^{2+} entry into the neuron through ASIC1a under ischemic conditions and, eventually, lead to cell death. Both blockade of endogenous spermine synthesis and blockade of the ASIC1a channels significantly increase neuronal survival in the *in vivo* and *in vitro* mouse models of ischemia [45].

FMRF amides

FMRF amides (Phe-Met-Arg-Phe-NH_2), which prevail in the nervous system of invertebrates, as well as related peptides in the mammalian nervous system, activate some degenerin/epithelial Na^+-channels [46]. They are unable to activate ASICs *per se* but can significantly potentiate the responses of ASIC1a and ASIC3 channels to the acidification of the medium [47, 48]. These peptides have a direct impact on the channel and slow down receptor desensitization, thus increasing the time for which the channel remains open after activation [49, 50]. These peptides also affect steady-state desensitization by shifting it towards stronger acidification [48]. Endogenous opioid neuropeptides, dynorphin and big dynorphin, also shift the steady-state desensitization and enhance the responses of ASIC1a upon weak acidification [51].

Psalmotoxin-1 (PcTx1)

The polypeptide toxin isolated from the venom of the South American tarantula *Psalmopoeus cambridgei* was the first-described specific inhibitor of ASIC1a channels (IC_{50} ~ 1 nM) [52]. PcTx1 consists of 40 amino acids and is formed by three antiparallel β-sheets twisted into loops, with a compact nucleus containing three disulfide bridges and residing in the center [53]. Psalmotoxin-1 inhibits ASIC1a channels by increasing receptor sensitivity to protons and shifting desensitization towards less acidic pH values [54]. Since ASIC1a are activated in response to a slight increase in proton concentration, even a small rise in the affinity of H^+ to proton-binding sites is sufficient to switch receptors to the desensitized state. As a result, most of the ASIC1a becomes inactive in the presence of PcTx1 at pH 7.4, due to enhanced steady-state desensitization. The toxin preferably binds to the desensitized channel and stabilizes it in this state [55].

MitTx

MitTx was isolated from the venom of the Texas coral snake *Micrurus tener tener* in 2011 [56]. This peptide toxin resembles β-bungarotoxin in terms of its structure and consists of two non-covalently bound subunits. MitTx does not inhibit ASICs but activates both homo- and heterotrimeric channels [56, 57]. ASIC1a and ASIC1b homomers (EC_{50} ~ 9 and 23 nm, respectively) are the most sensitive ones to its action; ASIC3 channels are much less sensitive (EC_{50} ~ 830 nm). When applied together with a neutral solution, MitTx has virtually no effect on ASIC2a channels but strongly potentiates proton-gated currents through these channels by shifting the activation curve towards less acidic values.

Mambalgins

Mambalgins constitute a group of three toxins with a length of 57 amino acids. Two of them, mambalgin-1 and -2, different by only one amino acid at position 4, were isolated from the venom of the black mamba *Dendroaspis polylepis polylepis* in 2012 [58]. Mambalgin-3 was isolated from the venom of the green Mamba and got its name because it differs from the

aforementioned two toxins only by the amino acid at position 23 [59]. All three peptides are structurally related to the three-finger toxin family, have similar pharmacological characteristics, and inhibit ASIC1a [59]. Mambalgin-1 inhibits ASIC1a via the following mechanism: it preferably binds to the closed channel and strongly shifts the pH dependence of activation to more acidic pH values. At the same time, the toxin moderately shifts the inactivation curve towards the alkaline region, thereby stabilizing the desensitized state of the channel and increasing inhibition [58].

Hydrophobic monoamines

Recently, the staff of the Laboratory of Biophysics of Synaptic Processes at the Sechenov Institute of Evolutionary Physiology and Biochemistry (Russian Academy of Sciences) has found that compounds with a simple chemical structure containing the hydrophobic/aromatic core and an amino group (hydrophobic monoamines) are modulators of native and recombinant ASICs [60, 61]. Among the four compounds tested in the first stage, only IEM-1921 exhibited no action against homomeric ASIC1a channels even at a concentration of 1,000 μM. The other three compounds, 9-aminoacridine (9AA), IEM-2117 and memantine, had a concentration-dependent inhibitory effect [60]. 9AA was the most active inhibitor. At a concentration of 1,000 μM, this compound, being co-applied with an activating solution with pH 6, caused 67 ± 8% (n = 6) inhibition. The action of 9-aminoacridine was pH-dependent: this compound at a concentration of 300 μM induced 80% inhibition at pH 6.8 and only 12% inhibition at pH 5.0. Therefore, the inhibitory effect of 9-aminoacridine is due to the shift in ASIC1a activation towards stronger acidification. A characteristic feature of memantine action was the abrupt acceleration of response desensitization. A similar effect of memantine on ASIC1b was demonstrated earlier [61]. A more detailed study of the mechanism of memantine action demonstrated that in this case the inhibitory effect is due to the open channel block. This conclusion is based on the fact that the effect of memantine was voltage- rather than pH-dependent [62].

Further structural and functional analysis [63] has identified potentiators of ASIC1a. We found that incorporation of a methylene group between the phenylcyclohexyl ring and the amino group in IEM-1921 conferred weak potentiation, while insertion of the second group enhanced potentiation (compound IEM-2044).

The detection of potentiating activity for IEM-2044 has intensified further search for novel, potentially active drugs. The chemical structure of this compound is similar to that of histamine, a number of histamine receptor ligands and other endogenous amines, such as

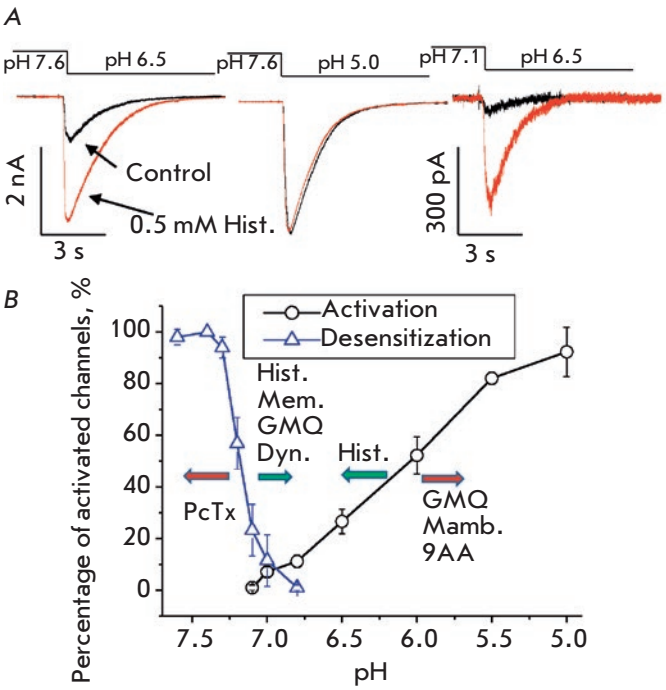

Fig. 2. The mechanisms of action of ASIC1a ligands. *A* – the effect of histamine on the recombinant ASIC1a expressed in CHO cells. Histamine does not affect the maximal response (caused by a pH decrease from 7.6 to 5.0) but potentiates the partial response (pH decrease from 7.6 to 6.5), especially under conditions of partial desensitization (pH decrease from 7.1 to 6.5). B – pH dependences of ASIC1a activation and desensitization. The arrows show the directions of the shifts caused by ligands

tyramine and tryptamine. Histamine [64] and its derivatives, alpha-methylhistamine and 1-methylhistamine [65], were shown to be strong and selective potentiators of ASIC1a. Potentiation takes place due to the shift in the activation curve, since the response to extreme acidification does not increase. Among the ligands of histamine receptors, this effect has been demonstrated for thioperamide and dimaprit. In contrast, compound A943931 caused inhibition that was dependent on the membrane voltage rather than on activating pH, which is indicative of a pore-blocking mechanism of action [65].

The initial study [64] did not reveal any effect of histamine on ASIC1a desensitization. However, a more detailed analysis showed that the effect of histamine increases at initial pH = 7.1 (i.e., under partial desensitization) (*Fig. 2*). A similar effect was also established for tyramine and tryptamine, which did not shift the activation curve [66]. Even memantine, an inhibitor of

open ASIC1a channels, exhibited potentiating activity when applied between channel activations at pH 7.1 (i.e., in the case of interaction with closed and desensitized channels only) [65]. Therefore, different monoamines shift the steady-state desensitization of ASIC1a towards stronger acidification.

Summarized data on the mechanisms of ASIC1a modulation

It is difficult to establish clear relationships for the variety of data and hypotheses on the action of specific ASIC1a ligands. However, the accumulated large body of experimental data reveals some patterns.

According to a combination of features, some compounds can be classified as ASIC1a pore blockers. Amiloride, memantine and 4-aminopyridine are typical members of this group. Binding of these compounds in the pore leads to inhibition of ion transport independently of the degree of channel activation and desensitization. Blockers of cation channel pores are usually cations; in this case, their action depends on the membrane potential.

The second common type of ligand action consists in a shifting of the activation curve, which leads to either inhibition or potentiation of currents (*Fig. 2B*). Peptide toxin mambalgin and the low-molecular-weight compounds GMQ and 9AA shift the curve towards stronger acidification, while histamine ensures channel activation at higher pH values. A feature of this mechanism is that the ligands are potent only at low acidification levels, when ASIC1a activation is rather low. The activation curve can be shifted due to the allosteric effect on receptor affinity to protons or due to direct interaction with the proton-binding site. In the latter case, ligands of this type act as agonists or competitive antagonists, depending on the direction of action.

The third type of action is alteration of the steady-state desensitization of ASIC1a (*Fig. 2B*). Psalmotoxin is the best known example of compounds that enhance desensitization. Spermine and monoamines reduce desensitization, thus allowing ASIC1a to function under long-term acidification of media. A number of ligands, such as GMQ and histamine, simultaneously affect activation and desensitization. There is no correlation between these effects. Thus, GMQ shifts both curves towards deeper acidification, while histamine shifts the activation curve towards less significant acidification (*Fig. 2A*). Psalmotoxin, which is well-known as a desensitization promoter, may cause channel activation at alkaline pH values.

The question pertaining to the binding sites is even more complicated. Site-directed mutagenesis of the receptor is the method conventionally used to detect the ligand binding site. However, this approach does not provide unambiguously interpretable results. Mutations can either directly affect the ligand binding site (if the mutated amino acids reside in it), or allosterically modulate receptor affinity to the ligand by changing receptor conformation. In addition, mutations can significantly affect the functional properties of the channel, its activation and desensitization, which may further complicate data interpretation. In some cases, mutations result in complete loss of channel function. In this case, it becomes no longer possible to determine the effect of mutation on ligand binding. Thus, despite the high value of mutagenesis data, their structural interpretation requires great care. Therefore, the problem related to the ligand binding site can be solved only with allowance for the data on the ASIC structure and the molecular mechanisms of their activation and desensitization.

ASIC STRUCTURE

The first X-ray crystallographic structure of chicken ASIC1a reported in 2007 [67] has made it possible to establish the main elements of its structure (*Fig. 3*). The crystal structure of the functioning mutant with a lacking C-terminal region but retained N-terminal region and the portion required for channel opening was obtained later with a lower resolution (3 Å) [68]. Both proteins crystallize at low pH. Under such conditions, the ASIC1a channels exist in a desensitized state. Later, the ASIC1a structures were obtained in the open and closed states [69], making it possible to determine the activation and desensitization mechanisms.

ASICs are trimers whose subunits are symmetrically arranged around the central channel pore. The extracellular domain (ECD) of each subunit resembles a clenched fist attached to the transmembrane segments by a movable "wrist" [67]. Given this similarity, Jasti et al. [67] described the ECD in terms of a human hand holding a ball. Subsequently, this terminology has become commonly used as it turns out to be quite convenient. ECD can be divided into five subdomains: the palm, the finger, the thumb, the knuckle and the β-ball domains (*Fig. 3*).

An important feature of the ECD structure is the so-called acidic pocket, where several acidic amino-acid residues occupy a small area. It is located at a distance of 45 Å from the transmembrane region and is formed by interactions between the thumb-, β-ball, and finger domains of one subunit and a portion of the palm domain of the neighboring subunit. There are closely located three pairs of acidic amino-acid residues (Asp238-Asp350, Glu239-Asp346 and Glu220-Asp408) inside this pocket. The electrostatic repulsion between the negative charges of the side chains in these pairs of amino-acid residues retains the expanded confor-

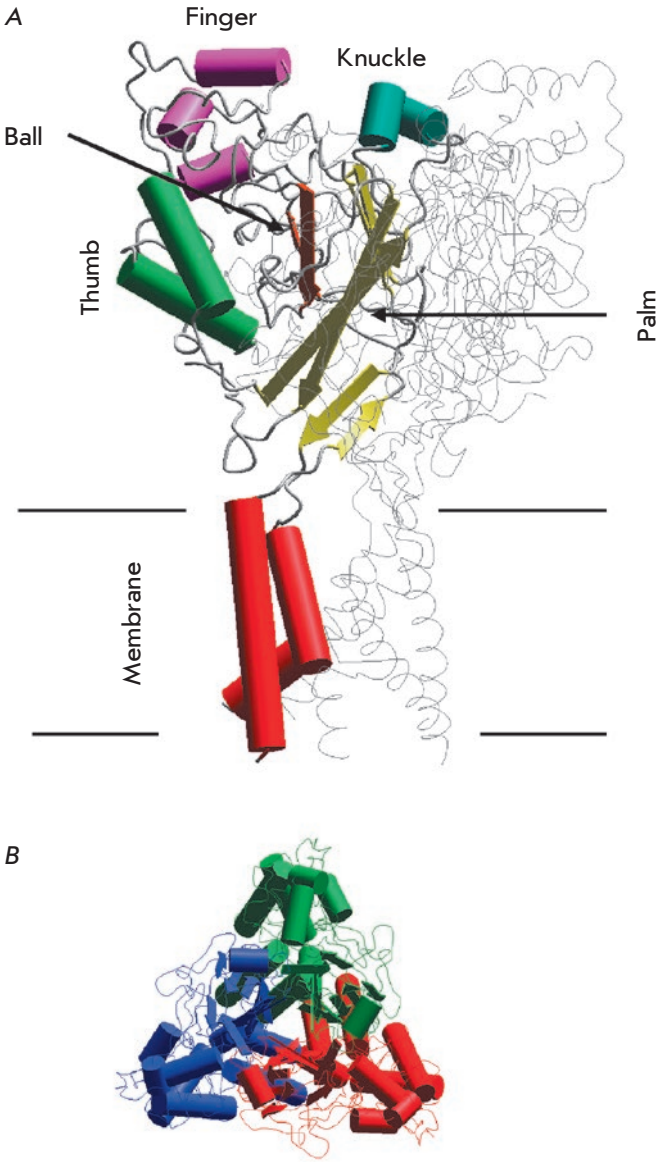

Fig. 3. The general structure of ASIC according to X-ray crystallography. *A* – side view with the main parts in one subunit highlighted: Finger, Knuckle, Ball, Thumb, and Palm. *B* – the top view shows that ASIC is a trimer, in which the subunits (shown with different colors) surround the channel pore in the center

mation of the acidic pocket; so the channel is closed. Binding of the protons between carboxyl pairs takes place when the external medium is acidified, making the pocket take a more compact conformation. This causes conformational changes in the thumb domain, which in turn alters the wrist and the transmembrane domain. Hence, the acidic pocket is a site of the proton binding required for channel activation [69].

However, in addition to the amino acids in the "pocket," there are several asparagine, glutamine and histidine residues in the lower portion of the palm domain (their pK_a value also lies within the pH range that activates ASIC1a channels) [70]. In addition, complete removal of all three pairs of amino acids from the "pocket" dramatically reduces receptor sensitivity to protons but does not eliminate its ability to be activated in response to strong acidification of the extracellular medium [71]. In this regard, it is believed that several sites responsible for proton binding and further channel activation reside within one subunit.

The transmembrane segment of the ASIC domain is formed by six α-helices: two (TM1 and TM2) from each of the three subunits composing the functioning ASIC channel pore. The transmembrane segments of each subunit are involved in channel pore formation. TM2 directly lines the pore lumen, while TM1 plays a supporting role: it is in contact with the lipid bilayer and forms many bonds with TM2 of the same subunit, as well as with TM2 and TM1 of the neighboring subunit. Only a small C-terminal portion of TM1 directly lines the channel pore [72].

Binding sites of ASIC modulators

The most accurate data on ligand binding sites are obtained by X-ray crystallography and cryogenic electron microscopy. Several high-resolution ASIC structures in combination with such ligands as psalmotoxin, MiTtx and amiloride have been obtained to date [73, 74].

A structure of ASIC1a in an open state was obtained using the activating MitTx toxin. Each heterodimer of the toxin binds to the channel subunit; i.e., three toxin molecules form multiple contacts along the entire thumb domain, from the membrane surface to the knuckle domain (*Fig. 4A*). Although the toxin molecule is revealed near the acidic pocket, MitTx does not penetrate directly into it. Therefore, the toxin mechanically stabilizes the open state of the channel without directly affecting the proton-binding center.

In addition to this peptide toxin, a complex formed between ASIC1a and amiloride has been resolved within the same structure. Three amiloride molecules reside in the upper portion of the channel pore, at the interfaces between subunits (*Fig. 4C*). Their charged groups are exposed to the pore lumen. On the other hand, mutagenesis data are indicative of deeper location of the amiloride binding sites in the pore [75]. Kellenberger et al. [75] put forward a hypothesis that the binding sites found in the X-ray crystallographic structure represent the intermediate position of amiloride; one molecule may go deeper, thus sterically blocking the channel. The second binding site of amiloride is lo-

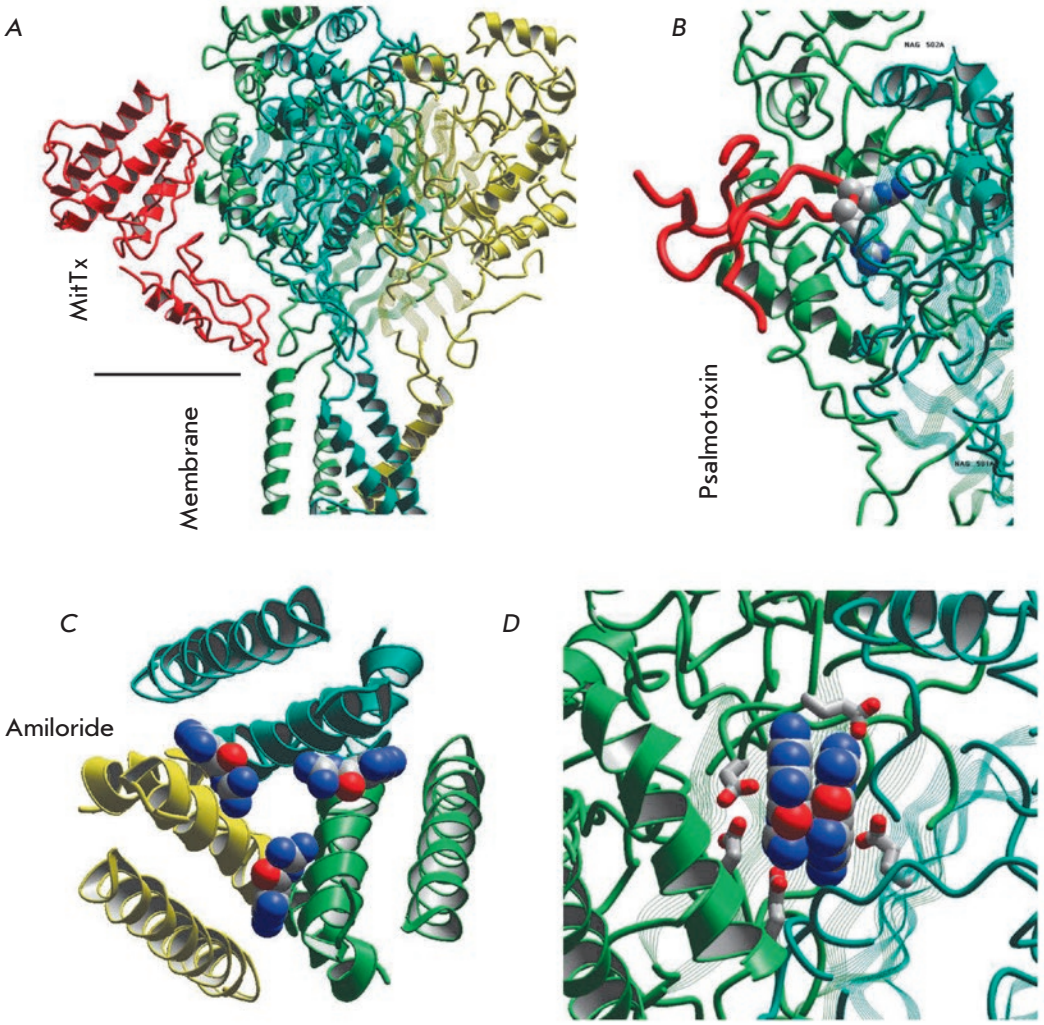

Fig. 4. Binding sites of ASIC 1a ligands according to structural studies. *A* – MitTx that activates the channels and binds to the palm domain; *B* – psalmotoxin binds to the upper portion of the palm domain, and the central loop penetrates the acidic pocket; *C* – three amiloride molecules bind at the interfaces to membrane-spanning helices; *D* – two amiloride molecules form a dimer, which binds in the acidic pocket

cated in the acidic pocket (*Fig. 4D*). Two molecules form a dimer, which is stabilized by stacking interactions between aromatic groups and the oppositely oriented guanidine groups. The functional role of this binding site is still unknown, but it seems likely that it is related to the ability of amiloride to activate ASICs [33].

The binding site of psalmotoxin identified by Baconguis et al. [73] significantly overlaps with the binding region of MitTx. However, the middle loop of a psalmotoxin molecule enters the acidic pocket, where the positively charged toxin residues directly interact with the acidic residues of the receptor (*Fig. 4B*). In other words, the stabilization mechanisms of the open state mediated by MiTtx and the desensitized state mediated by psalmotoxin differ fundamentally: psalmotoxin affects the proton receptor, whereas MiTtx affects the executive mechanism of activation.

The putative binding sites of other ASIC ligands can be derived from indirect evidence by analyzing the data on the mechanisms of action, the effect of point mutations, and competition with ligands whose binding sites are known. For example, the findings on the common binding regions of MitTx and psalmotoxin are consistent with the data on the mutually exclusive effect of these toxins [56]. It has been reported most recently [76] that mambalgins also bind near the acidic pocket (like psalmotoxin does).

Binding of several other types of ligands can be related to psalmotoxin. Thus, Duan et al. [45] analyzed the simultaneous action of spermine and psalmotoxin and demonstrated that these two compounds can compete for the common binding site, although they modulate the ASIC1a function in opposite directions. There also exists competition between psalmotoxin and calcium [54]; furthermore, calcium is known to compete with protons [43, 77]. Competition with palmotoxin was also shown for dynorphin [51]. Based on these data, it is fair to assume that the ligands affecting the pH depend-

ence of activation and steady-state desensitization of ASIC1a bind within the acidic pocket of the receptor and have a direct impact on its functional components. Since the acidic pocket contains several negatively charged amino-acid residues, a specific mode of action for each ligand can be determined by specific interactions with this area.

However, some data is not entirely consistent with this concept. First, as noted above, the acidic pocket is not the only proton-binding site required for channel activation [70, 71]. The substitution of amino-acid residues in the palm domain affects desensitization and activity of a number of ligands. In their recent paper [78], Besson *et al.* systematically studied the mutual effects of GMQ, amiloride, psalmotoxin, and mambalgine. They found that the impact of GMQ and mambalgine on the ASIC1a activation is fully additive, suggesting that their mechanisms of action are independent. On the contrary, the effects of GMQ and psalmotoxin on steady-state desensitization are not independent, since there exists a negative cooperativity between them. Hence, the question pertaining to the exact binding sites of the ligands affecting the activation and desensitization of ASIC1a remains open and requires further research.

CONCLUSIONS

The data on the effect of various ligands on ASIC1a suggest three main modes of action: blocking of the channel pore, shifting of the dependence of activation on pH, and shifting of the dependence of desensitization on pH. Many ligands simultaneously affect the latter two characteristics. Effects of this type are probably mediated by ligand binding to some extracellular site, which controls the activation and desensitization characteristics of ASIC1a. Although the ligand-induced shifts in these curves usually do not exceed 0.2–0.5 pH units, they have a substantial impact on the function of the channel, since ASIC1a activation takes place in a pH range between 7.0 and 5.0, while steady-state desensitization develops at pH between 7.5 and 7.0. Such characteristics significantly limit the possibility of ASIC1a functioning under physiological conditions. In particular, even insignificant acidification causes desensitization and loss of channel function. From this point of view, it seems promising to search for endogenous ligands that shift desensitization towards more acidic pH values and, contrariwise, shift activation towards smaller acidification. In the presence of such ligands, ASIC1a could be activated by small acidification of the external medium that occurs upon synaptic transmission. In this case, moderate acidification of the medium would not lead to desensitization, but rather enhance the response and the contribution of ASIC1a to neuronal excitability. If we take into account the fact that elevated activation of ASIC1a can have a beneficial impact on the course of many pathological processes, detection of ligands that potentiate ASIC1a acquires a clinical significance. ●

The authors are grateful to V.Yu. Shteinikov for providing the records of histamine action under various conditions.

This work was supported by the Russian Science Foundation (grant No. 16-14-00122).

REFERENCES

1. Krishtal O. A., Pidoplichko V.I. // Neuroscience. 1980. V. 5. № 12. P. 2325–2327.
2. Kellenberger S., Schild L. // Pharmacol. Rev. 2015. V. 67. № 1. P. 1–35.
3. Wemmie J. A, Askwith C.C., Lamani E., Cassell M.D., Freeman J.H., Welsh M.J. // J. Neurosci. 2003. V. 23. № 13. P. 5496–5502.
4. Coryell M.W., Wunsch A.M., Haenfler J.M., Allen J.E., Ziemann A.E., Cook M.N., Dunning J.P., Margaret P., Rainier J.D., Liu Z., et al. // J Neurosci. 2009. V. 29. № 17. P. 5381–5388.
5. Price M.P., Gong H., Parsons M.G., Kundert J.R., Reznikov L.R., Bernardinelli L., Chaloner K., Buchanan G.F., Wemmie J.A., Richerson G.B., et al. // Genes, Brain Behav. 2014. V. 13. № 2. P. 179–194.
6. Delaunay A., Gasull X., Salinas M., Noel J., Friend V., Lingueglia E., Deval E. // Proc. Natl. Acad. Sci. 2012. V. 109. № 32. P. 13124–13129.
7. Deval E., Lingueglia E. // Neuropharmacology. 2015. V. 94. P. 49–57.
8. Lin Y.C., Liu Y.C., Huang Y.Y., Lien C.C. // PLoS One. 2010. V. 5. № 9. P.735-744.
9. Bolshakov K. V, Essin K. V, Buldakova S.L., Dorofeeva N. a, Skatchkov S.N., Eaton M.J., Tikhonov D.B., Magazanik L.G. // Neuroscience. 2002. V. 110. № 4. P. 723–730.
10. Wemmie J. A, Chen J., Askwith C.C., Hruska-Hageman A.M., Price M.P., Nolan B.C., Yoder P.G., Lamani E., Hoshi T., Freeman J.H., et al. // Neuron. 2002. V. 34. № 3. P. 463–477.
11. Kreple C.J., Lu Y., Taugher R.J., Schwager-Gutman A.L., Du J., Stump M., Wang Y., Ghobbeh A., Fan R., Cosme C. V, et al. // Nat. Neurosci. 2014. V. 17. № 8. P. 1083–1091.
12. Baldwin D.S., Hou R., Gordon R., Huneke N.T.M., Garner M. // CNS Drugs. 2017. V. 31. № 4. P. 307–317.
13. Lin W., Ogura T., Kinnamon S.C. // J. Neurophysiol. 2002. V. 88. P. 133–141.
14. Ettaiche M., Guy N., Hofman P., Lazdunski M., Waldmann R. // J. Neurosci. 2004. V. 24. № 5. P. 1005–1012.
15. Ugawa S., Inagaki A., Yamamura H., Ueda T., Ishida Y., Kajita K., Shimizu H., Shimada S. // Neuroreport. 2006. V. 17. № 12. P. 1235–1239.

16. Grifoni S.C., Jernigan N.L., Hamilton G., Drummond H.A. // Microvasc. Res. 2008. V. 75. № 2. P. 202–210.
17. Wemmie J.A., Price M.P., Welsh M.J. // Trends Neurosci. 2006. V. 29. № 10. P. 578–586.
18. Damaghi M., Wojtkowiak J.W., Gillies R.J. // Front Physiol. 2013. V. 4. a. 370.
19. Lin S.H., Sun W.H., Chen C.C. // Neuropharmacology. 2015. V. 94. P. 99–118.
20. Miesenböck G., De Angelis D.A., Rothman J.E. // Nature. 1998. V. 394. № 6689. P. 192–195.
21. DeVries S.H. // Neuron. 2001. V. 32. № 6. P. 1107–1117.
22. Palmer M.J., Hull C., Vigh J. // J. Neurosci. 2003. V. 23. № 36. P. 11332–11341.
23. Vessey J.P. // J. Neurosci. 2005. V. 25. № 16. P. 4108–4117.
24. Du J., Reznikov L.R., Price M.P., Zha X. M., Lu Y., Moninger T.O., Wemmie J.A., Welsh M.J. // Proc. Natl. Acad. Sci. 2014. V. 111. № 24. P. 8961–8966.
25. González-Inchauspe C., Urbano F.J., Di Guilmi M.N., Uchitel O.D. // J. Neurosci. 2017. V. 37. № 10. P. 2589–2599.
26. Hesselager M., Timmermann D.B., Ahring P.K. // J. Biol. Chem. 2004. V. 279. № 12. P. 11006–11015.
27. Baron A., Waldmann R., Lazdunski M. // J. Physiol. 2002. V. 539. № 2. P. 485–494.
28. Coryell M.W., Ziemann A.E., Westmoreland P.J., Haenfler J.M., Kurjakovic Z., Zha X. ming, Price M., Schnizler M.K., Wemmie J.A. // Biol. Psychiatry. 2007. V. 62. № 10. P. 1140–1148.
29. Kleckner N., Dingledine R. // Science. 1988. V. 241. № 4867. P. 835–837.
30. Waldmann R., Champigny G., Voilley N., Lauritzen I., Lazdunski M. // J. Biol. Chem. 1996. V. 271. № 18. P. 10433–10436.
31. Waldmann R., Champigny G., Bassilana F., Heurteaux C., Lazdunski M. // Nature. 1997. V. 386. № 6621. P. 173–177.
32. Kleyman T.R., Cragoe E.J. // J. Membr. Biol. 1988. V. 105. № 1. P. 1–21.
33. Li W.G., Yu Y., Huang C., Cao H., Xu T.L. // J. Biol. Chem. 2011. V. 286. № 49. P. 42635–42646.
34. Chen X., Orser B. A, MacDonald J.F. // Eur. J. Pharmacol. 2010. V. 648. № 1–3. P. 15–23.
35. Kuduk S.D., Chang R.K., Wai J.M.C., Di Marco C.N., Cofre V., DiPardo R.M., Cook S.P., Cato M.J., Jovanovska A., Urban M.O., et al. // Bioorg. Med. Chem. Lett. 2009. V. 19. № 15. P. 4059–4063.
36. Yu Y., Chen Z., Li W., Cao H., Feng E., Yu F., Liu H., Jiang H., Xu T. // Neuron. 2010. V. 68. P. 61–72.
37. Yu Y., Li W.G., Chen Z., Cao H., Yang H., Jiang H., Xu T. // J. Biol. Chem. 2011. V. 286. № 28. P. 24996–25006.
38. Alijevic O., Kellenberger S. // J. Biol. Chem. 2012. V. 287. № 43. P. 36059–36070.
39. Boiko N., Kucher V., Eaton B.A., Stockand J.D. // J. Biol. Chem. 2013. V. 288. № 13. P. 9418–9427.
40. Staruschenko A., Dorofeeva N.A., Bolshakov K. V., Stockand J.D. // Dev. Neurobiol. 2007. V. 67. № 1. P. 97–107.
41. De Weille J., Bassilana F. // Brain Res. 2001. V. 900. № 2. P. 277–281.
42. Chu X.P., Wemmie J.A., Wang W.Z., Zhu X.M., Saugstad J.A., Price M.P., Simon R.P., Xiong Z.G. // J. Neurosci. 2004. V. 24. № 40. P. 8678–8689.
43. Babini E., Paukert M., Geisler H.S., Gründer S. // J. Biol. Chem. 2002. V. 277. P. 41597–41603.
44. Immke D.C., McCleskey E.W. // Nat. Neurosci. 2001. V. 4. № 9. P. 869–870.
45. Duan B., Wang Y.Z., Yang T., Chu X.P., Yu Y., Huang Y., Cao H., Hansen J., Simon R.P., Zhu M.X., et al. // J. Neurosci. 2011. V. 31. № 6. P. 2101–2112.
46. Lingueglia E., Deval E., Lazdunski M. // Peptides. 2006. V. 27. № 5. P. 1138–1152.
47. Askwith C.C., Cheng C., Ikuma M., Benson C., Price M.P., Welsh M.J. // Neuron. 2000. V. 26. № 1. P. 133–141.
48. Sherwood T.W., Askwith C.C. // J. Biol. Chem. 2008. V. 283. № 4. P. 1818–1830.
49. Deval E., Baron A., Lingueglia E., Mazarguil H., Zajac J.M., Lazdunski M. // Neuropharmacology. 2003. V. 44. № 5. P. 662–671.
50. Frey E.N., Pavlovicz R.E., Wegman C.J., Li C., Askwith C.C. // PLoS One. 2013. V. 8. № 8. e71733.
51. Sherwood T.W., Askwith C.C. // J. Neurosci. 2009. V. 29. № 45. P. 14371–14380.
52. Escoubas P., De Weille J.R., Lecoq A., Diochot S., Waldmann R., Champigny G., Moinier D., Menez A., Lazdunski M. // J. Biol. Chem. 2000. V. 275. № 33. P. 25116–25121.
53. Escoubas P., Bernard C., Lambeau G., Lazdunski M., Darbon H. // Protein Sci. 2003. V. 12. № 7. P. 1332–1343.
54. Chen X., Kalbacher H., Gründer S. // J. Gen. Physiol. 2005. V. 126. № 1. P. 71–79.
55. Chen X., Kalbacher H., Gründer S. // J. Gen. Physiol. 2006. V. 127. № 3. P. 267–276.
56. Bohlen C.J., Chesler A.T., Sharif-Naeini R., Medzihradszky K.F., Zhou S., King D., Sánchez E.E., Burlingame A.L., Basbaum A.I., Julius D. // Nature. 2011. V. 479. № 7373. P. 410–414.
57. Bohlen C.J., Julius D. // Toxicon. 2012. V. 60. № 3. P. 254–264.
58. Diochot S., Baron A., Salinas M., Douguet D., Scarzello S., Dabert-Gay A.S., Debayle D., Friend V., Alloui A., Lazdunski M., et al. // Nature. 2012. V. 490. № 7421. P. 552–555.
59. Baron A., Diochot S., Salinas M., Deval E., Noël J., Lingueglia E. // Toxicon. 2013. V. 75. P. 187–204.
60. Tikhonova T.B., Nagaeva E.I., Barygin O.I., Potapieva N.N., Bolshakov K.V., Tikhonov D.B. // Neuropharmacology. 2015. V. 89. P. 1–10.
61. Nagaeva E.I., Potapieva N.N., Tikhonov D.B. // Acta Naturae. 2015. V. 7. № 25. P. 95–101.
62. Shteinikov V.Y., Tikhonova T.B., Korkosh V.S., Tikhonov D.B. // Cell. Mol. Neurobiol. 2018. V.38. №4. P. 869-881.
63. Nagaeva E.I., Potapieva N.N., Nikolaev M. V., Gmiro V.E., Magazanik L.G., Tikhonov D.B. // Eur. J. Pharmacol. 2016. V. 788. P. 75–83.
64. Nagaeva E.I., Tikhonova T.B., Magazanik L.G., Tikhonov D.B. // Neurosci. Lett. 2016. V. 632. P. 136–140.
65. Shteinikov V.Y., Korosteleva A.S., Tikhonova T.B., Potapieva N.N., Tikhonov D.B. // Biochem. Biophys. Res. Commun. 2017. V. 490. № 4. P. 1314–1318.
66. Barygin O.I., Komarova M.S., Tikhonova T.B., Korosteleva A.S., Nikolaev M. V., Magazanik L.G., Tikhonov D.B. // Channels. 2017. V. 11. № 6. P. 648–659.
67. Jasti J., Furukawa H., Gonzales E.B., Gouaux E. // Nature. 2007. V. 449. № 7160. P. 316–323.
68. Gonzales E.B., Kawate T., Gouaux E. // Nature. 2009. V. 460. № 7255. P. 599–604.
69. Yoder N., Yoshioka C., Gouaux E. // Nature. 2018. V. 55. № 7696. P. 397-401.
70. Liechti L.A.L., Bernèche S., Bargeton B., Iwaszkiewicz J., Roy S., Michielin O., Kellenberger S. // J. Biol. Chem. 2010. V. 285. № 21. P. 16315–16329.
71. Li T., Yang Y., Canessa C.M. // J. Biol. Chem. 2009. V. 284. № 7. P. 4689–4694.
72. Li T., Yang Y., Canessa C.M. // Nat. Commun. 2011. V. 2. № 399. P. 1–7.

73. Baconguis I., Gouaux E. // Nature. 2012. V. 489. № 7416. P. 400–405.
74. Baconguis I., Bohlen C.J., Goehring A., Julius D., Gouaux E. // Cell. 2014. V. 156. № 4. P. 717–729.
75. Kellenberger S., Gautschi I., Schild L. // Mol. Pharmacol. 2003. V. 64. № 4. P. 848–856.
76. Schroeder C.I., Rash L.D., Vila-Farrés X., Rosengren K.J., Mobli M., King G.F., Alewood P.F., Craik D.J., Durek T. // Angew. Chemie - Int. Ed. 2014. V. 53. № 4. P. 1017–1020.
77. Duan B., Wang Y.-Z., Yang T., Chu X.-P., Yu Y., Huang Y., Cao H., Hansen J., Simon R.P., Zhu M.X., et al. // J. Neurosci. 2011. V. 31. № 6. P. 2101–2112.
78. Immke D.C., McCleskey E.W. // Neuron. 2003. V. 37. № 1. P. 75–84.
79. Besson T., Lingueglia E., Salinas M. // Neuropharmacology. 2017. V. 125. P. 429–440.

Consensus Integrase of a New HIV-1 Genetic Variant CRF63_02A1

Y. Y. Agapkina[1], M. A. Pustovarova[1], S. P. Korolev[1], D. P. Zyryanova[2], V. V. Ivlev[2], A. V. Totmenin[2], N. M. Gashnikova[2], M. B. Gottikh[1*]

[1]Lomonosov Moscow State University, Chemistry Department and Belozersky Institute of Physical Chemical Biology, Leninskie gory 1/40, 119991, Moscow, Russia

[2]State Research Center of Virology and Biotechnology "Vector", 630559, Koltsovo, Russia

*E-mail: gottikh@belozersky.msu.ru

Received October 12, 2018; in final form January 21, 2019

ABSTRACT **The high genetic variability of the human immunodeficiency virus (HIV-1) leads to a constant emergence of new genetic variants, including the recombinant virus CRF63_02A1, which is widespread in the Siberian Federal District of Russia. We studied HIV-1 CRF63_02A1 integrase (IN_CRF) catalyzing the incorporation of viral DNA into the genome of an infected cell. The consensus sequence was designed, recombinant integrase was obtained, and its DNA-binding and catalytic activities were characterized. The stability of the IN_CRF complex with the DNA substrate did not differ from the complex stability for subtype A and B integrases; however, the rate of complex formation was significantly higher. The rates and efficiencies of 3'-processing and strand transfer reactions catalyzed by IN_CRF were found to be higher, too. Apparently, all these distinctive features of IN_CRF may result from specific amino acid substitutions in its N-terminal domain, which plays an important role in enzyme multimerization and binding to the DNA substrate. It was also found that the drug resistance mutations Q148K/G140S and G118R/E138K significantly reduce the catalytic activity of IN_CRF and its sensitivity to the strand transfer inhibitor raltegravir. Reduction in sensitivity to raltegravir was found to be much stronger in the case of double-mutation Q148K/G140S.**

KEYWORDS **human immunodeficiency virus, CRF63_02A1 genetic variant, integrase, strand transfer inhibitor, drug resistance mutations.**

ABBREVIATIONS **HIV-1 – human immunodeficiency virus type 1; IN – integrase; IN_CRF – integrase of the HIV-1 genetic variant CRF63_02A1; IN_A – HIV-1 subtype A strain FSU-A integrase; IN_B – HIV-1 subtype B strain HXB-2 integrase; CRF – circulating recombinant forms of HIV-1; URF – unique recombinant forms of HIV-1; IC_{50} – inhibitor concentration suppressing enzyme activity by 50%; FC – change in the IC_{50} value for mutant proteins compared to the wild type; RT-PCR – reverse transcription polymerase chain reaction; SDS – sodium dodecyl sulfate; PAGE – polyacrylamide gel electrophoresis; DTT – dithiothreitol.**

INTRODUCTION

Human immunodeficiency virus type 1 (HIV-1) has high genetic variability, resulting in the occurrence of various subtypes, circulating recombinant forms (CRFs), and unique recombinant forms (URFs) [1]. The wide variety of HIV-1 genetic variants results from the high replication rate, the tendency toward recombination and reverse transcriptase errors [2–4]. Different HIV-1 subtypes have different geographical distributions. Subtype A prevails within the former USSR [5, 6], but there are also various CRFs [7–9]. Since 2010–2012, a new HIV-1 genetic variant, CRF63_02A1, has been found to dominate in regions of the Russian Federation characterized by the highest HIV epidemic rates, such as the Kemerovo, Novosibirsk, Tomsk, and the Altai regions [10–12]. Because of its rapid spread, this genetic variant requires in-depth research.

An important step in studying a new form of HIV-1 is the characterization of its enzymes, the integrase (IN) that catalyzes the integration of viral DNA into the genome of the infected cell being one of them [13]. Three IN inhibitors – raltegravir, elvitegravir and dolutegravir – are currently used as components of antiretroviral therapy [14]. However, the emergence of viral resistance to these inhibitors has been identified [15, 16]. It is known that both mutations conferring drug resistance and the mechanisms of their occurrence in viruses of different subtypes may vary [17–22]. In this regard, it is important to study the effect of the natural polymorphism of IN on its properties.

In this study, we have characterized IN of a new HIV-1 genetic variant, CRF63_02A1 (IN_CRF), and compared it to that of HIV-1 subtype A (IN_A), which is also widespread in Russia. In particular, we have studied the influence of the structural differences between the enzymes on their DNA-binding and catalytic activities. The influence of drug resistance mutations on the catalytic and DNA-binding activity of IN_CRF, as well as its sensitivity to the strand transfer inhibitor raltegravir, has also been analyzed.

MATERIALS AND METHODS

Designing the consensus sequence of IN_CRF

The HIV-1 subtype was determined using a phylogenetic and recombination analysis according to the procedure described earlier in [10, 11, 23]. The IN_CRF consensus sequence was created using the BioEdit software (Ibis Biosciences, Carlsbad, CA).

HIV-1 RNAs were isolated using a commercial Real-best DeltaMag HBV/HCV/HIV kit (Vector-Best JSC, Russia) from clinical blood plasma samples (250 μl) from two treatment-naïve patients infected with HIV-1 variants that carried the IN genes most similar to the calculated IN_CRF consensus sequence. DNA fragments (878 bps) encoding IN_CRF were prepared by RT-PCR from the isolated RNA samples using a commercial LongRange 2Step RT-PCR kit (Qiagen, USA) and primers containing restriction sites for subsequent cloning.

Preparation of the vector encoding IN_CRF

DNA fragments encoding IN_CRF were ligated in the plasmid pCR_2.1Topo using the commercial TOPO® TA Cloning® Kit (pCR™2.1-TOPO®, Thermo Fisher Scientific Inc., USA). Plasmid DNA was isolated from 60 pCR_2.1Topo_IN clones (30 clones for each HIV-1 variant) using a commercial Plasmid Purification Mini Kit (Qiagen, USA); all the DNA samples were sequenced. Plasmid pCR_2.1Topo_IN_CRF* containing an IN sequence differing from the consensus one by two amino acid substitutions was selected for further sub-cloning in expressing vector pET_15b in frame with the codons for the N-terminal His_6-tag (His-tag) (Novagen, USA).

The vector pET_15b_IN_CRF with the consensus IN_CRF sequence was obtained from the vector pET-15b_IN_CRF* by sequential site-directed mutagenesis, resulting in the amino acid substitutions I32V and I259V. The vectors encoding IN_CRF with substitutions Q148K/G140S and G118R/E138K were prepared by site-directed mutagenesis of the plasmid pET_15b_IN_CRF using a QuikChange II Site-Directed mutagenesis kit (Agilent Technologies, USA).

The prokaryotic expression vector pET_15b carrying the gene of IN_A was a kind gift from M.G. Belikova-Isaguliants (Ivanovsky Institute of Virology, Russia).

Preparation of recombinant proteins

Consensus IN_CRF and IN_A proteins and those with the mutations Q148K/G140S and G118R/E138K were expressed in *Escherichia coli* strain Rosetta (DE3) (Novagen) and purified according to [24, 25]. The proteins were analyzed by 12% Laemmli PAGE, followed by staining with SimplyBlue™ SafeStain (Invitrogen, USA).

Oligodeoxyribonucleotides

Oligodeoxyribonucleotides U5B (5'-GTGTGGAAAATCTCTAGCAGT-3'), U5B with fluorescein residue at 5'-end (5'-Fl-U5B), U5B-2 (5'-GTGTGGAAAATCTCTAGCA-3') and U5A (5'-ACTGCTAGAGATTTTCCACAC-3'), forming DNA substrates of IN, and all primers were purchased from DNA synthesis OJSC (Russia).

The radioactive ^{32}P-label was inserted at the 5'-end of the U5B and U5B-2 oligonucleotides, and DNA substrates were formed as described in [25].

Integrase DNA binding activity assays

The kinetics of DNA binding by IN was studied using a fluorescence polarization assay on a Cary Eclipse Fluorescence Spectrophotometer (Varian, USA) according to [26]. The duplex 5'-Fl-U5B/U5A (10 nM) was incubated with 100 nM IN in 200 μl of buffer A (20 mm HEPES (pH 7.2), 10 mm DTT, 7.5 mm $MgCl_2$) at 25°C, and the values of fluorescence polarization of fluorescein (λ_{ex} = 492 nm, λ_{em} = 520 nm) were recorded at certain time points. A curve corresponding to the time dependence of changes in fluorescence polarization was constructed, and the binding rate constant (k_{on}) was calculated using the equation $[IN/DNA] = [DNA]_0 \times (1\text{-}e^{-kon*t})$ [27].

The dissociation constant (K_d) of the IN/DNA complex was determined using the DRaCALA method (Differential Radial Capillary Action of Ligand Assay) [28]. The U5B/U5A duplex (5 nM) with the ^{32}P-labeled U5B-chain was incubated with IN at different concentrations (0–500 nM) in 10 μl of buffer A for 20 min at 25°C. Then, 5 μl aliquots of the mixture were applied on the Amersham™ Hybond™-ECL nitrocellulose membrane. A Typhoon FLA9500 Phosphorimager (GE Healthcare, USA) was used for membrane analysis and quantification.

Integrase catalytic activity assays

For the 3'-end processing reaction, 5 nM U5B/U5A duplex (with ^{32}P-labeled U5B-chain) was incubated with

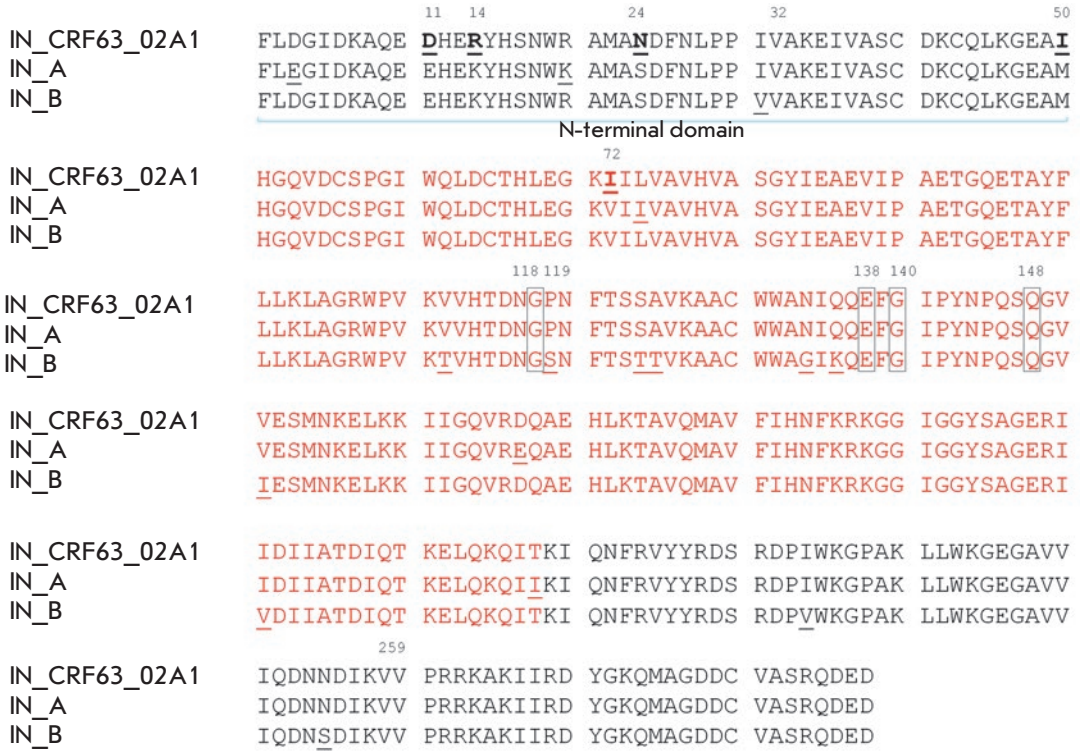

Fig. 1. Amino acid sequences of IN_CRF, IN_A, and IN_B. The amino acids specific to IN_CRF are highlighted in bold and underlined; amino acids specific to other subtypes are underlined; amino acids whose mutations lead to drug resistance of the virus are shown with rectangles; amino acids of the catalytic domain are shown in red

100 nM IN in buffer A as described in [25]. The reaction products were precipitated and analyzed by electrophoresis in 20% polyacrylamide/7 M urea gel in TBE buffer. Autoradiographic data analysis was performed using a GE Typhoon FLA 9500 scanner (GE Healthcare, USA). The efficiency of 3'-processing was determined using the ImageQuantTM 5.0 software as the ratio between the intensities of the bands corresponding to the U5B substrate and the reaction product U5B-2.

When analyzing the accumulation kinetics of the 3'-processing product, the reaction mixture was incubated at 37°C. The incubation time was varied from 5 min to 7 h; the reaction efficiency versus time was plotted. The initial reaction rate was determined from the angle of inclination of the initial section of the kinetic curve (~60 min).

The dependence between the 3'-processing efficiency and substrate concentration was determined by varying the DNA concentration (0; 2.5; 4; 10; 20; 50; 100 nM). The graphs showing the reaction efficiency versus substrate concentration were plotted; the maximum reaction rate (V_{max}) and the Michaelis constant (K_M) were determined.

For the strand transfer reaction, 10 nM U5B-2/U5A duplex (with ^{32}P-labeled U5B-2) was incubated with 100 nM IN in buffer A for 2 and 4 h at 37°C. The reaction products were separated and analyzed as described above.

Inhibition of the strand transfer reaction

The strand transfer reaction was carried out as described above for 2 h in the presence of increasing inhibitor concentrations (raltegravir, Santa Cruz Biotechnology Inc., USA). The IC_{50} value was determined based on the results of three independent experiments.

RESULTS AND DISCUSSION

Designing the consensus IN_CRF sequence and protein purification

IN genes from 324 HIV-1 isolates from HIV-infected treatment-naïve patients in the Siberian (n = 250) and Ural (n = 74) federal districts of Russia were sequenced. Phylogenetic analysis showed that genetic variants of subtypes A (24.3%) and B (3.3%) were present, as well as recombinant forms CRF63_02A1 (55.3%) and various URFs formed as a result of secondary recombination of HIV-1 CRF63_02A1 and subtype A (6.7%).

Multiple alignment of the identified nucleotide sequences of CRF63_02A1 IN was performed, followed by translation, construction of the consensus amino acid IN sequence and its alignment with the

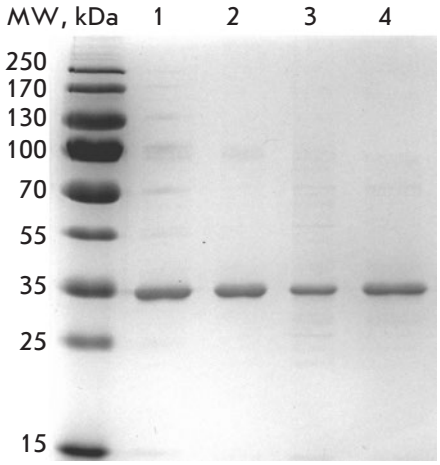

Fig. 2. SDS-PAGE analysis of purified consensus IN_CRF and its mutant forms G118R/E138K and Q148K/G140S. Lane *1* – IN_CRF; lane *2* – IN_A; lane *3* – IN_CRF (G118R/E138K); lane *4* – IN_CRF (Q148K/G140S); MW – molecular weight marker

sequences of IN from HIV-1 subtypes A and B (*Fig. 1*). Mutations typical of this HIV-1 genetic variant, e.g. E11D (93.8%), K14R (81.3%), S24N (100%), and M50I (75%), were found. The mutation L74I specific to IN_A was found only in 4% of the sequences of CRF63_02A1 IN.

Among all the studied HIV-1 IN sequences, we selected one variant that was the closest to the consensus IN_CRF. Preparation of the cDNA encoding IN_CRF and its consecutive cloning allowed us to obtain the pET-15b_IN_CRF* vector, which was then subjected to site-directed mutagenesis to introduce the I32V and I259V substitutions and to obtain the pET-15b_IN_CRF expression vector coding for a consensus IN sequence. Genetic constructions with the drug resistance mutations G118R/E138K and Q148K/G140S were obtained by site-directed mutagenesis of pET-15b_IN_CRF. The constructed vectors were used for prokaryotic expression of recombinant IN proteins and their subsequent purification on Ni-NTA-agarose to a purity ≥ 90% (*Fig. 2*).

Characterization of DNA-binding activity

During integration, retroviral integrases bind to the ends of viral DNA and then interact with cellular DNA; the latter interaction is not sequence-specific [29]. Recombinant HIV-1 IN protein usually has the same affinity for DNA duplexes of different structures [30]. We evaluated the capacity of IN_CRF to bind the 21-mer DNA substrate representing the terminal sequence of U5 LTR of viral DNA. The corresponding experiments with IN_A were carried out in parallel.

Stability of the IN/DNA complex was determined using the DRaCALA method (Differential Radial Capillary Action of Ligand Assay) [28] that had been used earlier to study the complexes formed between IN_B and DNA [31]. We found that the K_d values were similar for the complexes of DNA with both IN_CRF and IN_A (*Fig. 3A* and *Table 1*), as well as IN_B [32].

The fluorescence polarization method was applied to study the kinetics of IN binding to the fluorescein-labelled duplex 5'-Fl-U5B/U5A used as the DNA substrate. Having compared DNA binding by IN_CRF and IN_A, we found that the rate of DNA binding was higher for IN_CRF; the binding rate constants (k_{on}) for these enzymes differed 2.8-fold (*Fig. 3B* and *Table 1*). The binding rate constant k_{on} for IN_A (0.24 min^{-1}) was close to the value determined earlier for IN_B (0.18 min^{-1}) [27].

The sequences of INs of HIV-1 subtypes A and B differ by 16 amino acid substitutions, 11 of which reside in the catalytic core; two reside in the C-terminal; and three, in the N-terminal domain. The latter three substitutions are synonymous: D3E, R20K, and V31I (*Fig. 1*). IN_CRF differs from IN_A and IN_B by four unique amino acid substitutions in the N-terminal domain: E11D, K14R, S24N, and M50I (*Fig. 1*). Keeping in mind that the rates of DNA substrate binding to IN_A and IN_B were comparable and differed significantly from that for IN_CRF, we could assume that this rate is mainly affected by the structure of the IN N-terminal domain. It is responsible for the IN multimeric state, which is crucial for its catalytic activity [33], and participates in binding of IN to the DNA substrate (viral DNA) [34–36]. There are two substitutions, S24N and M50I, in the structure of IN_CRF, which seem to be of greatest interest. The presence of an amide group in Asn and a branched chain in Ile can affect the intermolecular interactions upon formation of the catalytically active state of IN. In addition, Lys14 is in direct contact with viral DNA and plays an important role in IN multimerization [35, 37]. In IN_CRF, Lys14 is substituted with Arg. Although both these amino acids are positively charged, the Arg residue is more bulky, less hydrophobic and has a higher pKa value than Lys [38, 39]. Besides, Arg is characterized by positively charged delocalization within the guanidine group and can form multiple hydrogen bonds with different orientations [40, 41], which can contribute to DNA substrate binding.

Thus, amino acid substitutions that are inherent to IN_CRF due to natural polymorphism did not affect the stability of its complex with the DNA substrate but significantly influenced the complex formation rate.

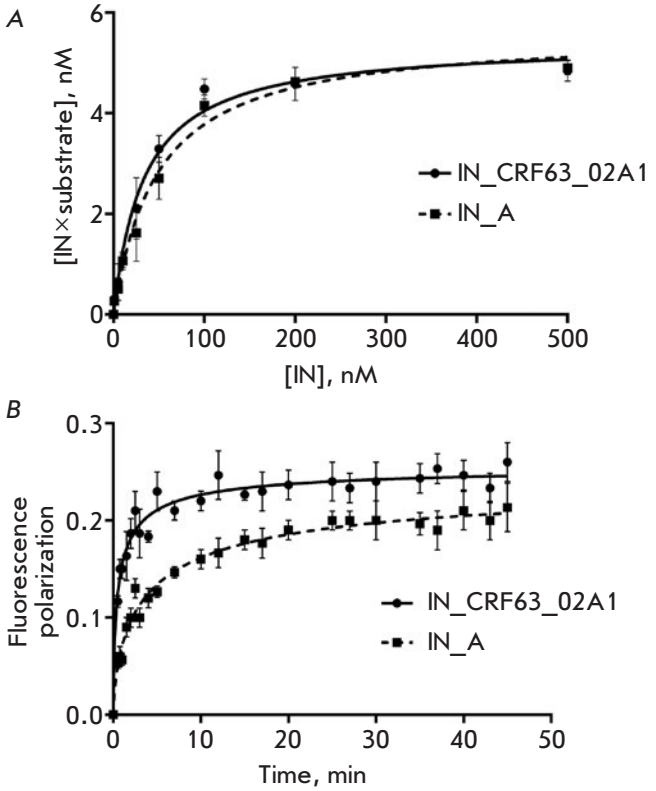

Fig. 3. Characterization of the DNA-binding activity of IN_CRF as compared to that of IN_A. The average values of at least three independent measurements for which the standard deviation did not exceed 15% are given. *A* – The dependence between the IN/DNA-substrate complex concentration and IN concentration. *B* – The kinetics of DNA-substrate fluorescence polarization after DNA binding to IN_CRF and IN_A

Table 1. DNA-binding and catalytic activities of IN_CRF and IN_A

Characteristics	IN_CRF	IN_A
K_d, nM	23 ± 6	25 ± 7
k_{on}, min^{-1*}	0.69 ± 0.09	0.24 ± 0.02
Relative efficiency of 3'-processing, %**	100	71
V_0 (3'-processing), pmol/min*	19.3 ± 2.1	9.8 ± 2.3
V_{max}, pM/min*	26 ± 1	16 ± 1
K_M, nM*	2.6 ± 0.3	4.6 ± 0.8
$V_{max}/K_M \times 10^3$, min^{-1*}	10 ± 1	3.5 ± 0.6
Relative strand transfer efficiency, %**	100	77
V_0 (strand transfer), pmol/min*	11.4 ± 3.2	6.5 ± 2.8

Note. The average values of at least three independent measurements (± standard deviation) are presented.
*$P \leq 0.05$.
**Reaction efficiency after 300 min as compared to that for the consensus IN_CRF taken as 100%.

Characterization of the catalytic activity of IN_CRF

IN is involved in two successive reactions during viral replication: 3'-end processing (in which it catalyzes the cleavage of the GT dinucleotide from both 3'-ends of viral DNA) and strand transfer (insertion of the processed viral DNA into the cell DNA). Both of these reactions can be studied *in vitro* using standard protocols [25]. We used a standard synthetic DNA duplex U5B/U5A mimicking the U5 region of HIV-1 DNA LTR for the 3'-processing reaction. The duplex contained a [5'-^{32}P]-labelled U5B strand, which was turned into a product shortened by two nucleotides as a result of the reaction. In the strand transfer reaction, the [5'-^{32}P]-U5B-2/U5A duplex with the already processed U5B-2 strand was used both as a substrate and a target.

Studying the kinetics of 3'-processing showed that IN_CRF processes its substrate more efficiently and faster than IN_A does (*Fig. 4*, *Table 1*). In order to thoroughly clarify the reasons for the increased reaction efficiency, we determined the kinetic parameters of 3'-processing (K_M and V_{max}). It turned out that the K_M is 1.8 times lower and V_{max} is 1.6 times higher for IN_CRF than for IN_A (*Table 1*). Therefore, IN_CRF is characterized by a higher 3'-processing rate, which is achieved at lower substrate concentrations. Accordingly, the catalytic efficiency (V_{max}/K_M) of IN_CRF was almost three times higher than that of IN_A (*Table 1*). Obviously, such a high activity of IN_CRF cannot be attributed only to the higher rate of the DNA substrate binding (*Fig. 3*), especially taking into account that the dissociation constants for the complexes of both enzymes with DNA were similar. As mentioned above, the N-terminal domain of IN is responsible for its multimeric state, which changes when IN binds to its DNA substrate [42, 43] to form the catalytically active enzyme-substrate complex. It is possible that amino acid substitutions located on the N-terminal domain of IN_CRF contribute to the formation of such a complex, thereby stimulating the more efficient reaction.

When studying the strand transfer reaction, we determined the reaction efficiency and rate, as well as the pattern of the reaction products, which demonstrates on which site the substrate is inserted into the target DNA. Strand transfer efficiency and rate were again higher for IN_CRF, whereas the pattern of products was the same (*Fig. 5*). Of note, the profiles of the strand

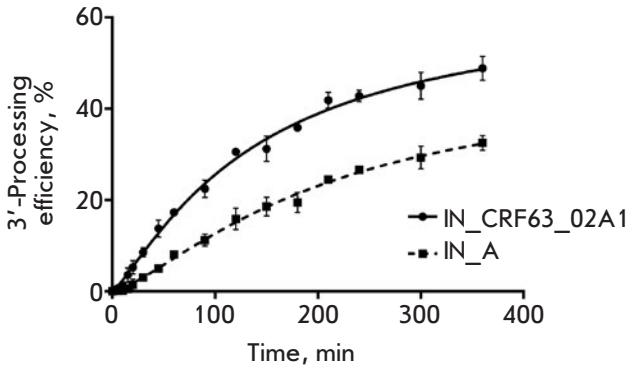

Fig. 4. 3'-Processing efficiency as a function of time

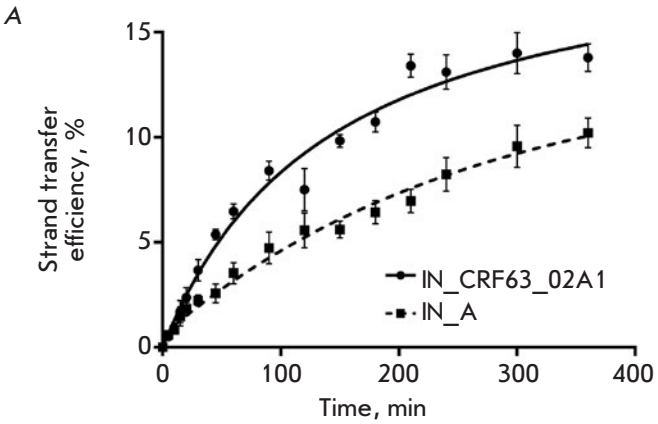

Fig. 5. Characteristics of the strand transfer reaction catalyzed by IN_CRF and IN_A. The average values of at least three independent measurements for which the standard deviation did not exceed 15% are given. *A* – Strand transfer kinetics. *B* – The products of the strand transfer reaction for IN_CRF and IN_A (electrophoretic analysis of the reaction products after 300 and 360 min)

transfer products were different for IN_A and IN_B [25]. The profiles of the integration products can vary if the modes of complex formation between IN and target DNA differ. The catalytic and especially C-terminal domains of IN are known to be mainly involved in the target DNA binding [36]; their structures are similar for IN-CRF and IN_A and significantly differ from that of IN_B (*Fig. 1*). Therefore, location of the target DNA in its complexes with IN_CRF and IN_A is similar and differs from its location in the complex with IN_B.

The influence of drug resistance mutations on IN_CRF activity and its sensitivity to raltegravir

Since no data are available about drug resistance mutations in the genetic variant of the virus under study, we introduced mutations known to confer resistance to strand transfer inhibitors in other HIV-1 subtypes in the IN_CRF gene. We chose the primary mutation Q148K and the secondary compensatory mutation G140S causing IN resistance to raltegravir and elvitegravir [44, 45]. The G118R and E138K substitutions resulting in reduced IN sensitivity to dolutegravir were also selected [46, 47]. Therefore, IN_CRF protein variants containing Q148K/G140S and G118R/E138K double substitutions were prepared (*Fig. 2*). We investigated their DNA binding activity and the dependence of their 3'-end processing efficiency on the IN concentration and reaction time. It turned out that the introduced mutations did not affect the stability of the enzyme-substrate complex but significantly reduced the IN catalytic activity (*Table 2*). Interestingly, the Q148K/G140S double substitution reduced the IN_CRF activity more significantly than G118R/E138K did. The initial rate of 3'-processing for the mutant IN proteins decreased 7.1- and 3.4-fold, respectively, as compared to that for the initial consensus IN_CRF. We had previously revealed a decline in the catalytic activity of IN_A in the 3'-processing reaction resulting from the Q148K/G140S and G118R/E138K mutations, but this decline was the same for both double mutations (3.8-fold) [25].

Similarly to IN_A [25], the Q148K/G140S and G118R/E138K substitutions significantly reduced the efficiency of strand transfer catalyzed by IN_CRF (*Table 2*). The decrease was slightly stronger in the case of G118R/E138K than for the Q148K/G140S mutation: 4.6-fold versus 3.7-fold, respectively. Interestingly, G118R/E138K substitutions in the case of IN_B affected the strand transfer efficiency very slightly [25]. The strong negative effect of these substitutions in both IN_CRF and IN_A is obviously related to the natural polymorphism S119P (*Fig. 1*), resulting in

Table 2. DNA-binding and catalytic activities, as well as raltegravir resistance of IN_CRF, IN_A, and their mutant forms Q148K/G140S, G118R/E138K

Characteristics	IN_CRF			IN_A		
	consensus	*Q148K/G140S*	*G118R/E138K*	*consensus*	*Q148K/G140S**	*G118R/E138K**
K_d, nM	23 ± 6	28 ± 9	25 ± 5	25 ± 7	ND	ND
V_0 (3'-processing), pmol/min	19.3 ± 2.1	2.7 ± 0.4	5.6 ± 1.2	9.8 ± 2.3	2.6 ± 0.1	2.6 ± 0.4
Relative efficiency of 3'-processing, %	100	22	31	100	25	24
Relative strand transfer efficiency, %	100	27	22	100	20	23
Raltegravir IC_{50}, nM	7 ± 2	500 ± 50	50 ± 3	5 ± 2	400 ± 150	7 ± 3
FC	1	71	7	1	80	1.4

Note. The average values of at least three independent measurements (± standard deviation) are presented. ND – the values were not determined.
*According to [25].

the more rigid conformation of the active center and the reduced ability of both integrases to adapt to the G118R mutation. We assume that it is the rigid conformation of the active center within IN_CRF and IN_A bearing the G118R/E138K double mutation that limits their ability to bind to the target DNA, thus resulting in a sharp decrease in the number of strand transfer products for the G118R/E138K mutants (*Fig. 6* and [25]). The Q148K/G140S substitutions did not change the pattern of the reaction products when compared to the initial IN_CRF (*Fig. 6*).

We also studied the sensitivity of IN_CRF and its Q148K/G140S and G118R/E138K mutants to inhibition by raltegravir, the drug used for treatment of HIV-infected patients in the Russian Federation. IN_CRF was efficiently inhibited by raltegravir (*Table 2*); the IC_{50} value was close to those obtained earlier for IN_A and IN_B [25]. Introduction of Q148K/G140S resistance mutations detected in other HIV-1 subtypes also led to the emergence of IN_CRF resistance. We observed a 70-fold increase in the IC_{50} value, which was consistent with the data previously obtained for IN_A [25]. The G118R/E138K mutations also reduced the sensitivity of IN_CRF to raltegravir but not substantially (FC = 7, *Table 2*). It should be noted that IN_A bearing G118R/E138K mutations exhibited almost no drop in sensitivity to raltegravir [25].

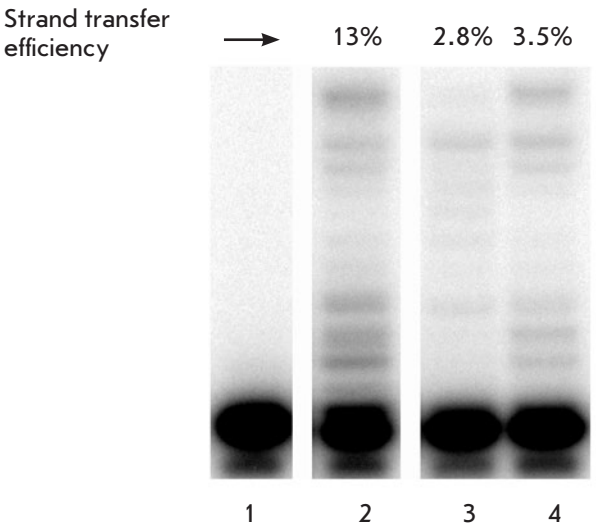

Fig. 6. Electrophoretic analysis of the strand transfer reaction products for IN_CRF (lane *2*) and its mutants G118R/E138K (lane *3*) and Q148K/G140S (lane *4*) (reaction time 300 min). Lane *1* – DNA control without IN added. The reaction efficiency is shown above the gel

CONCLUSIONS

The recombinant IN protein from a new HIV-1 genetic variant, CRF63_02A1, that is rapidly spreading across Siberia has been identified and characterized for the first time. IN_CRF was found to catalyze both 3'-processing and strand transfer reactions faster and more efficiently than IN of HIV-1 subtype A does. The high rates of these reactions are likely to be ensured by faster binding of the substrate DNA and the higher catalytic efficiency that were found for IN_CRF. Apparently, all these changes could be attributed to the E11D, K14R, S24N, and M50I amino acid substitutions residing in the N-terminal domain of IN_CRF, which plays an important role in IN multimerization and binding to viral DNA. However, due to the lack of significant differences in the catalytic and C-terminal domains of IN_CRF and IN_A, the pattern of the strand transfer products characterizing a mode of the target

DNA positioning in the active site of the enzyme-substrate complex was similar for both INs.

The results obtained allowed us to suggest that the resistance of the HIV-1 genetic variant CRF63_02A1 to raltegravir may develop primarily due to the emergence and fixation of Q148K/G140S mutations as it was described for other HIV-1 subtypes [48]. The introduction of these mutations in IN_CRF led to a 70-fold increase in resistance to this inhibitor as compared to the initial parental IN_CRF. The G118R/E138K mutations resulted in only a seven-fold increase of the resistance of IN_CRF to raltegravir. ●

This work was supported by the Russian Science Foundation (grant no. 16-15-10238).

REFERENCES

1. Foley B., Leitner T., Apetrei C., Hahn B., Mizrachi I., Mullins J., Rambaut A., Wolinsky S., Korber B. // Theoretical Biology and Biophysics Group. Los Alamos: Los Alamos National Laboratory. 2013. https://www.hiv.lanl.gov/content/sequence/HIV/CRFs/CRFs.html
2. Onafuwa-Nuga A., Telesnitsky A. // Microbiol Mol Biol Rev. 2009. V. 73. № 3. P. 451–480.
3. Li G., Piampongsant S., Faria N.R., Voet A., Pineda-Peña A.C., Khouri R., Lemey P., Vandamme A.M., Theys K. // Retrovirology. 2015. V. 12. P.18
4. Hemelaar, J. // Trends Mol Med. 2012. V.18. №3. P.182-192.
5. Diez-Fuertes F., Cabello M., Thompson M.M. // Infect Genet Evol. 2015. V. 33. P. 197-205.
6. Foley B.T., Leitner T., Paraskevis D., Peeters M. // Infect Genet Evol. 2016. V. 46. P. 150–158.
7. Bobkova M. // AIDS Rev. 2013. V. 15. № 4. P. 204-212.
8. Baryshev P. B., Bogachev V. V., Gashnikova N. M. // Russia Arch Virol. 2012. V. 157. № 12. P. 2335–2341.
9. Baryshev P. B., Bogachev V. V., Gashnikova N. M. // AIDS Res Hum Retroviruses. 2014. V. 30. № 6. P. 592–597.
10. Gashnikova N.M., Bogachev V.V., Baryshev P.B., Totmenin A.V., Gashnikova M.P., Kazachinskaya A.G., Ismailova T.N., Stepanova S.A., Chernov A.S., Mikheev V.N. // Russia AIDS Res Hum Retroviruses. 2015. V. 31. № 4. P. 456-460.
11. Gashnikova N.M., Zyryanova D.P., Astakhova E.M., Ivlev V.V., Gashnikova M.P., Moskaleva N.V., Aikin S.S., Bulatova T.N., Pustylnikov S.V, Bocharov EF, Totmenin AV. // Arch Virol. 2017. V.162. № 2. P. 379-390.
12. Kazennova E. V., Laga V., Lapovok I., Glushchenko N., Neshumaev D., Vasilyev A., Bobkova M. // AIDS Res Hum Retroviruses. 2014. V. 30. № 8. P. 742–752.
13. Krishnan L., Engelman A. // J. Biol. Chem. 2012. V. 287. № 49. P. 40858-40866.
14. Lennox J.L. // Curr Opin HIV AIDS. 2012. V. 7. № 5. P. 409-414.
15. Quashie P.K., Mesplède T., Wainberg M.A. // Curr Opin Infect. Dis. 2013. V. 26. № 1. P. 43–49.
16. Anstett K., Brenner B., Mesplede T., Wainberg M.A. // Retrovirology. 2017. V. 14. № 1. P. 36.
17. Maiga I., Malet I., Soulie C., Derache A., Koita V., Amellal B., Tchertanov L., Delelis O., Morand-Joubert L., Mouscadet J.F. et al. // Antivir Ther. 2009. V. 14. № 1. P. 123-129.
18. Brenner B.G., Lowe M., Moisi D., Hardy I., Gagnon S., Charest H., Baril J.G., Wainberg M.A., Roger M. // J Med Virol. 2011. V. 83. № 5. P. 751-759.
19. Bar-Magen T., Donahue D.A., McDonough E.I., Kuhl B.D., Faltenbacher V.H., Xu H., Michaud V., Sloan R.D., Wainberg M.A. // AIDS. 2010. V. 24. № 14. P. 2171-2179.
20. Quashie P.K., Oliviera M., Veres T., Osman N., Han Y.S., Hassounah S., Lie Y., Huang W., Mesplede T., Wainberg M.A. // J Virol. 2015. V. 89. № 6. P. 3163–3175.
21. Depatureaux A., Mesplede T., Quashie P., Oliveira M., Moisi D., Brenner B., Wainberg M. // J. Int. AIDS Soc. 2014. V. 17. № 4. P. 19738.
22. Depatureaux A., Mesplede T., Quashie P., Oliveira M., Moisi D., Plantier J.C., Brenner B., Wainberg M.A. // J. Acquir. Immune Defic. Syndr. 2015. V. 70. № 1. P. 9–15.
23. Gashnikova N.M., Astakhova E.M., Gashnikova M.P., Bocharov E.F., Petrova S.V., Pun'ko O.A., Popkov A.V., Totmenin A.V. // Biomed. Res. Int. 2016. V. 2016. Article ID 2496280.
24. Leh H., Brodin P., Bischerour J., Deprez E., Tauc P., Brochon J.C., LeCam E., Coulaud D., Auclair C., Mouscadet J.F. // Biochemistry. 2000. V. 39. № 31. P. 9285-9294.
25. Shadrina O. A., Zatsepin T. S., Agapkina Y. Y., Isaguliants M. G., Gottikh M. B. // Acta naturae. 2015. V. 7. № 1. P. 43-52.
26. Deprez E., Barbe S., Kolaski M., Leh H., Zouhiri F., Auclair C., Brochon J.C., Le Bret M., Mouscadet J.F. // Mol Pharmacol. 2004. V. 65. № 1. P. 85–98.
27. Smolov M., Gottikh M., Tashlitskii V., Korolev S., Demidyuk I., Brochon J.C., Mouscadet J.F., Deprez E. // FEBS J. 2006. V. 273. № 6. P. 1137-1151.
28. Donaldson G.P., Roelofs K.G., Luo Y., Sintim H.O., Lee V.T. // Nucleic Acids Res. 2012. V. 40. № 7, e48.
29. Khan E., Mack J.P., Katz R.A., Kulkosky J., Skalka A.M. // Nucleic Acids Res. 1991. V. 19. № 4. P. 851-860.
30. Agapkina J., Smolov M., Barbe S., Zubin E., Zatsepin T., Deprez E., Le Bret M., Mouscadet J-F., Gottikh M. // J Biol Chem. 2006. V. 281. № 17. P. 11530-11540.
31. Agapkina J., Yanvarev D., Anisenko A., Korolev S., Vepsäläinen J., Kochetkov S., Gottikh M. // Eur J Med Chem. 2014. V. 73. P. 73-82.
32. Shadrina O., Krotova O., Agapkina J., Knyazhanskaya E., Korolev S., Starodubova E., Viklund A., Lukashov V., Magnani M., Medstrand P. et al. // Biochimie. 2014. V. 102. P. 92–101.
33. Zheng R., Jenkins T.M., Craigie R. // Proc Natl Acad Sci USA. 1996. V. 93. № 24. P. 13659–13664.
34. Lesbats P., Engelman A.N., Cherepanov P. // Chem. Rev. 2016. V. 116. № 20. P. 12730–12757.
35. Zhao Z., McKee C.J., Kessl J.J., Santos W.L., Daigle J.E., Engelman A., Verdine G., Kvaratskhelia M. // J Biol Chem. 2008. V. 29. № 283. № 9. P. 5632-5641.
36. Passos D.O., Li M., Yang R., Rebensburg S.V., Ghirlando R., Jeon Y., Shkriabai N., Kvaratskhelia M., Craigie R., Lyumkis D. // Science. 2017. V. 355. № 6320. P. 89-92.
37. McKee C.J., Kessl J.J., Shkriabai N., Dar M.J., Engelman A., Kvaratskhelia M. // J Biol Chem. 2008. V. 283. № 46. P. 31802–31812.
38. Sokalingam S., Raghunathan G., Soundrarajan N., Lee S.G. // PLoS One. 2012. V. 7. № 7. e40410.

39. Mant C.T., Kovacs J.M., Kim H.M., Pollock D.D., Hodges R.S. // Biopolymers. 2009. V. 92. № 6. P. 573–595.
40. Dougherty D.A. // J Nutr. 2007. V. 137. P. 1504S–1508S.
41. Chan D.I., Prenner E.J., Vogel H.J. // Biochim Biophys Acta. 2006. V. 1758. P. 1184–1202.
42. Deprez E., Tauc P., Leh H., Mouscadet J.F., Auclair C., Hawkins M.E., Brochon J.C. // Proc Natl Acad Sci U S A. 2001. V. 98. № 18. P. 10090-10095.
43. Guiot E., Carayon K., Delelis O., Simon F., Tauc P., Zubin E., Gottikh M., Mouscadet J.F., Brochon J.C., Deprez E. // J Biol Chem. 2006. V. 281. № 32. P. 22707-22719.
44. Malet I., Delelis O., Valantin M.A., Montes B., Soulie C., Wirden M., Tchertanov L., Peytavin G., Reynes J., Mouscadet J.-F. et al. // Antimicrob Agents Chemother. 2008. V. 52. № 4. P. 1351–1358.
45. Nakahara K., Wakasa-Morimoto C., Kobayashi M., Miki S., Noshi T., Seki T., Kanamori-Koyama M., Kawauchi S., Suyama A., Fujishita T., et al. // Antiviral Res. 2009. V. 81. № 2. P. 141–146.
46. Quashie P.K., Mesplède T., Han Y.S., Veres T., Osman N., Hassounah S., Sloan R.D., Xu H.T., Wainberg M.A. // Antimicrob Agents Chemother. 2013. V. 57. № 12. P. 6223–6235.
47. Wainberg M.A., Han Y.S. // J Virus Erad. 2015. V. 1. № 1. P. 13-16.
48. Malet I., Gimferrer Arriaga L., Artese A., Costa G., Parrotta L., Alcaro S., Delelis O., Tmeizeh A., Katlama C., Valantin M.A. // J Antimicrob Chemother 2014. V. 69. № 8. P. 2118–2122.

Isolation, Purification and Characterization of L,D-transpeptidase 2 from *Mycobacterium tuberculosis*

S. M. Baldin[1,2], T. A. Shcherbakova[1], V. K. Švedas[1*]
[1]Lomonosov Moscow State University, Belozersky Institute of Physicochemical Biology, Leninskie gory 1, bldg. 40, 119991, Moscow, Russia
[2]Lomonosov Moscow State University, Faculty of Chemistry, Leninskie gory 1, bldg. 3, 119991, Moscow, Russia
*E-mail: vytas@belozersky.msu.ru
Received November 21, 2016; in final form, December 13, 2016

ABSTRACT ***L,D*-transpeptidase 2 from *Mycobacterium tuberculosis* plays a key role in the formation of nonclassical 3-3 peptidoglycan cross-links in a pathogen's cell wall making it resistant to a broad range of penicillin antibiotics. The conditions of cultivation, isolation, and purification of recombinant *L,D*-transpeptidase 2 from *M. tuberculosis* have been optimized in this study. Oxidation of the free SH groups of catalytic cysteine Cys354 is an important factor causing the inactivation of the enzyme, which occurs during both the expression and storage of enzyme preparations. The biochemical characteristics of purified *L,D*-transpeptidase 2 and *L,D*-transpeptidase 2 lacking domain A were determined; the kinetic constants of enzyme-catalyzed nitrocefin transformation were evaluated.**

KEYWORDS **L,D-transpeptidase, *Mycobacterium tuberculosis*, enzyme purification, recombinant enzyme, enzyme reactivation.**

ABBREVIATIONS **Ac – acetyl; Ldt – *L,D*-transpeptidase; LdtMt1 and LdtMt2 – *L,D*-transpeptidases from *Mycobacterium tuberculosis* type 1 and 2; m-DAP – meso-diaminopimelic acid; IG –immunoglobulin; Amp – ampicillin; IPTG – isopropyl-β-*D*-1-thiogalactopyranoside; LEW – lysis/equilibration/wash buffer; PAGE electrophoresis – polyacrylamide gel electrophoresis; DTT – dithiothreitol; DMSO – dimethyl sulfoxide.**

INTRODUCTION

Tuberculosis is a dangerous infectious disease caused by *Mycobacterium tuberculosis*. The number of cases of multidrug-resistant tuberculosis is increasing with every passing year [1]. Tuberculosis therapy consists in a combined use of four major first-line drugs: rifampicin (an inhibitor of DNA-dependent RNA polymerase), isoniazid and pyrazinamide (blockers of synthesis of mycolic acids essential to cell wall formation in *M. tuberculosis*), and ethambutol (an inhibitor of arabinosyltransferase, the enzyme involved in arabinogalactan synthesis). Treatment of patients in the active phase of the disease can last up to 6 months. In some cases, *M. tuberculosis* may persist in the lungs in the so-called stationary phase, when bacterial growth slows down and neither immune response nor resistance to various antibiotics is observed [2]. In this regard, it is of great interest to search for drugs specific to the previously unknown molecular targets related to the features of vital activity and the structural organization of the causative agent of tuberculosis.

Recently, the peculiarities of cell wall formation in numerous dangerous pathogens, including *Mycobacterium tuberculosis*, have been made clear. While the penicillin-binding enzymes *D,D*-transpeptidases catalyzing the transfer of the 3rd residue of meso-diaminopimelic acid (m-DAP) or L-Lys to the 4th *D*-Ala residue (the so called 4–3 crosslinks) play the major role in peptidoglycan crosslinking in most bacteria, most of the peptidoglycan crosslinks in *Mycobacterium tuberculosis* are formed by *L,D*-transpeptidases that catalyze transfer of the 3rd m-DAP residue to the analogous residue in another peptidoglycan chain (the so called 3–3 crosslinks [3, 4], whose content in the pathogen's cell wall can be as high as 80%).

Initially, *L,D*-transpeptidases were found in microorganisms such as *Escherichia coli* [5], *Bacillus subtilis* [6], and *Enterococcus faecium* [7]. It was not until very recently that the presence of these enzymes and their exceptional role in cell wall formation in such pathogens as *M. tuberculosis* [8] and *Helicobacter pylori* [9] were revealed. This discovery cast light on the reasons

for the poor efficacy of β-lactam antibiotics against tuberculosis and several other infectious diseases: unlike *D,D*-transpeptidases, *L,D* transpeptidases are not sensitive to the widely used penicillins and cephalosporins [10, 11]. The important role of these enzymes in mycobacteria functioning makes them one of the most attractive targets in the search for inhibitors that could help design novel antibiotics with anti-tuberculosis activity.

L,D-transpeptidases belong to the class of aminoacyl transferases [EC 2.3.2], the YkuD superfamily of proteins whose name (YkuD enzyme) originates from *B. subtilis*, the first enzyme with a known crystalline structure [6]. The *M. tuberculosis* genome encodes five proteins containing a domain with *L,D*-transpeptidase activity (Rv0116c, Rv0192, Rv0483, Rv1433, and Rv2518c regions) [11]. *L,D*-transpeptidase 2 (LdtMt2) [8] is the most actively expressed one; its presence in *M. tuberculosis* is associated with a high content of non-classical 3–3 peptidoglycan crosslinks in the pathogen's cell wall. The amino acid sequences of *L,D*-transpeptidases from *M. tuberculosis* were identified, but their structures were established only for types 1 and 2 enzymes (LdtMt1 and LdtMt2, respectively). The LdtMt2 precursor consists of 408 amino acid residues that form the signal peptide (Met1-Ala34) and the chain of the enzyme (Cys35-Ala408), which can be divided into three domains: two non-catalytic Ig-like domains A and B (residues Ala55-Ser147 and Pro148-Gly250, respectively) and the catalytic domain C (residues Asp251-Ala408) with transpeptidase activity [8]. Cys354, His336, and Ser337, which constitute the proton transfer chain, are the key residues involved in catalysis [8]. The active center of LdtMt2 is not directly exposed to solution and is located under the so-called Tyr298-Trp324 "lid" [12] that forms three channels (A, B and C). The substrate can be delivered to the active center through two of these channels (B and C).

The structure of the LdtMt2 complex with the dipeptide (N-γ-*D*-glutamyl-m-DAP) fragment of peptidoglycan in the active site of the enzyme PDB 3TUR [11] was determined. The crystal structures of the covalent LdtMt2–meropenem and LdtMt1–imipenem complexes [12, 13] were also obtained. The inactivation of LdtMt1 by various carbapenems (e.g., meropenem, imipenem, doripenem and ertapenem) was studied using the methods of pre-stationary kinetics [14]. Dhar et al. [15] demonstrated that not only carbapenems, but also faropenem (a β-lactam antibiotic belonging to the penem family) can effectively inhibit LdtMt. Our earlier molecular modeling study [16] focused on the interaction between the enzyme and the tetrapeptide fragment of cell wall peptidoglycan, as well as the known β-lactam inhibitors, and identified the features

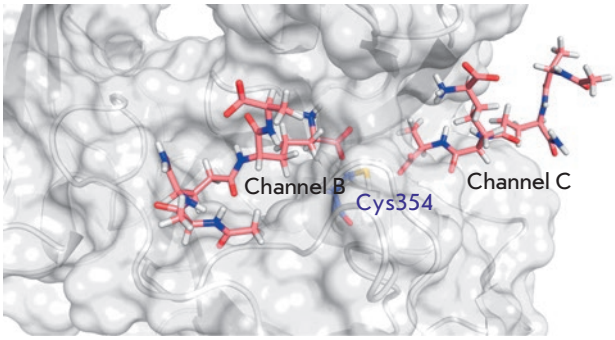

Fig. 1. Combined frames from molecular dynamic trajectories in which peptidoglycan fragments are connected to the active site through different channels (B and C) [16]

of binding of the N- and C-terminal fragments of the growing peptidoglycan chain with LdtMt2 upon formation of 3–3 crosslinks. We used these findings to build an adequate full-atom model of LdtMt2 for screening and optimization of the inhibitor structure (*Fig. 1*). A specific feature of the catalysis by *L,D*-transpeptidases is that these enzymes bind two substrate molecules at their active center. One bound molecule acts as an acyl donor that then forms the acyl-enzyme intermediate. The other bound molecule acts as a nucleophile giving rise to the 3–3 crosslink in the cell wall peptidoglycan after the nucleophile binds to acyl-enzyme and the acyl group of the L-center in the m-DAP residue of one peptidoglycan chain is transferred to the amino group of the D-center in the m-DAP residue of the other chain. Molecular modeling showed that binding of the N-terminal fragment of the growing peptidoglycan chain (an acyl donor), as well as β-lactams capable of inactivating the enzyme due to the formation of a stable acyl-enzyme, takes place in channel C, while the C-terminal (nucleophilic) fragment of the growing chain binds in channel B.

The objective of this work was to isolate, purify, and characterize LdtMt2 from *M. tuberculosis* to obtain enzyme preparations for experimental studies of the inhibitory activity of the compounds selected by computer-aided screening.

EXPERIMENTAL

Expression of LdtMt2 and LdtMt2_cut in *E. coli*, isolation and purification

When conducting this study, an enzyme preparation lacking the domain A (referred to as the LdtMt2_cut preparation) was obtained, along with full-length LdtMt2. A comparative study of these two enzymes (LdtMt2 and LdtMt2_cut) could help us understand

the effect of domain A on the catalytic activity of the enzyme. The pET-19b plasmid carrying either the *Rv2518c* gene (LdtMt2) that lacks the region encoding the signal peptide (Phe54-Ala408 residues) or the *Rv2518c_cut* gene (LdtMt2_cut) lacking both the signal peptide and domain A (residues Pro148-Ala408) was used for enzyme expression. In both cases, the terminal peptide consisting of 24 amino acid residues resided in the N-terminal portion of the protein: MGHHHHHHHHHHSSGHIDDDDKHM with the decahistidine terminal fragment (His-tag). *E. coli* BL21 (DE3) colonies with the transformed pET-19b plasmid were grown overnight in LB medium. Subsequently, 100 μl of the obtained culture was transferred to a flask with the LB medium containing 100 μg/ml ampicillin (Amp). The medium was incubated at 37°C and 180 rpm for 6–7 h until an optical density of 0.6–0.8 at λ = 600 nm was reached.

Enzyme expression was started by decreasing the temperature to 15°C and adding a $CaCl_2$ aqueous solution (until a 2 mM concentration was reached), isopropyl-β-*D*-1-thiogalactopyranoside (IPTG) (until a 0.5 mM concentration), and glycerol (until a 2 vol.% concentration). Expression was continued for 4, 24, and 48 h. All enzyme isolation steps were performed on ice; the samples were centrifuged at 4°C. Isolation was carried out according to the standard procedure, using Protino Ni-TED 1000 columns (MACHEREY-NAGEL GmbH & Co) for purification of His-tagged proteins [17]. Cells were precipitated from the medium by centrifugation at 4,000 rpm for 15 min; the wet cell mass was weighed, re-suspended in 3 ml of LEW buffer (50 mM NaH_2PO_4 pH 8.0, 0.3 M NaCl); lysozyme was added until a 1 mg/ml concentration. The mixture was incubated for 30 min and then disintegrated by ultrasound in ice-cold water for 10 min. The resulting mixture was centrifuged at 12,000 rpm for 30 min at 4°C. The supernatant was collected, filtered through a 0.2 μm filter, and purified using the Protino Ni-TED 1000 column equilibrated with 2 ml of the LEW buffer. Cellular proteins were washed off by adding two portions (2 ml) of the LEW buffer. LdtMt2 was eluted from the columns with three portions (1.5 ml each) of the elution buffer (50 mM NaH_2PO_4, 0.3 M NaCl, 0.25 mM imidazole, pH 8.0). The total protein concentration and enzyme yield were controlled at all purification stages using the microburet method [18].

Determination of the concentration of SH groups

Free SH groups were titrated with Ellman's reagent 5,5'-dithiobis(2-nitrobenzoic acid) (DTNB) using a 10 mM (4 mg/ml) solution in a denaturing buffer (0.1 M Tris-HCl pH 8.0 containing 6 M guanidine chloride). N-acetylcysteine (N-Ac-*L*-Cys) was used as a model compound to construct the calibration plot: 7 μl of the 10 mM solution of Ellman's reagent (4 mg/ml) and 5–55 μl of a 0.2 mM N-Ac-*L*-Cys solution (2–22 μM) were added to the denaturing buffer so that the total volume of the mixture was 500 μl. The resulting mixture was then incubated for 5 min, and absorbance was measured at 412 nm. The concentration of SH groups was calculated using the extinction coefficient of the resulting 2-nitro-5-thiobenzoic acid at 412 nm and pH 8.0 (14150 $M^{-1}cm^{-1}$) [19].

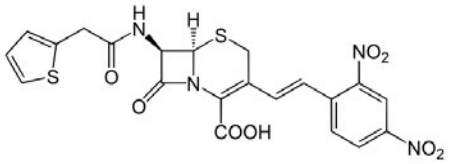

Fig.2. Structural formula of nitrocefin, the substrate of L,D-transpeptidase

Free SH groups in the LdtMt2 and LdtMt2_cut preparations were titrated using the same procedure: a 62–125 μl aliquot with the known enzyme concentration was added to the denaturing buffer supplemented with 7 μl of Ellman's reagent so that the final volume of the mixture was 500 μl. The mixture was incubated for 5 min, and the absorbance at 412 nm was measured. The concentration of the SH groups in the enzyme was calculated in a similar manner as it was done for N-Ac-*L*-Cys.

Determination of the activity of LdtMt2 and LdtMt2_cut using nitrocefin

There currently exist no appropriate low-molecular-weight analogs of the cell wall fragment that could be used as convenient substrates for determining enzyme activity. Therefore, the activity of LdtMt2 and the reaction kinetics are studied using the chromogenic substrate, nitrocefin (*Fig. 2*) [11]. The nitrocefin-hydrolyzing activity of enzyme preparations was determined by measuring the absorption of the product of β-lactam ring hydrolysis at 486 nm in 0.02 M HEPES buffer (pH 7.5) in the presence of 0.1 M KCl. The extinction coefficient of the product was taken as 20,500 $M^{-1}cm^{-1}$ [11].

Cultivation under reducing conditions to prevent enzyme inactivation

Our experiments aimed at isolating and purifying LdtMt2 demonstrated that reducing conditions preventing the oxidation of the catalytic cysteine residue are needed to obtain active enzyme preparations. Therefore, dithiothreitol (DTT) was added to the medium 3 h before expression termination until a total concentration

Table 1. Results of cultivation, isolation, and purification of LdtMt2 and LdtMt2_cut

Sample	Expression time, hrs	Raw cell mass after centrifugation, g	Protein concentration in cell extracts, mg/ml	Mass of purified enzyme, mg
LdtMt2	4	–	–	1.2
	24	0.62	3.7	2.4
	48	0.86	4.1	2.4
LdtMt2_cut	4	–	–	0.8
	24	0.71	3.1	1.9
	48	0.95	3.8	1.9

of 6 mM. Enzyme isolation was also performed in the presence of DTT.

RESULTS AND DISCUSSION

When obtaining the LdtMt2 and LdtMt2_cut samples, we performed expression during different time periods (4, 24 and 48 hrs) to identify the conditions under which the yield of the target enzyme would be optimal. *Table 1* summarizes the results of isolation and purification of the LdtMt2 and LdtMt2_cut preparations. The optimal cultivation time was 24 h: both gain in time and higher yield of the purified enzyme were observed compared to cultivation for 48 h.

PAGE demonstrated that extraneous proteins do not bind to the Ni-TED column. The resulting enzyme preparations were of high purity; their molecular weights corresponded to LdtMt2 40.9 kDa (Ala55-Ala408 + His-tag) and LdtMt2_cut 31.3 kDa (Pro148-Ala408 + His-tag) (*Fig. 3*). Meanwhile, the nitrocefin-hydrolyzing activity of the LdtMt2 preparation isolated without addition of reducing agents was significantly lower than expected. As shown earlier [11], the catalytic cysteine residue Cys354 might be oxidized, which may lead to irreversible inactivation of LdtMt2. When cultivation of *E. coli* cells and isolation of the enzyme were carried out under reducing conditions with dithiothreitol (DTT) added to the medium to prevent oxidation of the catalytic cysteine residue, the protein yield was not significantly changed and was equal to approximately 1.8 ± 0.2 mg per 50 ml of the culture medium. However, the catalytic activity of the enzyme was significantly higher. The degree of oxidation of SH groups in the LdtMt2 and LdtMt2_cut samples obtained upon cultivation and isolation of the enzyme under nonreducing and reducing conditions was evaluated by Ellman titration (see the Experimental section). The results are presented in *Table 2*. Addition of DTT to the culture medium and enzyme isolation under reducing conditions made it possible to prevent oxidation of the catalytic Cys354 and obtain a LdtMt2 preparation whose specific activity was almost twice as high.

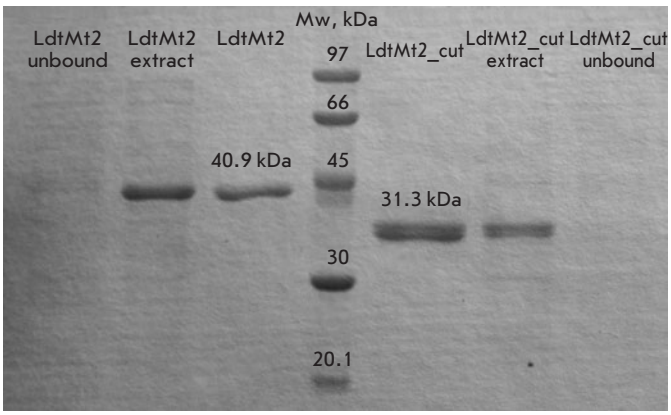

Fig.3. Denaturing protein electrophoresis of LdtMt2 40.9 KDa (Ala55-Ala408 + His-tag) and LdtMt2_cut 31.3 KDa (Pro148-Ala408 + His-tag) preparations purified on a Protino Ni-TED 1000 packed column, as well as cell extracts and fractions that failed to bind to the resin

Table 2. The proportion of free SH groups in LdtMt2 enzyme preparations obtained without and with addition of DTT to the culture medium

DTT, mM	Proportion of free SH groups [SH]/[LdtMt2], %
0	42±2
6	72±7

It should be mentioned that the purified enzyme samples were stable upon storage (4°C, pH 7.5, 20 mM HEPES, 0.1 M KCl) and hardly lost their activity after a month. This fact substantially speaks in favor of the application of the obtained enzyme preparations in studying their catalytic properties and testing potential inhibitors.

An important aspect of this work was understanding the effect of domain A on the catalytic activity of the enzyme. Comparison of the activities of LdtMt2 and

Table 3. Specific activity of the LdtMt2 and LdtMt2_cut preparations in the nitrocefin conversion reaction per protein content in the enzyme preparation and the content of active centers with allowance for the presence of free SH groups

Sample	Specific activity	
	Per protein content, μmol/min/mg	Per concentration of SH groups, μmol/min/μmol
LdtMt2 (Ala55–Ala408)	0.65	30.6
LdtMt2_cut (Pro148–Ala408)	0.03	2.6

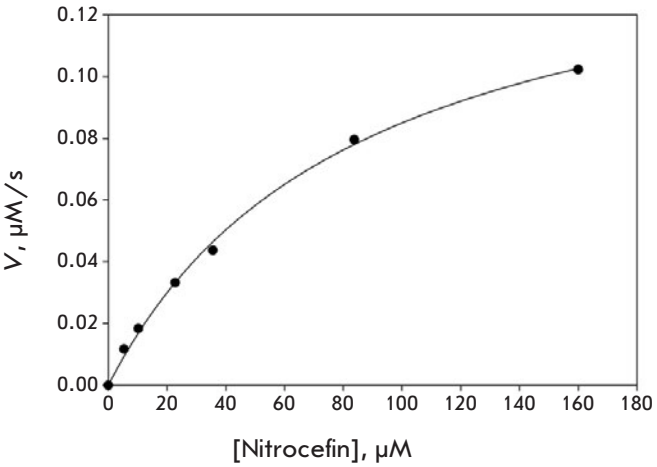

Fig. 4. The initial reaction rate of nitrocefin β-lactam ring hydrolysis catalyzed by LdtMt2 as a function of the nitrocefin concentration. The experimental data are shown with dots. The regression curve was built using the kinetic parameters presented in the text

LdtMt2_cut showed that, after domain A is removed, specific activity drops more than tenfold (see *Table 3*).

The K_M and V_{max} values of nitrocefin hydrolysis catalyzed by LdtMt2 and LdtMt2_cut were determined by analyzing the dependence of the initial rates on substrate concentrations in the range of 5–160 μM (*Fig. 4*). The concentration of the free SH groups was taken into account when determining the catalytic constants of the enzymatic reaction and evaluating the active site concentrations in the LdtMt2 and LdtMt2_cut preparations. The drop in the activity of the full-length enzyme after removal of the domain A was mainly due to the decrease in the catalytic constant of nitrocefin conversion, which went down from 0.98 ± 0.05 s^{-1} to 0.08 ± 0.03 s^{-1} when proceeding from LdtMt2 to LdtMt2_cut, while the value of the Michaelis constant worsened slightly: from 85 ± 7 to 102 ± 10 μM.

CONCLUSIONS

Optimization of the conditions of LdtMt2 expression and purification has shown that the most productive way to obtain active enzyme preparations is to cultivate *E. coli* cells for 24 h in a LB medium in the presence of 0.2 mM IPTG, 2 mM $CaCl_2$ and timely add reducing agents (DTT) to prevent the oxidation of catalytic Cys354. The resulting highly purified LdtMt2 preparation does not lose its activity after storage in 20 mM HEPES buffer, pH 7.5, at 4°C for at least a month and can be used for experimental studies of potential enzyme inhibitors selected by computer-aided screening. The biochemical and kinetic properties of a full-length LdtMt2 preparation and LdtMt2_cut preparation lacking domain A were characterized. It was shown that after domain A (which is not directly attached to the catalytic domain C) is removed, the activity of the full-length enzyme decreases significantly (more than 10 times), mainly because of the drop in the catalytic constant of nitrocefin hydrolysis. Interaction between the domains and their role in the functioning of the full-length enzyme need further investigation. ●

This work was supported by the Russian Science Foundation (grant no. 15-14-00069).

REFERENCES

1. Global tuberculosis report 2016. // World Health Organization. 2016.
2. Betts J.C., Lukey P.T., Robb L.C., McAdam R.A., Duncan K. // Mol. Microbiol. 2002. V. 43. № 3. P. 717–731.
3. Fisher J.F., Meroueh S.O., Mobashery S. // Chem. Rev. 2005. V. 105. № 2. P. 395–424.
4. Jankute M., Cox J.A.G., Harrison J., Besra G.S. // Annu. Rev. Microbiol. 2015. V. 69. № 1. P. 405–423.
5. Magnet S., Dubost L., Marie A., Arthur M., Gutmann L. // J. Bacteriol. 2008. V. 190. № 13. P. 4782–4785.
6. Bielnicki J., Devedjiev Y., Derewenda U., Dauter Z., Joachimiak A., Derewenda Z.S. // Proteins Struct. Funct. Genet. 2006. V. 62. № 1. P. 144–151.
7. Biarrotte-Sorin S., Hugonnet J.E., Delfosse V., Mainardi J.L., Gutmann L., Arthur M., Mayer C. // J. Mol. Biol. 2006. V. 359. № 3. P. 533–538.
8. Böth D., Steiner E.M., Stadler D., Lindqvist Y., Schnell R., Schneider G. // Acta Crystallogr. Sect. D Biol. Crystallogr. 2013. V. 69. № 3. P. 432–441.
9. Kim H.S., Im H.N., An D.R., Yoon J.Y., Jang J.Y., Mobashery S., Hesek D., Lee M., Yoo J., Cui M., et al. // J. Biol. Chem.

2015. V. 290. № 41. P. 25103–25117.
10. Gupta R., Lavollay M., Mainardi J.L., Arthur M., Bishai W.R., Lamichhane G. // Nat. Med. 2010. V. 16. № 4. P. 466–469.
11. Erdemli S.B., Gupta R., Bishai W.R., Lamichhane G., Amzel L.M., Bianchet M.A. // Structure. 2012. V. 20. № 12. P. 2103–2115.
12. Kim H.S., Kim J., Im H.N., Yoon J.Y., An D.R., Yoon H.J., Kim J.Y., Min H.K., Kim S.J., Lee J.Y., et al. // Acta Crystallogr. Sect. D Biol. Crystallogr. 2013. V. 69. № 3. P. 420–431.
13. Correale S., Ruggiero A., Capparelli R., Pedone E., Berisio R. // Acta Crystallogr. Sect. D Biol. Crystallogr. 2013. V. 69. № 9. P. 1697–1706.
14. Dubée V., Triboulet S., Mainardi J.L., Ethève-Quelquejeu M., Gutmann L., Marie A., Dubost L., Hugonnet J.E., Arthur M. // Antimicrob. Agents Chemother. 2012. V. 56. № 8. P. 4189–4195.
15. Dhar N., Dubeé V., Ballell L., Cuinet G., Hugonnet J.E., Signorino-Gelo F., Barros D., Arthur M., McKinney J.D. // Antimicrob. Agents Chemother. 2015. V. 59. № 2. P. 1308–1319.
16. Baldin S., Misiura N., Švedas V.K. // Acta Naturae. 2017. V. 9. № 1. P. 44–51.
17. Purification of His-tag proteins. // MACHEREY-NAGEL. 2014. V. Rev.06. .
18. Itzhaki R.F., Gill D.M. // Anal. Biochem. 1964. V. 9. № 4. P. 401–410.
19. Ellman G.L. // Arch. Biochem. Biophys. 1959. V. 82. № 1. P. 70–77.

Thermodynamics of the DNA Repair Process by Endonuclease VIII

O. A. Kladova[1], N. A. Kuznetsov[1,2*], O. S. Fedorova[1,2,*]
[1]Institute of Chemical Biology and Fundamental Medicine, Siberian Branch of the Russian Academy of Sciences, Akad. Lavrentiev Ave. 8, 630090, Novosibirsk, Russia
[2]Department of Natural Sciences, Novosibirsk State University, Pirogova Str. 2, 630090, Novosibirsk Russia.
*E-mail: fedorova@niboch.nsc.ru, nikita.kuznetsov@niboch.nsc.ru
Received October 12, 2018; in final form January 21, 2019

ABSTRACT In the present work, a thermodynamic analysis of the interaction between endonuclease VIII (Endo VIII) and model DNA substrates containing damaged nucleotides, such as 5,6-dihydrouridine and 2-hydroxymethyl-3-hydroxytetrahydrofuran (F-site), was performed. The changes in the fluorescence intensity of the 1,3-diaza-2-oxophenoxazine (tC^O) residue located in the complementary chain opposite to the specific site were recorded in the course of the enzyme-substrate interaction. The kinetics was analyzed by the stopped-flow method at different temperatures. The changes of standard Gibbs free energy, enthalpy, and entropy of sequential steps of DNA substrate binding, as well as activation enthalpy and entropy for the transition complex formation of the catalytic stage, were calculated. The comparison of the kinetic and thermodynamic data characterizing the conformational transitions of enzyme and DNA in the course of their interaction made it possible to specify the nature of the molecular processes occurring at the stages of substrate binding, recognition of the damaged base, and its removal from DNA.

KEYWORDS thermodynamics, pre-steady-state kinetics, kinetic mechanism, DNA glycosylase.

ABBREVIATIONS Endo VIII – endonuclease VIII; AP-site – apurinic/apyrimidinic site; F-site – (3-hydroxytetrahydrofuran-2-yl) methyl phosphate; DHU – 5,6-dihydrouridine.

INTRODUCTION

Endonuclease VIII (Endo VIII or Nei) is one of the key DNA glycosylases in *Escherichia coli* responsible for the elimination of a wide range of oxidized and reduced pyrimidine bases [1, 2]. The products of oxidation/reduction of pyrimidine bases in DNA are thymine glycol, 5,6-dihydrothymine, 5,6-dihydrouracil, urea, 5-formyluracil, 5-hydroxymethyluracil, 5-hydroxycytosine, 5-hydroxyuracil, uracil glycol, etc. Endo VIII catalyzes the hydrolysis of the N-glycosidic bond of a damaged base (N-glycosylase activity) with subsequent β-elimination of the 3' and 5' phosphate groups of the apurinic/apyrimidinic site (AP lyase activity), resulting in the formation of a single-strand break in DNA (*Fig. 1*) [3, 4].

X-ray structural analysis of the free enzyme and its complex with DNA showed that the interaction of Endo VIII with DNA leads to conformational changes both in the protein and substrate molecules [5, 6]. In the enzyme-substrate complex, the ribose-phosphate backbone of DNA is bent at approximately 45°, the damaged base is extruded from the DNA helix and inserted in the active center of the enzyme, while the Gln69, Leu70, and Tyr71 residues are positioned into the resulting cavity (*Fig. 2*). Such changes in the structure of interacting molecules lead to the formation of specific contacts, providing highly efficient recognition and binding of damaged DNA nucleotides.

Previously, we performed the kinetic analysis of conformational changes in Endo VIII and the DNA substrate during their interaction using the stopped-flow method with registration of the changes in the fluorescence intensity of tryptophan residues in the enzyme structure [7] and a number of fluorescent analogues of heterocyclic bases in DNA [8] located on the 3' side or complementary to the damaged nucleotide. Later [9], we used the strategy of site-directed

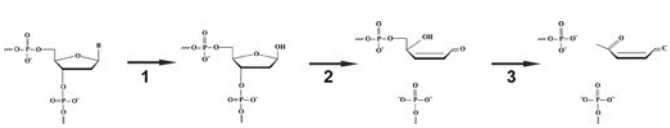

Fig. 1. Chemical steps in Endo VIII catalysis. Step 1, DHU base removal; step 2, β-elimination of the 3'-phosphate; step 3, β-elimination of the 5'-phosphate.

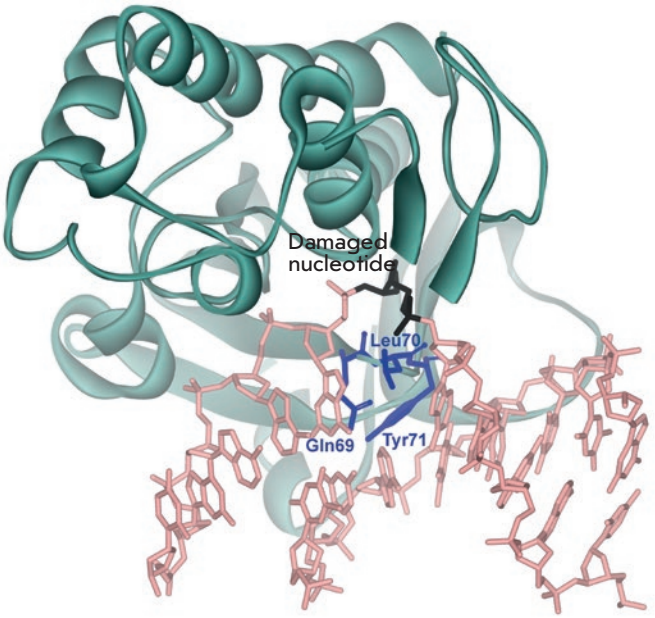

Fig. 2. The structure of Endo VIII complexed with DNA containing an AP-site (Protein Data Bank code 1K3W) [6]

mutagenesis to clarify the nature of the sequential stages of DNA binding. All the kinetic data characterizing conformational changes in the enzyme and DNA substrates, as well as the results of the mutational analysis, allowed us to propose a molecular kinetic mechanism for the recognition of a damaged nucleotide by the Endo VIII enzyme (*Scheme 1*). Stage 1 corresponds to a rapid initial binding of DNA and formation of a non-specific enzyme-substrate complex in which the N- and C-domains of the enzyme are in a closed position. At this stage, the Leu70 residue is wedged into the DNA duplex, which is the key stage of recognition of the damaged DNA region. Stage 2 involves the bending of the double helix at the damaged base site, the eversion of 5,6-dihydrouracil from the duplex, and the incorporation of the Tyr71 residue in the DNA helix, required for the stabilization of the inverted conformation of the damaged base. In stage 3, the conformation of the active center is adjusted in order to achieve a catalytically competent state. The Tyr71 residue is also utilized in stage 3. In this stage, contacts are formed between Phe121 and the ribose-phosphate backbone of DNA. The formation of the catalytic complex leads to the hydrolysis of the N-glycosidic bond, followed by the β-elimination of the 3' and 5' phosphate groups (stage 4). The final stage of the enzymatic cycle is the dissociation of the enzyme-product complex (stage 5).

Scheme 1. Kinetic mechanism of interaction between Endo VIII and DHU substrate

$$E + DHU \underset{k_{-1}}{\overset{k_1}{\rightleftharpoons}} (E{\bullet}DHU)_1 \underset{k_{-2}}{\overset{k_2}{\rightleftharpoons}} (E{\bullet}DHU)_2 \underset{k_{-3}}{\overset{k_3}{\rightleftharpoons}} (E{\bullet}DHU)_3 \xrightarrow{k_{cat}} E{\bullet}P \underset{K_p}{\rightleftharpoons} E + P,$$

where E is EndoVIII, DHU is DHU substrate, $(E \cdot DHU)_n$ are enzyme-substrate complexes, $E \cdot P$ is a complex of the enzyme with the product P, and k_i and k_{-i} are rate constants for i^{th} step.

In order to confirm the kinetic mechanism proposed (*Scheme 1*) and specify the nature of individual stages, we determined the thermodynamic parameters of the fast stages of the interaction between Endo VIII and DNA and the specific recognition of a damaged nucleotide based on the kinetic parameters obtained at different temperatures.

EXPERIMENTAL

Oligodeoxyribonucleotides

Oligonucleotides were purified by HPLC on an ion exchange column (PRP-X500 Hamilton Company 3.9×300 mm; particle size, 12–30 μm), followed by reverse phase chromatography (Nucleoprep 100–20 C_{18} 10×250 mm, Macherey-Nagel, Germany). The purity of the oligonucleotides was verified by denaturing electrophoresis in a 20% polyacrylamide gel (PAAG). The concentration of oligonucleotides was determined based on the optical density of solutions at a wavelength of 260 nm in electronic absorption spectra and molar extinction coefficients calculated using the nearest neighbor method [10].

DNA duplexes of 17 bp containing 1,3-diaza-2-oxophenoxazine fluorophore (tC^O), instead of a cytosine residue in the complementary chain opposite the specific site, were used as DNA substrates (*Table 1*). The specific sites were the 5,6-dihydrouridine residue, which served as the damaged base, and an F-site, which is an analog of an intermediate product of the

Table 1. Structure of the DNA-duplexes used in this study

Name	DNA-duplex
DHU-DNA, X = DHU **F-DNA**, X = F-site **G-DNA**, X = G	5'-TCTCTCTC**X**CCTTCCTT-3' 3'-AGAGAGAG(tC^O)GGAAGGAA-5'

enzymatic reaction; i.e., the apurinic/apyrimidinic site (AP site). A duplex containing no modified nucleotides was used as intact DNA.

Endonuclease VIII

Endo VIII was isolated from *E. coli* Rosetta II (DE3) cells transformed with a pET-24b plasmid carrying the enzyme gene. The *E. coli* Rosetta II (DE3) cells were cultivated in a LB medium (1 L) containing 50 μg/ml ampicillin at 37°C until it reached an optical density of 0.6–0.7 at a 600-nm wavelength. After this, the temperature was decreased to 30°C and transcription was induced by addition of isopropyl-β-*D*-thiogalactopyranoside to a final concentration of 0.2 mM. After induction, the cell culture was incubated for 8 h. Next, the cells were precipitated by centrifugation (10 min, 12,000 rpm) and the cell suspension was prepared in 30 ml of a buffer solution (20 mM HEPES-NaOH, pH 7.8; 40 mM NaCl). The cells were lysed using a French press (French Press Cell, Thermo Fisher Scientific, USA). All subsequent procedures were performed at 4°C. The cell lysate was centrifuged (40 min at 30,000 rpm); the supernatant was loaded onto column I (Q-Sepharose Fast Flow, Amersham Biosciences, Sweden) and washed with the buffer solution (20 mM HEPES-NaOH, pH 7.8; 40 mM NaCl). Protein-containing fractions were collected and loaded onto column II (HiTrap-Heparin™, Amersham Biosciences, Sweden). Chromatography was performed in a linear gradient of 40 → 1500 mM NaCl, and the optical density of the solution was measured at 280 nm. The degree of protein purity was determined by gel electrophoresis. Fractions containing the Endo VIII protein were dialyzed in 20 mM HEPES-NaOH buffer, pH 7.5, 1 mM EDTA, 1 mM dithiothreitol, 250 mM NaCl, 50% glycerol and stored at −20°C. Enzyme concentration was calculated based on the optical density of the protein at 280 nm and a molar extinction coefficient of 32680 $M^{-1}\times cm^{-1}$ [11].

Kinetic studies using the stopped-flow method

Kinetic curves were obtained based on the changes in tC^O fluorescence intensity on a stopped-flow spectrometer SX.20 (Applied Photophysics, Great Britain). The tC^O fluorescence excitation wavelength was 360 nm. Fluorescence was recorded at wavelengths greater than 395 nm (Schott filter GG 395). The instrument dead time was 1.4 ms; the maximum signal acquisition time was 500 s. All experiments were performed in a buffer solution of 50 mM Tris-HCl, pH 7.5, 50 mM KCl, 1 mM dithiothreitol, 1 mM EDTA, 7% glycerol at a temperature range of 5 to 25°C. Each kinetic curve was averaged over at least three experimental curves.

Analysis of kinetic curves

In order to calculate the rate constants for conformational transitions, a set of kinetic curves was obtained for different concentrations of the enzyme at different temperatures. The fluorescence intensity of tC^O was recorded under conditions close to one enzyme turnover; i.e., at enzyme and substrate concentrations of the same magnitude. To determine the minimum kinetic scheme describing the interaction of the enzyme with a substrate and to calculate rate constants for all elementary reactions corresponding to this scheme, the DynaFit software (BioKin, USA) was used [12]. Quantitative processing of the results was performed by optimization of the values of the parameters comprising the kinetic schemes as previously described [13–16].

Using the values obtained for the rate constants of direct and reverse reactions for individual reversible stages, we calculated the equilibrium constants K_i for these stages ($K_i = k_i/k_{-i}$, where i is the stage number) at different temperatures. The standard thermodynamic parameters of the i^{th} equilibrium stage were determined using the Van't Hoff equation (1) [17, 18] as previously described [19–23].

$$\ln(K_i) = -\Delta G_i^o/RT = -\Delta H_i^o/RT + \Delta S_i^o/R. \quad (1)$$

Analysis of the temperature dependence of the k_{cat} rate constant using the Eyring equation (2) allowed us to calculate the standard activation enthalpy ($\Delta H^{o,\ddagger}$) and the standard activation entropy ($\Delta S^{o,\ddagger}$) of the transition state [17].

$$\ln(k_{cat}/T) = \ln(k_B/h) + (\Delta S^{o,\ddagger}/R) - (\Delta H^{o,\ddagger}/RT), \quad (2)$$

where k_B and h are the Boltzmann and Planck constants, respectively; R is the universal gas constant; T is the absolute temperature in Kelvin degrees; and k_{cat} is the rate constant for the irreversible catalytic stage.

RESULTS AND DISCUSSION

Interaction between Endo VIII and intact G-DNA

Figure 3A presents the kinetic curves for the interaction between Endo VIII and the DNA duplex G-DNA containing a guanine residue complementary to the fluorophore group tC^O obtained by registration of the changes in the tC^O fluorescence intensity during the reaction. One phase of growth in the fluorescence intensity, which reaches a plateau, can be noted on the kinetic curves. When increasing the temperature, the time necessary to reach the plateau shifts from ~30 ms at 5°C to ~20 ms at 25°C (*Fig. 3C*). The kinetic curves obtained are satisfactorily described by single-stage

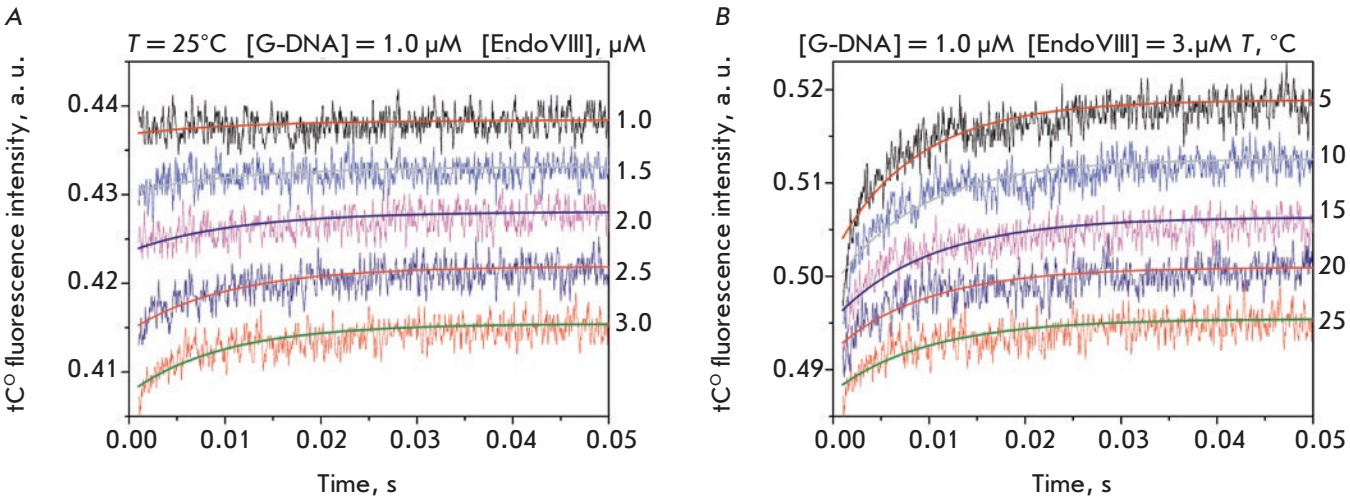

Fig. 3. Interaction of Endo VIII with intact G-DNA. *A* – Changes in the tC° fluorescence intensity. Jagged traces represent experimental data; smooth curves are the results of fitting to *Scheme 2*. [G-DNA] = 1.0 μM, concentrations of Endo VIII (1.0–3.0 μM) are shown on the right side of the plot. *B* – Changes in the tC° fluorescence intensity of the interaction of Endo VIII with G-DNA at different temperatures ([Endo VIII] = 3.0μM, [G-DNA] = 1.0μM)

Table 2. Rate and equilibrium constants of the interaction of Endo VIII with intact G-DNA

Constants	Temperature, ˚C				
	5	10	15	20	25
k_1, $M^{-1}s^{-1}$	$(16\pm7)\times10^6$	$(16\pm8)\times10^6$	$(15\pm9)\times10^6$	$(14\pm6)\times10^6$	$(9\pm2)\times10^6$
k_{-1}, s^{-1}	50±30	60±40	50±20	60±40	40±10
K_1, M^{-1}	$(0.31\pm0.21)\times10^6$	$(0.26\pm0.21)\times10^6$	$(0.29\pm0.20)\times10^6$	$(0.25\pm0.18)\times10^6$	$(0.19\pm0.08)\times10^6$

equilibrium kinetic *Scheme 2*. The rate constants characterizing this stage are presented in *Table 2*.

Scheme 2. Kinetic mechanism of interaction between Endo VIII and intact DNA

$$E + G \underset{k_{-1}}{\overset{k_1}{\rightleftharpoons}} E{\bullet}G,$$

where E is EndoVIII, G is intact DNA, E · G is the enzyme-DNA complex, and k_1 and k_{-1} are the rate constants.

Interaction of Endo VIII with AP site analog F-DNA

Interaction between Endo VIII and the AP site in DNA has been studied using a DNA duplex containing a noncleavable analog of the AP site (tetrahydrofuran F derivative) and the fluorophore group tC° opposite a damaged nucleotide in the complementary chain (*Fig. 4*). Two phases of tC° fluorescence intensity growth can be distinguished on the kinetic curves presented in Fig. 4. The first phase of growth takes place in the same time range (up to ~20 ms) as in the case of interaction with intact G-DNA. The same conformational transformation caused by binding to Endo VIII is likely to occur in the structure of DNA duplexes containing both the G and F sites at the initial time. However, there is a second stage of tC° fluorescence intensity growth for the F ligand which is completed by the 1st second at all temperatures (*Fig. 4*). In addition, the changes in the kinetic curves of the interaction between an F-containing DNA and Endo VIII have a higher amplitude than in the case of G-DNA, suggesting both greater efficiency of complex formation between the enzyme and DNA and more significant conformational rearrangements in the structure of the DNA duplex containing the F-site.

Processing of the data obtained resulted in the determination of a minimal kinetic reaction scheme which included two reversible stages of the formation of the enzyme-substrate complex (*Scheme 3*). The reaction rate constants and equilibrium constants calculated are presented in *Table 3*.

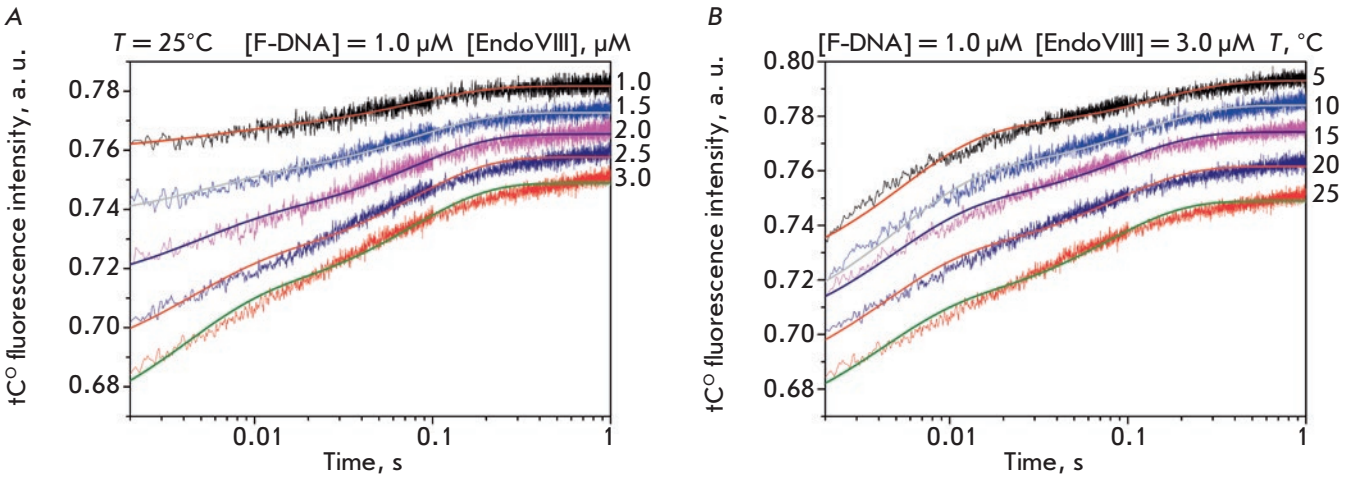

Fig. 4. Interaction of Endo VIII with F-DNA. *A* – Changes in the tC° fluorescence intensity. Jagged traces represent experimental data; smooth curves are the results of fitting to *Scheme 3*. [F-DNA] = 1.0 μM, concentrations of Endo VIII (1.0–3.0 μM) are shown on the right side of the plot. *B* – Changes in the tC° fluorescence intensity of the interaction of Endo VIII with F-DNA at different temperatures ([Endo VIII] = 3.0μM, [F-DNA] = 1.0μM)

Table 3. Rate and equilibrium constants of the interaction of Endo VIII with F-DNA

Constants	Temperature, °C				
	5	10	15	20	25
k_1, $M^{-1}s^{-1}$	(35±9)×10⁶	(35±5)×10⁶	(37±5)×10⁶	(39±5)×10⁶	(40±8)×10⁶
k_{-1}, s^{-1}	89±22	99±18	109±28	129±43	144±46
K_1, M^{-1}	(0.4±0.1)×10⁶	(0.35±0.08)×10⁶	(0.3±0.1)×10⁶	(0.3±0.1)×10⁶	(0.3±0.1)×10⁶
k_2, s^{-1}	0.3±0.1	0.9±0.3	1.4±0.2	3±1	3±1
k_{-2}, s^{-1}	7±2	8±1	10±1	11±1	12±1
K_2	0.04±0.02	0.11±0.03	0.13±0.02	0.24±0.09	0.26±0.08

Scheme 3. Kinetic mechanism of interaction between Endo VIII and F-DNA

$$E + F \underset{k_{-1}}{\overset{k_1}{\rightleftharpoons}} (E\bullet F)_1 \underset{k_{-2}}{\overset{k_2}{\rightleftharpoons}} (E\bullet F)_2,$$

where E is EndoVIII, F is F-DNA, $(E \cdot F)_n$ are enzyme-substrate complexes, and *ki* and k_{-i} are the rate constants for the i^{th} step.

Interaction of Endo VIII with DHU-DNA

Figure 5A presents the kinetic curves obtained for the interaction between Endo VIII and the DNA substrate containing 5,6-dihydrouridine (DHU-DNA). The curves are even more complicated than those obtained for G-DNA and F-DNA. Similar changes in the tC° fluorescence intensity can be noted for all concentration series at different temperatures (5–25°C) (*Fig. 5B*).

Analysis of the kinetic curves registered at 5–15°C demonstrated a rapid growth in the tC° fluorescence intensity at the initial region (up to 10 ms) (phase 1). At increased temperatures, this change in the fluorescence intensity disappears almost completely. Following the 1st growth phase, further increase in the fluorescence signal can be identified at all temperatures. The duration of the 2nd phase of growth decreased with an increase in the temperature from ~300 ms at 5°C to ~80 ms at 25°C.

It is known that the changes in the DNA helix structure, the extrusion of the damaged nucleotide, and the incorporation of a series of amino acid residues of the enzyme into the DNA helix occur when Endo VII binds to DNA [6]. Endo VIII forms an extensive network of contacts with DNA. However, the contacts formed by the amino acid residues of the triad Gln69–Leu70–Tyr71 play the most important role in the recognition of a damaged nucleotide.

For all the curves obtained, one can distinguish the phase of drop in the tC° fluorescence intensity (*phase 3*). This phase has a pronounced temperature dependence. For instance, the phase of drop in the tC° fluo-

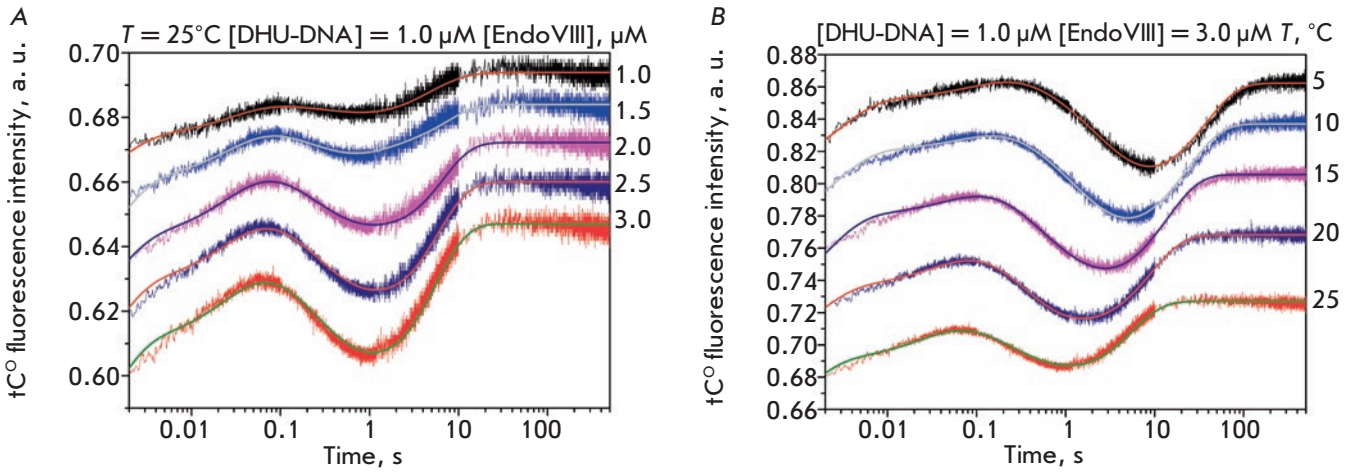

Fig. 5. Interaction of Endo VIII with DHU-DNA. *A* – Changes in the tC° fluorescence intensity. Jagged traces represent experimental data; smooth curves are the results of fitting to *Scheme 1*. [DHU-DNA] = 1.0 μM, concentrations of Endo VIII (1.0-3.0 μM) are shown on the right side of the plot. *B* – Changes in the tC° fluorescence intensity of the interaction of Endo VIII with DHU-DNA at different temperatures ([Endo VIII] = 3.0μM, [DHU-DNA] = 1.0μM)

Table 4. Rate and equilibrium constants of the interaction of Endo VIII with DHU-DNA

Constants	Temperature, ˚C				
	5	10	15	20	25
k_1, $M^{-1}s^{-1}$	35±7	40±6	45±7	61±4	80±13
k_{-1}, s^{-1}	230±30	270±40	320±10	440±70	580±50
K_1, M^{-1}	(0.149±0.038)×10⁶	(0.147±0.032)×10⁶	(0.140±0.023)×10⁶	(0.140±0.025)×10⁶	(0.138±0.027)×10⁶
k_2, s^{-1}	1.0±0.2	1.7±0.1	2.6±0.4	3.6±0.6	4±1
k_{-2}, s^{-1}	0.34±0.08	0.62±0.03	0.9±0.7	1.2±1	1.3±0.3
K_2	2.72±0.94	2.76±0.24	2.83±2	3.0±2.7	3.0±1
k_3, s^{-1}	6.5±1.4	8.1±0.6	12±2	18±4	29±3
k_{-3}, s^{-1}	1.6±0.3	1.9±0.6	2.5±0.6	3±1	4.4±1.6
K_3	4±1	4.3±1.4	4.6±1.3	5.3±1.9	6.6±2.5
k_{cat}, s^{-1}	0.06±0.02	0.09±0.05	0.15±0.05	0.22±0.08	0.34±0.02
K_5, M^{-1}	(0.06±0.03)×10⁶	(0.047±0.019)×10⁶	(0.042±0.016)×10⁶	(0.038±0.010)×10⁶	(0.034±0.18)×10⁶

rescence intensity lasts up to 10 s at 5˚C and only up to 1 s at 25˚C. Such a change corresponds to another stage occurring during the formation of the enzyme-substrate complex. Since a decrease in the tC° fluorescence intensity indicates a change in the microenvironment of the fluorophore group, one can assume the adjustment of the enzyme and DNA conformations to take place at this moment to form a catalytically competent enzyme-substrate complex.

An increase in the fluorescence signal (phase 4), followed by the reaching of a plateau, (phase 5) is observed immediately after a drop in tC° fluorescence intensity. It is most likely that the fourth stage of change in the fluorescence intensity reflects the catalytic stages in the enzymatic process, while the fifth stage represents the dissociation of the enzyme complex from the reaction product.

Thus, a total of five phases of changes in the tC° fluorescence intensity have been identified in the kinetic curves of interaction between endonuclease VII and a DNA substrate containing 5,6-dihydrouridine. A minimal kinetic scheme describing the kinetic curves includes three reversible stages that lead to the formation of an enzyme-substrate complex, one irreversible stage, which can be attributed to the catalytic reaction stage, and one reversible stage of the enzyme-product complex dissociation (*Scheme 1*). The calculated values of the rate constants for individual stages and equilibrium constants are presented in *Table 4*.

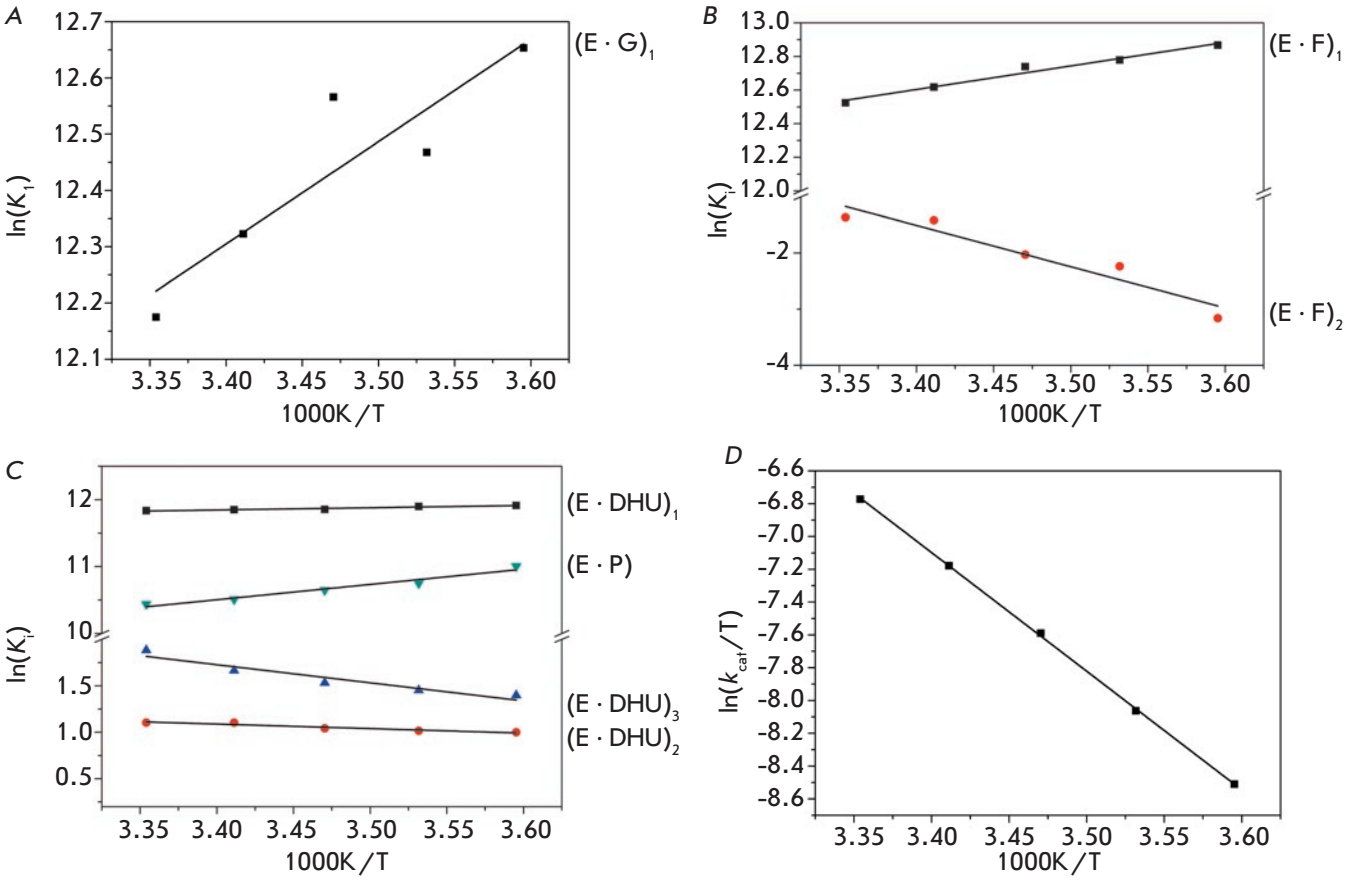

Fig. 6. Van't Hoff analysis of the temperature dependence of *Ki* for G-DNA (*A*), F-DNA (*B*), and DHU-DNA (*C*). (*D*) Analysis of the temperature dependence of $\ln(k_{cat}/T)$ characterizing the transition state of the catalytic step for DHU-DNA

Thermodynamic parameters of the interaction between Endo VIII and DNA substrates

The rate constants for the individual stages of the interaction between Endo VIII and all DNA substrates at different temperatures were used to calculate equilibrium constants for these stages (K_i). The equilibrium constants of individual stages were used for obtaining the dependence of $\ln(K_i)$ on 1/T (van't Hoff equation (1)) (*Fig. 6*). The dependence of $\ln(k_{cat}/T)$ on 1/T (Eyring equation (2)) that characterizes the irreversible catalytic reaction in the case of the DHU substrate was also obtained. All dependencies had a linear form and allowed us to calculate the changes in enthalpy and entropy for reversible stages (ΔH_i^o и ΔS_i^o) and the transition state of the catalytic stage ($\Delta H^{o,\ddagger}$ и $\Delta S^{o,\ddagger}$) (*Table 5*).

When analyzing the thermodynamic parameters of the interaction between Endo VIII and DNA substrates, we succeeded in identifying some common features. For instance, primary binding of the enzyme to all the DNA substrates used in the study is accompanied by a slight decrease in enthalpy and an increase in entropy. It leads to a negative value of the change in the Gibbs energy ΔG^o_1 for the first stage of the formation of the enzyme-substrate complex. It is worth noting that the value of $\Delta G^o_{1,298}$ (ranging from -7.0 to -7.4 kcal/mol) is similar for both damaged and intact DNA, indicating that the interaction of the enzyme with DNA is energetically favorable.

The thermodynamic parameters of the first stage obtained for G-DNA, F-DNA, and DHU-DNA indicate that the initial stage of interaction (up to 10 ms) between Endo VIII and DNA is identical for all of the DNA duplexes. No specific contacts with the damaged nucleotide take place at the stage of primary binding. The recognition of the damaged nucleotide occurs later, upon its eversion from the DNA helix and incorporation of the Gln69–Leu70–Tyr71 triad into the helix. Nevertheless, it has been established [9] that Endo VIII utilizes Leu70 as a "sensor" of damaged nucleotides and that its intercalation into the duplex structure takes place at early stages of specific enzyme-substrate interaction. Therefore, one can assume that an increase

Table 5. Thermodynamic parameters of interaction of Endo VIII with DNA

DNA substrate	Stage No	ΔH_i^o, kcal/mol	ΔS_i^o, cal/(mol×K)	$\Delta G^o_{i,298}$, kcal/mol	Stage description[a]
G/tC^O	1	-3.6 ± 0.9	12 ± 3	-7.2	Primary binding, attempt at incorporation of Leu70 residue, increase in the polarity of the tC^O environment
F/tC^O	1	-2.8 ± 0.3	16 ± 1	-7.4	Primary binding, intercalation of Leu70, increase in the polarity of the tC^O environment
	2	15 ± 3	47 ± 9	0.8	Bending of the double helix, increase in the polarity of the tC^O environment
	$\sum_{i=1}^{i=2}$	12.2 ± 3.3	60 ± 10	-6.6	
DHU/tC^O	1	-0.7 ± 0.1	21.3 ± 0.4	-7.0	Primary binding, increase in the polarity of the tC^O environment
	2	1.0 ± 0.2	5.5 ± 0.6	-0.65	Bending of the double helix, increase in the polarity of the tC^O environment
	3	3.9 ± 0.7	17 ± 2	-1.1	Formation of a catalytic complex, decrease in the polarity of the tC^O environment
	$\sum_{i=1}^{i=3}$	4.2	43.8	-8.75	
	4[b]	14.4 ± 0.1	-12.4 ± 0.5	18	Catalysis, increase in the polarity of the tC^O environment
	5	-4.5 ± 0.6	5 ± 2	-6.2	Formation of a complex with the reaction product, increase in the polarity of the tC^O environment

[a] According to [7–9].
[b] Parameters calculated using the Eyring equation (2).

in the tC^O fluorescence intensity at the initial regions of all kinetic curves reflects local conformational changes in the DNA duplex upon wedging of the Leu70 residue into the DNA helix.

The thermodynamic analysis of the second stage of recruitment of Endo VIII to DNA duplexes observed in the case of F- and DHU-containing duplexes revealed a degree of difference. A positive $\Delta G^o_{2,298}$ value in the case of F-DNA indicates that the process is unfavorable and does not appear to take place at low temperatures. In the case of the DHU-containing substrate, the second stage of enzyme-substrate complex formation is energetically neutral; the $\Delta G^o_{2,298}$ value is equal to -0.65 kcal/mol. This stage is accompanied by an increase in ΔH^o and ΔS^o for both DNA duplexes. According to previously obtained data, at this stage, duplex bending occurs, which should be accompanied by the insertion of the damaged nucleotide into the active center of the enzyme and complete incorporation of all residues of the Gln69–Leu70–Tyr71 triad into the DNA helix [8].

Final adjustment of the active center structure occurs for the transition to the catalytic stage at the third stage of interaction between Endo VIII and the DHU substrate, which precedes the catalytic reaction. The significant increase in entropy observed at this stage is most likely due to the dissolving of polar groups in the region of the enzyme–DNA contact, as well as the removal of water molecules from the grooves of the DNA substrate. A positive change in the enthalpy ΔH^o indicates energy costs in obtaining a catalytically active conformation. This is followed by the irreversible catalytic stage (stage 4), which includes hydrolysis of the N-glycosidic bond of the damaged nucleotide and formation of a gap in the sugar-phosphate backbone of the DNA at the 3'- and 5'-sides from the damaged nucleotide. The catalytic stage is accompanied by a large expenditure of energy, as indicated by the positive values of $\Delta G^{o,\ddagger}_{298}$ = 18.0 kcal/mol and $\Delta H^{o,\ddagger}$ = 14.4 kcal/mol. The final stage of interaction between Endo VIII and a DHU-containing substrate is the dissociation of the enzyme complex from the product. It should be noted that ΔG^o_{298} (-6.2 kcal/mol) of this stage has a value similar to that of ΔG^o_{298} for the primary DNA binding stage (-7.0 to -7.4 kcal/mol).

CONCLUSION

The changes in the fluorescence intensity of 1,3-diaza-2-oxophenoxazine in the X:tC^O pair (X = G, F, DHU) were recorded for all of the Endo VIII DNA glycosylase substrates used in the study. It has been shown that

the first phase of tC^O fluorescence intensity growth is characteristic of the kinetic curves obtained for all of the substrates. According to the thermodynamic parameters obtained, this stage reflects a similar stage of the primary binding of Endo VIII to DNA. According to [7–9], this stage presents closure of the enzyme domains and an attempt to incorporate Leu70 into the DNA helix. The second phase of growth in fluorescence intensity is recorded only for DNA duplexes carrying the damaged nucleotide F or DHU. This change corresponds to the stage of second enzyme-substrate complex formation. The insertion of the damaged nucleotide into the active center of Endo VIII and incorporation of the amino acid residues of Endo VIII into the DNA double helix is likely to occur at this stage. For DHU-DNA, this stage lasts up to 1 s. It is worth noting that both enthalpy and entropy increase in this case. However, the change in the Gibbs energy $\Delta G^{o}_{i,298}$ is close to zero (0.8 and -0.65 kcal/mol for F-DNA and DHU-DNA, respectively) at this stage. Hence, the energy costs of changing the structure of the enzyme and DNA substrate molecules are compensated by the increase in the entropy of the system. The kinetic curves (*Fig. 5*) obtained for the DHU-containing duplex show that the two phases of growth in the tC^O fluorescence intensity are followed by a phase of decrease, reflecting the formation of the third enzyme-substrate complex. The final verification of the structure of the damaged nucleotide and formation of a catalytically active complex is carried out at this stage. In this case, the fluorescence intensity of tC^O is minimal, indicating the formation of the most hydrophobic environment for the fluorophore group. Also, this stage is accompanied by an increase in entropy, probably indicating the removal of water molecules from the enzyme-substrate contact region and, consequently, compaction of the enzyme–substrate complex. The thermodynamic parameter values of the fast stages of interaction between Endo VIII and DNA are consistent with previously obtained data on the mechanism of recognition and conversion of the specific site by the enzyme [7–9]. The relative changes in the thermodynamic parameters of individual fast stages of the enzymatic process catalyzed by Endo VIII DNA glycosylase are in agreement with the values previously obtained by us for other DNA glycosylases, such as Fpg [19], hOGG1 [20], and Nth [22]. ●

REFERENCES

1. Jiang D., Hatahet Z., Melamede R.J., Kow Y.W., Wallace S.S. // J. Biol. Chem. 1997. V. 272. № 51. P. 32230–32239.
2. Melamede R.J., Hatahet Z., Kow Y.W., Ide H., Wallace S.S. // Biochemistry. 1994. V. 33. № 5. P. 1255–1264.
3. Burgess S., Jaruga P., Dodson M.L., Dizdaroglu M., Lloyd R.S. // J. Biol. Chem. 2002. V. 277. № 25. P. 2938–2944.
4. Kropachev K.Y., Zharkov D.O., Grollman A.P. // Biochemistry. 2006. V. 45. P. 12039–12049.
5. Golan G., Zharkov D.O., Feinberg H., Fernandes A.S., Zaika E.I., Kycia J.H., Grollman A.P., Shoham G. // Nucl. Acids Res. 2005. V. 33. № 15. P. 5006–5016.
6. Zharkov D.O., Golan G., Gilboa R., Fernandes A.S., Gerchman S.E., Kycia J.H., Rieger R.A., Grollman A.P., Shoham G. // EMBO J. 2002. V. 21. № 4. P. 789–800.
7. Kuznetsov N.A., Koval V.V., Zharkov D.O., Fedorova O.S. // DNA Repair. 2012. V. 11. № 11. P. 884–891.
8. Kuznetsova A.A., Kuznetsov N.A., Vorobjev Y.N., Barthes N.P.F., Michel B.Y., Burger A., Fedorova O.S. // PLoS One. 2014. V. 9. № 6. P. e100007.
9. Kladova O.A., Kuznetsova A.A., Fedorova O.S., Kuznetsov N.A. // Genes (Basel). 2017. V. 8. № 5. P. 1–13.
10. Fasman G.D. Handbook of Biochemistry and Molecular Biology. 3rd Ed.// Cleveland: CRC Press, 1975.
11. Gill S.C., von Hippel P.H. // Anal. Biochem. 1989. V. 182. P. 319–326.
12. Kuzmic P. // Anal. Biochem. 1996. V. 237. P. 260–273.
13. Yakovlev D.A., Kuznetsova A.A., Fedorova O.S., Kuznetsov N.A. // Acta Naturae. 2017. V. 9. № 1. P. 88–98.
14. Kuznetsova A.A., Iakovlev D.A., Misovets I.V., Ishchenko A.A., Saparbaev M.K., Kuznetsov N.A., Fedorova O.S. // Mol. Biosyst. 2017. V. 13. № 12. P. 2638–2649.
15. Kuznetsov N.A., Kiryutin A.S., Kuznetsova A.A., Panov M.S., Barsukova M.O., Yurkovskaya A.V., Fedorova O.S. // J. Biomol. Struct. Dyn. 2017. V. 35. № 5. P. 950–967.
16. Miroshnikova A.D., Kuznetsova A.A., Vorobjev Y.N., Kuznetsov N.A., Fedorova O.S. // Mol. BioSyst. 2016. V. 12. № 5. P. 1527–1539.
17. Atkins P., Paula J. Atkins' Physical Chemistry. 8th Ed.// Oxford university press, 2006.
18. Ragone R., Colonna G., Ambrosone L. // J. Phys. Chem. 1995. V. 99. № 34. P. 13050.
19. Kuznetsov N.A., Vorobjev Y.N., Krasnoperov L.N., Fedorova O.S. // Nucl. Acids Res. 2012. V. 40. № 15. P. 7384–7392.
20. Kuznetsov N.A., Kuznetsova A.A., Vorobjev Y.N., Krasnoperov L.N., Fedorova O.S. // PLoS One. 2014. V. 9. № 6. P. e98495.
21. Miroshnikova A.D., Kuznetsova A.A., Kuznetsov N.A., Fedorova O.S. // Acta Naturae. 2016. V. 8. № 1. P. 103–110.
22. Kladova O.A., Krasnoperov L.N., Kuznetsov N.A., Fedorova O.S. // Genes (Basel). 2018. V. 9. № 4. E190.
23. Kuznetsov N.A., Fedorova O.S. // Biochem. 2016. V. 81. № 10. P. 1136–1152.

Immunogenicity of Different Forms of Middle East Respiratory Syndrome S Glycoprotein

T. A. Ozharovskaia[1], O. V. Zubkova[1], I. V. Dolzhikova[1], A. S. Gromova[1], D. M. Grousova[1], A. I. Tukhvatulin[1], O. Popova[1], D. V. Shcheblyakov[1], D. N. Scherbinin[1], A. S. Dzharullaeva[1], A. S. Erokhova[1], M. M. Shmarov[1], S. Y. Loginova[2], S. V. Borisevich[2], B. S. Naroditsky[1], D. Y. Logunov[1], A. L. Gintsburg[1]

[1]Federal Research Centre of Epidemiology and Microbiology named after Honorary Academician N. F. Gamaleya, Ministry of Health of Russian Federation, Gamaleya Str. 18, 123098, Moscow, Russia

[2]«48 Central Research Institute», Ministry of Defense of Russian Federation, Oktyabrskaya Str. 11, 141306, Sergiev Posad, Russia

*E-mail: logunov@gamaleya.org

Received November 30, 2018; in final form January 30, 2019

ABSTRACT **The Middle East respiratory syndrome coronavirus (MERS-CoV) was identified in 2012 during the first Middle East respiratory syndrome (MERS) outbreaks. MERS-CoV causes an acute lower-respiratory infection in humans, with a fatality rate of ~35.5%. Currently, there are no registered vaccines or means of therapeutic protection against MERS in the world. The MERS-CoV S glycoprotein plays the most important role in the viral life cycle (virus internalization). The S protein is an immunodominant antigen and the main target for neutralizing antibodies. In the present study, the immunogenicities of five different forms of the MERS-CoV S glycoprotein were compared: the full-length S glycoprotein, the full-length S glycoprotein with the transmembrane domain of the G glycoprotein of VSV (S-G), the receptor-binding domain (RBD) of the S glycoprotein, the membrane-fused RBD (the RBD fused with the transmembrane domain of the VSV G glycoprotein (RBD-G)), and the RBD fused with Fc of human IgG1 (RBD-Fc). Recombinant vectors based on human adenoviruses type 5 (rAd5) were used as delivery vehicles. Vaccination with all of the developed rAd5 vectors elicited a balanced Th1/Th2 response in mice. The most robust humoral immune response was induced after the animal had been vaccinated with the membrane-fused RBD (rAd5-RBD-G). Only immunization with membrane forms of the glycoprotein (rAd5-S, rAd5-S-G, and rAd5-RBD-G) elicited neutralizing antibodies among all vaccinated animals. The most significant cellular immune response was induced after vaccination of the animals with the full-length S (rAd5-S). These investigations suggest that the full-length S and the membrane form of the RBD (RBD-G) are the most promising vaccine candidates among all the studied forms of S glycoprotein.**

KEYWORDS **Middle East respiratory syndrome, MERS; MERS-CoV, glycoprotein; adenoviral vector, immunity.**

ABBREVIATIONS **95% CI – 95% confidence interval; APC – allophycocyanin; DPP4 – dipeptidyl peptidase 4; Fc – fragment crystallizable; FFU – focus-forming units; rAd5 – recombinant vector based on adenovirus type 5; RBD – receptor-binding domain of MERS-CoV S glycoprotein; RBD-Fc – receptor-binding domain of MERS-CoV S glycoprotein fused with Fc of human IgG1; RBD-G – receptor-binding domain of MERS-CoV S glycoprotein fused with the transmembrane domain of the VSV G glycoprotein; S – MERS-CoV glycoprotein; S1, S2 – domains of MERS-CoV S glycoprotein; S-G – full-length S glycoprotein with the transmembrane domain of the G glycoprotein of VSV; Th – T helper; VSV – vesicular stomatitis virus; MERS – Middle East respiratory syndrome; MERS-CoV – Middle East respiratory syndrome coronavirus; PFU – plaque-forming unit; v.p. – viral particles; GMT – geometric mean titer; IFNγ – interferon gamma; TM – transmembrane domain; SARS – severe acute respiratory syndrome; SARS-CoV – severe acute respiratory syndrome coronavirus; PBS – phosphate-buffered saline; PBST – PBS supplemented with 0.1% Tween 20; ER – endoplasmic reticulum.**

INTRODUCTION

The Middle East respiratory syndrome (MERS) is an acute inflammatory respiratory infection that was first identified in Saudi Arabia in June 2012. The causative agent of MERS was officially called the Middle East respiratory syndrome coronavirus (MERS-CoV) in 2013 [1, 2]. MERS-CoV is a single-stranded RNA virus belonging to the Coronaviridae family, genus Betacoro-

navirus. Dromedary camels are the natural reservoir of MERS-CoV; viral transmission to humans occurs during consumption of unpasteurized camel milk; airborne transmission is also possible [3–5].

To date, a total of 2,260 laboratory-confirmed cases of MERS-CoV infection have been reported, including 803 deaths [6–7]. Due to its high mortality rate (~ 35.5%) [6], combined with a wide distribution of the reservoir and absence of effective preventive drugs or treatment, WHO experts classify MERS-CoV as a virus with the potential to cause a pandemic [8]. Therefore, vaccine development is necessary in order to stave off such a pandemic.

The main protective MERS-CoV antigen is the S glycoprotein presented as a trimer on the virus surface. The S glycoprotein plays an important role in the virus' internalization into the cell [9]. The S glycoprotein is subdivided into two subunits: the S1 subunit containing the receptor-binding domain (RBD), and the S2 subunit responsible for the fusion of the virus and cell membrane [10–13]. These features make the S protein an important target for MERS-CoV vaccine development [14–17]. The RBD of the MERS-CoV S glycoprotein is a key target for the development of preventive and therapeutic means against MERS [18–20], because the RBD mediates the interaction between MERS-CoV and the receptor DPP4 on the cell surface.

In order to develop an effective MERS-CoV vaccine, it is important to understand which form of the glycoprotein to include in the vaccine to provide protection against MERS. There are data that demonstrate the immunogenicity of various forms of the MERS-CoV glycoprotein [21–25]. However, the question of which form is preferable for a vaccine remains open, since an antigen panel has not been tested under the same conditions. In order to address this knowledge gap, we constructed five recombinant vectors based on human adenovirus type 5 (rAd5) expressing different forms of the MERS-CoV S glycoprotein:

– the full-length S glycoprotein localized in the endoplasmic reticulum (ER);

– two secreted variants of the receptor binding domain of the MERS-CoV S glycoprotein containing the alkaline phosphatase leader peptide (the RBD and the RBD fused with Fc of human IgG1 to increase stability and immunogenicity [18,19]); and

– two transmembrane (TM) forms localized in the plasma membrane of the cell: either the full-length S or the RBD with the TM domain of the vesicular stomatitis virus (VSV) G glycoprotein. Because the full-length S glycoprotein is localized in the ER [26], we constructed an S-G variant with a deleted ER localization signal.

We chose a platform based on the recombinant viral vectors rAd5 for delivering the S glycoprotein, because such vectors can efficiently deliver the transgene to multiple cell types [27, 28], their genome has been fully characterized, they are able to grow to high titers [29], and they can induce a strong humoral and cellular immune response [30, 31].

The present study compares the humoral and cellular immune responses induced by vaccination of mice with rAd5 carrying different forms of the MERS-CoV S glycoprotein.

EXPERIMENTAL

Cell lines

The HEK293 and A549 cell lines were obtained from the Russian collection of vertebrate cell lines (Russia). The HEK293T and Vero E6 cells were obtained from ATCC (USA). All cells were cultured in DMEM (Dulbecco's modified Eagle medium) supplemented with 10% fetal bovine serum at 37°C with 5% CO_2.

Construction of recombinant adenoviral particles expressing different forms of the MERS-CoV S glycoprotein

The MERS-CoV S glycoprotein amino acid sequences of strains (2015–2017) were obtained from the NCBI database [32]. The consensus sequence of the MERS-CoV S glycoprotein was made on the basis of amino acid sequences using the Geneious® 10.2.3 software. The nucleotide sequences of different glycoprotein forms were optimized for expression in mammalian cell lines and synthesized by Evrogen JSC (Russia). Five recombinant plasmids (pAd5-S, pAd5-S-G, pAd5-RBD, pAd5-RBD-G, and pAd5-RBD-Fc) were generated. rAd5 was obtained according to the procedure described previously [33].

Generation of lentiviral particles pseudotyped with MERS-CoV S glycoprotein (pseudoviruses)

HEK293T cells were seeded in 15-cm culture Petri dishes and co-transfected with three plasmids (pCMVΔR8,2; pLV-CMV-EGFP; pCMV-MERS-CoV-S) to obtain pseudoviruses. Seventy-two hours later, the supernatants were collected, filtered, divided into aliquots, and stored at –80°C. Vero E6 cells were used for titrating the pseudoviruses. The titer of the pseudotyped virus was determined in terms of focus-forming units (FFUs).

Evaluating the expression of different forms of the MERS-CoV S glycoprotein by western blotting

HEK293 cells were seeded in 35 mm Petri dishes and incubated overnight to 70% confluence. Then, rAd5

were added to the cells at 100 PFUs/cell. rAd5-null was used as a control virus. After 24 h, the expression of different forms of the MERS-CoV S glycoprotein was evaluated by western blotting using S-specific antibodies (40069-RP02, Sino Biological, China) and antibodies specific to rabbit IgG (NA934V, GE, Great Britain). Expression of the membrane-fused forms of the glycoprotein (S, S-G, RBD-G) was detected in cell lysates prepared using the Cell Culture Lysis Reagent (Promega, USA). Expression of the secreted versions of the glycoprotein (RBD, RBD-Fc) was evaluated in the culture medium. Lysate samples were loaded onto wells (10 μg of total protein in a volume of 10 μl/well). Samples of the medium were loaded in volume 10 μl/well.

Laboratory animals

All animal experiments were performed in strict accordance with the recommendations of the National Standard of the Russian Federation (GOST R 53434–2009; Principles of Good Laboratory Practice). Six-week-old female C57/BL6 mice (18–20 g) were obtained from the Pushchino Breeding Facility (Russia). The mice had free access to water and food. The mice were housed in an ISOcage system (Tecniplast, Italy).

Immunization and serum samples collection

The mice were randomly distributed into groups (n = 5 per group for the analysis of the humoral immune response and n = 9 per group for the analysis of the T-cell response) and intramuscularly vaccinated with the obtained recombinant adenoviral particles at a dose of 10^8 v.p./mouse in a total volume of 0.1 mL. Serum specimens were collected on day 21 post-vaccination for detection of S-specific IgG antibodies.

Determination of antibody titers in mouse serum samples using enzyme-linked immunosorbent assay (ELISA)

Glycoprotein-specific antibody titers in mouse serum samples were determined by enzyme-linked immunosorbent assay (ELISA). The following recombinant proteins were used for analysis: the S glycoprotein (40069-V08B; Sino Biological) and the RBD (40071-V08B1; Sino Biological). Non-specific antibody binding sites were blocked with PBS with 0.1% Tween 20 (PBST) containing 5% fat-free milk (A0830; AppliChem, Spain). The serum samples were titrated with two-fold serial dilutions in PBST containing 3% fat-free milk. The following anti-mouse IgG horseradish peroxidase-conjugated secondary antibodies were used for detection: for the total IgG titer, NXA931 (GE Healthcare, USA); for IgG1, ab97240 (Abcam, UK); for IgG2a, ab97245 (Abcam, UK); for IgG2b, ab97250 (Abcam, UK); and for IgG3, ab97260 (Abcam, UK). A tetramethylbenzidine solution (Research Institute of Organic Semiproducts and Dyes, Russia) was used as a visualizing reagent. The reaction was stopped by adding 1M H_2SO_4, and the optical density was measured at 450 nm (OD_{450}) using a Multiscan FC spectrophotometric plate reader (Thermo Fisher Scientific). The IgG titer was determined as the maximum serum dilution in which the OD_{450} value of a serum sample from an immunized animal exceeded that of the control animal serum sample more than twofold.

Pseudovirion-based neutralization assay (PsVNA)

The pseudovirion-based neutralization assay (PsVNA) was performed as described previously [34]. Briefly, heat-inactivated serum samples were diluted 1:10, 1:40, 1:160, and 1:640. These samples were then mixed with an equal volume of DMEM containing 10^5 FFUs/ml of the pseudovirions. The mixture was incubated at 37°C for 1 h, then inoculated onto a Vero E6 cell monolayer and incubated at 37°C for 42 h. The number of EGFP fluorescent cell focuses was counted. The pseudovirion neutralization titer of serum samples from an immunized animal was determined as the maximum dilution where 50% reduction of EGFP fluorescent cell focuses compared with the serum samples of intact (non-immunized) animals was determined.

Analysis of T-cell response (lymphocyte proliferation assay)

Mice were euthanized on day 8 post-vaccination, and their spleens were collected. The spleens were homogenized by passage through a 100 μm sieve in sterile PBS. Splenocytes were isolated by Ficoll (1.09 g/mL; PanEco, Russia) density gradient centrifugation (800 *g* for 30 min). For T-cell proliferation assay, the splenocytes were stained with carboxyfluorescein using a succinimidyl ester (CFSE) tracer kit (Invitrogen, USA) according to the procedure described previously [35]. The cells were seeded in 96-well plates (2×10^5 cells/well) in a complete RPMI1640 medium re-stimulated with the recombinant MERS-CoV S protein (40071-V08B1; Sino Biological) at 1 μg/well. After 3 days, the cells were harvested, washed with PBS, stained with antibodies specific to CD3, CD4, and CD8: allophycocyanin (APC)-labelled anti-CD3, APC–Cy7-labelled anti-CD8, and phycoerythrin-labelled anti-CD4 (BD Biosciences, USA), and fixed in 1% paraformaldehyde. Proliferating CD4+ and CD8+ T lymphocytes were determined in the cell mixture using a BD FACS Aria III flow cytometer (BD Biosciences). The resulting percentage of proliferating cells (X) was determined using the formula X = %st − %, where %st is the percentage of proliferating cells after splenocyte re-stimulation with the recombinant MERS-CoV S glycoprotein, and % is

the percentage of proliferating cells in the absence of splenocyte re-stimulation (intact cells).

Analysis of interferon gamma (IFN-γ) production

Splenocytes were isolated on day 15 post-vaccination using the procedure described above. The cells were seeded in 96-well plates (2×10^5 cells/well) in a RPMI1640 medium, followed by re-stimulation with recombinant MERS-CoV S (40071-V08B1; Sino Biological) at a concentration of 1 μg/well. Forty-eight h post-treatment, the culture supernatants were collected. The concentration of IFN-γ in the supernatants was measured by ELISA using a commercial kit (mouse IFN-γ ELISA kit; Invitrogen) according to the manufacturer's instructions. The increase in IFN-γ concentration was determined using the formula X = Cst /Cint, where X is the fold increase in IFN-γ concentration, Cst is the IFN-γ concentration in the medium from the stimulated cells (pg/ml), and Cint is the IFN-γ concentration in the medium from the non-stimulated (intact) cells (pg/ml).

Statistical analysis

The statistical analysis was performed using the GraphPad 7.0 software (GraphPad Software, USA). When analysing data from unpaired samples, either the Student's t-test for independent samples or the Mann–Whitney U-test was used depending on the data distribution normality. Distribution normality was determined using the generalized D'Agostino–Pearson test.

RESULTS

Generation of rAd5 vectors

In order to determine and compare the immunogenicities of different forms of the MERS-CoV S protein, we constructed five rAd5 vectors: rAd5-S, rAd5-S-G, rAd5-RBD, rAd5-RBD-G, and rAd5-RBD-Fc. The schemes for the target transgenes in the rAd5 genomes are shown in *Fig. 1A*. Expression levels of different forms of the MERS-CoV S glycoprotein were evaluated by western blot analysis (*Fig. 1B*). In the samples of the full-length glycoprotein (rAd5-S and rAd5-S-G), the S protein was detected as two polypeptides (*Fig. 1B*), with the upper band representing the glycosylated form of the S protein (~230–250 kDa), and the lower band (~100 kDa) representing the S1 subunit resulting from S-protein cleavage by host-cell proteases. The molecular weights of the bands were higher than those calculated according to the nucleotide sequences, being indicative of tentative protein glycosylation [14, 16, 36–38]. A single polypeptide specifically recognized by the antibody was detected in the RBD (RBD, RBD-G and RBD-Fc) samples (*Fig. 1B*), its molecular weight being ~25 kDa, ~30 kDa, and ~55 kDa, respectively. The molecular weights of the polypeptides based on the RBD corresponded to the calculated weights.

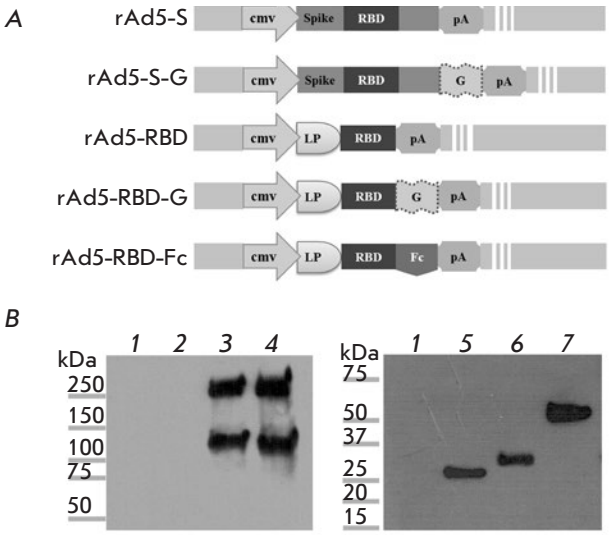

Fig. 1. *A* – Schematic structures of target transgenes in the rAd5-S, rAd5-S-G, rAd5-RBD, rAd5-RBD-G, and rAd5-RBD-Fc genomes. Cmv – a promoter of the E1 region of human cytomegalovirus; G – the gene of the G glycoprotein of the vesicular stomatitis virus; LP – the leader-peptide sequence directing protein secretion; pA – polyadenylation signal; RBD – the receptor-binding domain of MERS-CoV S glycoprotein; Spike – MERS CoV S glycoprotein. *B* – Western blot analysis of the MERS-CoV S glycoprotein variants expressed by each rAd5. Lane *1* – lysate from control Ad5-null cells; lane *2* – intact cells; lane *3* – lysate from rAd5-S cells; lane *4* – lysate from rAd5-S-G cells; lane *5* – the medium from the rAd5-RBD cell culture; lane *6* – lysate from rAd5-RBD-G cells; lane *7* – the medium from the rAd5-RBD-Fc cell culture

rAd5 expressing different MERS-CoV S glycoprotein variants induce a humoral immune response

Mice were intramuscularly immunized with single doses of rAd5-S, rAd5-S-G, rAd5-RBD, rAd5-RBD-G, and rAd5-RBD-Fc (10^8 v.p. per mouse). Serum samples were collected three weeks after the immunization, and the titers of antibodies specific to S protein and RBD were analyzed (*Fig. 2*). No glycoprotein-specific IgG was detected in the serum samples from mice in the control groups (non-immunized mice and those immunized with rAd5-null). The highest titer of IgG specific to S glycoprotein was detected in the group

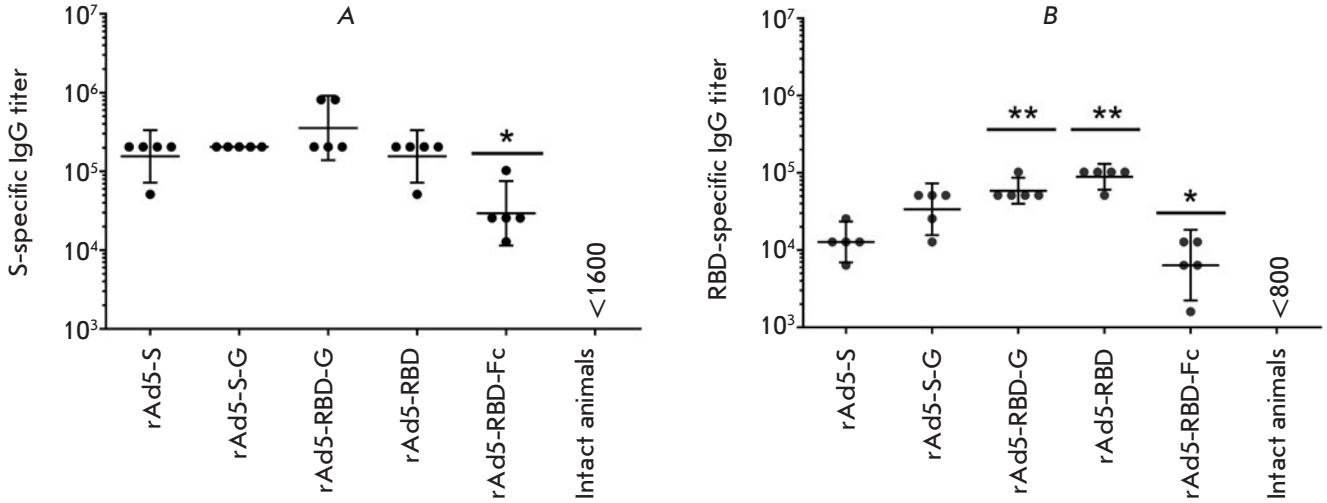

Fig. 2. Glycoprotein-specific IgG titers in the blood serum of immunized animals. The figure shows IgG titers: (*A*) specific to the MERS-CoV S glycoprotein and (*B*) specific to the RBD. Scatter plots show the geometric mean titer (GMT) and 95% confidence interval (CI) for each group (n = 5 mice/group). Asterisks indicate significant intergroup differences in IgG titers. * $p < 0.05$, rAd5-RBD-Fc is compared with other groups; ** $p < 0.05$, rAd5-RBD, and rAd5-RBD-G are compared with other groups, except for rAd5-RBD and rAd5-RBD-G (the Mann–Whitney U test)

immunized with rAd5-RBD-G [geometric mean titer (GMT) was 356,055; the 95% confidence interval (CI) was 139,042–911,772]. The lowest titer of IgG specific to the S glycoprotein was observed in the group immunized with rAd5-RBD-Fc [GMT: 29,407; 95% CI: 11,455–75,492] (*Fig. 2A*). ELISA for RBD-specific IgG antibodies showed that rAd5-RBD-G [GMT: 89,144; 95% CI: 60,665–130,994] and rAd5-RBD [GMT: 58,831; 95% CI: 40,024–86,424] were the constructs with the highest immunogenicity, while rAd5-RBD-Fc [GMT: 6,400; 95% CI: 2,230–18,364] had the lowest immunogenicity. No significant differences in RBD-specific IgG titers were detected between rAd5-RBD and rAd5-RBD-G (*Fig. 2B*).

There are four IgG isotypes known in mice to be responsible for identification and clearance of many antigens: IgG1, IgG2a, IgG2b, and IgG3 [39]. Determination of the titers of IgG isotypes three weeks post-immunization showed that all four IgG isotypes were detected in all vaccinated animals (*Fig. 3*). For the IgG1, IgG2a, and IgG2b isotypes in immunized animals, titers were as follows for each group: rAd5-S (GMT: 409,600, 409,600, and 89,144, respectively); rAd5-S-G (GMT: 54,0470, 470,506, and 155,209, respectively); rAd5-RBD (GMT: 540,470,713,155, and 135,118, respectively); and rAd5-RBD-G (GMT: 356,578, 713,155, and 204,800, respectively). We observed no significant intergroup difference in isotype titers. Following vaccination with rAd5-RBD-Fc, IgG1, IgG2a, and IgG2b, the titers were significantly lower than those in the other groups (GMT:102,400, 89,144, and 12,800, respectively). The IgG3 titers did not differ significantly between the groups (rAd5-S, rAd5-S-G, rAd5-RBD, rAd5-RBD-G, and rAd5-RBD-Fc; GMT: 33,779, 14,703, 51,200, 33,779, and 5572, respectively). Hence, according to these findings, the IgG1 and IgG2a isotypes make the greatest contribution to the total titer of glycoprotein-specific IgG.

rAd5 expressing membrane forms of the MERS-CoV S glycoprotein elicit the production of neutralizing antibodies in mice

Determination of the titers of neutralizing antibodies (in the pseudovirion-based neutralization assay) showed that all mice immunized with rAd5-S, rAd5-S-G, and rAd5-RBD-G generated neutralizing antibodies (*Fig. 4*) with the GMT of 1:121, 1:160 and 1:70, respectively; no significant differences in PsVNA titers were observed ($p > 0.05$). In the rAd5-RBD group, neutralizing antibodies were detected only in three mice while no neutralizing antibodies were detected in the rAd5-RBD-Fc group and in intact animals. Hence, the results of the conducted experiment showed that only immunization with rAd5 expressing the membrane forms of the glycoprotein (S, S-G, RBD-G) leads to the generation of neutralizing antibodies.

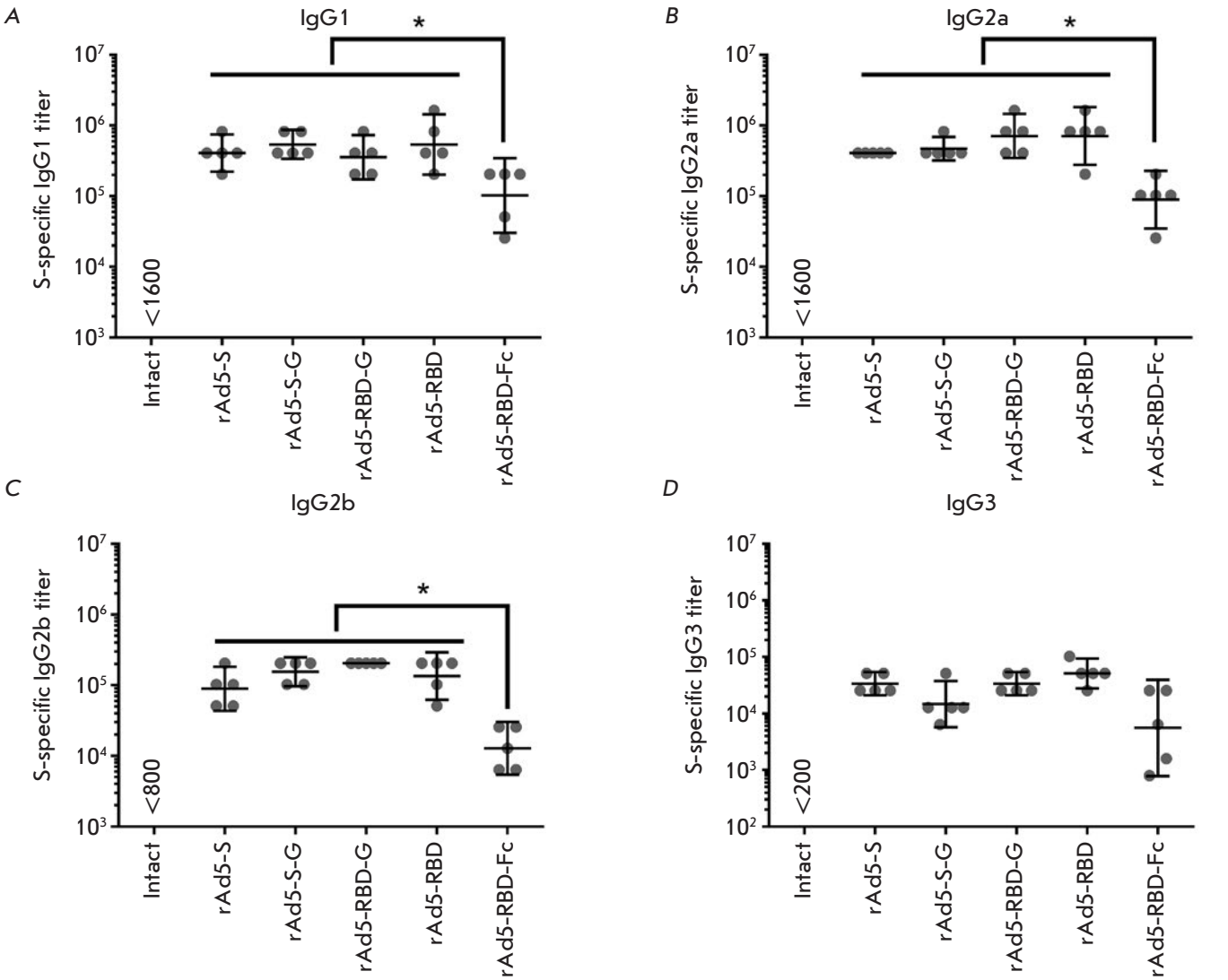

Fig. 3. Analysis of IgG antibody isotypes in mice after immunization with rAd5 expressing different forms of the MERS-CoV S glycoprotein. The figure shows the titers of IgG1 (*A*), IgG2a (*B*), IgG2b (*C*), and IgG3 (*D*) specific to the MERS-CoV S glycoprotein in the serum samples of immunized animals. Scatter plots show the geometric mean titer (GMT) and 95% confidence interval (CI) for each group (n = 5). Asterisks indicate significant intergroup differences in IgG titers. * $p < 0.05$, Mann–Whitney U test

rAd5 expressing the MERS-CoV S protein variants elicit the T-cell response

The post-vaccination cellular immune response was evaluated using two methods: according to the number of proliferating T cells and according to IFN-γ production by T cells in response to glycoprotein re-stimulation. The full-length MERS-CoV S protein was used for re-stimulation, since it contains the largest number of epitopes and is present in MERS-CoV particles. The proliferation assay of CD4+ cells on day 8 post-vaccination (*Fig. 5*, left-side panel) showed that the highest lymphoproliferative activity was observed in the rAd5-S group (2.10%), while the lowest one was detected in the rAd5-RBD-Fc group (0.25%). Significant differences in the lymphoproliferative response of CD4+ cells between the groups of immunized and intact animals were observed in the rAd5-S (2.10%) and rAd5-S-G (1.63%) groups. CD8+ cells proliferation assay (*Fig. 5*, right-side panel) showed that the highest lymphoproliferative response was observed in the rAd5-S group (1.90%), while the lowest one was detected in the rAd5-RBD-Fc group (0.35%). Signifi-

cant differences in the lymphoproliferative response of CD8+ cells between the groups of immunized and intact animals were observed in the rAd5-S (1.90%), rAd5-S-G (1.15%), and rAd5-RBD (0.55%) groups. An analysis of IFN-γ production by splenocytes after the MERS-CoV S glycoprotein re-stimulation also showed that the strongest cellular immune response developed in groups of animals immunized with rAd5-S and rAd5-S-G (*Fig. 6*): IFN-γ secretion increased as compared to that for intact cells 15.12 ± 0.43-fold and 10.14 ± 0.97-fold, respectively.

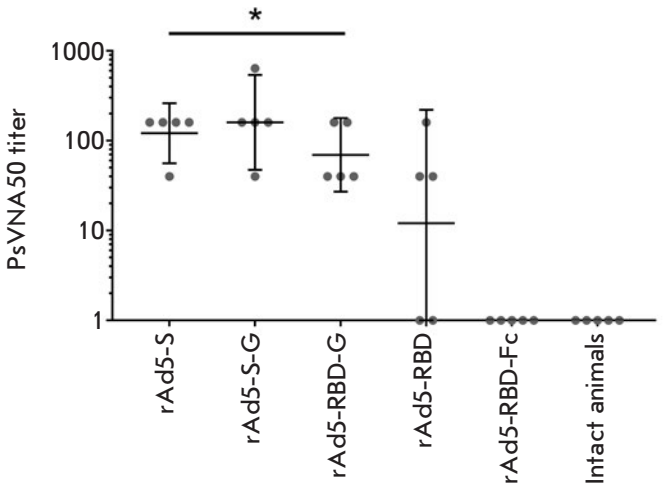

Fig. 4. The titers of neutralizing antibodies in the blood serum of immunized animals. The neutralization assay was performed using lentiviral particles pseudotyped with MERS-CoV S glycoprotein. Scatter plots show the geometric mean titer (GMT) and 95% confidence interval (CI) for each group (n = 5). Asterisks indicate no significant intergroup differences in the titers of neutralizing antibodies. * $p > 0.05$, Mann–Whitney U test

DISCUSSION

Currently, there are no specific prophylactic or therapeutic agents against the Middle East respiratory syndrome in the world. Intensive research focusing on the development of vaccines against this disease is being conducted in the USA, Germany, South Korea, and other countries [40–41]. Several candidate vaccines based on MERS-CoV glycoprotein are known: recombinant viral vectors based on the recombinant vaccinia virus, adenovirus, measles virus and others; DNA vaccines; combined candidate vaccines based on DNA and recombinant protein; and candidate vaccines based on virus-like particles and recombinant proteins [22, 38, 41–46].

The key in vaccine development is antigen selection. Most of the developed vaccines against MERS are based on the application of different forms of the MERS-CoV glycoprotein (the full-length S, the S1 subunit, and RBD) [14–16, 18, 22, 24, 47–55], which is the main target for neutralizing antibodies. However, the question that still remains open is which form to choose for the development of an effective vaccine? It is known that the full-length S glycoprotein ensures

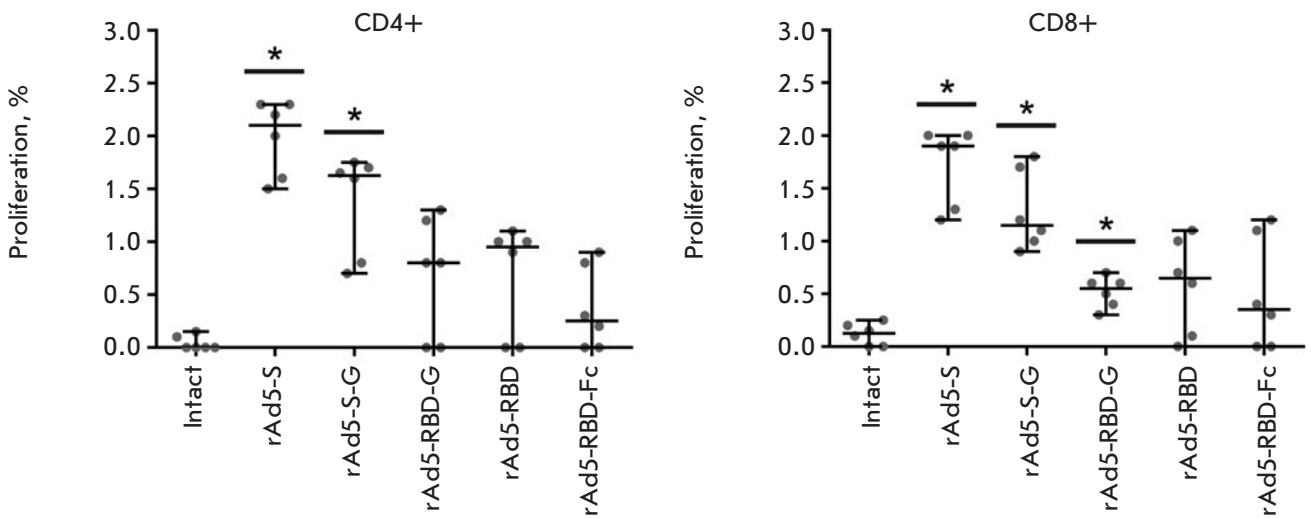

Fig. 5. The study of lymphoproliferative activity of splenocytes in immunized mice. The figure shows the levels (%) of proliferating CD4+ and CD8+T cells re-stimulated by the MERS-CoV S protein on day 8 post-vaccination. Scatter plots show the median lymphoproliferative activity of re-stimulated cells (%) with 95% CIs for each group from one representative experiment (n = 6 mice/group). Asterisks indicate significant differences in the percentage of proliferating cells between vaccinated and intact animals. * $p < 0.05$, Mann–Whitney U test

100% protection against lethal infection caused by MERS-CoV in animals [44]. However, some authors have expressed concern about the use of full-length MERS-CoV S in the vaccine. Thus, it has been reported that a vaccine based on a full-length glycoprotein of the severe acute respiratory syndrome (SARS) coronavirus (which, like MERS-CoV, belongs to the genus Betacoronavirus) induces immunopathology in the lungs of a vaccinated organism because of the strong antibody response to the SARS-CoV glycoprotein and weak T cell (Th2-skewed) immune response [56, 57].

Glycoprotein modifications were for the most part based on the fact that the receptor-binding domain of the glycoprotein was included in the antigen. Various studies showed immunogenicity of the S1 subunit, the RBD or the RBD fused with Fc of human IgG1 (RBD-Fc) [15, 18, 19, 49, 58]. Studies focused on protection of drugs based on RBD (subunit vaccines) showed that RBD vaccination protected ~ 80% of animals from MERS-CoV, despite the high titers of neutralizing antibodies capable of blocking the interaction between the virus and the DPP4 receptor on the cell surface [42, 59]. The lack of 100% protection seems to be related to the need to develop a cellular immune response, as well as the need to block fusion of the viral and cell membranes, which is mediated by the S2 subunit. Furthermore, application of subunit-based vaccines, as well as inactivated ones, prevents the emergence of a balanced Th1/Th2 response and often leads to the development of Th2-skewed immunity [22, 42]. In the case of MERS, its development can lead to lung immunopathologies [48]. Therefore, it is important to take into account the fact that the vaccine-induced immunity must be Th1/Th2-balanced when developing an anti-MERS vaccine.

Numerous antigens based on the MERS-CoV S glycoprotein have been studied. However, these antigens, under the same conditions (using the same antigen delivery platform), have not been compared directly. In the present study, direct comparison of the immunogenicities of five different forms of the MERS-CoV S glycoprotein under the same conditions was carried out; rAd5 was used for delivery. Strong antibody (mainly IgG1 and IgG2a) and T-cell immune responses developed in animals vaccinated with rAd5 expressing various forms of the MERS-CoV S glycoprotein. Each of the rAd5 variants allowed for the emergence of a balanced Th1/Th2 response, which is one of the key aspects in the development of an anti-MERS vaccine. In a study focused on the intensity of the humoral immune response, the membrane form of the RBD (rAd5-RBD-G) elicited a more powerful IgG response than the other studied forms. It was also demonstrated

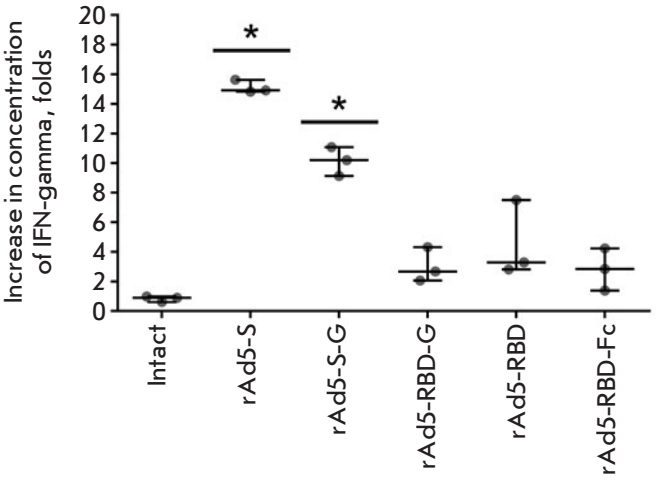

Fig. 6. The increase in the concentration of IFN-γ in the media of splenocytes from immunized mice after re-stimulation with the recombinant full-length MERS-CoV S protein. Scatter plots show the median (95% CI) increase (fold change) in IFN-γ production following re-stimulation for each group from one representative experiment (n = 3 mice/group). Asterisks indicate significant differences in IFN-γ production between the cells taken from vaccinated and intact animals. * $p < 0.05$, Student's t-test for independent samples

that only the membrane forms of the MERS-CoV glycoprotein (rAd5-S, rAd5-S-G, and rAd5-RBD-G) stimulate the production of neutralizing antibodies. In the investigation of cellular immune response intensity, the forms of the full-length MERS-CoV glycoprotein (rAd5-S and rAd5-S-G) were characterized by the strongest immunogenicity.

To sum up, the findings obtained in our study suggest that, among all the studied forms of the MERS-CoV S glycoprotein, the full-length S glycoprotein and the membrane form of RBD (RBD-G) are the most promising candidates for inclusion in a vaccine.

CONCLUSIONS

The immunogenicities of five forms of MERS-CoV S glycoprotein in mice were compared in this study. A platform based on the recombinant adenoviral vectors rAd5 was used for antigen delivery. The studies have yielded the following results:

– The most powerful humoral immune response was observed in animals immunized with the membrane-bound form of the RBD (rAd5-RBD-G);

– Only the membrane forms of MERS-CoV glycoprotein (rAd5-S, rAd5-S-G and rAd5-RBD-G) induced

the generation of neutralizing antibodies in all vaccinated mice;

– The most significant cellular immune response developed after immunization of animals with the full-length glycoprotein (rAd5-S); and

– Vaccination of mice with all developed rAd5 vectors elicited a balanced Th1/Th2 response. ●

This work was supported by the Ministry of Health of the Russian Federation (State Assignment no. 056-00108-18-00).

The authors declare that there is no conflict of interest regarding the publication of this article.

REFERENCES

1. de Groot R.J., Baker S.C., Baric R.S., Brown C.S., Drosten C., Enjuanes L., Fouchier R.A.M., Galiano M., Gorbalenya A.E., Memish Z.A., et al. // J. Virol. 2013. V. 87. № 14. P. 7790–7792.
2. Zaki A.M., van Boheemen., Bestebroer T.M., Osterhaus A.D., Fouchier R.A. // N. Engl. J. Med. 2012. V. 367. № 19. P. 1814–1820.
3. Memish Z.A., Cotten M., Meyer B., Watson S.J., Alsahafi A.J., Al Rabeeah A.A., Corman V.M., Sieberg A., Makhdoom H.Q., Assiri A., et al. // Emerg. Infect. Dis. 2014. V. 20. № 6. P. 1012–1015.
4. Reusken C.B., Farag E.A., Jonges M., Godeke G.J., El-Sayed A.M., Pas S.D., Raj V.S., Mohran K.A., Moussa H.A., Ghobashy H., et al. // Euro. Surveill. 2014. V. 19. № 23. P. 1–5.
5. Azhar E.I., Hashem A.M., El-Kafrawy S.A., Sohra S.S., Aburizaiza A.S., Farraja S.A., Hassan A.M., Al-Saeeda M.S., Jamjoom G.A., Madani T.A. // MBio. 2014. V. 5. № 4. P. 1–4.
6. World Health Organisation | Middle East respiratory syndrome coronavirus (MERS-CoV). http://www.who.int/emergencies/mers-cov/en/.
7. Aly M., Elrobh M., Alzayer M., Aljuhani, S., Balkhy, H. // PLoS One. 2017. V. 12. № 10. P. 1–11.
8. World Health Organisation | WHO Research and Development Blueprint: 2017 Annual review of diseases prioritized under the Research and Development Blueprint. http://www.who.int/blueprint/what/research-development/2017-Prioritization-Long-Report.pdf.
9. Qian Z., Dominguez S.R., Holmes K.V. // PLoS. One. 2013. V. 8. № 10. P. e76469.
10. Millet J.K., Whittaker G.R. // Proc. Natl. Acad. Sci. USA. 2014. V. 111. № 42. P. 15214–15219.
11. Lu G., Wang Q., Gao G.F. // Trends Microbiol. 2015. V. 23. № 8. P. 468–478.
12. Lu L., Liu Q., Zhu Y., Chan K.-H., Qin L., Li Y., Wang Q., Chan J.F.-W., Du L., Yu F., et al. // Nat. Commun. 2014. V. 5. № 3067. P. 1–12.
13. Raj V.S., Mou H., Smits S.L., Dekkers D.H., Müller M.A., Dijkman R., Muth D., Demmers J.A., Zaki A., Fouchier R.A., et al. // Nature. 2013. V. 495. № 7440. P. 251–254.
14. Song F., Fux R., Provacia L.B., Volz A., Eickmann M., Becker S., Osterhaus A.D., Haagmans B.L., Sutter G. // J. Virol. 2013. V. 87. № 21. P. 11950–11954.
15. Kim E., Okada K., Kenniston T., Raj V.S., AlHajri M.M., Farag E.A.B.A., AlHajri F., Osterhaus A.D.M.E., Haagmans B.L., Gambotto A. // Vaccine. 2014. V. 32. № 45. P. 5975–5982.
16. Guo X., Deng Y., Chen H., Lan J., Wang W., Zou X., Hung T., Lu Z., Tan W. // Immunology. 2015. V. 145. № 4. P. 476–484.
17. Liu R., Wang J., Shao Y., Wang X., Zhang H., Shuai L., Ge J., Wen Z., Bu Z. // Antiviral Res. 2018. V. 150. P. 30–38.
18. Du L., Kou Z., Ma C., Tao X., Wang L., Zhao G., Chen Y., Yu F., Tseng C.T.K., Zhou Y., Jiang S. // PLoS One. 2013. V. 8. № 12. P. 2–10.
19. Du L., Zhao G., Kou Z., Ma C., Sun S., Poon V.K.M., Lu L., Wang L., Debnath A.K., Zheng B.-J., et al. // J. Virol. 2013. V. 87. № 17. P. 9939–9942.
20. Ma C., Li Y., Wang L., Zhao G., Tao X., Tseng C.T.K., Zhou Y., Du L., Jiang S. // Vaccine. 2014. V. 32. № 18. P. 2100–2108.
21. Al-Amri S.S., Abbas A.T., Siddiq L.A., Alghamdi A., Sanki M.A., Al-Muhanna M.K., Alhabbab R.Y., Azhar E.I., Li X., Hashem A.M. // Sci. Rep. 2017. V. 7. № 44875. P. 1–8.
22. Ma C., Wang L., Tao X., Zhang N., Yang Y., Tseng C.T.K., Li F., Zhou Y., Jiang S., Du L. // Vaccine. 2014. V. 32. № 46. P. 6170–6176.
23. Pallesen J., Wang N., Corbett K.S., Wrapp D., Kirchdoerfer R.N., Turner H.L., Cottrell C.A., Becker M.M., Wang L., Shi W., et al. // Proc. Natl. Acad. Sci. USA. 2017. V. 114. № 35. P. E7348–E7353.
24. Wang L., Shi W., Joyce M.G., Modjarrad K., Zhang Y., Leung K., Lees C.R., Zhou T., Yassine H.M., Kanekiyo M., et al. // Nat. Commun. 2015. V. 6. P. 7712.
25. Zhang N., Channappanavar R., Ma C., Wang L., Tang J., Garron T., Tao X., Tasneem S., Lu L., Tseng C.T., Zhou Y., Perlman S., Jiang S., Du L. // Cell. Mol. Immunol. 2016. V. 13. № 2. P. 180–190.
26. Du L., Yang Y., Zhou Y., Lu L., Li F., Jiang S. // Expert Opin. Ther. Targets. 2017. V. 21. № 2. P. 131–143.
27. Appaiahgari M.B., Vrati S. // Expert Opin. Biol. Ther. 2015. V. 15. № 3. P. 337–351.
28. Benihoud K., Yeh P., Perricaudet M. // Curr. Opin. Biotechnol. V. 10. № 5. P. 440–447.
29. Kamen A., Henry O. // J. Gene Med. 2004. V. 6. № S1. P. 184–192.
30. Muruve D.A. // Hum. Gene Ther. 2004. V. 15. № 12. P. 1157–1166.
31. Dolzhikova I.V., Tokarskaya E.A., Dzharullaeva A.S., Tukhvatulin A.I., Shcheblyakov D.V., Voronina O.L., Syromyatnikova S.I., Borisevich S.V., Pantyukhov V.B., Babira V.F., et al. // Acta Naturae. 2017. V. 9. № 3. P. 4–11.
32. Hatcher E.L., Zhdanov S.A., Bao Y., Blinkova O., Nawrocki E.P., Ostapchuck Y., Schäffer A.A., Brister J.R. // Nucl. Acids. Res. 2017. V. 45. № D1. P. D482–D490.
33. Gribova I.Y., Tillib S.V, Tutykhina I.L., Shmarov C.E., Logunov D.Y., Verkhovskaya L.V., Naroditskii B.S., Gintsburg A.L. // Acta Naturae. 2011. V. 3. № 3. P. 64–70.
34. Grehan K., Ferrara F., Temperton N. // Methods X. 2015. V. 2. P. 379–384.
35. Quah B.J., Warren H.S., Parish C.R. // Nat. Protoc. 2007. V. 2. № 9. P. 2049–2056.
36. Chi H., Zheng X., Wang X., Wang C., Wang H., Gai W., Perlman S., Yang S., Zhao J., Xia X. // Vaccine. 2017. V. 35. № 16. P. 2069–2075.

37. Deng Y., Lan J., Bao L., Huang B., Ye F., Chen Y., Yao Y., Wang W., Qin C., Tan W. // Emerg. Microbes Infect. 2018. V. 7. № 60. P. 1–10.
38. Nyon M.P., Du L., Tseng C.K., Seid C.A., Pollet J., Naceanceno K.S., Agrawal A., Algaissi A., Peng B.H., Tai W., et al. // Vaccine. 2018. V. 36. № 14. P. 1853–1862.
39. Snapper C.M., Mond J.J. // Immunol. Today. 1993. V. 14. № 1. P. 15–17.
40. Perlman S., Vijay R. // Int. J. Infect. Dis. 2016. V. 47. P. 23–28.
41. Okba N.M., Raj V.S., Haagmans B.L. // Curr. Opin. Virol. 2017. V. 23. P. 49–58.
42. Tai W., Zhao G., Sun S., Guo Y., Wang Y., Tao X., Tseng C.K., Li F., Jiang S., Du L., Zhou Y. // Virology. 2016. V. 499. P. 375–382.
43. Alharbi N.K., Padron-Regalado E., Thompson C.P., Kupke A., Wells D., Sloan M.A., Grehan K., Temperton N., Lambe T., Warimwe G., et al. // Vaccine. 2017. V. 35. № 30. P. 3780–3788.
44. Munster V.J., Wells D., Lambe T., Wright D., Fischer R.J., Bushmaker T., Saturday G., van Doremalen N., Gilbert S.C., De Wit E., et al. // NPJ. Vaccines. 2017. V. 2. P. 28.
45. Malczyk A.H., Kupke A., Prüfer S., Scheuplein V.A., Hutzler S., Kreuz D., Beissert T., Bauer S., Hubich-Rau S., Tondera C., et al. // J. Virol. 2015. V. 89. № 22. P. 11654–11667.
46. Lan J., Deng Y., Song J., Huang B., Wang W., Tan W. // Virol. Sin. 2018. V. 33. № 5. P. 453–455.
47. Modjarrad K. // Vaccine. 2016. V. 34. № 26. P. 2982–2987.
48. Agrawal A.S., Tao X., Algaissi A., Garron T., Narayanan K., Peng B.H., Couch R.B., Tseng C.T.K. // Hum. Vaccin. Immunother. 2016. V. 12. № 9. P. 2351–2356.
49. Coleman C.M., Liu Y.V., Mu H., Taylor J.K., Massare M., Flyer D.C., Glenn G.M., Smith G.E., Frieman M.B. // Vaccine. 2014. V. 32. № 26. P. 3169–3174.
50. Haagmans B.L., van den Brand J.M.A., Raj V.S., Volz A., Wohlsein P., Smits S.L., Schipper D., Bestebroer T.M., Okba N., Fux R., et al. // Science. 2016. V. 351. № 6268. P. 77–81.
51. Lan J., Deng Y., Chen H., Lu G., Wang W., Guo X., Lu Z., Gao G.F., Tan W. // PLoS. One. 2014. V. 9. № 11. P. 1–9.
52. Mou H., Raj V.S., van Kuppeveld F.J.M., Rottier P.J.M., Haagmans B.L., Bosch B.J. // J. Virol. V. 87. № 16. P. 9379–9383.
53. Muthumani K., Falzarano D., Reuschel E.L., Tingey C., Flingai S., Villarreal D.O., Wise M., Patel A., Izmirly A., Aljuaid A., et al. // Sci. Transl. Med. 2015. V. 7. № 301. P. 1–29.
54. Yang Y., Deng Y., Wen B., Wang H., Meng X., Lan J., Gao G.F., Tan W. // Viral Immunol. 2014. V. 27. № 10. P. 543–550.
55. Zhao J., Li K., Wohlford-Lenane C., Agnihothram S.S., Fett C., Zhao J., Gale Jr. M.J., Baric R.S., Enjuanes L., Gallagher T., McCray Jr. P.B., Perlmana S. // Proc. Natl. Acad. Sci. USA. 2014. V. 111. № 13. P. 4970–4975.
56. Iwata-Yoshikawa N., Uda A., Suzuki T., Tsunetsugu-Yokota Y., Sato Y., Morikawa S., Tashiro M., Sata T., Hasegawa H., Nagata N. // J. Virol. 2014. V. 88. № 15. P. 8597–8614.
57. Tseng C.T., Sbrana E., Iwata-Yoshikawa N., Newman P.C., Garron T., Atmar R.L., Peters C.J., Couch R.B. // PLoS. One. 2012. V. 7. № 4. P. e35421.
58. Tang J., Zhang N., Tao X., Zhao G., Guo Y., Tseng C.T., Jiang S., Du L., Zhou Y. // Hum. Vaccin. Immunother. 2015. V. 11. № 5. P. 1244–1250.
59. Lan J., Yao Y., Deng Y., Chen H., Lu G., Wang W., Bao L., Deng W., Wei Q., Gao G.F., et al. // EBioMedicine. 2015. V. 2. № 10. P. 1438–1446.

A Novel Dipeptide NGF Mimetic GK-2 Selectively Activating the PI3K/AKT Signaling Pathway Promotes the Survival of Pancreatic β-Cells in a Rat Model of Diabetes

R. U. Ostrovskaya*, S. V. Ivanov, T. A. Gudasheva, S. B. Seredenin
V. V. Zakusov Research Institute of Pharmacology, Baltiyskaya Str. 8, 125315, Moscow, Russia
*E-mail: rita.ostrovskaya@gmail.com
Received October 04, 2018; in final form January 22, 2019

ABSTRACT **We investigated the cytoprotective effect of a novel low-molecular-weight NGF mimetic, GK-2 (hexamethylenediamide *bis*-N-monosuccinyl-*L*-glutamyl-*L*-lysine), on pancreatic β-cells. The neuroprotective effect of GK-2 had been previously shown to be associated with selective activation of the PI3K/Akt signaling pathway. In this study, rats with streptozotocin (STZ)-induced type 2 diabetes mellitus were used. Metformin was used as a reference drug. STZ was immunohistochemically demonstrated to reduce the number of β-cells and affect their morphological structure. Treatment of diabetic animals with GK-2 (at a dose of 0.5 mg/kg intraperitoneally or 5 mg/kg orally) or metformin (300 mg/kg orally) for 28 days reduced the damaging effect of STZ. The effect of GK-2 on manifestations of STZ-induced diabetes, such as hyperglycemia, weight loss, polyphagia, and polydipsia, was comparable to that of metformin, while the cytoprotective activity of GK-2 was slightly stronger than that of metformin. A strong positive correlation between morphometric parameters and the blood glucose level was revealed. The GK-2 cytoprotective effect on β-cells is supposed to manifest through the PI3K/Akt signaling pathway.**
KEYWORDS **diabetes, GK-2, metformin, NGF, neurotrophins, PI3K/Akt pathway.**
ABBREVIATIONS **T2DM – type 2 diabetes mellitus; AD – Alzheimer's disease; STZ – streptozotocin; NGF – nerve growth factor; TrkA – tropomyosin receptor kinase A.**

INTRODUCTION

In their search for new ways to treat diabetes mellitus, the attention of researchers has focused on the similarity between the neurochemical mechanisms regulating the functions of neurons and pancreatic β-cells. This similarity includes common receptors (in particular, GABA [1], serotonin [2], and glutamate [3] receptors), as well as similar enzymes (e.g., glycogen synthase kinase 3 (GSK-3) [4]) and transcription factors (in particular, HIF [5, 6]). An additional argument in favor of neuron and β-cell similarity is the fact that β-cells, during their development, effect neuron-like processes [7] and that the neurons of the developing brain contain insulin (a pancreatic β-cell hormone), glucagon (a pancreatic α-cell hormone), and ghrelin (a hormone secreted by gastrointestinal tract cells) [8].

The similarity between the mechanisms regulating the functions of neurons and β-cells is supported by the involvement of the neurotrophic factors NGF [7] and BDNF [9] in the growth and differentiation of these cells. Along with the misfolding of proteins (β-amyloid in neurons, amyloid polypeptide in pancreatic islets), oxidative stress, and insulin resistance [10], neurotrophin dysfunctions [11] are common to Alzheimer's disease (AD) and type 2 diabetes mellitus (T2DM).

Pancreatic β-cells were found to secrete a biologically active NGF, with its secretion being enhanced by glucose. Even short-term exposure to NGF dramatically increases glucose-stimulated insulin secretion. Insulin secretion drops in the presence of monoclonal NGF antibodies [12]. Along with this, compound K252a, a specific TrkA inhibitor [13], inhibits increased insulin secretion. It is important to emphasize that TrkA receptors are found only in β-cells but not in the α-cells of the pancreas [14].

By using a primary culture of human pancreatic islets, Peerucci *et al.* [15] not only confirmed that human β-cells, like rat ones, express the NGF but also showed

that inhibition of this neurotrophin by monoclonal anti-NGF antibodies enhances β-cell apoptosis. Increased apoptosis of β-cells in the case of NGF deficiency was found to be associated with a decreased activity of PI3K/Akt, one of the main TrkA signaling pathways [15].

Attempts to create drugs that are effective, in particular in neurodegenerative diseases, have been underway since the discovery of NGF [16]. However, pharmacokinetic limitations related to the properties of a full-length NGF molecule, such as low biological stability, inability to penetrate biological barriers upon systemic administration, and side effects, have prevented the use of NGF for replacement therapy. Several companies and laboratories have searched for neurotrophin mimetics [17], but there have been no reports of NGF mimetics with satisfactory pharmacokinetic properties.

A working hypothesis positing that certain neurotrophins interacting with the same receptor may activate different signaling pathways, causing different neurotrophins effects, was formulated at the Department of Pharmaceutical Chemistry of the Zakusov Research Institute of Pharmacology [18]. This hypothesis provided a basis for a new direction in pharmacological research for the development of effective low-molecular-weight neurotrophin mimetics free of side effects. According to the proposed hypothesis, a β-turn Asp^{93}-Glu^{94}-Lys^{95}-Gln^{96} of the 4th NGF loop, which is the most exposed to the outside and, therefore, may play a major role in the interaction between the NGF and the receptor, was used to create a dipeptide mimetic called GK-2 (Patent of the Russian Federation No. 2410392, 2010; Patent US 9,683,014 B2, 2017; Patent CN 102365294 B, 2016) [19]. The compound comprises a central dipeptide fragment Glu^{94}-Lys^{95} that, according to stereochemical principles, may exhibit the most deep penetration into the receptor-binding site and be the most fully recognized by the receptor. The peripheral Asp^{93} residue was substituted by its bioisostere, a succinic acid moiety, and the Gln^{96} residue was substituted by an amide group. The purpose of these substitutions was to stabilize the β-turn conformation and increase the resistance of the compound to peptidases. The NGF is a homodimer; therefore, the linking of two β-turn mimetics with a hexamethylenediamine spacer provided a dimeric dipeptide, hexamethylenediamine *bis*-(monosuccinyl-glutamyl-lysine).

The main activities of NGF are known to be effected through its interaction with the TrkA receptor tyrosine kinase; wherein, signal transduction associated with TrkA activation mainly involves the phosphatidylinositol 3-kinase (PI3K/Akt) and mitogen-activated protein kinase (MAPK/Erk) signaling pathways, with the first being associated with the regulation of survival [20], and the second being mainly associated with morphological differentiation.

The neuroprotective activity of GK-2 was studied *in vitro* on both immortalized and primary cell cultures. Micromolar and nanomolar GK-2 concentrations were shown to increase the cell survival impaired by exposure to hydrogen peroxide, glutamic acid, and 1-methyl-4-phenyl-1,2,3,6-tetrahydropyridine (MPTP) [21]. Experiments on HT-22 cells using the Western blot analysis with antibodies to phosphorylated and non-phosphorylated Akt and Erk kinases demonstrated that GK-2 activated Akt within the same time intervals as full-length NGF did (after 15, 30, 60, and 180 min). Under similar conditions, GK-2, unlike NGF, did not cause increased phosphorylation of Erk kinases. The effects of the selective inhibitors of phosphatidylinositol 3-kinase and MAPK kinase LY294002 and PD98059, respectively, was studied to clarify the role played by various signaling pathways in the neuroprotective activity of GK-2. Incubation of HT-22 cells with LY294002 (100 μM) or PD98059 (50 μM) demonstrated that the neuroprotective effects of both NGF and GK-2 were completely inhibited by LY294002, but not by PD98059. These data suggest that implementation of the neuroprotective effects of GK-2 is associated with activation of the PI3K/Akt pathway, but not with the MAPK/Erk signaling pathway [22].

In vivo experiments provided convincing evidence of the GK-2 neuroprotective effects. The efficacy of GK-2 was demonstrated in various models of Alzheimer's disease (septo-hippocampal transection, cholinergic deficiency caused by prolonged administration of scopolamine, and on a model induced by administration of streptozotocin into the cerebral ventricles [23]), focal and global cerebral ischemia [24], and hemorrhagic stroke [25].

In recent years, we have developed the concept of a potential antidiabetic effect of neuroprotective agents [26, 27]. Based on this concept, we studied compound GK-2 on a model of streptozotocin (STZ)-induced type 2 diabetes mellitus. We demonstrated that systemic administration of GK-2 eliminates the hyperglycemic effect of the diabetogenic toxin [Patent of the Russian Federation 2613314, 2017] and reduces the behavioral disorders associated with diabetes in mice [28].

This study was performed to determine whether the NGF mimetic GK-2, which exhibits pronounced neuroprotective activity, could also protect β-cells. It was reasonable to compare the cytoprotective effect of GK-2 with that of metformin not only because metformin is an antidiabetic drug of the first choice [29], but also because metformin, like GK-2, activates the PI3K/Akt signaling pathway [30]. The study's ob-

jective was also to compare the effects of GK-2 and metformin on T2DM manifestations, such as hyperglycemia, weight loss, polydipsia, and polyphagia. It was important to evaluate the extent to which the cytoprotective and antihyperglycemic effects of these compounds correlate with each other.

EXPERIMENTAL

Animals

The experiments were performed on adult Wistar male rats with an initial body weight of 250–270 g, which were received from the Stolbovaya Central Laboratory for Animal Breeding (Moscow Region, Russia). The animals had free access to feed (except for 16 hours before STZ administration) and to drinking water. The animals were kept in accordance with SP 2.2.1.3218-14 No. 51 of August 29, 2014. The experiments were approved by the Committee for Biomedical Ethics of the Zakusov Research Institute of Pharmacology.

Compounds

STZ (Sigma, USA) was used as a diabetogenic toxin. The NGF mimetic GK-2 and metformin (Siofor, Berlin-Chemie Menarini, Germany) dissolved in saline solution (SS) were used.

Experiment design

T2DM was induced by a single intraperitoneal injection of a freshly prepared STZ solution at a dose of 45 mg/kg dissolved in cold citrate buffer (pH 4.5). The choice of this dose for the induction of T2DM was associated with a previously detected decrease in the blood insulin level by 48% and preservation of 30% of viable β-cells in the pancreas [27]. The glucose level in blood sampled from the tail vein was determined using a One Touch Ultra device (USA). The first measurement was performed 72 h after administration of STZ. Only animals with a blood glucose level of at least 15 mmol/L were included further in the experiment. The experiment included two series. In the first series, rats (n = 48) were randomly divided into four groups: 1) rats of the passive control group (n = 12) received a single intraperitoneal injection of citrate buffer on day 1 of the experiment and then 2 mL/kg of SS for the next 28 days; 2) rats of the active control group (n = 12) were administered 45 mg/kg of STZ on day 1 of the experiment, followed by administration of SS for the next 28 days; 3) rats of the first experimental group (n = 12) received a single intraperitoneal injection of 45 mg/kg STZ, followed by intraperitoneal injections of GK-2 at a dose of 0.5 mg/kg for the next 28 day; 4) rats of the second experimental group (n = 12) received a STZ injection, followed by oral administration of GK-2 at a dose of 5 mg/kg for 28 days (a tenfold increase in the dose when switching from intraperitoneal to oral administration is used for most dipeptide drugs) [31, 32]. In the second series of the experiment (n = 36), rats were divided into three groups: the passive control group (n = 12); the active control group (n = 12) (with a design similar to that of the first series); the experimental group (n = 12) that received a single injection of STZ at a dose of 45 mg/kg, followed by oral administration of metformin at a dose of 300 mg/kg (the most common dose used in the experiment) for the next 28 days. The glucose level in all groups of both series was determined at 1, 7, 14, 21, and 28 days of drug administration. Food and water consumption were measured daily; the animals were weighed every 3 days. The animals were euthanized by decapitation, and then the pancreatic islet was immunohistochemically analyzed.

Sample preparation

The extracted pancreases of rats from the experimental groups were fixed in 10% neutral formalin (pH 7.4) (Sigma, USA). The samples were dehydrated in an ascending series of alcohols and xylene and immersed in paraffin blocks. Sections 5 μm thick were prepared using a microtome (Jung RM2035, Germany). Slides (4 to 5 sections per glass) were kept in a dry bath at 40°C for 60 min. Before treatment with antibodies, the slides were washed out twice in xylene, hydrated in a descending series of alcohols, and washed in phosphate buffer (PBS, Sigma, USA) for 10 min. The slides were treated with a 3% hydrogen peroxide solution for 10 min to neutralize endogenous peroxidases.

Immunohistochemical reaction

The slides were incubated with a 10% solution of normal goat serum (Abcam, UK) at room temperature for 1 h to prevent nonspecific staining due to binding of primary antibodies to tissue components. Sections were treated with primary monoclonal anti-insulin antibodies (anti-insulin GP 1:500, Abcam, UK) in phosphate buffer. The treated slides were left in a wet chamber at temperatures of 2–4°C for 24 h.

To visualize the immunohistochemical reaction results, the slides were incubated with secondary monoclonal peroxidase-labeled antibodies (anti-GP Rabbit 1:500, Abcam, UK) at room temperature for 1 h, followed by treatment with a reagent kit (DAB Vector Peroxidase, USA). The ready slides were again dehydrated in an ascending series of alcohols and xylene and immersed in a Eukitt medium (Panreac, Spain). The reliability of the study results was achieved using negative antigen and antibody controls.

Microscopic analysis

A morphometric analysis was performed using an Aristoplan microscope (Leitz, Germany) equipped with a DCM-800 digital camera (Micromed, Russia), a personal computer, and the ScopePhoto software, at a magnification of ×400 (to calculate the total area of the slides) and ×1,600 (to calculate the area of islets and β-cells). The proportion of β-cells in the total slide area, the number of pancreatic islets, and the mean islet size were calculated.

Given the published data on a heterogeneous response of pancreatic islets of various sizes to the damaging effects of STZ [33], we performed a differential analysis of the islet area and calculated the percentage of islets of each size range (less than 500 μm^2, 501–2,500 μm^2, 2,501–10,000 μm^2, and more than 10,001 μm^2).

Statistical analysis

Statistical data processing was performed using the Biostat software. The distribution of data was characterized using the Shapiro-Wilk test. Due to the normal data distribution, the statistical significance of differences among groups was assessed by the ANOVA test. The mean value M and the standard error of the mean SEM were calculated. The difference of means was considered statistically significant at $p < 0.05$.

To comparatively characterize the dynamics and strength of the drug effect, a relative antihyperglycemic activity indicator (A_r) was calculated using the formula:

$$A_r = [\text{glc (act. contr.)} - \text{glc (comp.)}] \times \\ \times 100\% / [\text{glc (act. contr.)} - \text{glc (pass. contr.)}],$$

where glc (act. contr.) is the plasma glucose level in the STZ/SS group; glc (comp.) is the glucose level in the STZ/GK-2 or STZ/metformin groups; and glc (pass. contr.) is the glucose level in animals injected with SS.

To compare the cytoprotective activity of GK-2 and metformin, a relative indicator (Cp_a) was calculated using the formula:

$$Cp_a = [\text{Cp (act. contr.)} - \text{Cp (comp.)}] \times \\ \times 100\% / [\text{Cp (act. contr.)} - \text{Cp (pass. contr.)}],$$

where Cp (act. contr.) is the percentage of β-cells in the cross section of the pancreases of rats from the STZ/SS group; Cp (comp.) is the percentage of β-cells in the cross section of the pancreases of rats from the STZ/GK-2 or STZ/metformin group; and Cp (pass. contr.) is the percentage of β-cells in the cross section of the pancreases of rats injected with SS.

RESULTS

As follows from the data presented in *Table 1*, the blood glucose level in the animals of the passive control group was 5–6 mmol/L during the entire observation period, while in rats with DM it increased more than 3-fold on day 7 of the experiment. At days 14, 21, and 28, the glucose level in the active control animals remained consistently high (more than 20 mmol/L). Pronounced decompensation of DM in the active control group was also evidenced by weight loss, polyphagia, and polydipsia. Pronounced antidiabetic activity of GK-2 was revealed. By the end of the first week of GK-2 i/p administration, a significant decrease in the glycemic level was observed. Orally administered GK-2 retained its activity. Metformin also reduced the glycemic level (*Table 2*). According to the relative indicator A_r (*Table 3*), the effect of metformin developed later than that of GK-2; however, on the 3rd and 4th weeks, the A_r indicator of metformin was slightly higher than that of GK-2.

A favorable effect of both drugs was also confirmed by changes in body weight. While healthy rats gained weight over the experimental period (+16.2% of the baseline value), STZ caused a significant decrease in the body weight (−10.3%). GK-2 and metformin therapy attenuated the STZ-induced weight loss (the difference between the initial and final values was 1.6 and −0.7% for i/p and oral GK-2 administration, respectively, and −1.3% for metformin) (differences from active control animals were statistically significant, $p < 0.01$).

The antidiabetic activity of GK-2 is confirmed by a decrease in polydipsia, which is the important DM indicator. While the animals from the active control group had a marked thirst (daily water consumption in untreated diabetic rats was 450% higher than that in healthy rats), diabetic animals treated with GK-2 consumed 62% and 27% less water in the case of i/p and oral administration, respectively, while metformin-treated rats consumed 33% less water than animals of the active control group (differences from active control values were significant, $p < 0.01$) (*Fig. 1*).

GK-2 and metformin also affected polyphagia. While, by the end of the experiment, animals of the active control group consumed 18.3% more feed than healthy rats, this difference in the GK-2 group amounted to 2.0 and 8.5% (i/p and oral administration, respectively) (differences from active control indicators were statistically significant, $p < 0.01$). For metformin, this difference was less pronounced and amounted to 15.0%.

The cytoprotective activity of both compounds was evaluated by immunohistochemical analysis, which is highly specific for Langerhans β-cells. The results of a

Table 1. The effect of GK-2 on the basal glucose level in rats of series 1

	Group	Basal glucose level (mmol/L; M ± m)				
		Day 1	Day 7	Day 14	Day 21	Day 28
1	Passive control	6.0±0.3	5.9±0.2	6.4±0.2	6.2±0.2	6.4±0.2
2	Active control	21.0±1.5**	30.0±1.2**	23.6±1.9**	23.4±2.1**	24.5±1.9**
3	Intraperitoneal GK-2	23.1±1.5	19.1±2.9*	14.3±2.1*	12.5±1.4*	10,8±0.9*
4	Oral GK-2	21.9±2.4	25.2±2.4*#	13.5±1.5*	13.2±2.1*	12.2±1.4*

* – Statistical significance of differences between the experimental group and active control, $p < 0.05$.
** – Statistical significance between passive control and active control, $p < 0.05$.
# – Statistical significance between experimental groups, $p < 0.05$.

Table 2. The effect of metformin on the basal glucose level in rats of series 2

	Group	Basal glucose level (mmol/L; M ± m)				
		Day 1	Day 7	Day 14	Day 21	Day 28
1	Passive control	5.4±0.3	5.6±0.2	5.8±0.4	5.8±0.2	5.9±0.3
2	Active control	17.6±0.9**	20.5±1.8**	22.2±1.2**	25.6±2.0**	29.3±1.7**
3	Metformin, 300 mg/kg	18.1±0.7	21.3±2.8	15.6±2.2*	8.8±1.0*	11.0±1.6*

* – Statistical significance of differences between the experimental group and active control, $p < 0.05$.
** – Statistical significance of differences between passive control and active control, $p < 0.05$.

Table 3. Relative indicators of antihyperglycemic activity (A_r) of GK-2 and metformin

	Compound	A_z (%)				
		Day 1	Day 7	Day 14	Day 21	Day 28
1	Intraperitoneal GK-2	−13.5	45.2	54	63.3	75.4
2	Oral GK-2	−6	19.9	59.1	59.2	68.2
3	Metformin	−4.2	−5.7	40.3	84.8	78.2

morphometric analysis of pancreatic sections are given in *Tables 4* and *5*.

The obtained data indicate a decrease in the number of islets, as well as in the absolute and relative numbers of β-cells in the group of untreated diabetic animals. The islets of rats in this group are characterized by changed shapes and the presence of dystrophic elements (*Fig. 2B*). Treatment of diabetic rats with GK-2 and metformin for 28 days leads to noticeable restoration in the proportion of β-cells and their morphological characteristics (*Fig. 2C, D, E*). The relative cytoprotective activity of GK-2 is slightly higher than that of metformin: C_p is 49.5 and 43.4 for GK-2 upon i/p and oral administration, respectively, and 30.3 for metformin.

The results of a differential assessment of the β-cell islet area are of particular interest (*Fig. 3*). Large islets (2,501–10,000 μm² and more than 10,001 μm²) prevailed in the group of healthy animals; in untreated diabetic animals, the number of large islets sharply decreased and the number of small ones (501–2,500 μm² and 2,501–10,000 μm²) increased. The use of GK-2 and metformin led to an increase in the proportion of large islets.

The area of β-cells (percentage of the total pancreatic islet area), which characterizes the degree of pancreas damage upon treatment with GK-2 and metformin, correlates with the blood glucose level (the correlation coefficients were 0.7256 and 0.6629, respectively) (*Fig. 4*).

DISCUSSION

An important trend in modern diabetology is the search for ways to protect β-cells from the damaging effects of metabolic changes characteristic of T2DM: lipoglucotoxicity, oxidative stress, DNA alkylation, ATP deficiency, and reduced levels of mature neurotrophins [34, 35]. In the review *Regulating the beta cell mass as a strategy*

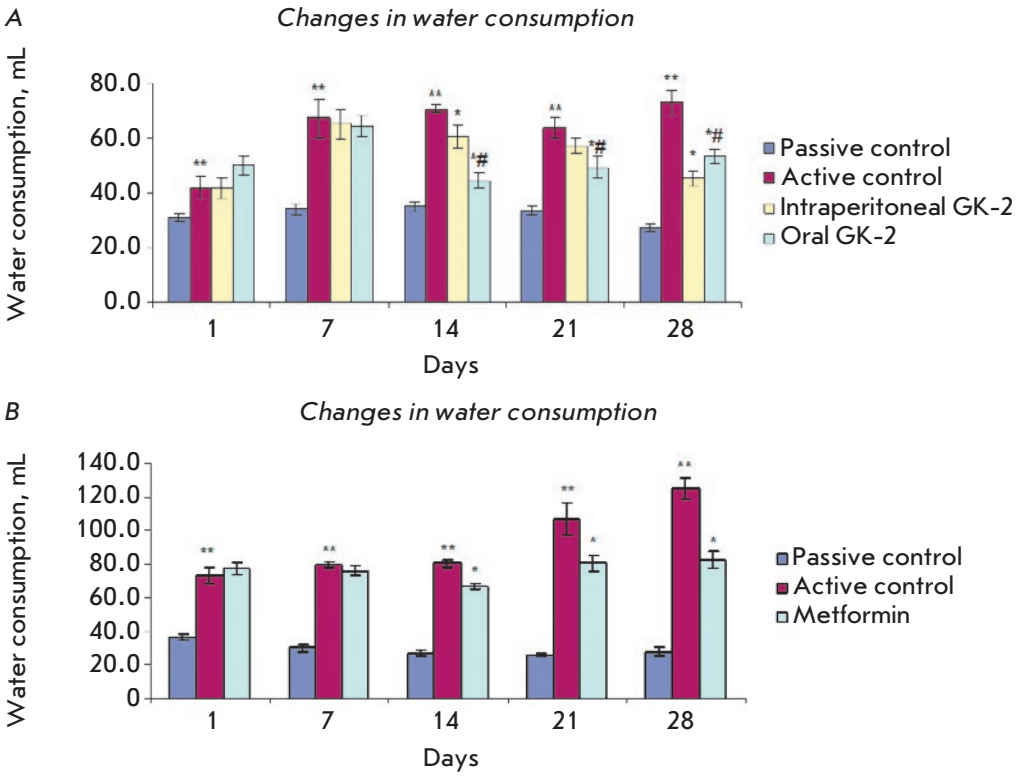

Fig. 1. The influence of GK-2 and metformin on water consumption in Wistar rats. *A* – GK-2; *B* – metformin. * – Statistical significance of differences between the experimental group and active control, $p < 0.05$. ** – Statistical significance of differences between passive control and active control, $p < 0.05$. # – Statistical significance of differences between experimental groups, $p < 0.05$

Table 4. The effect of GK-2 on the morphometric parameters of rat pancreatic islets

	Group	Total β-cell area		Mean islet area, μm²	Number of islets
		absolute, μm²	% of the islet area		
1	Passive control	259,925±46,353	19.9±2.3	20,088±3,920	13±2
2	Active control	79,131±21,266**	8.3±2.1**	5,983±1,805**	14±3
3	Intraperitoneal GK-2	180,076±36,026*	13.3±1.7*	15,567±3,820*	12±3
4	Oral GK-2	175,907±31,357	14.0±2.0*	15,167±1,895*	12±2

* – Statistical significance of differences between the experimental group and active control, $p < 0.05$.
** – Statistical significance of differences between passive and active control, $p < 0.05$.

Table 5. The effect of metformin on the morphometric parameters of rat pancreatic islets

	Group	Total β-cell area		Mean islet area, μm²	Number of islets
		absolute, μm²	% of the islet area		
1	Passive control	225,270±17,005	20.0±1.3	18,477±2,142	12±1
2	Active control	70,181±20,313**	5.8±2.1**	7,646±1,654**	9±2
3	Metformin	115,353±23,845	10.1±0.8*	9,749±1,714	12±2

* – Statistical significance of differences between the experimental group and active control, $p < 0.05$.
** – Statistical significance of differences between passive and active control, $p < 0.05$.

for type-2 diabetes treatment [36], L. Song and co-authors indicate that modern antidiabetic therapy, which is mainly aimed at increasing the secretion and efficacy of insulin as well as at glucose uptake, is symptomatic. It is emphasized that etiotropic (disease-modifying) therapy should be based on the use of substances that prevent the loss of β-cells, increasing their survival rate without toxic effects on other organs.

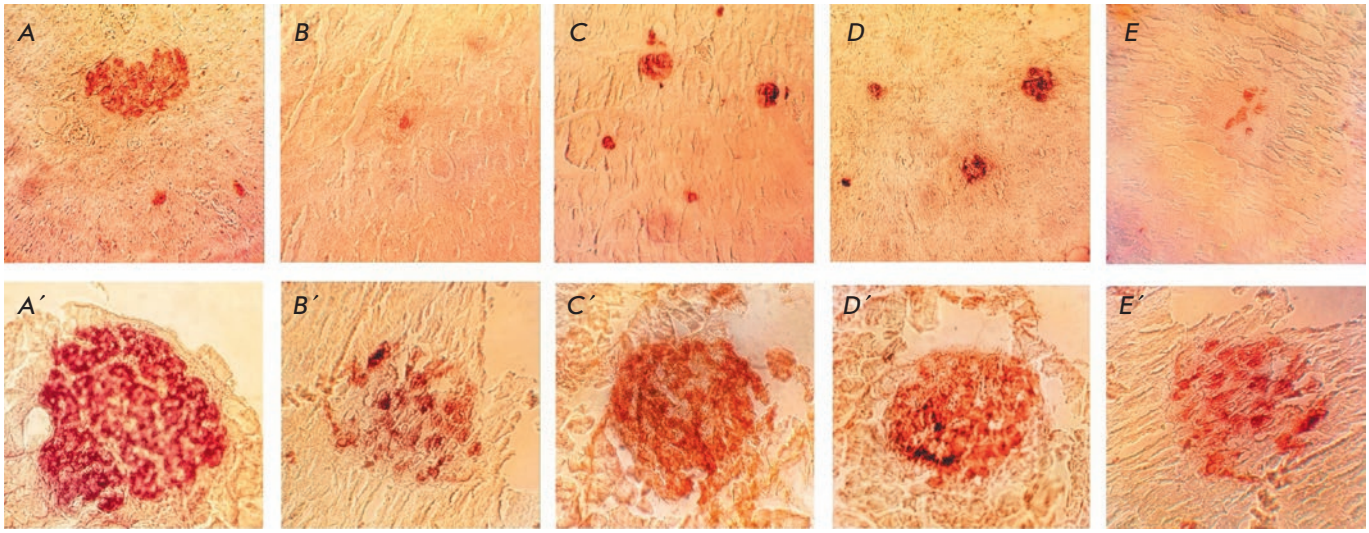

Fig. 2. Pancreatic islets of animals from different groups. Magnification ×620 (upper panel) and ×1,600 (bottom panel). *A*, *A′* – passive control animals; *B*, *B′* – active control animals; *C*, *C′* – diabetic rats treated with intraperitoneal GK-2; *D*, *D′* – diabetic rats treated with oral GK-2; *E*, *E′* – diabetic rats treated with metformin

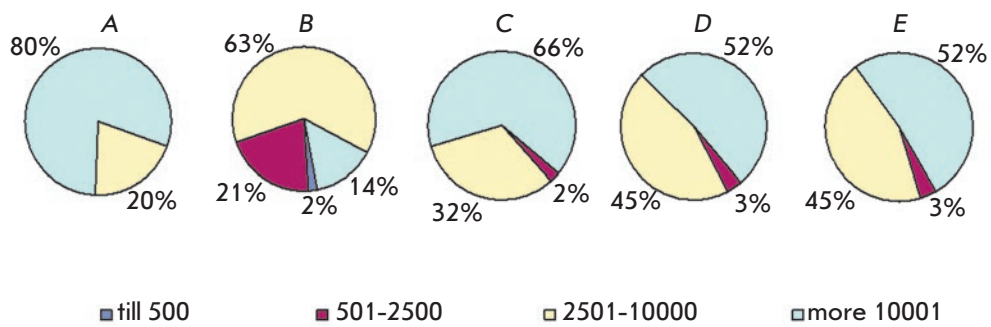

Fig. 3. Percentage (%) of β-cell islets of different areas (μm²). *A* – passive control animals; *B* – active control animals; *C* – diabetic rats treated with intraperitoneal GK-2; *D* – diabetic rats treated with oral GK-2; *E* – diabetic rats treated with metformin

These substances could include a wide group of antioxidant compounds that neutralize free radicals, thereby protecting pancreatic β-cells from death. However, a number of researchers indicate the risk of overestimating the efficacy of antioxidants in DM, which are able only to absorb existing radicals but are not able to prevent the generation of new ones [37]. Compounds of other classes, such as histone deacetylase and GSK-3β inhibitors, may be used. However, these molecules are involved in the regulation of a variety of processes; therefore, there is a risk of undesirable reactions, including a pro-oncogenic effect. The most convincing evidence of this effect was obtained for dipeptidyl peptidase-4 (DPP-4) inhibitors [38].

Neurotrophins that are able to increase survival by reducing apoptosis not only in neuronal, but also in nonneuronal systems might be promising agents for T2DM, but they possess unfavorable pharmacokinetic properties. An original approach to the development of systemically active low-molecular-weight NGF and BDNF mimetics free of the disadvantages of a full-length molecule, which was developed at the Zakusov Research Institute of Pharmacology, has led to the creation of a series of compounds (Patent RF No. 2410392, 2010; Patent US 9,683,014 B2, 2017; Patent CN 102365294 B, 2016). One of them is compound GK-2, a NGF loop 4 mimetic with a wide spectrum of *in vivo* and *in vitro* neuroprotective activities.

By using a highly sensitive and selective immunohistochemical analysis, we revealed for the first time the cytoprotective effect of compound GK-2 on pancreatic β-cells. While STZ at a diabetogenic dose reduces the number of Langerhans islets, reduces the absolute and relative numbers of β-cells, changes their shape, and induces the emergence of dystrophic elements, administration of the original dimeric dipeptide NGF mimetic, compound GK-2, to animals with developed diabetes (glycemia above 20 mmol/L) significantly

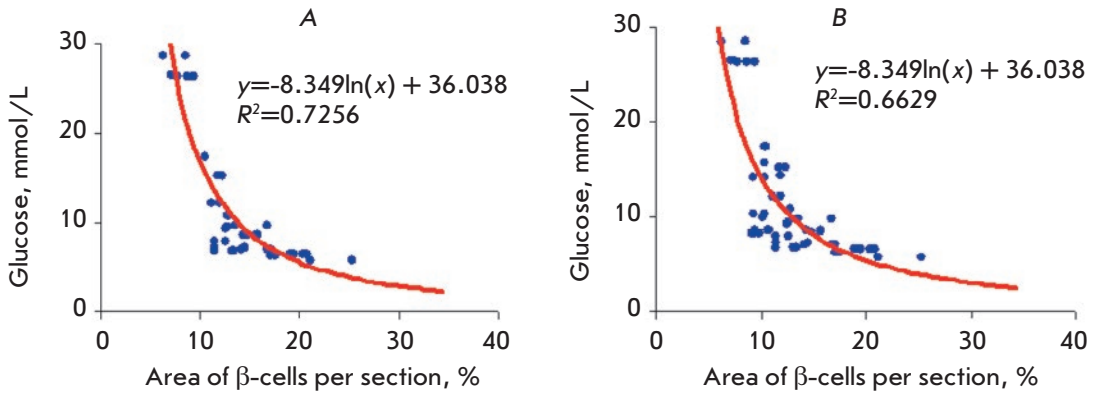

Fig. 4. Correlation between the blood glucose level and the relative β-cell area in pancreatic sections. *A* – GK-2; *B* – metformin

reduces the severity of these morphological changes. A differential analysis of the islet size showed large islets (with an area of 2,501–10,000 μm² and more than 10,001 μm²) predominant in healthy animals, small islets (up to 500 μm²) prevailing in the untreated STZ group, while the use of GK-2 increased the number of large islets in diabetic rats. It is interesting to correlate this fact with the ideas [33] that this increase indicates an attenuation of apoptosis. The degree of morphological changes, which is evaluated based on the ratio of the β-cell area to the total pancreatic islet area, clearly correlates with the antihyperglycemic effect of GK-2.

The glucose transporter GLUT2 has been repeatedly reported to enable selective accumulation of STZ in β-cells, which causes their apoptosis [39, 40]. STZ-induced apoptosis is associated with oxidative stress and a shift in the ratio of the NGF precursor and mature NGF towards a predominance of the precursor with a characteristic pro-apoptotic effect [41]. Earlier, GK-2, like the full-length NGF molecule, was shown to increase the survival of neuronal cells exposed to hydrogen peroxide, glutamic acid, and MPTP [21]. Also, the effect of neurotrophin mimetics, which affect different translational pathways, on manifestations of STZ-induced diabetes was studied. Only mimetics activating the PI3K/Akt pathway (the NGF loop 4 mimetic GK-2 and the BDNF loop 1 mimetic GSB-214) exhibited an antihyperglycemic effect, while the BDNF loop 2 mimetic activating the MAPK/Erk pathway (GTS-201) lacked antihyperglycemic activity [42].

Dysfunction of β-cells in T2DM is known to be related to a decreased activity of the PI3K/Akt pathway [43], whose role as a factor controlling maintenance of the β-cell volume and function has been shown *in vivo* and *in vitro* [44]. Genetically modified mice with PI3K/Akt pathway deficiency develop severe diabetes in the setting of enhanced β-cell apoptosis [45, 46]. The PI3K/Akt pathway deficiency characteristic of diabetes is reproduced in a STZ-induced diabetes model [47].

It is important to emphasize that transgenic mice overexpressing a constitutively active form of this pathway are characterized by an increased size and number of pancreatic β-cells, as well as by elevated tolerance to a glucose load [48].

The data on the role of PI3K/Akt pathway deficiency in the development of β-cell apoptosis in DM, along with the data on the involvement of this pathway in the implementation of the antihyperglycemic effect of GK-2 [42], suggest that the protective effect of GK-2 is also associated with the ability of this NGF mimetic to activate the abovementioned pathway. The fact that GK-2 exerts a cytoprotective effect not only on neurons, as shown earlier [49], but also on β-cells is an important argument in favor of the idea of a similarity between the mechanisms underlying the protection of neurons and β-cells. This is the fundamental aspect of our work. The ability of this systemically active NGF mimetic to protect pancreatic β-cells is of practical importance, because this compound is currently being investigated as a treatment for strokes, and the "coexistence" of stroke and diabetes is well established [50]. The use of GK-2 for combined vascular and diabetic pathology may be associated with long-term administration of the drug; therefore, it is important that both the neuroprotective and cytoprotective GK-2 activities towards pancreatic β-cells are retained upon long-term oral administration.

Metformin is a first-line drug for T2DM and has been successfully used by millions of people worldwide for over 50 years [51]. The mechanism of antidiabetic action of metformin is multicomponent [52]. The most important component of this mechanism is obviously the activation of 5'-AMP-activated protein kinase (AMPK) [53], which leads to the suppression of key gluconeogenesis enzymes in the liver. Metformin increases glucose utilization by the muscles and enhances anaerobic glycolysis in the small intestine. Also, metformin was shown to enhance the expression of NGF

and BDNF in a culture of Schwann cells [54]. The effect of metformin was found to be inhibited by a selective inhibitor of the translational PI3K/Akt pathway [30]. The similarity between one of the mechanisms underlying the metformin and GK-2 action, whose effects depend on PI3K/Akt, was the reason for our comparative study of their effects in a STZ-induced T2DM model. High activity of GK-2, which is comparable to that of metformin, defines the practical value of this study.

CONCLUSION

In this study, the antidiabetic effect of an original systemically active NGF mimetic, GK-2 (hexamethylenediamine-*bis*-(N-monosuccinyl-*L*-glutamyl-*L*-lysine)), previously detected in mice, was reproduced in experiments on rats [28]. Direct evidence of the cytoprotective effect of GK-2 on pancreatic β-cells was, for the first time, obtained in a STZ-induced T2DM model. Cytoprotection of β-cells is a new actual direction attracting the attention of diabetes researchers. Because the protective effect of GK-2 on neurons subjected to different damaging factors was described earlier, the present findings on the attenuation of STZ-induced apoptosis of β-cells during GK-2 therapy represent additional confirmation of the similarity between the neurochemical mechanisms regulating the functions of neurons and pancreatic β-cells and their mechanisms of protection. An important scientific and practical result of this work is the comparability of the effects of GK-2 and metformin, a first-choice standard antidiabetic drug, on the functional manifestations of T2DM (hyperglycemia, weight loss, polyphagia, polydipsia); the cytoprotective effect of GK-2 slightly exceeds that of metformin. ●

This study was performed within the framework of the government contract for 2019–2021, theme No. 0521-2019-0003 "Searching for pharmacological methods to selectively activate pathways for signal transduction of tyrosine kinase neurotrophin receptors as a basis for creating drugs free of the side effects of native neurotrophins."

REFERENCES

1. Baekkeskov S., Aanstoot H., Christgau S., Reetz A., Solimen M., Cascalho M., Folli F., Richter-Olesen H., Camilli P. // Nature. 1990. V. 347. P. 151–157.
2. Noble E.E, Billington C.J., Kotz C.M., Wang C. // Am. J. Physiol. Regul. Integr. Comp. Physiol. 2011. V. 300. № 5. P. 1053–1069.
3. Otter S., Lammert E. // Trends Endocrinol. Metab. 2016. V. 27. № 3. P. 177–188.
4. Woodgett J.R. // Curr. Drug Targets Immune Endocr. Metabol. Disord. 2003. V. 3 № 4. P. 281–290.
5. Heinis M., Simon M.T., Ilc K., Mazure N.M., Pouysségur J., Scharfmann R., Duvillié B. // Diabetes. 2010. V. 59. № 3. P. 662–669.
6. Cheng K., Ho K., Stokes R., Scott C., Scott C., Lau S.M., Hawthorne W.J., O'Connell P.J., Loudovaris T., Kay T.W., et al. // J. Clin. Invest. 2010. V. 120. № 6. P. 2171–2183.
7. Polak M., Scharfmann R., Seilheimer B., Eisenbarth G., Dressler D., Verma I.M., Potter H. // Proc. Natl. Acad. Sci. USA. 1993. V. 90. P. 5781–5785.
8. Cruz S.A., Tseng Y.C., Kaiya H., Hwang P.P. // Comp. Biochem. Physiol, Part A: Mol. Integr. Physiol. 2010. V. 156. P. 190–200.
9. Bathina S., Das U.N. // Arch. Med. Sci. 2015. V. 11. № 6. P. 1164–1178.
10. Ribe E.M., Lovestone S. // J. Intern. Med. 2016 V. 280 № 5. P. 430–442.
11. Passaro A., Dalla Nora E., Morieri M.L., Soavi C., Sanz J.M., Zurlo A., Fellin R., Zuliani G. // J. Gerontol. Biol. Sci. Med. Sci. 2015. V. 70. № 3. P. 294–302.
12. Rosenbaum T., Vidaltamayo R, Sánchez-Soto M.C., Zentella A., Hiriart M. // Proc. Natl. Acad. Sci. USA. 1998. V. 23. № 13. P. 7784–7788.
13. Rosenbaum T., Sanchez-Soto M.C., Hiriart M. // Diabetes. 2001. V. 50. № 8. P. 1755–1762.
14. Kanaka-Gantenbein C., Tazi A., Czernichow P., Scharfmann R. // Endocrinology. 1995. V. 136. № 2. P. 761–769.
15. Pierucci D., Cicconi S., Bonini P., Ferrelli F., Pastore D., Matteucci C., Marselli L., Marchetti P., Ris F., Halban P., et al. // Diabetologia. 2001. V. 44. P. 1281–1295.
16. Aloe L., Rocco M.L., Bianchi P., Manni L. // J. Transl. Med. 2012. V. 10. P. 239–252.
17. Cirillo G., Colangelo A.M., Bianco M.R., Cavaliere C., Zaccaro L., Sarmientos P., Alberghina L., Papa M. // Biotechnol. Adv. 2012. V. 30. № 1. P. 223–232.
18. Gudasheva T.A., Antipova T.A., Seredenin S.B. // Dokl. Biochem. Biophys. 2010. V. 434. P. 262–265.
19. Seredenin S.B., Gudasheva T.A. // Zh. Nevrol. Psikhiatr. Im S.S. Korsakova. 2015. V. 115. № 6. P. 63–70.
20. Kaplan D.R., Miller F.D. // Curr. Opin. Neurobiol. 2000 V. 10. № 3. P. 381–391.
21. Antipova T.A., Gudasheva T.A., Seredenin S.B. // Bull. Exp. Biol. Med. 2011. V. 150. № 5. P. 607–609.
22. Gudasheva T.A., Povarnina P.Y., Antipova T.A., Firsova Y.N., Konstantinopolsky M.A., Seredenin S.B. // J. Biomed. Sci. 2015. V. 8. № 22. P. 106.
23. Povarnina P.Y., Vorontsova O.N., Gudasheva T.A., Ostrovskaya R.U., Seredenin S.B. // Acta Naturae. 2013. V. 5. № 3. P. 84–91.
24. Seredenin S.B., Silachev D.N., Gudasheva T.A., Pirogov Y.A., Isaev N.K. // Bull. Exp. Biol. Med. 2011. V. 151. № 5. P. 584–587.
25. Krayneva V.A., Gudasheva T.A., Kotelnikova S.O., Antipova T.A., Seredenin S.B. // Bull. Exp. Biol. Med. 2013. V. 154. № 5. P. 642–644.
26. Ostrovskaya R.U., Yagubova S.S. // Psychiatry. 2014. V. 61. № 1. P. 35–43.
27. Ostrovskaya R.U., Zolotov N.N., Ozerova I.V., Ivanova E.A., Kapitsa I.G., Taraban K.V., Michunskaya A.M., Voronina T.A., Gudasheva T.A., Seredenin S.B. // Bul. Exp. Biol. Med. 2014. V. 157. № 3. P. 344–349.
28. Ostrovskaya R.U., Yagubova S.S., Gudasheva T.A.,

Seredenin S.B. // Acta Naturae. 2017. V. 9. № 33. P. 94–102.
29. Bolen S., Feldman L., Vassy J., Wilson L., Yeh H.C., Marinopoulos S., Wiley C., Selvin E., Wilson R., Bass E.B., et al. // Ann. Intern. Med. 2007. V. 147. № 6. P. 386–399.
30. Garabadu D., Krishnamurthy S. // Pharm. Biol. 2017. V. 55. № 1. P. 722–728.
31. Zherdev V.P., Kolyvanov G.P., Litvin A.A., Smirnov V.V., Kolik L.G., Raskin S.Yu., Ivashkina N.Yu., Gudasheva T.A., Seredenin S.B. // Pharmacokinetics and Pharmacodynamics. 2017. № 1. P. 52–55.
32. Povarnina P.Yu..\, Gudasheva T.A., Vorontsova O.N., Bondatenko N.A., Seredenin S.B. // Bull. Experim. Biol. And Med. 2011. V. 151. № 6. P. 690–693.
33. Feng Z.C., Donnelly L., Li J., Krishnamurthy M., Riopel M., Wang R. // Lab. Invest. 2012. V. 92 № 4. P. 543–555.
34. Novelli M., Bonamassa B., Masini M., Funel N., Canistro D., De Tata V., Funel N., Martano M., Soleti A., Campani D., et al. // Naunyn-Schmiedeberg's Arch. Pharmacol. 2010. V. 382. P. 127–137.
35. Goyal S.N., Reddy N.M., Kalpesh R.P., Kartik T.N., Shreesh O., Chandragouda R.P., Yogeeta O.A., Patel R.C. // Chem.-Biol. Inter. 2016. V. 244. P. 49–63.
36. Song I., Muller C., Louw J., Bouwens L. // Curr. Drug Targets. 2015. V. 16. № 5. P. 516–524.
37. Johansen J.S., Harris A.K., Rychly D.J., Ergul A. // Cardiovasc. Diabetology. 2005. V. 4. № 5. P. 1–11.
38. Tseng C.H., Lee K.Y., Tseng F.H. // J. Environ. Sci. Health. Environ. Carcinog. Ecotoxicol. Rev. 2015. V. 33. № 1. P. 67–124.
39. Schnedl W.J., Ferber S., Johnson J.H., Newgard C.B. // Diabetes. 1994. V. 43. P. 1326–1333.
40. Szkudelski T. // Physiol. Res. 2001. V. 50. № 6. P. 536–546.
41. Al-Gayyar M.M., Mysona B.A., Matragoon S., Abdelsaid M.A., El-Azab M.F., Shanab A.Y., Ha Y., Smith S.B., Bollinger K.E., El-Remessy A.B. // PLoS One. 2013. V. 8. № 1. e54692.
42. Ostrovskaya R.U., Yagubova S.S., Gudasheva T.A., Seredenin S.B. // Bull. Exp. Biol. Med. 2018. V. 164. № 6. P. 734–737.
43. Lorna M., Rhodes J. // Am. J. Physiol. Endocrinol. Metab. 2004. V. 287. P. 192–198.
44. Elghazi L., Rachdi L., Weiss A.J., Cras-Meneur C., Bernal-Mizrachi E. // Diabetes, Obesity Metabolism. 2007. V. 9. № 2. P. 147–157.
45. Garofalo R.S., Orena S.J., Rafidi K., Torchia A.J., Stock J.L., Hildebrandt A.L., Coskran T., Black S.C., Brees D.J., Wicks J.R., et al. // J. Clin. Invest. 2003. V. 112. P. 197–208.
46. Bernal-Mizrachi E., Fatrai S., Johnson J.D., Ohsugi M., Otani K., Han Z., Polonsky K.S., Permutt M.A. // J. Clin. Invest. 2004. V. 114. P. 928–936.
47. Cui W., Zhang Y., Lu D., Ren M., Yuan G. // Mol. Med. Rep. 2016. V. 13. P. 543–549.
48. Bernal-Mizrachi E., Wen W., Stahlhut S., Welling C.M., Permutt M.A. // J. Clin. Invest. 2001. V. 108. P. 1631–1638.
49. Gudasheva T.A., Povarnina P.Y., Seredenin S.B. // Bull. Exp. Biol. Med. 2017. V. 162. № 4. P. 454–457.
50. Al-Rubeaan K., Al-Hussain F., Youssef A.M., Subhani S.N., Al-Sharqawi A.H., Ibrahim H.M. // J. Diabetes Res. 2016. V. 4132589. P. 1–9.
51. Clodi M., Abrahamian H., Drexel H., Fasching P., Hoppichler F., Kautzky-Willer A., Lechleitner M., Ludvik B., Prager R., Roden M., et al. // Wien Klin. Wochenschr. 2012. V. 124. № 2. P. 10–16.
52. Rena G., Pearson E.R., Sakamoto K. // Diabetologia. 2013. V. 56. P. 1898–1906.
53. Zhou G., Myers R., Li Y., Chen Y., Shen X., Fenyk-Melody J., Wu M., Ventre J., Doebber T., Fujii N., et al. // J. Clin. Invest. 2011. V. 108. P. 1167–1174.
54. Ma J., Liu J., Yu H., Chen Y., Wang Q., Xiang L. // Int. J. Clin. Exp. Pathol. 2015. V. 8. № 6. P. 6748–6755.

Structure of the Anti-C_{60} Fullerene Antibody Fab Fragment: Structural Determinants of Fullerene Binding

E. M. Osipov[1], O. D. Hendrickson[1], T. V. Tikhonova[1], A. V. Zherdev[1], O. N. Solopova[2], P. G. Sveshnikov[2], B. B. Dzantiev[1], V. O. Popov[1]*

[1]Bach Institute of Biochemistry, Research Center of Biotechnology of the Russian Academy of Sciences, Leninsky Ave. 33, 119071, Moscow, Russia

[2]Russian Research Center of Molecular Diagnostics and Therapy, Simpheropolsky Blvd. 8, 113149, Moscow, Russia

*E-mail: vpopov@inbi.ras.ru

Received October 11, 2018; in final form February 12, 2019

ABSTRACT **The structure of the anti-C_{60} fullerene antibody Fab fragment ($FabC_{60}$) was solved by X-ray crystallography. The computer-aided docking of C_{60} into the antigen-binding pocket of $FabC_{60}$ showed that binding of C_{60} to $FabC_{60}$ is governed by the enthalpy and entropy; namely, by π-π stacking interactions with aromatic residues of the antigen-binding site and reduction of the solvent-accessible area of the hydrophobic surface of C_{60}. A fragment of the mobile CDR H3 loop located on the surface of $FabC_{60}$ interferes with C_{60} binding in the antigen-binding site, thereby resulting in low antibody affinity for C_{60}. The structure of apo-$FabC_{60}$ has been deposited with pdbid 6H3H.**

KEYWORDS **antibodies, fullerene, molecular modeling, X-ray analysis.**

ABBREVIATIONS **STI – soybean trypsin inhibitor; TG – thyroglobulin; TMB – 3,3′,5,5′-tetramethylbenzidine; PBS – phosphate buffered saline; PBST – phosphate buffered saline supplemented with 0.05% Triton X-100; CDR – complementarity-determining region; $FabC_{60}$ – Fab-fragment of anti-fullerene C_{60} antibody; K_d – dissociation constant; r.m.s.d. – root mean square deviation; $SolC_{60}$ – fullerene aminocaproic acid.**

INTRODUCTION

The problem of immune recognition is one of the main challenges of modern biochemistry, important both for understanding biological processes and for designing new drugs and vaccines. A considerable body of theoretical and experimental data accumulated in recent years provides deeper understanding of the structural and functional patterns of immune interactions [1–5]. X-ray crystallography is among the most powerful methods used to study the three-dimensional structures of specific antibody–antigen complexes and gather detailed insights into the interactions of antibodies with various high-molecular-weight antigens (proteins, polysaccharides, lipids, etc.) and water-soluble low-molecular-weight haptens [6–9].

In recent years, there has been a significant expansion of the range of potential targets for immune recognition, in particular due to particles with a structurally degenerate surface. This class includes engineered nanoparticles (ENPs) that are characterized by a growing production and applications in various fields of science and technology [10]. The opportunity to manipulate the physicochemical parameters of nanoparticles opens new prospects for the synthesis of nanoparticles with desired properties for application in targeted drug delivery, disease diagnosis, imaging of organs and tissues, etc. [11–13]. The use of ENPs in medicine and biotechnology raises the question of their immunogenic properties.

Antigens that do not fit into the standard patterns of the immune reaction include fullerenes: nanoparticles consisting exclusively of carbon atoms and characterized by a unique geometry and properties [14]. A number of studies provide evidence of the possible formation of fullerene-specific antibodies [15–18].

The structure of the fullerene-binding site of antibodies was considered in the only study [15]. Using X-ray crystallography and computer simulation, the specific fullerene-binding site was shown to be a spherical cavity 7 Å in diameter that is formed by a cluster of hydrophobic amino acids. However, in the structural model of the fullerene-Fab complex [15], hydrophobic

residues outside the CDR are included in the interaction with fullerene.

The aim of this investigation is to study the structural parameters of epitopes that specifically recognize insoluble antigens and elucidate the characteristic features of the formation of appropriate immune complexes by X-ray analysis and molecular modeling of the Fab-fullerene complex. We used the Fab fragment ($FabC_{60}$) of the previously obtained monoclonal antibody to C_{60} fullerene [18].

EXPERIMENTAL

Materials

The soluble form of C_{60}, fullerene aminocaproic acid ($C_{60}(H)_3(NH(CH_2)_5COONa)_3 \times 10\ H_2O$) ($SolC_{60}$, 98% purity), was purchased from Intelfarm (Russia). Peroxidase-labeled goat anti-mouse lambda light chain antibodies were purchased from Bethyl Laboratories, Inc. (USA). 3,3′,5,5′-Tetramethylbenzidine (TMB) and Triton X-100 were purchased from Sigma-Aldrich (USA). Other reactants and buffer components were of analytical grade.

For the ELISA, Costar 9018 microplates (Corning, USA) were used.

Production of mouse monoclonal Fab fragments

In this study, we used the Fab fragment of clone B1 of mouse monoclonal antibody (Ful B1, IgG2a lambda) obtained in our previous work [18]. The antibody Ful B1 was purified from ascitic fluid using one-step protein G–Sepharose affinity chromatography and dialyzed overnight against 200 mM sodium phosphate buffer, pH 7.4, containing 2 mM EDTA and 10 mM cysteine. To obtain Fab fragments of Ful B1 ($FabC_{60}$), papain (2x crystallized from Papaya Latex, Sigma, USA) was dissolved in the same buffer, mixed with the antibody solution at a 1 : 100 ratio, and incubated for 4 h at 37 ˚C with gentle shaking. The digestion was stopped by adding iodoacetic acid to a final concentration of 10 mM. To remove the Fc fragments, the reaction mixture was applied onto a Protein A Sepharose column and the flow-through was collected and dialyzed against PBS. The $FabC_{60}$ fragment concentration was determined by spectrophotometry at 280 nm using E (1 mg/ml) = 1.4. The purity of the samples was assessed using 12 % SDS-PAGE.

Characterization of mouse monoclonal Fab fragments

Indirect ELISA. The C_{60}–TG immunoconjugate (5 μg/mL) in PBS was added to microplate wells and incubated for 16 h at 4˚C. The plate was washed four times with PBS supplemented with 0.05% Triton X-100 (PBST). Then, a series of dilutions of the Ful B1 antibody and its $FabC_{60}$ fragment in PBST were added to the microplate wells and incubated for 1 h at 37˚C. After washing the microplate, peroxidase-labeled goat anti-mouse lambda light chain antibodies were added to the wells (1:10,000 dilution of the commercial preparation) and incubated for 1 h at 37˚C. After the final washing, the peroxidase activity of the resulting complexes was measured. For this purpose, a substrate solution containing 0.42 mM TMB and 1.8 mM hydrogen peroxide in 0.1 M sodium citrate buffer, pH 4.0, was added to each microplate well and the incubation was carried out for 15 min at room temperature. The enzymatic reaction was terminated by adding 50 μL of 1 M H_2SO_4 to each well. The optical density of the oxidation product was measured at 450 nm using a Zenyth 3100 microplate photometer (Anthos Labtec Instruments, Austria).

Competitive ELISA of $SolC_{60}$ using Fab fragments. To detect $SolC_{60}$, the C_{60}–STI conjugate (1 μg/mL) in PBS was added to microplate wells and incubated for 16 h at 4˚C. The plate was washed four times with PBST. After that, a series of dilutions of $SolC_{60}$ (from 5 μg/mL to 0.1 ng/mL) and $FabC_{60}$ at a concentration of 5 μg/mL were added to the microplate wells and the microplate was incubated for 90 min at 37˚C. After washing, peroxidase-labeled goat anti-mouse lambda light chain antibodies were added to the wells (1:10,000 dilution of the commercial preparation) and the microplate was incubated for 1 h at 37˚C. After the final washing, the peroxidase activity of the resulting complexes was measured as described above.

The plots of optical density (y) versus antigen concentration in the sample (x) were fitted to a four-parameter logistic function using the Origin 7.5 software (OriginLab, USA):

$$y = A_2 + \frac{A_1 - A_2}{1 + (\frac{x}{x_0})^p},$$

where A_1 is the maximum signal, A_2 is the minimum signal, p is the slope of the calibration curve, and x_0 is the antigen concentration causing 50% inhibition of antibody binding (IC_{50}).

Crystallization

Two protein solutions were used for crystallization: a solution of $FabC_{60}$ (7 mg/ml) in 50 mM HEPES, pH 7.0, and a solution of the $FabC_{60}$ complex with $SolC_{60}$. The complex was prepared by mixing 100 μL of the 0.16 mM (7 mg/ml) $FabC_{60}$ solution with 20 μL of a 1 mM $SolC_{60}$ solution in water.

For both protein solutions, crystallization conditions were screened and optimized using the hanging-drop vapor-diffusion technique at 298 K. Screening was per-

formed using crystallization screens Index HR2-134 and Crystal Screen HR2-110/112 (Hampton Research, USA). The drops were composed of equal volumes (1 μL) of the protein and reservoir solutions. $FabC_{60}$ crystals suitable for the diffraction experiments were obtained using the following conditions: 25 % w/v PEG 3350, 0.2 M $(NH_4)_2SO_4$, 0.1 M Bis-Tris, pH 6.5. The crystals appeared on the third day and grew to a maximum size of 200×200×50 μm within a week.

X-ray data collection and structure determination

The X-ray data set was collected from a $FabC_{60}$ crystal on the K4.4e beamline at the Belok station for protein crystallography at the Kurchatov synchrotron-radiation source (Moscow, Russia) at a wavelength of 0.98 Å equipped with a Rayonix SX165 CCD detector at 100 K under nitrogen flow. Prior to data collection, the crystal was soaked in the reservoir solution supplemented with 20 % v/v glycerol and then flash-cooled in liquid nitrogen. The X-ray data were processed and merged with XDS [19]. The crystallographic calculations were performed using the CCP4 suite of programs [20]. The $FabC_{60}$ structure was solved by the molecular replacement method with the BALBES pipeline [21]. The structure with the PDB ID 1MFB [22] was the best scoring search model. The structure was refined with REFMAC5 [23]. Visual inspection and manual rebuilding of the model were performed with COOT [24]. Data collection and structure solution statistics are summarized in *Table*. The figures were prepared using PyMOL [25]. The structure was deposited with the Protein Data Bank (PDB entry 6H3H).

Small-molecule docking

Docking and preparation of the receptor/ligand structures were performed in Autodock Vina [26] implemented in Pymol-Script-repo (https://github.com/Pymol-Scripts/Pymol-script-repo). The coordinates for C_{60} were derived from ChemSpider (http://www.chemspider.com). The receptor grid for docking in $FabC_{60}$ was defined as a box with a side of 22.5 Å, the center at (13.95; -9.51; 38.74), and 60 grid points in each dimension.

RESULTS AND DISCUSSION

Characterization of mouse monoclonal Fab fragments

$FabC_{60}$ used in the present work were produced by papain digestion of the full-size anti-C_{60} fullerene mouse monoclonal antibody Ful B1 and purified to a homogeneous state, which was confirmed by 12% SDS-PAGE under non-reducing conditions (*Fig. 1A*).

The immune reactivity of the obtained $FabC_{60}$ was assessed by indirect ELISA using immobilized C_{60}–TG immunoconjugate (*Fig. 1B*). Indirect ELISA showed that the immunoreactivity of $FabC_{60}$ was ~ 80 times lower than that of the full-size antibody.

The antigen-binding capacity of $FabC_{60}$ was characterized by competitive ELISA. In this assay, the C_{60}–protein conjugate adsorbed on the solid phase and the water-soluble fullerene derivative, $SolC_{60}$, competitively interacted with $FabC_{60}$. The Fab fragment of monoclonal antibody to another antigen (potato virus X), as well as a protein conjugate with another hapten (pesticide atrazine) immobilized on the solid phase, was

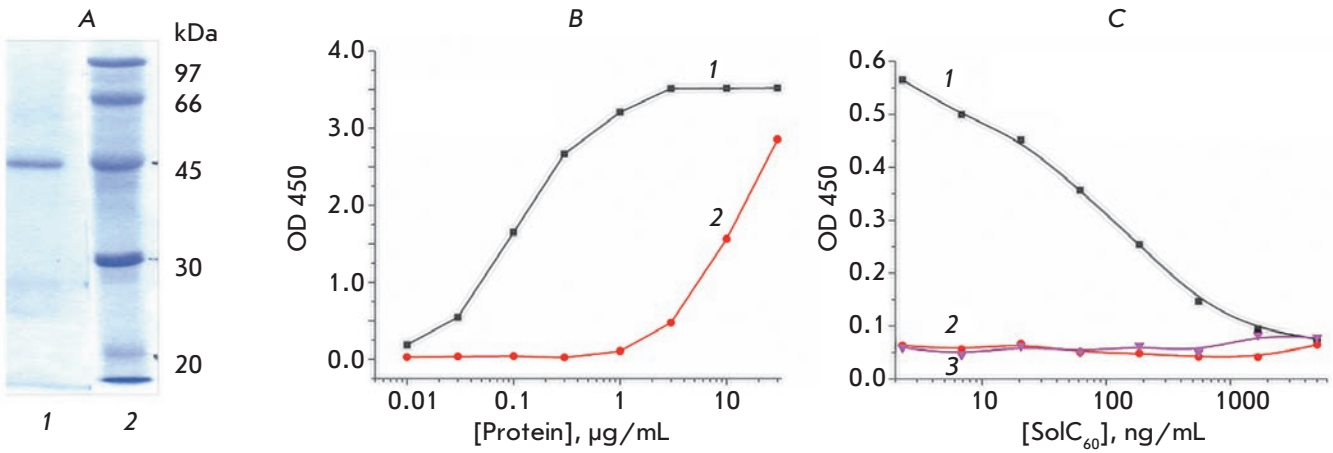

Fig. 1. *A* – 12% SDS-PAGE of $FabC_{60}$; lane *1*, $FabC_{60}$; lane *2*, molecular weight markers (phosphorylase B, 97 kDa; bovine serum albumin, 66 kDa; ovalbumin, 45 kDa; carbonic anhydrase, 30 kDa; trypsin inhibitor, 20 kDa). *B* – Titration curves for Ful B1 monoclonal antibody (*1*) and $FabC_{60}$ (*2*) in the indirect ELISA. *C* – Competitive ELISA curves for $SolC_{60}$ obtained using immobilized C_{60}–STI and $FabC_{60}$ (*1*), immobilized C_{60}–STI and Fab fragment of monoclonal antibody against potato virus X (*2*), and immobilized atrazine–STI and $FabC_{60}$ (*3*)

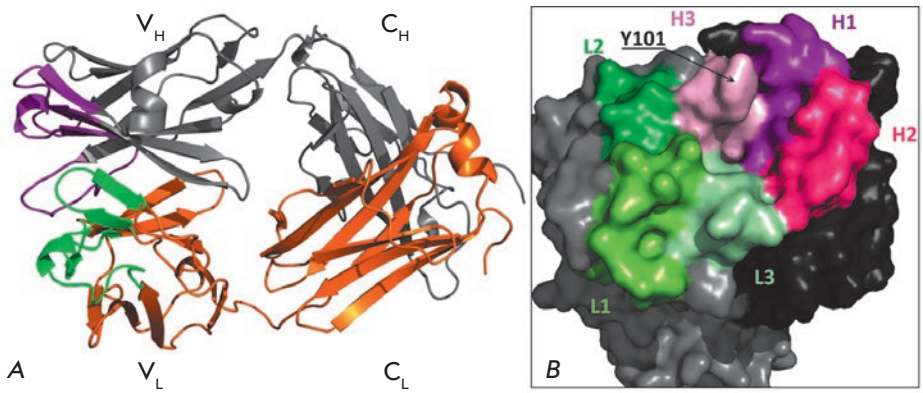

Fig. 2. *A* – $FabC_{60}$ structure. The H chain and its CDR are shown in gray and violet, respectively; the L chain and its CDR, in orange and green, respectively. *B* – The surface of the antigen-binding pocket in $FabC_{60}$ viewed approximately along the largest dimension of the $FabC_{60}$ molecule. The surfaces of the H and L chains are shown in black and gray, respectively. The surfaces of the H and L CDRs are depicted by shades of purple and green, respectively

used as control to confirm the specificity of interaction (*Fig. 1C*). As can be seen in *Fig. 1C*, $FabC_{60}$ does not interact with the adsorbed atrazine–protein conjugate (curve 3). In addition, the immobilized C_{60}–STI showed no binding to non-specific antibodies (curve 2 in *Fig. 1C*). Curve 1 in *Fig. 1C* demonstrates the competition between free $SolC_{60}$ in solution and the adsorbed C_{60}–STI conjugate for the binding sites of the antibody. All these effects confirm the specific nature of the immune interaction.

$FabC_{60}$ structure

Crystallization of the $FabC_{60}$ complex with $SolC_{60}$ yielded crystals of the free form of $FabC_{60}$. Since the structures of $FabC_{60}$ obtained in the presence and absence of $SolC_{60}$ were identical, hereinafter we will consider only the data set collected from the crystals of the free form of $FabC_{60}$.

The $FabC_{60}$ structure was solved by X-ray crystallography at a 1.9 Å resolution. Data collection and refinement are summarized in *Table*. There are two $FabC_{60}$ molecules per asymmetric unit. The RMSD between 2,717 equivalent atoms upon superposition of these $FabC_{60}$ molecules is 1.0 Å. When superimposed by C_α atoms of the variable domain, RMSD was 0.4 Å. Two crystallographically independent molecules differ in the conformation of the C-terminus and in intermolecular contacts (see below).

$FabC_{60}$ has a two-domain structure typical of Fab fragments, consists of heavy (H) and light (L) λ chains, and has the dimensions 45×50×100 Å (*Fig. 2A*). The variable domain of the heavy chain (V_H) includes residues 1–119, and the variable domain of the light chain (V_L) includes residues 1–108. The constant C_H domain includes residues 123–222, and the C_L domain includes residues 115–215. All the amino acid residues of the light chains are seen on electron density maps. The residues 135–139 located in the loop between the V_H and C_H domains are disordered and are not visible on electron density maps.

The complementarity-determining regions (CDRs) are defined as follows: **L1** (Arg23–Asn36), **L2** (Gly51–Ala57), **L3** (Ala91-Val99), **H1** (Gly26–His35), **H2** (Tyr50–Glu59), and **H3** (Gly99-Trp109) [27, 28] (*Fig. 2B*). The residues in these regions form an antigen-binding pocket with the sizes 9×7 Å and a depth of 5 Å (the diameter of C_{60} is 7 Å). Taking into account the presence of the π–π conjugated system in fullerene, we expected the CDR to contain aromatic residues prone to π–π stacking interactions. Indeed, the surface of the antigen-binding pocket is partially formed by aromatic residues located in CDR – Tyr50 (H2), Tyr101 (H3), Tyr34 (L1), Trp93 (L3), and Trp98 (L3). The side chain of Tyr101 of the Asp100–Tyr101 loop in CDR H3 is poorly seen on electron density maps, and the B-factors of the side-chain atoms of Tyr101 (B_{mean} = 54 Å^2) are higher than those of the main-chain atoms of Tyr101 (B_{mean} = 28 Å^2). This difference in the B-factors indicates the mobility of the side chain of Tyr101 and may be associated with the location of Tyr101 on the protein surface. The mobile Tyr101 can act as a lid of the pocket, thereby hindering the access of C_{60} to the antigen-binding pocket and reducing the affinity of the antibody-antigen interaction (*Fig. 2B*).

The residues Thr33 and His35 of CDR H1 on the surface of the antigen-binding site can form hydrogen bonds that can be involved in fullerene binding [15]. However, in the $FabC_{60}$ free-form structure, the residues Thr33 and His35 of the $FabC_{60}$ molecules formed hydrogen bonds with the C-termini of the H or L chain of the symmetry-related $FabC_{60}$ (*Fig. 3A,B*). In one crystallographically independent $FabC_{60}$ molecule, the antigen-binding pocket was occupied by the C-terminal peptide Ala219–Ser222 of the H chain of the symmetry-related molecule, the carboxyl group of Ser222 forming hydrogen bonds with Thr33 and His35.

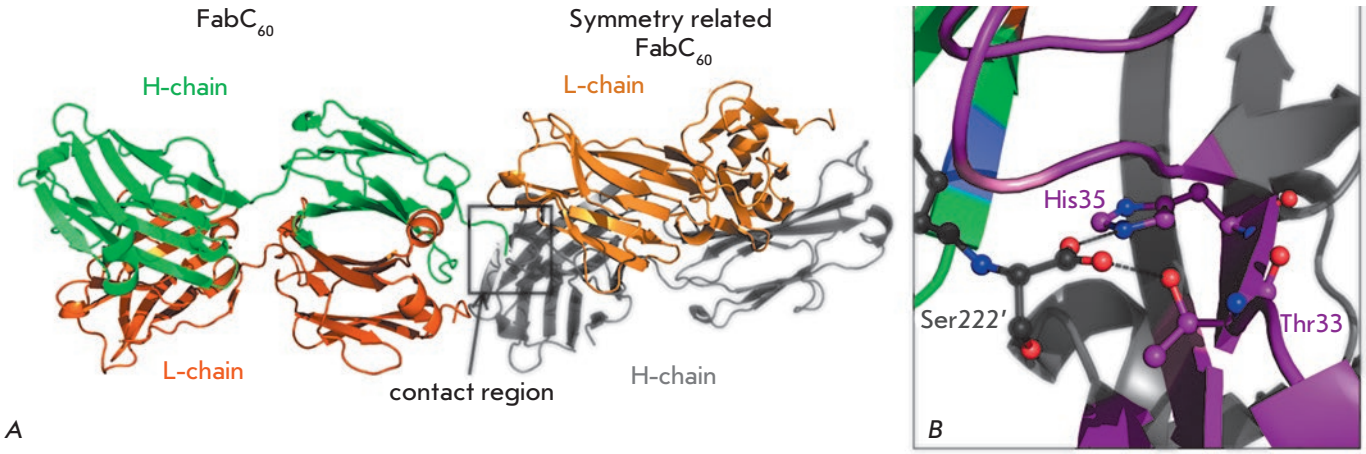

Fig. 3. *A* – Crystal packing of $FabC_{60}$ in space group $P2_1$. The C-terminus of the H chain (green) of $FabC_{60}$ protrudes into the antigen-binding site of the symmetry-related $FabC_{60}$. *B* – The contact region (the orientation and coloring differ from those in *Fig. 3a*). Binding of C-terminal Ser222′ of the H chain of the symmetry-related molecule in the antigen-binding pocket of $FabC_{60}$. The CDRs of the H and L chains are shown in purple and green, respectively. The hydrogen bonds of the carboxyl group of C-terminal Ser222′ (carbon atoms being shown in black) are indicated by black dashed lines

The antigen-binding pocket of the second crystallographically independent $FabC_{60}$ molecule was occupied by the C-terminal peptide Asp213–Ser215 of the L chain of another symmetry-related $FabC_{60}$ molecule. In this case, the hydrogen bonds of C-terminal Ser215 with the residues Thr33 and His35 of the H chain occured via a water molecule. Most likely, the binding of the C-terminus of one $FabC_{60}$ molecule in the antigen-binding pocket of another molecule was an artifact of the crystal packing and is unrelated to the biological role of $FabC_{60}$. However, this crystal packing stabilized by additional intermolecular hydrogen bonds with CDR apparently hinders the antigen binding, which may be responsible for the unsuccessful attempts to crystallize $FabC_{60}$ in complex with $SolC_{60}$.

The degree of homology between the primary structures of the $FabC_{60}$ and Fab fragments of anti-fullerene antibodies that had been structurally characterized earlier [15] was rather high and amounted to 76% and 40% for the H and L chains, respectively. $FabC_{60}$ contains the λ-chain, while Fab fragments of anti-fullerene antibodies contained the κ-chain. However, the structures of antibodies are dissimilar due to the different mutual arrangements of the V- and C-domains (RMSD > 3 Å). Therefore, it is difficult to perform a comparative analysis of these two structures. When superimposed by the V_H domains, RMSD is 0.4 Å (*Fig. 4A*). The antigen-binding pockets of these two antibodies also differ in their composition and structure; the maximum difference is observed in CDR H3 and the L-chain fold (*Fig. 4B*). The H3 loop of the Fab fragment described by Braden et al. [15] is seven residues shorter (four residues) than that in $FabC_{60}$ (11 residues).

Table. Statistics of data collection and structure refinement

Data collection	
Space group	$P2_1$
Unit cell parameters a, b, c(Å), β (°)	40.18;137.58;83.15 91.9
Resolution	28.83–1.91 (2.02–1.91)
I / σ	17.5 (3.2)
Completeness (%)	99.5 (97.3)
Total reflections	349716 (52972)
Unique reflections	69665 (10963)
Multiplicity	5.0 (4.8)
*R_{meas} (%)	8.4 (2.3)
$CC_{1/2}$	99.9 (83.0)
Wilson plot B-factor	29.7
Refinement	
R_{cryst} (%)	19.3 (27.9)
R_{free} (%)	23.5 (34.3)
Bond r.m.s.d. from ideal values:	
Length (Å)	0.02
Angle (°)	1.9
Torsion angle (°)	7.2
Number of atoms	
Protein	6535
Water	456
Average B-factors (Å²)	
Protein	30.1
Water	32.5
Statistics of Ramachandran plot	
Allowed region(%)	97.4
Disallowed region(%)	0.2

*For R_{meas}, the value in parentheses is given for the inner shell.

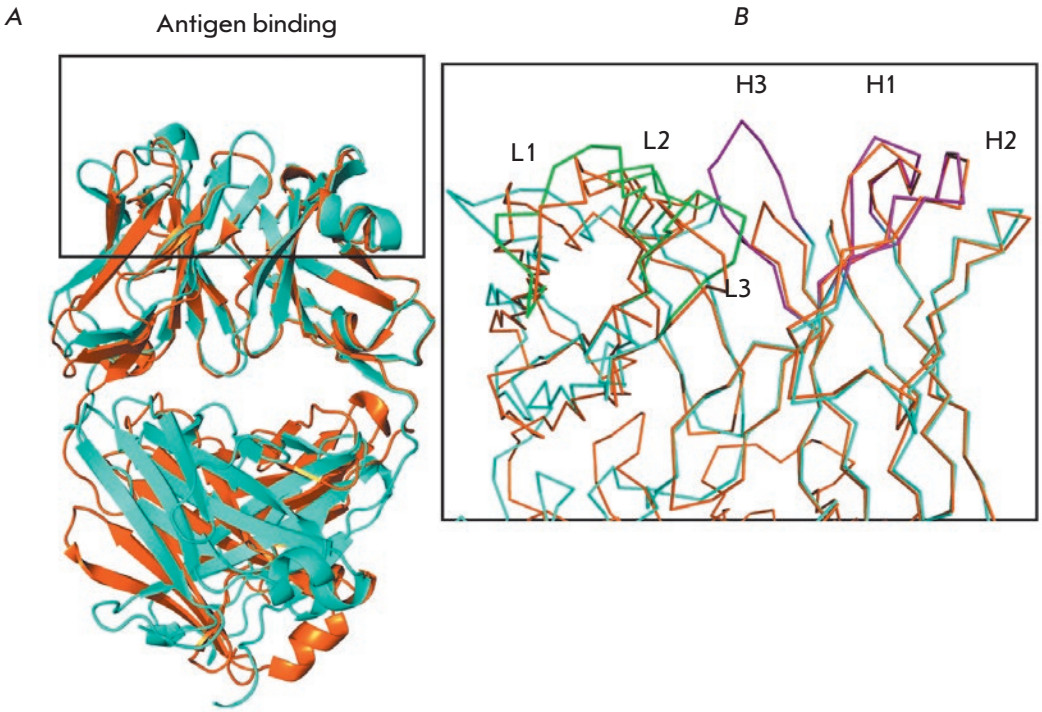

Fig. 4. *A* – Structures of $FabC_{60}$ (cyan) and anti-C_{60} Fab (orange) [15] superimposed on the V_H domains. The antigen-binding pocket is highlighted by a black box. *B* – The zoomed antigen-binding pockets of $FabC_{60}$ (cyan) and anti-C_{60} Fab (orange) superimposed on the V_H domains. The CDRs of the H and L chains are shown in purple and green for $FabC_{60}$. Note the difference in the length of CDR H3

Docking of C_{60} into $FabC_{60}$ and analysis of C_{60} binding to $FabC_{60}$

Since we failed to obtain a structure of $FabC_{60}$ in complex with C_{60}, we performed rigid body docking of C_{60} into the antigen-binding pocket of $FabC_{60}$ [26] in order to elucidate the structural features of the antigen-binding site of anti-fullerene antibodies. The antigen binding is known to be accompanied by conformational changes within CDRs [29, 30]. The largest structural rearrangements are observed in the most mobile CDR H3 loop, which is the one most difficult to simulate as compared to all other loops of the antigen-binding region [31]. To gain insight into the possible influence of the CDR H3 loop on C_{60} binding, we compared two models of the complex of C_{60} with the native form of $FabC_{60}$ (Complex I) and with a modified model of $FabC_{60}$ containing the CDR H3 with deleted Asp100 and Tyr101 residues (Complex II) (*Fig. 5*).

In Complex I, the C_{60} molecule binds to the surface of the antigen-binding site and forms π–π stacking interactions with residues Tyr50 (H2), Tyr101 (H3), and Trp93 (L3). C_{60} binding leads to a 40% decrease in the solvent-accessible area of the C_{60} hydrophobic surface. The AutoDock Vina-generated binding energy is -7 kcal mol^{-1}, which corresponds to a dissociation constant (K_d) of the complex equal to 7.4×10^{-6} M. The K_d constant experimentally determined earlier for the C_{60} complex with full-length anti-fullerene antibody was 1.1×10^{-7} M [18]. Taking into account the 80-fold decrease in the affinity of interaction between C_{60} and $FabC_{60}$, K_d for the complex of C_{60} with $FabC_{60}$ can be estimated at 9×10^{-6} M, which correlates well with the value of K_d calculated for the docking-simulated model of C_{60} in a complex with the native form of $FabC_{60}$.

The removal of the Asp100 and Tyr101 residues allows the C_{60} molecule in Complex II to penetrate deeper into the antigen-binding cavity and bind at a distance of about 4 Å from the position of C_{60} in Complex I (*Fig. 5*). The AutoDock Vina-generated binding energy increases from -7 to -12 kcal mol^{-1}, which corresponds to a decrease in K_d of the complex from 7.4×10^{-6} to 1.6×10^{-9} M. The increase in affinity in the absence of Asp100 and Tyr101 can be attributed to the formation of additional (apart from those mentioned above) π–π interactions with His35 (H1) and Tyr34 (L1) and also to a 40% decrease in the solvent-accessible area of the C60 hydrophobic surface. Thus, the Asp100 and Tyr101 residues of the CDR H3 can play a key role in the reduction of the affinity of interaction between C_{60} fullerene and the corresponding antibodies.

Earlier attempts to obtain a complex between the antibody and fullerene were unsuccessfull [15]. The complex was simulated with INSIGHT 2 by a procedure different from that used in our work: the C_{60} molecule was manually placed into the cavity of the variable domain between the H and L chains, followed by minimization of the energy of the system [15]. Binding of C_{60} to anti-C60 Fab was ensured by interactions with

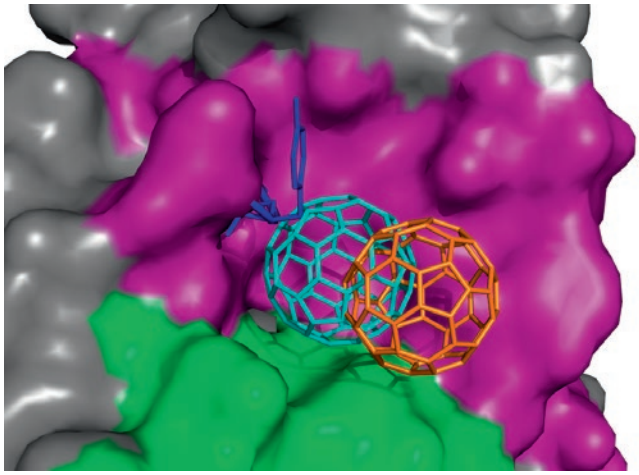

Fig. 5. Docking of C_{60} (represented by the stick model) to the unmodified (orange C_{60}) and modified (cyan C_{60}) antigen-binding pockets of $FabC_{60}$. The residues Asp100–Tyr101 that are absent in the modified structure are represented by the blue stick model. The surfaces of the H and L chains of the modified antigen-binding pocket used to generate the receptor in Autogrid are shown in purple and green, respectively

the Tyr36, Gln89, Phe96, and Phe98 residues of the L chain and the Asn35, Trp47, and Trp106 residues of the H chain. Binding was accompanied by 90% reduction in the solvent-accessible area of the fullerene hydrophobic surface. At the present time, the structures of the complex of C_{60} with a synthetic protein (pdbid 5hkn, 5hkr, 5et3) [32] are the only experimentally established structures that can be used to verify the validity of our conclusions about the driving forces for the formation of the antibody–fullerene complex. In these complexes, C_{60} fullerene was bound in the hydrophobic pocket. C_{60} binding led to a ~90% decrease in the solvent-accessible area of the C_{60} hydrophobic surface and formation of a π–π interaction with the Tyr9 residue. The analysis of the structures performed in the present study revealed a π-π interaction between C_{60} and the Leu19-Ala20 peptide bond that was not mentioned in [32].

CONCLUSION

In summary, the docking simulation data obtained in this study are in agreement with the experimental results [32]. Thus, π–π stacking interactions between fullerene and aromatic residues of the antigen-binding site and reduction in the solvent-accessible area of C_{60} make the defining contribution to the formation energy of the fullerene–antibody complex. A fragment of the mobile CDR H3 loop located on the surface of $FabC_{60}$ that hinders the access of C_{60} to the antigen-binding site is the key structural factor responsible for the low affinity of the antibodies under consideration for C_{60} (K_d is about 10^{-7} M).

The Thr33 and His35 residues of the antigen-binding pocket, which are probably involved in fullerene binding in the solution, formed hydrogen bonds with the C-terminal residues of the symmetry-related $FabC_{60}$ molecule under the crystallization conditions used, thereby stabilizing the crystal packing of the free form of $FabC_{60}$ and interfering with the crystallization of the complex formed by C_{60} and $FabC_{60}$. ●

This work was supported by the Program of the Presidium of the Russian Academy of Sciences No. 32 "Nanostructures: Physics, Chemistry, Biology, Basis of Technologies".

REFERENCES

1. Sundberg E.J., Mariuzza R.A. // Adv. Protein Chem. 2002. V. 61. P. 119–160.
2. Sundberg E.J. In: Methods Mol Biol. // 2009. V. 524. P. 23–36.
3. Calvaresi M., Zerbetto F., Ciamician C.G., Bologna U., Selmi V.F. // ACS Nano. 2010. V. 4. № 4. P. 2283–2299.
4. Dunbar J., Krawczyk K., Leem J., Baker T., Fuchs A., Georges G., Shi J., Deane C.M. // Nucleic Acids Res. 2014. V. 42. № D1. P. D1140–D1146.
5. Abbott W.M., Damschroder M.M., Lowe D.C. // Immunology. 2014. V. 142. № 4. P. 526–535.
6. Wilson I.A., Rini J.M., Fremont D.H., Fieser G.G., Stura E.A. // Methods Enzymol. 1991. V. 203. P. 153–176.
7. Clementi N., Mancini N., Castelli M., Clementi M., Burioni R. // Drug Discov. Today. 2013. V. 18. № 9–10. P. 464–471.
8. Narciso J.E.T., Uy I.D.C., Cabang A.B., Chavez J.F.C., Pablo J.L.B., Padilla-Concepcion G.P., Padlan E.A. // Nat. Biotechnol. 2011. V. 28. № 5. P. 435–447.
9. Malito E., Carfi A., Bottomley M. // Int. J. Mol. Sci. 2015. V. 16. № 12. P. 13106–13140.
10. Jeevanandam J., Barhoum A., Chan Y.S., Dufresne A., Danquah M.K. // Beilstein J. Nanotechnol. 2018. V. 9. № 1. P. 1050–1074.
11. Boraschi D., Italiani P. // Vaccines. 2015. V. 3. № 4. P. 930–939.
12. Sun T., Zhang Y.S., Pang B., Hyun D.C., Yang M., Xia Y. // Angew. Chemie Int. Ed. 2014. V. 53. № 46. P. 12320–12364.
13. Stylianopoulos T., Jain R.K. // Nanomedicine Nanotechnology, Biol. Med. 2015. V. 11. № 8. P. 1893–1907.
14. Castro E., Garcia A.H., Zavala G., Echegoyen L. // J. Mater. Chem. B. 2017. V. 5. № 32. P. 6523–6535.
15. Braden B.C., Goldbaum F.A., Chen B.X., Kirschner A.N., Wilson S.R., Erlanger B.F. // Proc. Natl. Acad. Sci. U. S. A. 2000. V. 97. № 22. P. 12193–12197.
16. Chen B.-X., Wilson S.R., Das M., Coughlin D.J., Erlanger B.F. // Proc. Natl. Acad. Sci. USA. 1998. V. 95. № 18. P. 10809–10813.
17. Hendrickson O.D., Fedyunina N.S., Martianov A.A., Zherdev A. V., Dzantiev B.B. // J. Nanoparticle Res. 2011. V. 13. № 9. P. 3713–3719.

18. Hendrickson O., Fedyunina N., Zherdev A., Solopova O., Sveshnikov P., Dzantiev B. // Analyst. 2012. V. 137. № 1. P. 98–105.
19. Kabsch W. // Acta Crystallogr. Sect. D. 2010. V. 66. № 2. P. 125–132.
20. Winn M.D., Ballard C.C., Cowtan K.D., Dodson E.J., Emsley P., Evans P.R., Keegan R.M., Krissinel E.B., Leslie A.G.W., McCoy A., et al. // Acta Crystallogr. Sect. D. 2011. V. 67. № Pt 4. P. 235–242.
21. Long F., Vagin A.A., Young P., Murshudov G.N. // Acta Crystallogr. Sect. D. 2008. V. 64. № Pt 1. P. 125–132.
22. Cygler M., Wu S., Zdanov A., Bundle D.R., Rose D.R. // Biochem. Soc. Trans. 1993. V. 21. № 2. P. 437–441.
23. Murshudov G.N., Vagin A.A., Dodson E.J. // Acta Crystallogr. Sect. D. 1997. V. 53. № 3. P. 240–255.
24. Emsley P., Lohkamp B., Scott W.G., Cowtan K. // Acta Crystallogr. Sect. D. 2010. V. 66. № 4. P. 486–501.
25. The PyMOL Molecular Graphics System, Version 2.0 Schrödinger, LLC.
26. Trott O., Olson A.J. // J. Comput. Chem. 2009. V. 31. № 2. P. 455–461.
27. Kabat E.A., Te Wu T., Foeller C., Perry H.M., Gottesman K.S. Sequences of Proteins of Immunological Interest. Diane Publ. Comp., 1992, Bethesda, MD, USA.
28. Martin A.C. // Proteins. 1996. V. 25. № 1. P. 130–133.
29. Stanfield R.L., Wilson I.A. // Trends Biotechnol. 1994. V. 12. № 7. P. 275–279.
30. Weitzner B.D., Dunbrack R.L., Gray J.J. // Structure. 2015. V. 23. № 2. P. 302–311.
31. Regep C., Georges G., Shi J., Popovic B., Deane C.M. // Proteins. 2017. V. 85. № 7. P. 1311–1318.
32. Kim K.H., Ko D.K., Kim Y.T., Kim N.H., Paul J., Zhang S.Q., Murray C.B., Acharya R., Degrado W.F., Kim Y.H., et al. // Nat. Commun. 2016. V. 7. A. 11429.

Adaptation of the Newcastle Disease Virus to Cell Cultures for Enhancing Its Oncolytic Properties

K. S. Yurchenko[1*], Yi. Jing[2], A. M. Shestopalov[1]
[1]Federal State Budget Scientific Institution «Federal Research Center of Fundamental and Translational Medicine», Timakova Str. 2, 630117, Novosibirsk, Russia
[2]Federal State Budgetary Educational Institution of higher professional education "Novosibirsk national research state University», Pirogova Str. 1, 630090, Novosibirsk, Russia
*E-mail: xenia7yurchenko@gmail.com
Received October 30, 2018; in final form February 11, 2019

ABSTRACT **This study focuses on the adaptation of natural Newcastle disease virus (NDV) strains isolated from wild birds to human tumor cells. Many candidates for virotherapy are viruses pathogenic for human. During recombination of genetic material, there always exists a risk of getting a virus with an unstable genome. This problem can be solved by using natural apathogenic viruses as oncolytic agents. The Newcastle disease virus is the causative agent of contagious avian diseases. Its natural strains exhibit an antitumor effect and are considered safe for humans. As shown in earlier studies, the oncolytic properties of natural strains can be enhanced during adaptation to cell cultures, without interference in the virus genome. This study demonstrates that serial passaging increases the viral infectious titer in cancer cells. Moreover, the viability of tumor cells decreases post-infection when Newcastle disease virus strains are adapted to these cell cultures. The findings of this study complement the well-known data on the adaptation of the Newcastle disease virus to human cancer cells. Hence, it is possible to obtain a NDV strain with a more pronounced oncolytic potential during adaptation. This should be taken into account when choosing a strategy for designing anticancer drugs based on this virus.**
KEYWORDS **adaptation, Newcastle disease virus, oncolytic properties, tumor cells, cytotoxic effect.**
ABBREVIATIONS **NDV – Newcastle disease virus; DMSO – dimethyl sulfoxide; IFN – interferon; ECE – embryonated chicken eggs; TCID50 – 50% tissue culture infective dose; FBS – fetal bovine serum; CTE – cytotoxic effect; VCL – virus-containing liquid.**

INTRODUCTION

Virotherapy is an experimental method of targeted therapy of malignant diseases that employs oncolytic viruses, including the Newcastle disease virus (NDV) (family Paramyxoviridae, genus *Avulavirus*), for selective destruction of tumor cells [1]. Oncolytic viruses selectively infect tumor cells and use their activated synthetic apparatus for replication, which causes a cytotoxic effect (CTE) and leads to cell death [2]. Normal healthy cells remain unharmed due to the development of an early antiviral interferon response, which prevents viral genome replication [3]. The Newcastle disease virus drew researchers' attention as a potential oncolytic agent in the mid-20th century and has proved to be a safe and effective antitumor agent [4].

NDV strains for virotherapy studies are divided into lytic and non-lytic ones based on the properties of the F protein [5]. Both lytic and non-lytic strains can act as powerful anticancer agents. Lytic strains are advantageous, as infectious viral progeny is produced by multiple replication cycles and the cytotoxic effect spreads in tumor tissue. Non-lytic strains have only one replication cycle. The new virions of non-lytic strains contain inactive variants of the F protein, and the antitumor effects are mainly associated with the stimulation of the immune response [6].

A significant part of virotherapy research focuses on the creation of recombinant strains to enhance the antitumor properties of viruses. However, the development of viral constructs is associated with the need to regulate the biological properties of the recombinant virus, its cancer tropism, and the elimination of possible inertial mutagenesis and recombinations related to the restoration of the properties of viruses that initially were pathogenic for humans [7, 8]. The natural oncolytic potential of NDV strains isolated from wild birds can be used for virotherapy without any complicated modifications of the genome. Different lentogenic (low-pathogenic) and

mesogenic (medium-pathogenic) NDV strains have been studied since the 1960s *in vitro*, *in vivo,* and in clinical studies involving cancer patients [9].

Despite the popularity of the genetic engineering methods used to design viruses for virotherapy, natural unmodified strains also can be a powerful antitumor agent. Wild-type NDV strains exhibit a high oncolytic activity. The best studied and clinically tested strains are 73-T, MTH-68, PV701, and NDV-HUJ [10]. These strains belong to the lytic type of virus, which directly kill tumor cells. In addition, virulent mesogenic strains induce a more powerful apoptotic response in tumor cells, in contrast to apatogenic and low-virulent ones [11, 12].

The natural attenuated nonrecombinant strain PV701 obtained from the mesogenic strain MK107 (Gaithersburg, USA) [13] exhibits an antitumor activity against a broad range of tumors of epithelial, neuroectodermal, and mesenchymal origin [10]. Another lytic strain, MTH-68/H, derived from the natural strain Hertfordshire (Herts'33), exhibits a cytotoxic effect on various human tumor cells [10]. Systemic or locoregional administration of this virus leads to partial or complete regression of primary and metastatic tumors [14, 15]. The adapted natural strain 73-T causes syncytia formation and death of a wide range of malignant cells, both *in vitro* and *in vivo* [16, 17]. Meanwhile, natural mesogenic strains exhibiting a cytotoxic effect on malignant cells are safe for normal human cells [12, 16–18].

Investigation of the mechanism of viral antitumor cytotoxic action allowed researchers to put forward a hypothesis that a strain with more pronounced lytic properties can be obtained during viral adaptation to a cell culture [19]. During adaptation, variants of the wild-type virus with more effective reproduction in host cells may emerge. On the one hand, there is a risk that the increased infectious potency of the natural virus against adapted cells can reduce its virulence [20, 21]. This may have a negative effect on its oncolytic properties. On the other hand, adaptation of the virus to a specific cell line can increase the cytotoxic potential of the adapted virus against these cells [22].

Thus, the strain based on natural MD20Z (USA, 1945) was obtained by serial (n = 38) passaging in Ehrlich ascites carcinoma cells and was tested on an *in vivo* model. The overall weekly survival rate of mice with ascites tumors after treatment with the late-passage virus increased from 0 to 63.6%. Moreover, the virus actively replicated in tumor cells and exhibited a cytotoxic effect faster than the wild-type strain [23]. Cassel W.A. and Garrett R.E. [24] confirmed that the oncolytic effect is enhanced after adaptation of NDV 379-SI from a natural MD20Z strain by the method of serial (n = 73) passages in Ehrlich ascites carcinoma *in vitro* followed by 13 passages *in vivo*. Later, a number of successful clinical trials of allogeneic and autologous vaccines based on the NDV 73-T strain against metastatic melanoma were conducted in the USA [25].

Therefore, taking into account the data confirming successful adaptation of wild-type strains with an enhanced antitumor effect during sequential passaging, we studied the adaptation of wild-type strains of various pathotypes on lines of human tumor cells in order to verify the effectiveness of the cytotoxic properties acquired after passaging of the strains.

EXPERIMENTAL

Cell lines

We studied transplantable cell lines: Vero – kidney epithelial cells extracted from the African green monkey; HCT116 – human colon carcinoma cell line (State Research Center of Virology and Biotechnology Vector, Novosibirsk region, Russia); Hela – human epithelioid cervix carcinoma (Institute of Clinical and Experimental Lymphology, Novosibirsk, Russia); MCF7 – human breast adenocarcinoma cell line (Institute of Cytology of the Russian Academy of Sciences, St. Petersburg, Russia); and A549 – human non-small lung carcinoma cell line (Research Institute of Fundamental and Clinical Immunology, Novosibirsk, Russia).

Vero and tumor cell lines were grown in Dulbecco's modified Eagle's media (DMEM) supplemented with 10% heat-inactivated fetal bovine serum (FBS) and 50 mg/ml gentamicin. Cells were maintained in cultural flasks (25 cm^2) at 37°C in an incubator with 5% CO_2.

Newcastle disease virus strains

Our study was performed using four NDV strains: two virulent mesogenic NDV strains isolated from rock doves in Russia (NDV/Altai/pigeon/770/2011 [26] and NDV/Altai/pigeon/**777**/2010 [27]) and two lentogenic strains (NDV/mallard/Amur/264/2009 and NDV/teal/Novosibirsk_region/320/2010) isolated from a mallard and a teal, respectively.

Preparation of Newcastle disease virus strains

The viral strains were amplified in the allantoic fluid of 10-day-old embryonated eggs. The presence of the virus was determined by hemagglutination assay (HA) with rooster erythrocytes. The hemagglutinin titers of each viral strain were determined according to the standard procedure recommended by the WHO [28].

Titration of the Newcastle disease virus on Vero cell line (TCID50)

Titration of the Newcastle disease virus on the Vero cell line, which is sensitive to the cytopathic effect of

NDV, was performed according to the procedure described in [29]. The cell suspension was cultured in the growth medium on 96-well plates at a concentration of 30,000 cells per well under standard conditions.

The next day, the cell monolayer was washed with Hanks' solution and 10-fold viral dilutions per well were added. The dilutions were prepared using MEM maintenance medium supplemented with 1% heat-inactivated FBS. The plates were incubated under standard conditions for 1 h to adsorb the virus; the virus-containing liquid (VCL) was then replaced with the maintenance medium. Every day, the cell monolayer was inspected under a microscope to detect the presence of CTE. The final titration was carried out on day 4. The infectious titers of the virus on the Vero cell line were calculated according to the Cerberus method in the Ashmarin's modification and presented as lgTCID50/ml [30].

Serial passages of NDV strains in transplantable Vero cell line and tumor human cell lines

Preparation of the cells and infection with 10-fold dilutions of the virus were performed using the same procedure as the one described in the titration method. On day 4 post-infection, the infectious titer was counted and VCL of the extreme dilutions was collected. The next passage was carried out with infection of Vero cells with the virus collected in extreme dilution using the same method. Hence, we conducted a total of eleven passages and calculated the infectious titer of each passage.

Colorimetric analysis of cell viability after infection with NDV strains (the MTT assay)

The viability of human tumor cell lines was analyzed using the MTT assay 4 days post-infection with viral strains. The one-day-old monolayer of tumor cells on the 96-well plate was washed with Hanks' solution and incubated with viruses (titer 8 HAU per 10,000 cells) for 1 h under standard conditions. The cells were then washed with Hanks' solution and incubated in 200 µl of the maintenance medium for 4 days under standard conditions. Control tumor cells without the virus were incubated in MEM maintenance medium.

On day 4, the cells were washed with Hanks' solution. The MTT working solution at a concentration of 5 mg/ml was prepared using the MEM maintenance medium. The MTT solution (100 µl) was added to each well. The plate was incubated for 4 h under standard conditions. The MTT solution was then replaced with DMSO (150 µl per well), and the cells were incubated for 1 h in the dark at room temperature. The optical density was measured at wavelengths of 540 nm and 630 nm on a LonzaBiotek ELX808 absorbance microplate reader (USA). Cell viability was evaluated according to the ratio between the relative percentage of living and control uninfected cells using the formula: $(V_{540}-V_{630})/(K_{540}-K_{630}) \times 100\%$, where V and K denote the values for virus-infected and control wells, respectively.

Infection of human tumor cell lines with mesogenic NDV strains to assess the replicative activity of the virus in different tumor cells

The replicative activity of NDV strains in different tumor cell lines was assessed by titration on HCT116, HeLa, A549, and MCF7 cells after infection with NDV strains.

Human tumor cell lines and control Vero cells were cultured in a growth medium in culture flasks (25 cm^2) under standard conditions. The one-day-old cell monolayer was washed twice with Hanks' solution and incubated with viruses in a 1-ml volume (titer 8 HAU per 10,000 cells) with adsorption for 45 min under standard conditions. The cells were then washed twice with Hanks' solution, and a fresh 10 ml of the MEM maintenance medium was added. The flasks were incubated under standard conditions. The infectious titer of the culture medium was determined 3, 6, 24, 48, and 72 h post-infection with NDV strains by titration on the respective tumor and model cell lines using the conventional method.

Statistical analysis

Statistical data were obtained using the Statistica 6.0 software. The Student's t-test was used to determine the statistical significance for comparing the individual data points.

RESULTS AND DISCUSSION

Newcastle disease virus strains were propagated in the allantoic fluid of 10-day-old embryonated eggs. The presence of the virus in allantoic fluid was confirmed by hemagglutination assay with rooster erythrocytes; infectious viral titer was determined in the Vero cell line (*Table 1*). A high titer of the mesogenic strains isolated from rock doves was shown in hemagglutination assay and during titration on Vero cells.

Two possible systems for enhancing the antitumor properties of the Newcastle disease virus were used in the next step. The first system consisted in passaging NDV strains in transplantable sensitive Vero cells with viral adaptation to this line, followed by testing of the viability of tumor cells after infection with adapted NDV strains. Vero cells do not synthesize IFNα and IFNβ, which allows the Newcastle disease virus to reproduce freely, release new viral progeny, and form CTE.

Table 1. Titers of wild-type Newcastle disease virus strains

Strain	HA assay/50 µl	lgTCID50/ml
NDV/Altai/pigeon/770/2011	512	6.7
NDV/Altai/pigeon/777/2010	256	6.5
NDV/mallard/Amur/264/2009	64	3.0
NDV/teal/Novosibirsk_region/320/2010	64	3.0

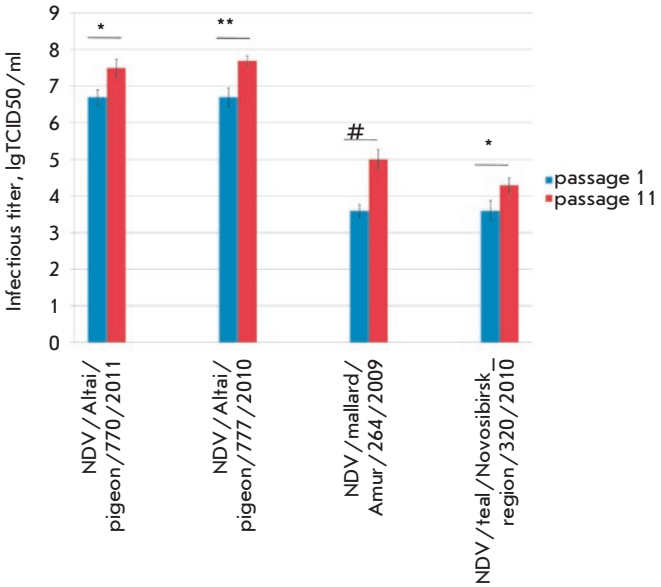

Fig. 1. The increasing infectious titers of Newcastle disease virus strains during the adaptation to the Vero cell culture. * $p = 0.05$; ** $p = 0.01$; # $p = 0.001$ (Student's t-test)

The second system consisted in the adaptation of strains to tumor cell lines with assessment of the dynamics of changes in the viability of tumor cells after infection with adapted strains in late passages.

According to the first scheme, the viral titers of the mesogenic strains NDV/Altai/pigeon/770/2011 and NDV/Altai/pigeon/777/2010 increased to 7.5 and 7.7 lgTCID50/ml, respectively (*Table 2*, *Fig. 1*) after 11 passages in the Vero cell line. The titer of these strains was initially higher than those of lentogenic strains and was 6.7 lgTCID50/ml after the first passage. We failed to reach values as high as the titers of the lentogenic strains NDV/mallard/Amur/264/2009 and NDV/teal/Novosibirsk_region/320/2010 for mesogenic strains in late passages, despite the fact that the titers increased from 3.6 to 5.0 lgTCID50/ml and from 3.6 to 4.3 lgTCID50/ml, respectively. The presence of a "virulent" sequence at the F protein cleavage site is probably affected not only by the virus' ability to efficiently replicate in cells with the formation of CTE. It is quite possible that belonging to a certain pathotype, which is directly associated with the cytolytic capacity, also plays a role, since all the studied strains contained a "virulent" sequence at the cleavage site, but only the NDV/Altai/pigeon/770/2011 and NDV/Altai/pigeon/777/2010 belonged to the mesogenic type [26, 27].

During adaptation to the Vero cell line, the titer of all studied viral strains increased and remained unchanged after seven or eight passages. In addition to the increase in infectious titer in the TCID50 assay, the morphological changes in the cell monolayer became more pronounced. After infection with mesogenic strains, a cytotoxic effect was observed in the 1st–3rd passages in Vero cells on day 2 or 3 of cultivation. Areas of rounded dead cells formed in the culture: they were detached from the plate surface and spread in the monolayer by day 4. In the next 5–11 passages, bundles consisting of cell agglomerates formed in the

Table 2. The dynamics of titer changes for Newcastle disease virus strains during adaptation to the Vero cell line: mean relative value ± standard deviation

NDV strains	Passage										
	1	2	3	4	5	6	7	8	9	10	11
NDV/Altai/pigeon/770/2011	6.7± 0.21	6.8± 0.52	6.7± 0.39	6.9± 0.15	6.9± 0.18	6.9± 0.23	7.0± 0.25	7.5± 0.31	7.5± 0.14	7.5± 0.34	7.5± 0.24
NDV/Altai/pigeon/777/2010	6.7± 0.26	6.7± 0.28	6.9± 0.31	6.9± 0.21	7.0± 0.19	7.0± 0.23	7.2± 0.33	7.7± 0.23	7.7± 0.21	7.7± 0.40	7.7± 0.14
NDV/mallard/Amur/264/2009	3.6± 0.18	3.6± 0.19	3.8± 0.22	3.8± 0.25	4.5± 0.24	4.7± 0.36	4.7± 0.33	5.0± 0.40	5.1± 0.36	5.0± 0.22	5.0± 0.28
NDV/teal/Novosibirsk_region/320/2010	3.6± 0.28	3.6± 0.21	3.8± 0.18	3.7± 0.19	4.3± 0.31	4.2± 0.14	4.3± 0.29	4.3± 0.18	4.3± 0.26	4.4± 0.33	4.3± 0.20

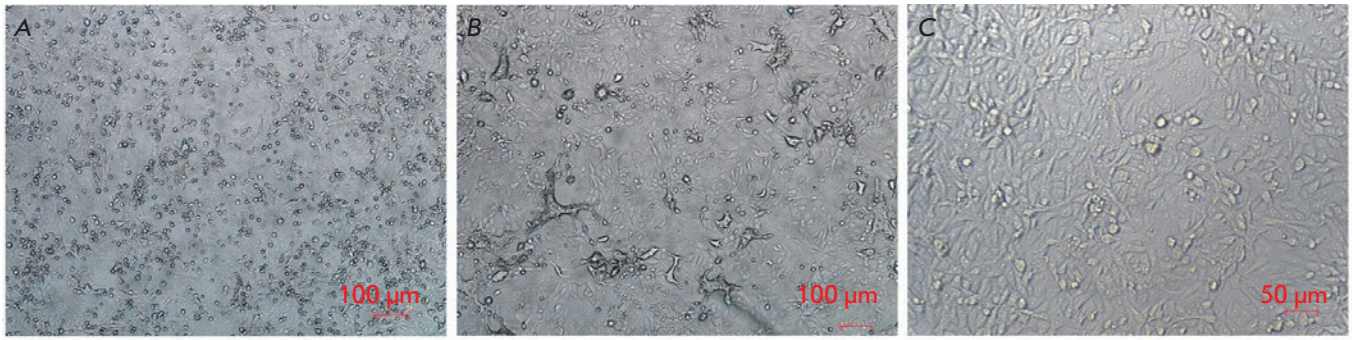

Fig. 2. The cytotoxic effect of the NDV/Altai/pigeon/770/2011 strain on a Vero cell culture, 7th passage on cells. *A* – cells infected on day 3 after incubation with the virus; *B* – cells infected on day 4 after incubation with the virus; *C* – syncytium formation in the infected cell culture on day 2 after incubation with the virus

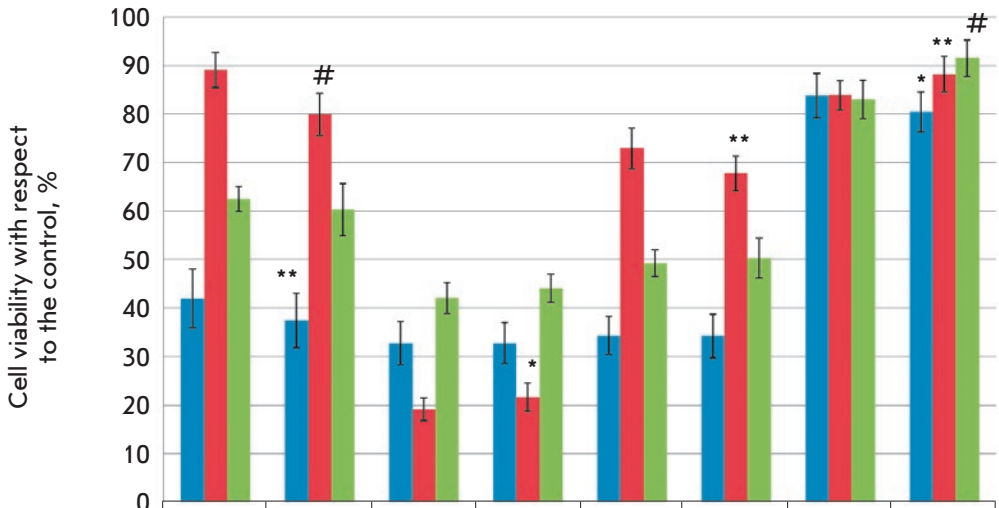

Virus	HCT116		HeLa		A549		MCF7	
	1 p	10 p	1 p	10 p	1 p	10 p	1 p	10 p
NDV/Altai/pigeon/770/2011	42.00	37.50	32.81	32.90	34.40	34.30	83.80	80.40
NDV/Altai/pigeon/777/2010	89.00	79.90	19.22	21.70	72.90	67.80	83.90	88.20
NDV/mallard/Amur/264/2009	62.45	60.30	42.14	44.12	49.20	50.30	83.00	91.50

Fig. 3. Comparative assessment of the viability of human tumor cell cultures depending on infection with NDV strains of the 1st (1 p) and 10th (10 p) passages in a Vero cell line. MTT assay, * $p = 0.05$; ** $p = 0.01$; # $p = 0.001$ (Student's t-test)

monolayer on days 3–4, in addition to the dead rounded cells (the standard manifestation of the cytotoxic effect). Syncytia-like structures appeared by the 7th–10th passages (on days 2–3), which are characteristic of CTE upon infection with paramyxoviruses (*Fig. 2*). Despite the difference in CTE in different passages, the maximum lesion of the monolayer amounted to about 90%, regardless of passage; the destructive changes were usually most pronounced on day 4 post-infection.

Syncytia formation, which is typical in cultivation of different paramyxoviruses, took place only in a few cases: the NDV/Altai/pigeon/770/2011 strain in the 7th passage in Vero cells (*Fig. 2B*) and the NDV/mallard/Amur/264/2009 strain in the 10th passage on days 2 and 3, respectively. Syncytia formation was not observed during primary passaging of these viruses in Vero cells.

No morphological changes in the monolayer were observed during passaging of the NDV/mallard/Amur/264/2009 and NDV/teal/Novosibirsk_region/320/2010 strains, except for a single case of syncytium formation in the monolayer.

The adapted mesogenic strains NDV/Altai/pigeon/770/2011, NDV/Altai/pigeon/777/2010, and lentogenic strain NDV/mallard/Amur/264/2009 in the 10th passage were used to perform a comparative evaluation of their anticancer properties against tumor cell lines (HCT116, HeLa, A549, and MCF7).

The multiplicity of infection of tumor cell lines was 8 HAU/10,000 cells. Cell survival after infection was assessed by MTT assay on day 4 (*Fig. 3*).

A comparison of the viability of tumor cell lines infected with viral strains of the 1st and 10th passages in

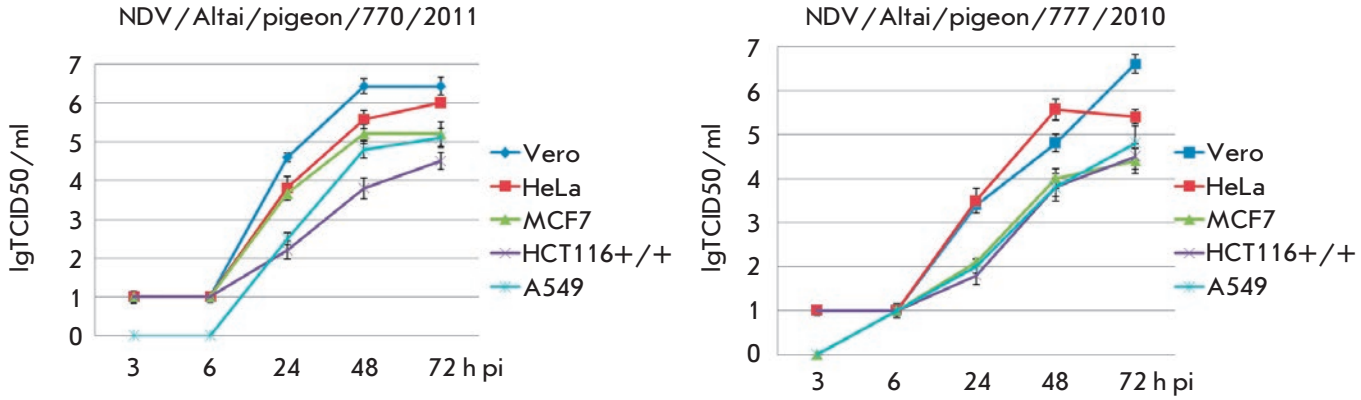

Fig. 4. The dynamics of the replicative activity of Newcastle disease virus strains in a Vero cell culture and human tumor cell cultures, h pi – hours post-infection

Table 3. The dynamics of titer changes for the NDV/Altai/pigeon/770/2011 strain during adaptation to tumor cell lines: mean relative value ± standard deviation

Tumor cell lines	Passage										
	1	2	3	4	5	6	7	8	9	10	11
HCT116	4.5± 0.33	4.6± 0.32	4.6± 0.47	4.6± 0.40	5.0± 0.60	5.4± 0.28	5.2± 0.39	5.6± 0.41	6.0± 0.14	6.4± 0.63	6.4± 0.56
HeLa	6.0± 0.54	5.8± 0.44	5.6± 0.61	5.8± 0.56	5.8± 0.36	5.4± 0.42	6.0± 0.55	6.0± 0.61	6.2± 0.21	6.8± 0.61	6.6± 0.78
A549	5.1± 0.58	5.4± 0.41	5.2± 0.37	5.6± 0.26	5.8± 0.33	5.8± 0.29	5.8± 0.34	5.8± 0.36	6.2± 0.36	6.0± 0.52	6.0± 0.45
MCF7	5.2± 0.43	5.2± 0.43	5.2± 0.51	5.0± 0.44	5.6± 0.49	5.8± 0.52	5.8± 0.55	5.8± 0.32	5.8± 0.26	5.8± 0.48	5.8± 0.36

Vero cells did not reveal any significant increase in the antitumor activity of NDV. The HCT116 cell line was an exception: infection with NDV/Altai/pigeon/770/2011 and NDV/Altai/pigeon/777/2010 of the 10th passage in Vero cells reduced the viability of this cell line by 5.0 and 9.9%, respectively.

In the next step of this study, the strains were adapted to each tumor cell line in order to check whether their antitumor potential increases upon adaptation to a specific tumor cell line or not.

The dynamics of the replication activity of mesogenic strains was determined for all tumor cell lines and for the Vero cell line as a positive control (*Fig. 4*). Titration of VCL of NDV/Altai/pigeon/770/2011 collected after 3, 6, 24, 48 and 72 h showed the dynamics of viral titer growth. The highest titer on day 3 was observed for Vero cells; the lowest titer, for the HCT116 cell line. Similar data were obtained for the NDV/Altai/pigeon/777/2010 strain. The lowest titer was obtained on the HCT116 and MCF 7 cell lines.

The NDV/Altai/pigeon/770/2011 and NDV/Altai/pigeon/777/2010 strains are similar in their characteristics and replication activity, so one strain, NDV/Altai/pigeon/770/2011, was selected for further study focused on virus adaptation to tumor cell lines with a view to increasing the oncolytic potential. This strain was cultured on tumor cell lines until the 11th passage as described above (*Table 3*, *Fig. 5*).

The titer increased after virus passage (passages 1–11) in the cell lines: in HCT116, by 1.9 lgTCID50/ml; in HeLa, by 0.6 lgTCID50/ml; in A549, by 0.9 lgTCID50/ml; and in MCF7, by 0.6 lgTCID50/ml. However, an increase in viral titer by almost two orders of magnitude was observed only in viral adaptation to HCT116 cells. The viability of tumor cell lines after infection with 10th passage strains decreased by 1.6, 4.1, and 6.0% in HCT116 HeLa, and A549 cells, respectively, and increased by 0.8% in MCF7 cells (*Fig. 6*).

A different technique might be required for the adaptation to tumor cells, which would include culturing in higher passages or passaging in the allantoic fluid of ECE and in its combination with ECE *in vitro*.

Therefore, there probably is no direct correlation between the dynamics of virus development in tumor

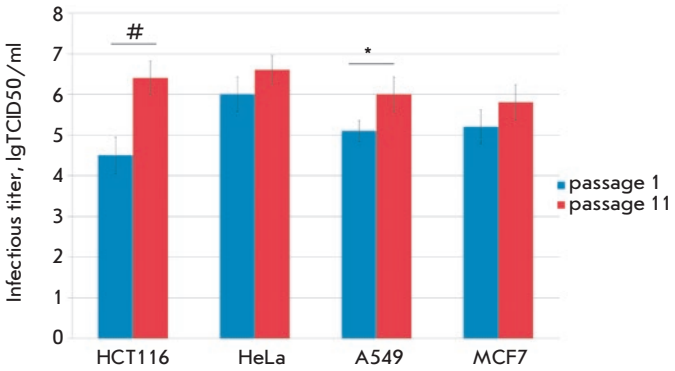

Fig. 5. The increasing infectious titers of Newcastle disease virus strains during adaptation to human tumor cell cultures, * $p = 0.05$; # $p = 0.001$ (Student's t-test)

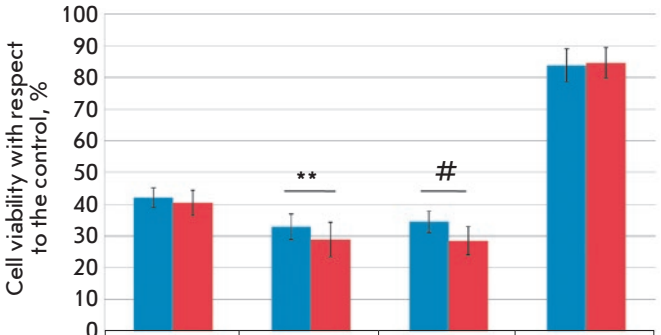

	HCT116	HeLa	A549	MCF7
1 p Vero	42.00	32.81	34.40	83.80
10 p TC	40.40	28.80	28.40	84.60

Fig. 6. Comparative assessment of the viability of human tumor cell cultures depending on infection with NDV/Altai/pigeon/770/2011 strain of the 1st passage (1 p) in Vero cells and 10th passage (10 p) in tumor cells (TC), MTT assay. ** $p = 0.01$; # $p = 0.001$ (Student's t-test)

cell lines and the effectiveness of antitumor action via direct oncolysis of these cells. This fact can be used to confirm the differences in the sensitivity of each specific cell line to the oncolytic activity of the virus. Thus, we managed to reduce the viability of HCT116 cells by 5 and 10% after they had been infected with the NDV/Altai/pigeon/770/2011 and NDV/Altai/pigeon/777/2010 strains, which were passaged in transplantable Vero cells. The HCT116 cell line is perhaps more sensitive to infection with adapted strains. We assume that this effect can be enhanced by longer passaging of strains (probably, in combination with passaging in the allantoic fluid of ECE).

CONCLUSION

Virus adaptation can be employed as a method to increase the infectious titer in order to subsequently use the virus as an antitumor agent exhibiting more pronounced oncolytic properties. The sensitive Vero cell line can be used to develop wild-type NDV strains. Adaptation of NDV strains to Vero cells (11 passages) statistically significantly increases the viral titer regardless of virulence and initial titer: the average infectious titer was increased by 0.8 and 1.1 lgTCID50/ml for mesogenic strains and by 0.7 and 1.4 lgTCID50/ml for lentogenic strains.

The viability of tumor cells sensitive to NDV in the 1st passage decreased after infection with the adapted strain NDV/Altai/pigeon/770/2011 in the 11th passage. MCF7 cells remained insusceptible to both NDV in the 1st and 11th passages. This result indicates that it is possible to enhance oncolytic properties by strains adaptation and optimization of the passaging procedure. ●

The reported study was funded by RFBR according to the research project № 18-34-00139.

REFERENCES

1. Buijs P.R., Verhagen J.H., van Eijck C.H., van den Hoogen B.G. // Hum. Vaccin. Immunother. 2015. V. 11. № 7. P. 1573–1584.
2. Schirrmacher V. // Expert Opin. Biol. Ther. 2015. V. 15. № 12. P. 1757–1771.
3. Biswas M., Kumar S.R., Allen A., Yong W., Nimmanapalli R., Samal S.K., Elankumaran S. // Viral Immunol. 2012. V. 25. № 4. P. 268–276.
4. Schirrmacher V. // Biomedicines. 2016. V. 4. № 3. P. pii: E16.
5. Schirrmacher V., Fournier P. // Methods Mol. Biol. 2009. V. 542. P. 565–605.
6. Ginting T.E., Suryatenggara J., Christian S., Mathew G. // Oncolytic Virother. 2017. V. 6. P. 21–30.
7. Chen N., Bellone C.J., Schriewer J., Owens G., Fredrickson T., Parker S., Buller R.M. // Virology. 2011. V. 409. № 2. P. 328–337.
8. Lee P., Knight R., Smit J.M., Wilschut J., Griffin D.E. // J. Virol. 2002. V. 76. № 12. P. 6302–6310.
9. PDQ Integrative, Alternative, and Complementary Therapies Editorial Board. Newcastle Disease Virus (PDQ®): Health Professional Version. 2018 Aug 22. In: PDQ Cancer Information Summaries [Internet]. Bethesda (MD): National Cancer Institute (US); 2002-. Available from: https://www.ncbi.nlm.nih.gov/books/NBK65752/
10. Lam H.Y., Yeap S.K., Rasoli M., Omar A.R., Yusoff K., Suraini A.A., Alitheen N.B. // J. Biomed. Biotechnol. 2011. V. 2011. P. 718710.

11. Ghrici M., El Zowalaty M., Omar A.R., Ideris A. // Int. J. Mol. Med. 2013. V. 31. № 3. P. 525–532.
12. Bian J., Wang K., Kong X., Liu H., Chen F., Hu M., Zhang X., Jiao X., Ge B., Wu Y., Meng S. // Arch. Virol. 2011. V. 156. № 8. P. 1335–1344.
13. Pecora A.L., Rizvi N., Cohen G.I., Meropol N.J., Sterman D., Marshall J.L., Goldberg S., Gross P., O'Neil J.D., Groene W.S., et al. // J. Clin. Oncol. 2002. V. 20. № 9. P. 2251–2266.
14. Csatary L.K., Bakács T. // JAMA. 1999. V. 281. № 17. P. 1588–1589.
15. Apostolidis L., Schirrmacher V., Fournier P. // Int. J. Oncol. 2007. V. 31. № 5. P. 1009–1019.
16. Reichard K.W., Lorence R.M., Cascino C.J., Peeples M.E., Walter R.J., Fernando M.B., Reyes H.M., Greager J.A. // J. Surg. Res. 1992. V. 52. № 5. P. 448–453.
17. Lorence R.M., Katubig B.B., Reichard K.W., Reyes H.M., Phuangsab A., Sassetti M.D., Walter R.J., Peeples M.E. // Cancer Res. 1994. V. 54. № 23. P. 6017–6021.
18. Yurchenko K.S., Zhou P., Kovner A.V., Zavjalov E.L., Shestopalova L.V., Shestopalov A.M. // PLoS One. 2018. V. 13. № 4. P. e0195425.
19. Moore A.E. // Ann. N.Y. Acad. Sci. 1952. V. 54. № 6. P. 945–952.
20. Ahamed T., Hossain K.M., Billah M.M., Islam K.M.D., Ahasan M.M., Islam M.E. // Int. J. Poult. Sci. 2004. V. 3. № 2. P. 153–156.
21. Visnuvinayagam S., Thangavel K., Lalitha N., Malmarugan S., Sukumar K. // Braz. J. Microbiol. 2015. V. 46. № 3. P. 861–865.
22. Kumar R., Tiwari A.K., Chaturvedi U., Kumar G.R., Sahoo A.P., Rajmani R.S., Saxena L., Saxena S., Tiwari S., Kumar S. // Appl. Biochem. Biotechnol. 2012. V. 167. № 7. P. 2005–2022.
23. Flanagan A.D., Love R., Tesar W. // Proc. Soc. Exper. Bid. Med. 1955. V. 90. № 1. P. 82–86.
24. Cassel W.A., Garrett R.E. // Cancer. 1965. V. 18. P. 863–868.
25. Cassel W.A., Murray D.R., Torbin A.H., Olkowski Z.L., Moore M.E. // Cancer. 1977. V. 40. № 2. P. 672–679.
26. Yurchenko K.S., Sivay M.V., Glushchenko A.V., Alkhovsky S.V., Shchetinin A.M., Shchelkanov M.Y., Shestopalov A.M. // Genome Announ. 2015. V. 3. № 1. P. e01514-14.
27. Kabilov M.R., Alikina T.Y., Yurchenko K.S., Glushchenko A.V., Gunbin K.V., Shestopalov A.M., Gubanova N.V. // Genome Announ. 2016. V. 4. № 6. pii: e01348-16.
28. World Health Organization. Global Influenza Surveillance Network. Manual for the laboratory diagnosis and virological surveillance of influenza. 2011. http://apps.who.int/iris/bitstream/handle/10665/44518/9789241548090_eng.pdf.
29. World Health Organization. Virus titration and determination of tissue culture infectious dose (TCID50) for microneutralization assay. 2013. http://www.who.int/influenza/gisrs_laboratory/cnic_serological_diagnosis_microneutralization_a_h7n9.pdf.
30. Ashmarin I.P., Vorobiev A.A. Statistical methods in microbiological studies. Leningrad: Medgiz, Leningrad branch, 1962. 180 p.

CASBench: A Benchmarking Set of Proteins with Annotated Catalytic and Allosteric Sites in Their Structures

A. Zlobin, D. Suplatov, K. Kopylov, V. Švedas*
Lomonosov Moscow State University, Belozersky Institute of Physicochemical Biology and Faculty of Bioengineering and Bioinformatics, Lenin hills 1, bldg. 73, 119991, Moscow, Russia
*E-mail: vytas@belozersky.msu.ru
Received November 06, 2017; in final form December 13, 2017

ABSTRACT **In recent years, the phenomenon of allostery has witnessed growing attention driven by a fundamental interest in new ways to regulate the functional properties of proteins, as well as the prospects of using allosteric sites as targets to design novel drugs with lower toxicity due to a higher selectivity of binding and specificity of the mechanism of action. The currently available bioinformatic methods can sometimes correctly detect previously unknown ligand binding sites in protein structures. However, the development of universal and more efficient approaches requires a deeper understanding of the common and distinctive features of the structural organization of both functional (catalytic) and allosteric sites, the evolution of their amino acid sequences in respective protein families, and allosteric communication pathways. The CASBench benchmark set contains 91 entries related to enzymes with both catalytic and allosteric sites within their structures annotated based on the experimental information from the Allosteric Database, Catalytic Site Atlas, and Protein Data Bank. The obtained dataset can be used to benchmark the performance of existing computational approaches and develop/train perspective algorithms to search for new catalytic and regulatory sites, as well as to study the mechanisms of protein regulation on a large collection of allosteric enzymes. Establishing a relationship between the structure, function, and regulation is expected to improve our understanding of the mechanisms of action of enzymes and open up new prospects for discovering new drugs and designing more efficient biocatalysts. The CASBench can be operated offline on a local computer or online using built-in interactive tools at https://biokinet.belozersky.msu.ru/casbench.**
KEYWORDS **ligand binding sites, catalytic site; allosteric site, benchmarking set, protein function and regulation, structure-function relationship, bioinformatics, web server.**
ABBREVIATIONS **ASD – Allosteric Database; CASBench – Catalytic and Allosteric Sites Benchmark set; CSA – Catalytic Site Atlas; HTML5 – HyperText Markup Language version 5; PDB – Protein Data Bank; PSE – Pymol Session (binary file format).**

INTRODUCTION

Allostery is a mechanism by which the activity of proteins is regulated due to binding of a ligand or other protein in a special site on the surface [1]. Fifty years ago, when the classical models for cooperativity binding were proposed based on the first known cases of allostery, this phenomenon was considered an exclusive feature of multi-subunit proteins functioning at the level of the quaternary structure [2, 3]. Recent studies have provided a large body of evidence for allostery in proteins having different structures and functions, including small monomeric proteins. It has become clear that allostery is not an exclusive property of sophisticated multi-subunit complexes, but rather a widespread phenomenon that plays a key role in the regulation of many biological processes [4–8]. Computational biology methods were applied to study allostery in an attempt to understand the relationship between function and regulation [6, 9]. Bioinformatic analysis showed that the amino acid sequence of regulatory sites is less conserved and more variable compared to that in catalytic sites [10]. The catalytic and allosteric sites are saturated by the so-called specific positions that are conserved only within functional subfamilies but differ between them and can define the functional diversity of homologs within one superfamily (e.g., they can be responsible for varying specificity to substrates and regulatory ligands) [11–13].

Analysis of correlated substitutions in the amino acid sequences of topologically independent but functionally coupled sites on the surface of evolutionary related proteins is increasingly being used to study the molecular mechanisms of allostery [9, 14]. It was shown that such correlating/co-evolving positions can form a network of interacting residues located between the catalytic and regulatory sites in a protein structure, which provides communication between them due to the sequential conformational changes initiated by the binding of a regulatory agent [15, 16]. Co-evolution between positions located in different binding sites at a considerable distance from each other was described (e.g., in the bacterial transcription factors belonging to the LacI family [17]). Spatially proximal co-evolving residue pairs, as well as long-range correlations, can potentially be used to annotate new binding sites and study the molecular mechanisms of allosteric communication [18].

The current understanding is that the protein structure exists in equilibrium between a set of conformers, and this balance can change as a result of the binding of almost any substance to the surface of the globule; the question is only how efficient this shift is and how it affects the protein function [19–22]. This effectively means that allostery can present a universal phenomenon that applies to the majority of existing proteins. The anticipation of the discovery of a new regulatory mechanism in proteins currently considered as non-allosteric has generated intense attention to the field, driven by a fundamental interest in establishing new ways of regulating proteins/enzymes, and the prospects for creating novel allosteric drugs having a lower toxicity due to higher binding selectivity [4, 23–26]. In recent years, a number of computational methods have been developed to search for new regulatory sites in protein structures, as well as complementary selective ligands that can influence the functional activity upon binding to the biopolymer [9]: using geometric [27–30], energy-based [31, 32] or bioinformatic criteria [13, 33–35], training sets of experimentally annotated sites [36, 37], and high-throughput virtual screening procedures [38, 39]. The currently available computer programs usually predict multiple sites in the structure of a selected protein (tens or even hundreds, depending on the globule size and the selected parameters). The functional importance of the detected pockets is then estimated by ranking them according to a chosen evaluation function (e.g., according to the occurrence of statistically significant conserved [34, 35] or specific positions [13]). The currently available bioinformatic methods can sometimes correctly detect previously unknown ligand binding sites in protein structures, but it is clear that the efficiency of the available software for allosteric site prediction remains very limited and that new universal computational approaches are needed to proceed from individual case studies towards a wider solution to this problem. We can also note the common limitation of the known search algorithms: they do not take into account the differences between the functional (catalytic) and regulatory (allosteric) sites and, therefore, are unable to discriminate between sites of different types. To elaborate more efficient strategies, it is necessary to systematically study the common patterns, as well as the distinctive features of structural organization of sites of different types and the evolution of their amino acid sequences in families of homologous proteins.

The first attempt to summarize the accumulated experimental information on allosteric sites was the ASD database, which contains almost two thousand entries [40]. The ASD database is an important resource on allosteric proteins but contains redundant (duplicated) data and low-quality annotations; so, only a small part of this collection can be used in practice to study allostery and train/evaluate new algorithms (235 entries [41]). In addition, annotation of functional (catalytic) sites is not provided in the ASD database: this information is presented in the separate CSA database [42]. The CSA database relies on experimental findings for one thousand enzymes. The bioinformatics methods are used to annotate conserved catalytic residues in the closest homologs with a known structure, thus expanding the database to dozens of thousands of entries. The combined use of experimental information on known catalytic and allosteric sites in the structures of proteins/enzymes can help in the study of the relationship between the structure, function, and regulation, but certain issues regarding data management and the format of entries in the ASD and CSA databases make their joint use a challenging task.

Here, we report on the CASBench set of enzymes with catalytic and allosteric binding sites, with their structures annotated according to the experimental data in the ASD, CSA, and PDB public databases. The CASBench can be used as a benchmarking set to evaluate the efficiency of existing methods and to develop new, promising algorithms to search for functional and regulatory sites in protein structures. The availability of annotations for both sites in each protein provides an opportunity to study the organization of sites of different types and to train computer algorithms to recognize them. The CASBench can be operated offline on a local computer or online using built-in interactive tools.

METHODS

Collection of the CASBench set

The latest versions of three public databases (annotations of allosteric sites in the ASD, annotations of catalytic sites in the CSA, and structural information contained in the PDB database) were analyzed by the original Python 3 software using the BioPython package [43], as well as the numpy and ProDy libraries. The protocol employed to collect the CASBench dataset contained four key steps: (1) numbering of allosteric site residues in the ASD was synchronized with the numbering of amino acid residues in the corresponding representative PDB structures; (2) for each protein in the ASD, all its structures in the PDB were retrieved; (3) the ASD entries were compared to the CSA entries to identify proteins deposited in both databases; and (4) annotations of catalytic and allosteric sites in the ASD and CSA databases were refined using information about the presence of ligands in all collected PDB structures of crystallographic complexes and taking into account the quaternary structure of each protein (when available).

At the first step, annotations of allosteric sites in the ASD were synchronized with the corresponding PDB entries regarding the numbering of amino acid residues. The primary difficulty in working with the ASD is the ambiguous numbering of amino acid residues that are part of a regulatory site; i.e., it may fail to match the numbering in the PDB and/or Uniprot, and can even be represented by only a keyword (e.g., DFG motif), which in some cases prevents conclusive identification of the site in a protein structure. If the numbering of amino acid residues in the ASD annotation failed to match the numbering in the PDB or UniProt, it was automatically corrected by considering all possible locations of the amino acid residues of the site in question in the sequence of each corresponding PDB chain, with allowance for potential substitutions, deletions, or insertions. All entries in the ASD whose automatic synchronization had failed (i.e., it was not possible to conclusively identify the allosteric site in the PDB structure given the ASD numbering) were removed from analysis. At the second step, for each protein in the ASD, all of its structures currently available in the PDB were collected. The amino acid sequences of all proteins presented in the PDB were clustered at a 95% sequence similarity level using the CD-HIT program [44] (i.e., the PDB95 set). All members of a cluster that contained a representative PDB-structure were included in the corresponding ASD entry for further analysis. The quaternary structure of each protein (if any) was restored according to the corresponding BIOMT records. At the third stage, the ASD and CSA databases were compared. Annotations of catalytic sites in CSA for the proteins with at least 95% sequence similarity were merged into one entry. Proteins that were present in the ASD but not in the CSA (i.e., none of the PDB structures retrieved at the previous stage was annotated in the CSA) were excluded from further consideration. At the final step of the protocol, the primary annotations of catalytic and allosteric sites in proteins were refined as follows: Sites in the ASD and CSA databases can be represented by only a few residues whose role in function or regulation has been confirmed experimentally (e.g., the key catalytically important amino acids studied by site-directed mutagenesis), which gives no information about the dimensions and boundaries of the corresponding binding sites. All the available experimental information from the crystallographic complexes of proteins with ligands was used to refine these primary annotations. For each protein present in both the ASD and CSA databases, the collected information on all its structures in the PDB was used to select ligands bound to corresponding sites within 5 Å of any amino acid residue included in the primary annotation. Then, this primary annotation of catalytic and allosteric sites from the ASD and CSA databases was supplemented with the secondary annotation obtained by analyzing the available crystallographic complexes. In each structure, all residues located within 5 Å of the selected ligand were considered and the resulting secondary annotations of each site were merged for all the PDB structures of the protein. The collected CASBench set contained 91 enzymes.

Construction of multiple alignments of protein families

Unique chains of each protein in the CASBench were used as queries to construct multiple alignments of the corresponding families using the Mustguseal method [45]. For each query, protein sequence similarity search versus the UniProtKB database was used to collect at most 5,000 homologs for further analysis [46]. The resulting sets were filtered to exclude the too similar and too distant proteins. Sequences were dismissed if their length differed by more than 20% from the query to exclude incomplete entries and prevent the formation of columns with an excess of gaps in the final alignment. The CD-HIT algorithm [44] was then used to cluster proteins at a sequence similarity threshold of 95%. One representative sequence was automatically selected from each cluster, and the remaining proteins were dismissed from further consideration. Finally, proteins that differed significantly in their amino acid sequence from the query (shared less than 0.25 bits per column) and, therefore, could have caused align-

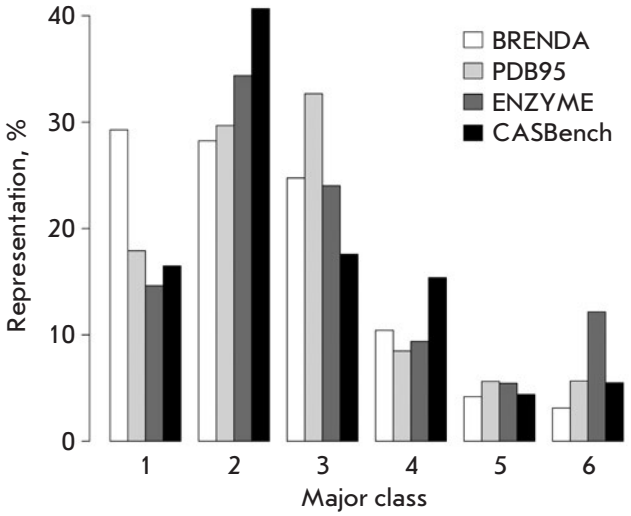

Fig. 1. Distributions of the six major enzyme classes according to the EC classification in the BRENDA database, 95%-non-redundant set of proteins in the PDB (PDB95), the ENZYME database, and the CASBench benchmarking set. Information from the BRENDA database was obtained using the SOAP web service (https://www.brenda-enzymes.org/soap.php). The protocol for preparing the PDB95 set is described in Methods. Clusters within the PDB95, which included different chains of the same protein, were combined, and all the major EC classes provided in the PDB annotations were counted once for each obtained cluster. Information on the representation of enzymes in the ENZYME database was taken from [10]

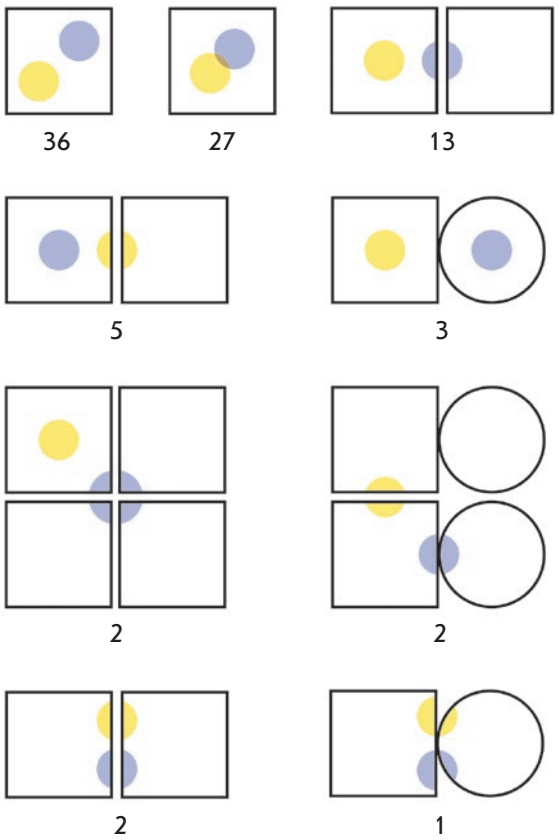

Fig. 2. Topological classification of catalytic (yellow) and allosteric (blue) sites in the structures of enzymes presented in CASBench. The number of entries in the CASBench with each topology is shown. Identical chains of multimeric proteins are shown as squares; different chains, as squares and circles

ment errors were removed [47, 48]. Multiple sequence alignments of the obtained representative collections of each family were finally constructed using the MAFFT algorithm [49].

RESULTS AND DISCUSSION

The CASBench benchmarking set contains 91 entries of enzymes with annotated catalytic and allosteric binding sites based on the information retrieved from the ASD and CSA databases and the results of the analysis of all crystallographic complexes with ligands in the respective sites. The CASBench includes enzymes of all major functional EC classes, which are presented in proportion to their occurrence in other databases (*Fig. 1*). Topological analysis showed that the CASBench contains proteins with different three-dimensional organizations; the catalytic and allosteric sites can be arranged in a variety of ways relative to each other (*Fig. 2*). In 70% of cases, the annotations describe monomeric proteins consisting of only one chain, and 30% of the entries correspond to multi-chain proteins consisting of several identical or unique subunits. In 5% of entries, both sites are formed within the intersubunit contact; in 22% of cases, only one site is located between the subunits and 73% of entries correspond to both sites being formed within the subunits. In all the CASBench annotations, different sites are topologically independent from each other (i.e., they are represented by separate cavities in the enzyme structure). In 30% of cases, the catalytic and allosteric sites either overlap or share a common border; in 70% of entries, both sites reside at a considerable distance from each other and do not overlap within the structure.

A CASBench entry for each listed protein has an identifier written as CAS0001 (CAS0002, CAS0003, etc.) and contains annotation of all sites, as well as associated ligands in all available crystallographic

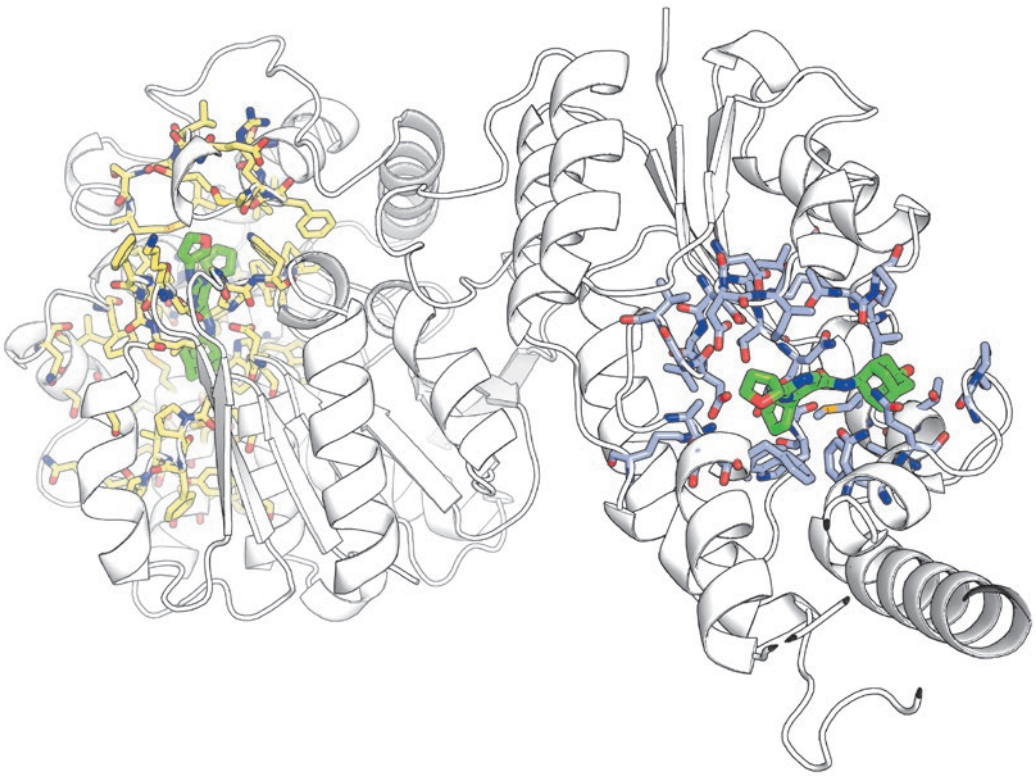

Fig. 3. An example of a CASBench annotation. The catalytic (yellow) and allosteric (blue) sites are annotated in the structure of epoxide hydrolase from *Spodoptera frugiperda*; all the amino acid residues directly involved in the accommodation of ligands in the corresponding crystallographic complexes are shown. The crystallographic ligands are shown in green. The illustration was prepared using the structural annotation file in PSE format included in the CASBench distribution for entry CAS0002 (PDB code 5ALU)

structures from the PDB database. The information is available as binary files in the PSE format for the PyMOL Molecular Graphics System (which can be used for visual expert analysis) and text files intended for automated processing. It should be noted that the original annotations of catalytic and allosteric sites in the ASD and CSA databases can consist of only several residues whose role in the protein function and regulation was verified experimentally. An important feature of the CASBench dataset is that the annotations of sites from the ASD and CSA databases are refined using the information from the crystallographic complexes of proteins with ligands. All residues directly interacting with ligands are shown in the benchmark set, which seems more convenient for further analysis and provides clear understanding of the size and boundaries of the binding sites (*Fig. 3*). For each CASBench entry, multiple alignments of a representative set of a corresponding protein family are also available in the FASTA format, which can be useful when testing algorithms that employ bioinformatic analysis to search for and/or rank ligand binding sites in protein structures (e.g., pocketZebra [13] and the like). All the data available in the CASBench can be operated offline on a local computer or online using built-in interactive tools. The web version of CASBench can be browsed via a single list of all available entries, or by searching by the protein PDB ID or keywords contained in the PDB annotation. Each CASBench entry is presented on a separate web page that contains information on all available PDB structures of the corresponding protein, annotated sites, and associated ligands. The annotated catalytic and allosteric sites can be visualized on the 3D structure or amino acid sequence of the selected protein using the built-in interactive tools (JSMol [50] and Strap [51], respectively). Online interactivity is implemented in HTML5 and requires neither plug-ins nor Java on the user's computer.

CONCLUSIONS

The trend in recent years has been increasing attention to allosteric regulation of the functional properties of proteins/enzymes and the search for complementary modulators as prototypes of novel drugs with lower toxicity thanks to a higher binding selectivity. Despite the growing interest in studying the relationship between the structure, function, and regulation, and in elaborating methods to search for new regulatory sites in protein structures, many questions are still to be answered. Therefore, further research into the field is required. In this paper, the CASBench benchmarking set was proposed, containing all enzymes with the catalytic and allosteric sites in their structures experimentally annotated based on the ASD, CSA, and PDB databases.

The obtained set can be used to evaluate the efficiency of the existing methods and to develop/train prospective algorithms to search for new sites in protein structures, as well as to study the mechanisms of allosteric communication between topologically independent sites in a large collection of enzyme families. Establishing a relationship between structure, function, and regulation is expected to improve our understanding of the mechanisms of action of enzymes and open up new prospects for creating new drugs and designing more efficient biocatalysts. ●

This work was supported by the Russian Science Foundation (grant no. 15-14-00069). The research was carried out using the equipment of the shared research facilities of high-performance computing resources at Lomonosov Moscow State University [52].

REFERENCES

1. Laskowski R.A., Gerick F., Thornton J.M. // FEBS Lett. 2009. V. 583. № 11. P. 1692–1698.
2. Monod J., Wyman J., Changeux J.P. // J. Mol. Biol. 1965. V. 12. № 1. P. 88–118.
3. Koshland D.E., Nemethy G., Filmer D. // Biochemistry. 1966. V. 5. № 1. P. 365–385.
4. Nussinov R., Tsai C.J. // Cell. 2013. V. 153. № 2. P. 293–305.
5. Cui Q., Karplus M. // Protein Sci. 2008. V. 17. № 8. P. 1295–1307.
6. Goodey N.M., Benkovic S.J. // Nat. Chem. Biol. 2008. V. 4. № 8. P. 474–482.
7. Arkin M.R., Wells J.A. // Nat. Rev. Drug Discov. 2004. V. 3. № 4. P. 301–317.
8. Hardy J.A., Wells J.A. // Curr. Opin. Struct. Biol. 2004. V. 14. № 6. P. 706–715.
9. Suplatov D., Švedas V. // Acta Naturae. 2015. Vol. 7. N. 4. P. 34–45.
10. Yang J.S., Seo S.W., Jang S., Jung G.Y., Kim S. // PLoS Comput Biol. 2012. V. 8. № 7. P. e1002612.
11. Suplatov D., Shalaeva D., Kirilin E., Arzhanik V., Švedas V. // J. Biomol. Struct. Dyn. 2014. V. 32. № 1. P. 75–87.
12. Suplatov D., Kirilin E., Takhaveev V., Švedas V. // J. Biomol. Struct. Dyn. 2014. V. 32. № 11. P. 1752–1758.
13. Suplatov D., Kirilin E., Arbatsky M., Takhaveev V., Švedas V. // Nucl. Acids Res. 2014. V. 42. № W1. P. W344–W349.
14. de Oliveira S., Deane C. // F1000 Research. 2017. V. 6. P. 1224.
15. Anishchenko I., Ovchinnikov S., Kamisetty H., Baker D. // Proc. Natl. Acad. Sci. USA. 2017. V. 114. № 34. P. 9122–9127.
16. Reynolds K.A., McLaughlin R.N., Ranganathan R. // Cell. 2011. V. 147. № 7. P. 1564–1575.
17. Raman S., Taylor N., Genuth N., Fields S., Church G.M. // Trends Genet. 2014. V. 30. № 12. P. 521–528.
18. Suplatov D.A., Sharapova Ya.A., Timonina D.S., Kopylov K.E., Švedas V. // J. Bioinform. Comput. Biol. 2018. V. 16. № 2. P. 1840005.
19. Gunasekaran K., Ma B., Nussinov R. // Proteins. 2004. V. 57. № 3. P. 433–443.
20. Chennubhotla C., Yang Z., Bahar I. // Mol. Biosyst. 2008. V. 4. № 4. P. 287–292.
21. Hilser V.J., Thompson E.B. // Proc. Natl. Acad. Sci. USA. 2007. V. 104. № 20. P. 8311–8315.
22. Popovych N., Sun S., Ebright R.H., Kalodimos C.G. // Nat. Struct. Mol. Biol. 2006. V. 13. № 9. P. 831–838.
23. Wenthur C.J., Gentry P.R., Mathews T.P., Lindsley C.W. // Annu. Rev. Pharmacol. Toxicol. 2014. V. 54. P. 165–184.
24. Lu S., Li S., Zhang J. // Med. Res. Rev. 2014. V. 34. № 6. P. 1242–1285.
25. Eglen R., Reisine T. // Pharmacol. Ther. 2011. V. 130. № 2. P. 144–156.
26. Nussinov R., Tsai C.J., Csermely P. // Trends Pharmacol. Sci. 2011. V. 32. № 12. P. 686–693.
27. Yu J., Zhou Y., Tanaka I., Yao M. // Bioinformatics. 2010. V. 26. № 1. P. 46–52.
28. Le Guilloux V., Schmidtke P., Tuffery P. // BMC Bioinformatics. 2009. V. 10. № 1. P. 168.
29. Yaffe E., Fishelovitch D., Wolfson H.J., Halperin D., Nussinov R. // Nucl. Acids Res. 2008. V. 36. № suppl 2. P. W210–W215.
30. Weisel M., Proschak E., Schneider G. // Chem. Cent. J. 2007. V. 1. № 7. P. 1–17.
31. Hernandez M., Ghersi D., Sanchez R. // Nucl. Acids Res. 2009. V. 37. № suppl 2. P. W413–W416.
32. Laurie A.T.R., Jackson R.M. // Bioinformatics. 2005. V. 21. № 9. P. 1908–1916.
33. Saroj Devi N., Shanmugam R., Ghorai J., Ramanan M., Anbarasan P., Doble M. // Mol. Inform. 2017. V. 36. P. 1700073.
34. Kalinina O.V., Gelfand M.S., Russell R.B. // BMC Bioinformatics. 2009. V. 10. № 1. P. 174.
35. Huang B., Schroeder M. // BMC Struct. Biol. 2006. V. 6. № 1. P. 19.
36. Huang W., Lu S., Huang Z., Liu X., Mou L., Luo Y., Zhao Y., Liu Y., Chen Z., Hou T., Zhang J. // Bioinformatics. 2013. V. 29. № 18. P. 2357–2359.
37. Volkamer A., Kuhn D., Grombacher T., Rippmann F., Rarey M. // J. Chem. Inf. Model. 2012. V. 52. № 2. P. 360–372.
38. Gushchina I.V., Nilov D.K., Zakharenko A.L., Lavrik O.I., Švedas V.K. // Acta Naturae. 2017. V. 9. N. 2. P. 59–66.
39. Suplatov D., Popova N., Zhumatiy S., Voevodin V., Švedas V. // J. Bioinform. Comput. Biol. 2016. V. 14. № 2. P. 1641008.
40. Huang Z., Zhu L., Cao Y., Wu G., Liu X., Chen Y., Wang Q., Shi T., Zhao Y., Wang Y., et al. // Nucl. Acids Res. 2011. V. 39. № suppl 1. P. D663–D669.
41. Huang W., Wang G., Shen Q., Liu X., Lu S., Geng L., Huang Z., Zhang J. // Bioinformatics. 2015. V. 31. № 15. P. 2598–2600.
42. Furnham N., Holliday G.L., de Beer T.A., Jacobsen J.O., Pearson W.R., Thornton J.M. // Nucl. Acids Res. 2014. V. 42. № D1. P. D485–D489.
43. Cock P.J.A., Antao T., Chang J.T., Chapman B.A., Cox C.J., Dalke A., Friedberg I., Hamelryck T., Kauff F., Wilczynski B., De Hoon M.J. // Bioinformatics. 2009. V. 25. № 11. P. 1422–1423.
44. Fu L., Niu B., Zhu Z., Wu S., Li W. // Bioinformatics. 2012. V. 28. № 23. P. 3150–3152.
45. Suplatov D., Kopylov K., Popova N., Voevodin V., Švedas V. // Bioinformatics. 2018. V. 34. № 9. P. 1583–1585.

46. Vouzis P.D., Sahinidis N.V. // Bioinformatics. 2010. V. 27. № 2. P. 182–188.
47. Fischer J.D., Mayer C.E., Söding J. // Bioinformatics. 2008. V. 24. № 5. P. 613–620.
48. Söding J., Biegert A., Lupas A.N. // Nucl. Acids Res. 2005. V. 33. № S2. P. W244–W248.
49. Katoh K., Standley D.M. // Mol. Biol. Evol. 2013. V. 30. № 4. P. 772–780.
50. Hanson R.M., Prilusky J., Renjian Z., Nakane T., Sussman J.L. // Isr. J. Chem. 2013. V. 53. № 3–4. P. 207–216.
51. Gille C., Fähling M., Weyand B., Wieland T., Gille A. // Nucl. Acids Res. 2014. V. 42. № W1. P. W3–W6.
52. Sadovnichy V., Tikhonravov A., Voevodin Vl., Opanasenko V. Contemp. High Perform. Comput. Petascale Exascale. Boca Raton, USA, 2013. P. 283–307.

Mauritian Endemic Medicinal Plant Extracts Induce G2/M Phase Cell Cycle Arrest and Growth Inhibition of Oesophageal Squamous Cell Carcinoma *in Vitro*

N. Rummun[1,2,3], R. E. Hughes[4], R. Beesoo[1,2,4,5], W. W. Li[3], O. Aldulaimi[3], K. G. Macleod[4], T. Bahorun[2], N. O. Carragher[4**], A. Kagansky[4,6***], V. S. Neergheen-Bhujun[1,2*]

[1]Department of Health Sciences, Faculty of Science, University of Mauritius, Réduit, 80837, Republic of Mauritius

[2]ANDI Centre of Excellence for Biomedical and Biomaterials Research, MSIRI Building, University of Mauritius, Réduit, 80837, Republic of Mauritius

[3]Guy Hilton Research Centre, Institute for Science and Technology in Medicine, Faculty of Medicine and Health Sciences, ST5 5BG, Keele University, UK

[4]Cancer Research UK Edinburgh Centre, MRC Institute of Genetics and Molecular Medicine, Western General Hospital, University of Edinburgh, Edinburgh, EH4 2XU, United Kingdom

[5]Department of Biosciences and Ocean Sciences, Faculty of Science, University of Mauritius, Réduit, 80837, Republic of Mauritius

[6]Centre for Genomic and Regenerative Medicine, School of Biomedicine, Far Eastern Federal University, 690091, Vladivostok, Russia

*E-mail: v.neergheen@uom.ac.mu, **E-mail: N.Carragher@ed.ac.uk, ***E-mail: kagasha@yahoo.com

Received December 10, 2018; in final form, February 25, 2019

ABSTRACT **Terrestrial plants have contributed massively to the development of modern oncologic drugs. Despite the wide acceptance of Mauritian endemic flowering plants in traditional medicine, scientific evidence of their chemotherapeutic potential is lacking. This study aimed to evaluate the *in vitro* tumor cytotoxicity of leaf extracts from five Mauritian endemic medicinal plants, namely *Acalypha integrifolia* Willd (Euphorbiaceae), *Labourdonnaisia glauca* Bojer (Sapotaceae), *Dombeya acutangula* Cav. subsp. *rosea* Friedmann (Malvaceae), *Gaertnera psychotrioides* (DC.) Baker (Rubiaceae), and *Eugenia tinifolia* Lam (Myrtaceae). The cytotoxicities of the extracts were determined against six human cancer cell lines, including cervical adenocarcinoma, colorectal carcinoma, oesophageal adenocarcinoma, and oesophageal squamous cell carcinoma. The potent extracts were further investigated using cell cycle analysis and reverse phase protein array (RPPA) analysis. The antioxidant properties and polyphenolic profile of the potent extracts were also evaluated. Gas chromatography mass spectrometry (GC-MS) analyses revealed the presence of (+)-catechin and gallocatechin in *E. tinifolia* and *L. glauca*, while gallic acid was detected in *A. integrifolia*. *L. glauca*, *A. integrifolia*, and *E. tinifolia* were highly selective towards human oesophageal squamous cell carcinoma (KYSE-30) cells. *L. glauca* and *E. tinifolia* arrested KYSE-30 cells in the G2/M phase, in a concentration-dependent manner. RPPA analysis indicated that the extracts may partly exert their tumor growth-inhibitory activity by upregulating the intracellular level of 5'AMP-activated kinase (AMPK). The findings highlight the potent antiproliferative activity of three Mauritian endemic leaf extracts against oesophageal squamous cell carcinoma and calls for further investigation into their chemotherapeutic application.**

KEYWORDS **Mauritian endemic, medicinal plant, oesophageal carcinoma, tumor cytotoxicity, AMPK,**

ABBREVIATIONS **AMPK – 5'AMP-activated kinase; CCE – cyanidin chloride equivalent; DPPH – 2-2 diphenyl-1-picrylhydrazyl; EDTA – ethylenediaminetetraacetic acid; FRAP – ferric reducing antioxidant power; GAE – gallic acid equivalent; GC-MS – gas chromatography coupled to mass spectrometry; HPLC – high-performance liquid chromatography; LW – lyophilized weight; mTORC1 – mammalian target of rapamycin complex 1; OC – oesophageal cancer; QE – quercetin equivalent; RFI – relative fluorescence intensity; RPPA – reverse phase protein array; TFC – total flavonoid content; TMSi – trimethylsilylimidazole; TPC – total phenolic content; TPrC – total proanthocyanidin content.**

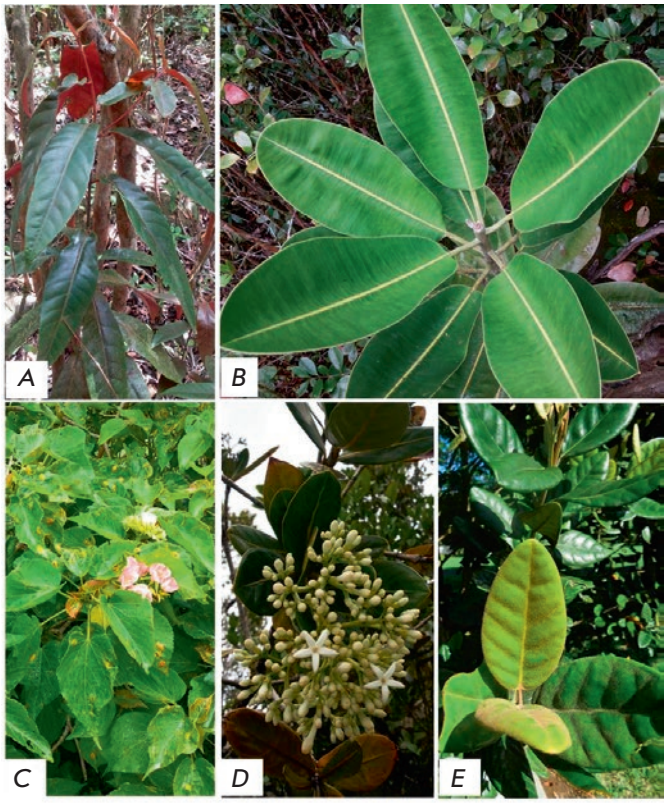

Fig. 1. The Mauritian endemic medicinal plants under study. The Mauritius herbarium voucher specimen barcode number is given in brackets ( ). *A* – *A. integrifolia* (MAU 0016402); *B* – *L. glauca* (MAU 0016430); *C* – *D. acutangula* (MAU 0016638); *D* – *G. psychotrioides* (MAU 0009450); – *E. tinifolia* (MAU 0016540)

INTRODUCTION

Oesophageal cancer (OC) is of increasing global concern due to poor prognosis, aggressive disease course, and a lack of efficient selective therapeutics. Oesophageal squamous cell carcinoma and oesophageal adenocarcinoma represent the sixth leading cause of cancer death worldwide and are associated with a 5-year survival of less than 15% and a median overall survival of less than a year [1]. Current treatment options rely primarily on broad-spectrum cytotoxic chemotherapeutics such as cisplatin, fluorouracil, and paclitaxel, which are associated with toxic side effects and limited efficacy, in addition to resistance [2]. Therefore, there is a dire need for searching for novel agents targeted against oesophageal cancer cells.

Plant-sourced bioactive molecules have provided architectural scaffolds for numerous lifesaving clinical agents, including 27% of the approved natural anticancer drugs, since 1980 [3]. Furthermore, over 3,000 global plant taxa have documented ethno-medicinal uses in the treatment of cancer [4].

Mauritius is a biodiversity hotspot located off the southeast coast of the African continent in the Indian Ocean. To date, the ethno-medicinal uses of about 32% of Mauritian endemic plants are documented with limited insight into their anticancer potential [5]. Therefore, this untapped unique resource represents a fertile ground for the bioprospecting of novel oncologic agents.

Thus, the present work evaluated the *in vitro* antioxidant and tumor cytotoxicity of *A. integrifolia*, *D. acutangula*, *E. tinifolia*, *G. psychotrioides,* and *L. glauca* Bojer (*Fig. 1*), in relation to their polyphenolic content. The effect of the three most potent extracts on cell cycle progression, mode of induced cell death, and their ability to modulate AMPK in oesophageal adenocarcinoma cells was also studied.

METHODS

Plant material and preparation of extracts

Fresh leaves of *L. glauca*, *A. integrifolia*, and *G. psychotrioides* were collected at Gaulette serré, near Camp Thorel (coordinates 20˚ 12` 09`` S, 57˚ 25` 11`` E; 20˚ 12` 43`` S, 57˚ 38` 29`` E and 20˚ 12` 43`` S, 57˚ 38` 29`` E, respectively), while leaves of *E. tinifolia* and *D. acutangula* were collected at lower gorges national park, 'Morne Sec' (coordinates 20˚ 23` 35`` S, 57˚ 38` 05`` E) and Réduit (coordinates 20˚ 14` 05`` S, 57˚ 29` 45`` E), respectively. Dried leaves were exhaustively extracted with aqueous methanol (80 %, v/v) and freeze-dried as described [6].

Estimation of polyphenolic contents

The Folin-Ciocalteu assay, aluminum chloride assay, and HCl/Butan-1-ol assay were used to estimate the phenolic, flavonoid, and proanthocyanidin contents, respectively [6]. The results were expressed as mg of gallic acid equivalent (GAE)/g lyophilized weight (LW), quercetin equivalent (QE)/gLW, and cyanidin chloride equivalent (CCE)/gLW, respectively.

Chromatographic determination of phenolic compounds

The GC-MS analysis of trimethylsilylimidazole derivatized extracts of *L. glauca*, *E. tinifolia* and *A. integrifolia* was carried out using an Agilent 7890A gas chromatography system (Agilent Technologies, USA) as described in [7]. The analysis began with the initial oven temperature set at 150˚C, which increased at the rate of 10˚C/min to 300˚C, and was maintained for another 4–5 min to yield a total run of 20 min under constant helium pressure (10 psi). The chromatogram was analyzed by matching the MS spectra of the peaks with those stored in the NIST 2011 Mass Spectral Library.

In vitro antioxidant capacities of extracts

The *in vitro* antioxidant activities of the extracts were evaluated using ferric reducing antioxidant power (FRAP) assay; iron chelating assay; superoxide anion radical scavenging assay; and nitric oxide radical inhibition assay, as described in [6]. The modified method proposed by Chu et al. [8] was employed for the DPPH (2-2 diphenyl-1-picrylhydrazyl) radical scavenging activity. Briefly, 100 µl of a methanolic extract (of varying concentration) and 200 µl of 100 µM DPPH dissolved in methanol were incubated for 30 min at room temperature and the absorbance was read at 492 nm.

The negative and positive controls contained extract vehicle and gallic acid (or otherwise stated), respectively, instead of the extract. The percentage of metal chelating and free radical scavenging activity of the extracts were calculated with reference to the negative control according to equation 1. A concentration response curve was generated, and the IC_{50} value was determined using the GraphPad Prism 6 software (GraphPad Inc., USA). All the experiments were performed in triplicates in three independent assays.

Equation 1

$$\%\ \text{Chelating/ Scavenging/ cytotoxic activity} = \frac{(\text{Absorbance negative control} - \text{Absorbance extract})}{(\text{Absorbance negative control})} \times 100$$

Human cell cultures

Human cancer cell lines purchased from American Type Culture Collection included cervical adenocarcinoma (HeLa), colorectal carcinoma (HCT 116), oesophageal adenocarcinoma (OE 33, FLO-1, OE 19 (platinum resistant)), and oesophageal squamous cell carcinoma (KYSE-30), while non-malignant ones included retinal pigment (RPE-1) and fibroblast (FIBR) cell lines. HeLa, HCT 116, FLO-1, RPE-1, and FIBR were grown in DMEM, while OE 33, OE 19, and KYSE-30 were cultured in RPMI-1640, both media supplemented with 10% (v/v) fetal calf serum (FCS), 2 mM *L*-glutamine, 1% Penicillin-Streptomycin solution with the medium for RPE-1 having an additional supplementation of 20% sodium carbonate. The cells were grown under standard culture conditions.

Cell proliferation analysis using the metabolic assay

The HeLa, HCT 116, FLO-1, OE 33, OE 19, KYSE-30, RPE-1, and FIBR cell lines were plated at 1×10^4 cells per well in a 96-well plate and incubated for 24 h before treatment. The medium was replaced with a fresh medium containing the test extracts (0.78, 1.56, 3.13, 6.25, 12.5, 25 and 50 µg/ml). The experimental negative and positive controls included 0.1% (v/v, final concentration) dimethyl sulfoxide (DMSO) and etoposide (0.78, 1.56, 3.13, 6.25, 12.5 and 25 µg/ml), respectively. After 24 h, 10 µl of Alamar blue reagent (10% (v/v)) was added and the plates were incubated at 37°C for 4 h. Fluorescence was measured using an excitation wavelength of 544 nm and an emission wavelength of 590 nm in a Synergy H4 Hybrid Multi-Mode Microplate Reader (BioTek, USA). Cell viability of the treated cells was calculated as a percentage of the number of viable cells in the negative control (equation 1) and the IC_{50} value determined. The results were expressed as the mean IC_{50} ± SD µg/ml (n=3). The selectivity index (SI) values for the test extracts were calculated as the ratio of IC_{50} values of RPE-1 cells to cancer cells.

Cell death assay and cell cycle analysis

FLO-1 and KYSE-30 cells were seeded (2.6×10^4 and 1.8×10^4, respectively) in 384-well Greiner, black, tissue culture plates. The plates were incubated for 24 h under standard culture conditions before test extracts (*L. glauca*, *E. tinifolia* and *A. integrifolia*) were added using a Biomek FX liquid handler (Beckman Coulter Inc., USA), to give 6-point dose responses with final assay concentrations of 30, 10, 3, 1, 0.3, 0.1 µg/ml with four replicates. DMSO and Staurosporine (3, 1, 0.3, 0.1, 0.03, 0.01 µM) were added as controls. The cells were further incubated for 48 h before staining. The media were aspirated from the plate wells and replaced with the staining mixture (Hoechst 33342 (2 µg/ml, Invitrogen) and MitoTracker Deep Red FM (500 nM, Invitrogen)). The plates were incubated in the dark (30 min), before washing three times with PBS. The staining solution was replaced with normal media, and the plates were imaged on an ImageXpress system (Molecular Devices, UK), taking four images per well. The percentage of cells in each cell cycle phase was determined using the cell cycle application module within the MetaXpress software (Molecular Devices, UK)

Reverse phase protein array (RPPA)

Samples were analyzed by Zeptosens RPPA as described previously [9]. Briefly, tumor lysates were normalized to 2 mg/ml with CLB1 lysis buffer and diluted 1:10 in CSBL1 spotting buffer (Zeptosens-Bayer) prior to preparing a final 4-fold concentration series of 0.2, 0.15, 0.1, and 0.75 mg/ml. The diluted concentration series of each sample was printed onto Zeptosens protein microarray chips (ZeptoChip™, Zeptosens-Bayer) under environmentally controlled conditions (constant 50% humidity and 14°C) using a non-contact printer (Nanoplotter 2.1e, Gesim). A single 400 picoliter droplet of each lysate concentration was deposited onto the Zeptosens chip (thus representing four spots per single biological replicate). A reference grid of AlexaFluor647 conjugate BSA consisting of four column X 22 rows was

spotted onto each subarray; each sample concentration series was spotted in between the reference columns. After array printing, the arrays were blocked with an aerosol of a BSA solution using a custom-designed nebulizer device (ZeptoFOG™, Zeptosen-Bayer) for 1 h. The protein array chips were subsequently washed in double-distilled water and dried prior to performing the dual antibody immunoassay comprising 24-hour incubation of primary antibody, followed by 2.5-hour incubation with the secondary Alexa-Fluor conjugated antibody detection reagent (anti-rabbit A647 Fab).

A selected panel of antibodies, pre-validated for RPPA application, was used. Following secondary antibody incubation and final wash step in the BSA solution, the immune stained arrays were imaged using the ZeptoREADER™ instrument (Zeptosens-Bayer, Germany). For each subarray, five separate images were acquired using different exposure times ranging from 0.5-10 s. Microarray images representing the longest exposure without saturation of fluorescent signal detection were automatically selected for analysis using the ZeptoView™ 3.1 software (Zeptosens-Bayer, Germany). An error weighted least squares linear fit through the fourfold concentration series was used to calculate the median relative fluorescence intensity (RFI) value for each sample replicate. Local normalization of the sample signal to the reference BSA grid was used to compensate for any intra- inter-array/chip variation. Local normalized RFI values were used for the subsequent analysis, and the data are presented as a fold change over DMSO control samples.

Statistical analysis

Statistical analysis was carried out using the GraphPad Prism 6 software. The mean values were compared using One-Way ANOVA. Student's t-test and/or Tukey's multiple comparisons as the Post Hoc test was used to determine the significances of the mean cytotoxic activities of phytochemicals and antioxidants among different extracts and the positive control. All charts were generated using the Microsoft Excel software (version 2010).

RESULTS

Phytochemical analysis

The TPC varied significantly between the investigated leaf extracts ($p < 0.05$), with the highest level measured in *L. glauca* (*Fig. 2*). The TPC in terms of gallic acid equivalent ranged from 298.9 ± 9.4 to 110.4 ±13.7 mg GAE/gLW. *G. psychotrioides* had the most abundant TPrC in terms of the cyanidin chloride equivalent, while a negligible amount was measured in the *A. integrifolia* leaf extract. The total flavonoid levels ranged between 7.6 mg ± 0.3 and 0.4 ± 0.1 mg QE/gLW, with *D. acutangula* having the most prominent flavonoid level followed by *L. glauca*. GC-MS analysis revealed the presence of (+)-catechin and gallocatechin in *E. tinifolia* and *L. glauca*, while gallic acid was detected only in *A. integrifolia* (*Fig. 3*).

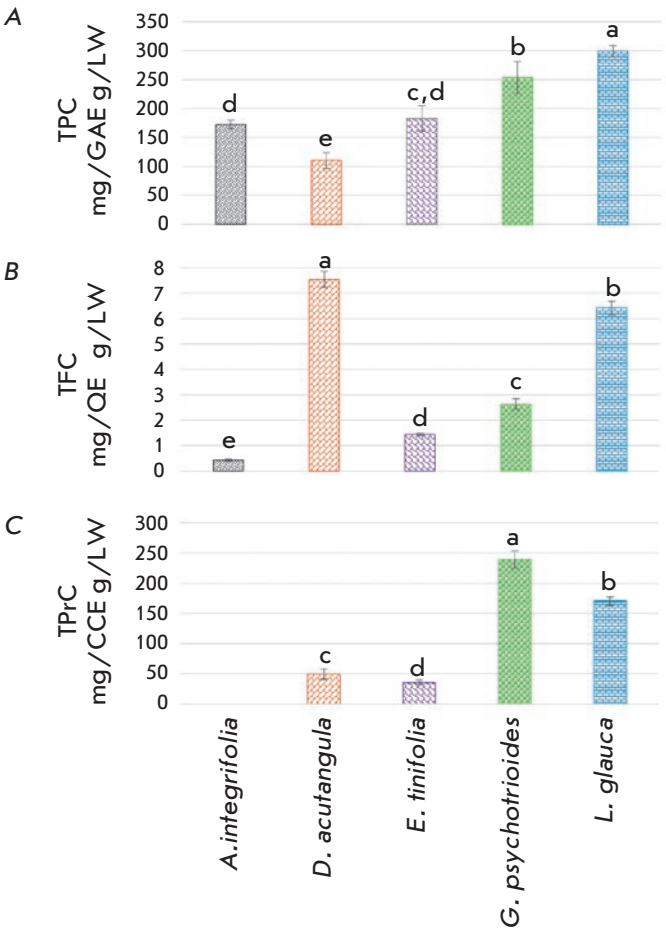

Fig. 2. Total phenolic, flavonoid, and proanthocyanidin contents in the investigated extracts. LW – Lyophilized weight; CCE – cyanidin chloride equivalent; GAE – gallic acid equivalent; QE – quercetin equivalent; TPC – total phenolic content; TFC – total flavonoid content; TPrC – total proanthocyanidin content. The different superscripts between the columns represent a significant difference between the extracts ($p < 0.05$). The data are expressed as the mean ± standard deviation ($n = 3$)

Antioxidant activities of extracts in *in vitro* models

The trend in antioxidant potential between the extracts differed in each of the investigated assays (*Table 1*). The FRAP value of *L. glauca* was significantly higher than that of other endemic plant extracts ($p < 0.05$), and 2.4-fold lower compared to the positive control gallic acid (24.9 mmol Fe^{2+}). All the extracts under

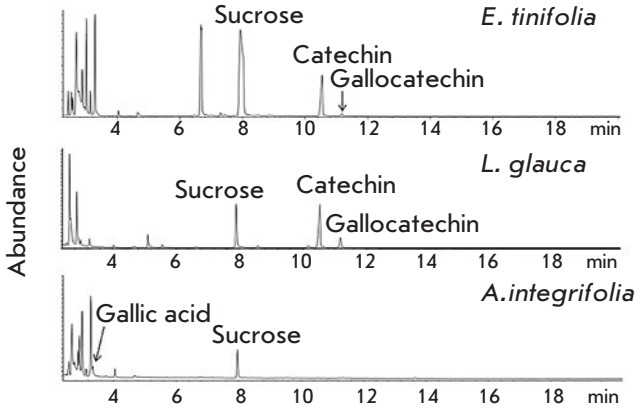

Fig. 3. GC Chromatogram of TMSi derivatives of crude extracts

study showed dose-dependent metal chelating and free radical scavenging activity; the IC_{50} values are shown in *Table 1*. *L. glauca* had the most potent radical scavenging activity against DPPH and NO radicals. While *G. psychotriodes* had the highest $O_2^{\cdot-}$ radical scavenging activity, the metal ion chelating activities of *A. integrifolia* and *E. tinifolia* were notable compared to those of other investigated extracts.

Cytotoxicity of herbal extracts

The *A. integrifolia* and *E. tinifolia* extracts exhibited dose-dependent growth inhibition of the tested cancer cell lines. Both extracts were strongly cytotoxic towards KYSE-30 cells and were 6.9- and 5.6-fold, respectively, less toxic with respect to the immortalized normal RPE-1 cell line. The chemotherapeutic agent etoposide exhibited greater cytotoxicity toward all the tested cancer cell lines, relative to the extracts. However, it is worth noting that etoposide was more cytotoxic towards RPE-1 (SI = 2.3) and fibroblast (SI = 1.5) cells compared to KYSE-30 cells. The calculated IC_{50} value for each extract against the tested cell lines is shown in *Table 2*.

Cell cycle analysis

The cell cycle stage of cells determined using the Cell Cycle Application Module within the MetaXpress software (Molecular Devices, UK) revealed that the extracts affected oesophageal squamous cell carcinoma (KYSE-30) selectively, showing no changes in the oesophageal adenocarcinoma (FLO-1) cell line. Both the *E. tinifolia* and *L. glauca* extracts exhibited a concentration-dependent effect on the cell cycle (*Fig. 4*), causing significant G2/M arrest of KYSE-30 cells, down to 3 μg/ml ($p < 0.05$). Even though the *A. integrifolia* extract also caused cell cycle arrest at G2/M, the effect was less concentration-dependent. None of the extracts caused any changes in the cell cycle of FLO-1 cells (*Fig. 4*).

Interestingly, a similar selectivity pattern was observed in the cell death assays. The number of nuclei per image was determined using the MetaXpress software. Extracts of *E. tinifolia* and *L. glauca* induced cell death in KYSE-30 cells in a concentration-dependent manner. However, both extracts had no effect on FLO-1 cells. The calculated IC_{50} for *E. tinifolia* against KYSE-30 was 1.37 μg/ml; IC_{50} for *L. glauca was* 1.77 μg/ml. *E. tinifolia* at a concentration of 1 μg/ml significantly decreased the KYSE-30 cell number relative to the negative control ($p < 0.05$), while for *L. glauca* a significant reduction in the cell number was observed at 3 μg/ml ($p < 0.05$) (*Fig. 5*).

The selective effect on KYSE-30 was based on the effects of the extracts on cell morphology (*Fig. 6*). The three extracts had a marked effect on the cell number, cell and nuclear morphology, being indicative of cytotoxic and cytokinesis defects. However, there were

Table 1. Antioxidant potential of the investigated medicinal plants leaf extracts

Extracts	Ferric reducing antioxidant power[1]	Iron chelating activity[2]	DPPH Scavenging activity[3]	Superoxide scavenging activity[3]	Nitric oxide scavenging activity[3]
A. integrifolia	5.8 ± 0.6^{d,****}	**655.7 ± 50.4**^{a,****}	9.4 ± 0.9^{c,****}	9.4 ± 2.6^{b,****}	528.4 ± 18.0^{b,****}
L. glauca	**12.1 ± 0.5**^{a,****}	6783.0 ± 1562.0^{c,*}	**2.2 ± 0.1**^{a,**}	**7.6 ± 0.3**^{a,b,*}	**10.5 ± 1.0**^{a}
G. psychotrioides	9.9 ± 0.7^{b,****}	2189.0 ± 483.3^{b,****}	**2.8 ± 0.3**^{a,****}	**6.4 ± 0.6**^{a}	21.7 ± 6.4^{a}
E. tinifolia	8.4 ± 0.5^{c,****}	674.1 ± 87.7^{a,****}	**4.4 ± 0.4**^{b,****}	8.9 ± 1.1^{b,***}	**15.6 ± 2.0**^{a}
D. acutangula	3.9 ± 0.4^{e,****}	1289.0 ± 44.6^{a,b,****}	9.9 ± 1.3^{c,****}	23.2 ± 1.6^{c,****}	43.9 ± 14.0^{a}
Gallic acid	24.9 ± 0.9	8002.0 ± 169.6 (47.0 ± 1.0 mM)	0.7 ± 0.1 (3.9 ± 0.6 μM)	5.5 ± 0.2 (32.1 ± 1.3 μM)	9.9 ± 3.4 (58.4 ± 20.1 μM)

[1]Values are expressed in mmol Fe^{2+}; [2]IC_{50} values are expressed in μg/ml; [3]IC_{50} values are expressed in μg/ml; Data represent a mean ± standard deviation (n = 3). Different letters between rows in each column represent significant differences between the extracts ($p < 0.05$). Asterisks represent significant differences between the extracts and gallic acid (positive control), * $p \leq 0.05$, ** $p \leq 0.01$, *** $p \leq 0.001$, **** $p \leq 0.0001$.

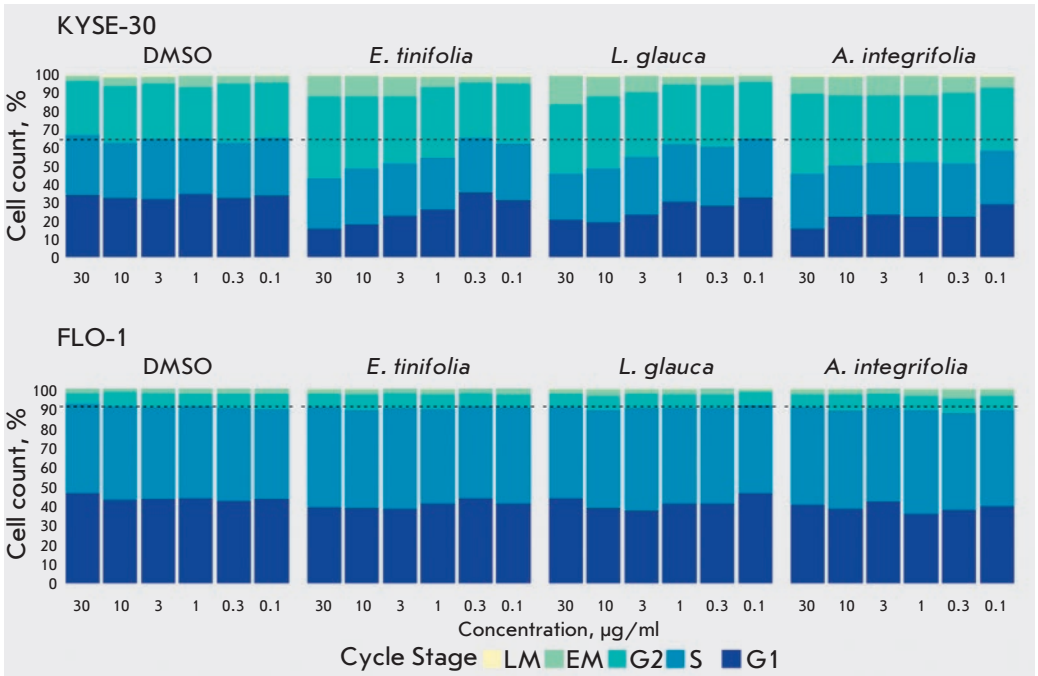

Fig. 4. Cell cycle distribution after extract treatment in the KYSE-30 and FLO-1 cell lines. Cell cycle distribution was analyzed by high-content microscopy (ImageXpress-Micro). *E. tinifolia* and *L. glauca* caused significant G2/M arrest down to 3 µg/ml (Student's *t*-test, $p < 0.05$), and the effect caused by *A. intergrifolia* was significant at all concentrations

Table 2: Cytotoxicity (IC_{50} µgLW/ml) of extracts against Human cell lines

Extracts	Flo-1	OE 33	OE 19	KYSE-30	HeLa	HCT 116	Fibroblast	RPE1
A. integrifolia	10.43 ± 2.10 [SI = 4.2]^{c*}	28.03 ± 4.21 [SI = 1.6]^{a****}	39.28 ± 7.52 [SI = 1.1]^{a}	6.42 ± 2.21 [SI = 6.9]^{a}	7.67 ± 1.58 [SI = 5.7]^{a}	14.51 ± 1.23 [SI = 3.0]^{b,c****}	36.93 ± 6.41 ^{b****}	43.99 ± 4.76 ^{a,b****}
D. acutangula	45.72 ± 7.93 [SI = 0.8]^{a****}	ND	ND	ND	14.27 ± 2.97 [SI = 2.6]^{b****}	14.13 ± 2.62 [SI = 2.7]^{c****}	45.30 ± 4.33 ^{a****}	37.47 ± 4.50 ^{b****}
E. tinifolia	48.62 ± 3.24 [SI = 0.8]^{a****}	45.72 ± 7.93 [SI = 0.9]^{b****}	44.65 ± 8.87 [SI = 0.9]^{b}	6.99 ± 0.38 [SI = 5.6]^{a}	35.26 ± 5.01 [SI = 1.1]^{c****}	19.54 ± 5.16 [SI = 2.0]^{b****}	27.04 ± 1.84 ^{c****}	38.94 ± 4.10 ^{b****}
L. glauca	11.19 ± 2.53 [SI = 4.3]^{c*}	ND	ND	9.22 ± 1.16 [SI = 5.2]^{b**}	41.53 ± 3.28 [SI = 1.2]^{d****}	31.58 ± 5.25 [SI = 1.5]^{a****}	26.74 ± 1.64 ^{c****}	48.49 ± 6.12 ^{a****}
Etoposide	5.23 ± 0.56 [SI = 3.1]	6.74 ± 0.66 [SI = 2.4]	ND	7.05 ± 0.89 [SI = 2.3]	5.47 ± 0.66 [SI = 3.0]	4.93 ± 0.35 [SI = 3.3]	10.24 ± 2.77	16.17 ± 3.93

Data represent mean IC_{50} values ± standard deviation (n = 3). Selectivity index determined as a ratio of the IC_{50} immortalized RPE-1 normal cell to the IC_{50} of cancer cell lines is indicated. ND = at 50 and 25 µg/ml the extracts and etoposide, respectively, failed to induce 50% growth; hence, no IC_{50} value was determined. Different letters between the rows in each column represent significant differences between the extracts ($p < 0.05$). Asterisks represent significant differences between the extracts and etoposide (positive control), *$p \leq 0.05$, **$p \leq 0.01$, ***$p \leq 0.001$, ****$p \leq 0.0001$.

no apparent morphological changes in the FLO-1 cells (*Fig. 6*).

RPPA results

A selected panel of antibodies, pre-validated for RPPA application, was used to compare the individual levels of the corresponding proteins in cancer cells treated with each of the extracts (at different concentrations) with the mock-treated cells. The comparison of the RPPA analysis revealed that, at the 3-h time point, all three extracts upregulated the level of Thr-172 phosphorylation of the alpha subunit of AMPK in a dose-dependent manner, peaking at 3 µg/ml (*Fig. 7*), suggesting the AMPK pathway of activation in cancer cells.

DISCUSSION

The role played by the chemical scaffolds provided by terrestrial plants for lifesaving drugs is immense [3]. To date, only about 15% of the global plant species have been appraised for their curative potential [10]. In Mauritius, about 32% of the endemic flora have ethnomedicinal uses, although there has been limited scientific validation of their efficacies [5]. The majority

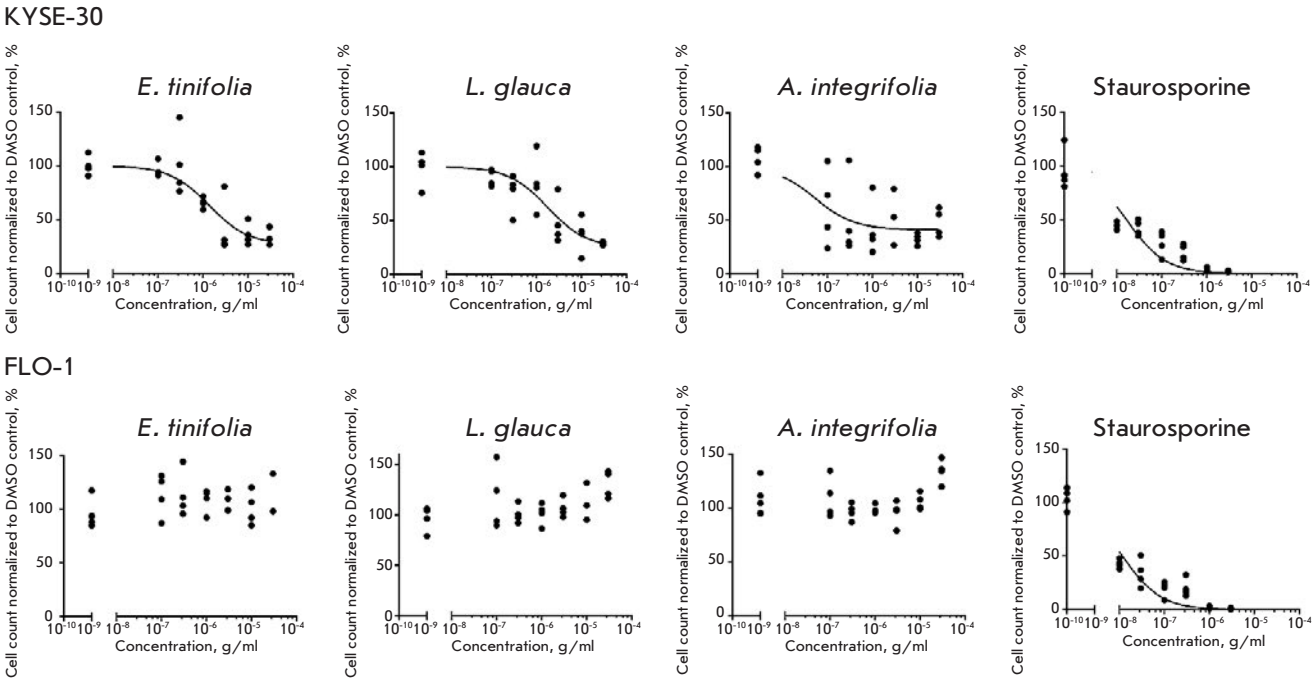

Fig. 5. Concentration response graphs for the extracts and Staurosporine control cytotoxicity on the KYSE-30 and FLO-1 cell lines. The DMSO controls to which the data were normalized were included for reference (data points left of the break on the x-axis)

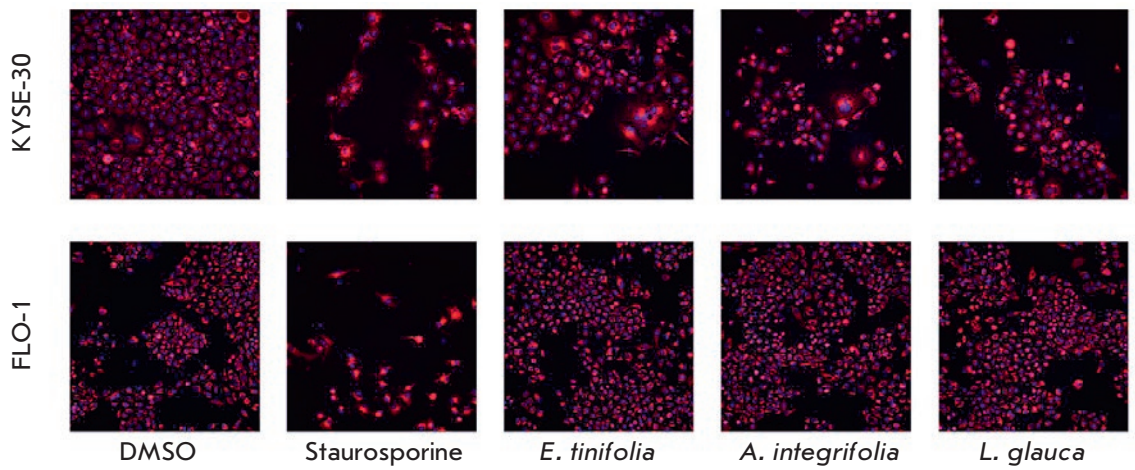

Fig. 6. Fluorescence microscopy images showing cell number and morphological changes in the KYSE-30 and FLO-1 cells. The cells were treated with the extracts (3 μg/ml) and Staurosporine (0.3 μM) for 48 h

of the untapped endemic species, both medicinal and non-medicinal, continue to represent a valuable source of novel chemotypes that await discovery. The therapeutic benefits of plants are ascribed to their secondary metabolites, which are broadly grouped into alkaloids, terpenoids, and phenolics, of which the latter represent an interesting class [11].

A high level of phenolics was estimated in *L. glauca*, *G. psychotriodes*, *E. tinifolia,* and *A. integrifolia. D. acutangula* had the highest flavonoid level, although a low total phenolic content was measured, closely followed by *L. glauca.* The polyphenolic richness of Mauritian plant extracts has been extensively reported on and may be attributed to the high sunlight conditions of the island [12]. Furthermore, a number of reports have delineated the phenolic composition of selected Mauritian endemic plant leaf extracts [13–17]. Consistent with the current findings, previous reports by Neergheen and co-workers demonstrated the relatively higher abundance of total proanthocyanidin

compared to total flavonoid components in a *G. psychotriodes* leaf extract [15, 18]. Moreover, the occurrence of flavan-3-ols, namely, (+)-catechin and (-)-epigallocatechin, detected in the *E. tinifolia* leaf extract (*Fig. 3*) is concordant with findings in the literature [18]. Polyphenolic compounds, inclusive of flavan-3-ols derivatives, are extensively documented with regard to their antioxidant capacities [11, 19].

The pivotal role of plant polyphenols in modulating intracellular redox homeostasis and mitigating oxidative stress-induced pathologies is well established [19]. Mechanistically, antioxidants may neutralize free radicals either by single electron or hydrogen atom transfer [20]. The antioxidant capacity of phenolic compounds emanates from the presence and degree of an electron-donating hydroxyl group on the aromatic ring [21]. Polyphenols, for instance flavonoids, are multifunctional in their antioxidative ability and prevent oxidative damage in multiple ways, including free radical scavenging through direct donation of hydrogen atoms, inactivating enzymes due to hydrogen bonding of hydroxyl groups to proteins and chelating of the metal iron involved in free radical generation, among others [22]. Given the diverse mode of action of phenolic antioxidants, the present study employed a battery of five independent *in vitro* models to determine the antioxidant potential of the extracts. *L. glauca* exhibited the most effective antioxidant capacity in terms of ferric-reducing potential and scavenging of DPPH and nitric oxide free radicals. The antioxidant capacity of the endemic leaf extracts correlated significantly with the total phenolic content $r = -0.887$ ($p < 0.05$) for DPPH free radical scavenging activity and $r = 0.970$ ($p < 0.01$) for FRAP. The strong correlation between TPC and FRAP may be partly attributed to the fact that both assays share a similar redox mechanism [23]. Similar linear correlation between the TPC and FRAP values of Mauritian endemic leaf extracts was previously reported [17]. The positive association between the phenolics and antioxidant activity is not restricted only to Mauritian endemic plants, as comparable relationships have also been reported for Mauritian citrus fruits [24] and Mauritian tea infusate extracts [14].

Given the involvement of oxidative stress in the multistage carcinogenic process [25], polyphenol-rich extracts are expected to prevent or halt the progression of cancerous cell growth. Polyphenolics are reported to attenuate *in vitro* cancerous cell growth via diverse mechanisms [26]. The *in vitro* antiproliferative potential of selected Mauritian endemic *Eugenia* and *Syzygium* species against breast cancer cells (MDA-MB and MCF-7) has been described earlier [27]. However, this study reports for the first time on the growth inhibitory activity of Mauritian endemic leaf extracts against cervical adenocarcinoma, colorectal carcinoma, and oesophageal squamous cell carcinoma. The leaf extracts of *A. integrifolia*, *L. glauca,* and *E. tinifolia* exhibited dose-dependent growth inhibition against the selected cancer cell lines (*Table 2*). However, oesophageal squamous cell carcinoma KYSE-30 cells were the most sensitive to the extracts' treatment. As per the United States National Cancer Institute cytotoxicity guidelines, crude extracts having an IC_{50} value below 20 μg/ml are considered active against tested cell lines [28]. In the present study, the calculated IC_{50} values ranged between 6.42 and 9.89 μg/ml when KYSE-30 cells were co-cultured with *A. integrifolia*, *L. glauca,* and *E. tinifolia* extracts for 24 h. Furthermore, the selective cytotoxicity of the extracts toward KYSE-30 cells was fivefold or greater compared to immortalized non-malignant normal cells.

Guided by the AlamarBlue™ assay results, the effects of the three extracts on cell death and cell cycle stages of KYSE-30 and FLO-1 cells were further investigated across a concentration dilution series using fluorescence staining and high-content image analysis. The findings indicated that extract treatment for 48 h induces considerable dose-dependent cell death in KYSE-30 cells but not in FLO-1 cells (*Figs. 5, 6*). A similar trend was also observed in cell cycle analysis, as extracts treatment induced accumulation of KYSE-30 cells in the G2/M phase, but no effect on the FLO-1 cell cycle was apparent (*Fig. 4*). The blockade of KYSE-30 cells through G2/M was concentration-dependent for both *E. tinifolia* and *L. glauca*, while in the case of *A. integrifolia* the effect was less influenced by the extract dose.

In cancerous cells, signaling components of different cellular pathways are often mutated [29]. In this vein, activation of AMPK and subsequent inhibition of the mTOR pathway is an area of active research [30]. It was previously suggested that activators of AMPK, which include plant polyphenols, can interfere with tumor growth via cell cycle arrest [31] and apoptosis [32, 33] in cancerous cells. The RPPA analysis of the canonical signaling pathways that regulate the cell cycle progression and survival pathways, which in turn regulate cell cycle progression and survival, revealed that all three extracts increase the level of Thr-172 phosphorylation of the alpha subunit of AMPK in KYSE-30 cells (*Fig. 7*), suggesting its activation. This study showed for the first time that the antiproliferative effect of Mauritian endemic medicinal plant leaf extracts is related to their influence on the AMPK pathway modulation.

CONCLUSIONS

In conclusion, the specific selectivity of *A. integrifolia*, *E. tinifolia,* and *L. glauca* to KYSE-30 oesophageal

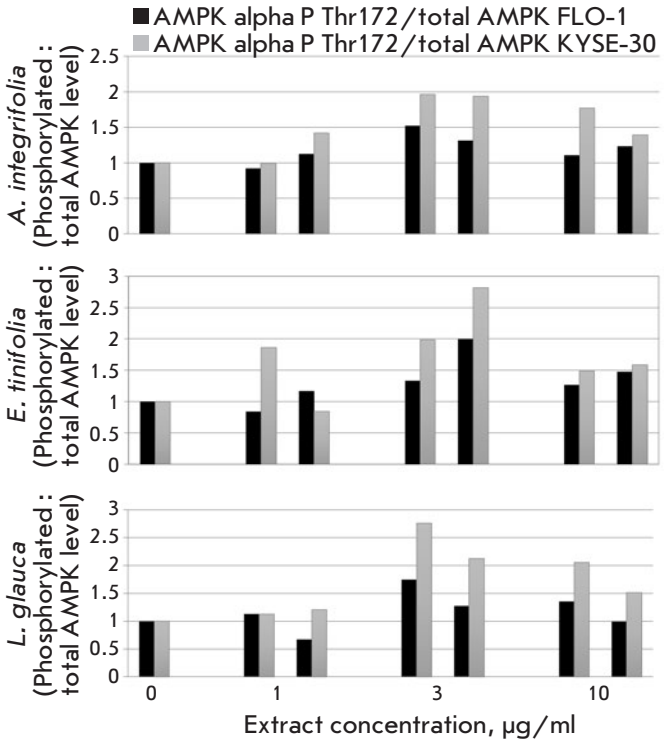

Fig. 7. Graphs showing the changes in the activated phosphorylated AMPK level in the FLO-1 and KYSE-30 cell lines. The cells were treated for 3 h at different concentrations. The results represent the ratio of phosphorylated to total AMPK levels and are expressed as a fold change over DMSO control for each cell type

squamous cell carcinoma relative to oesophageal adenocarcinoma (FLO-1) calls for further investigation into the anticancer effect of these medicinal plants. This is further substantiated by the G2/M phase cell cycle arrest, leading to cell death. AMPK pathway modulation following the exposure of KYSE-30 cells to the extracts provides novel insight into the mechanism of action of these leaf extracts as a potential chemotherapeutic treatment. This is particularly important since esophageal cancer is among the leading causes of cancer mortality worldwide as treatment is limited due to adverse systemic effects, limited efficacy, and emergence of drug resistance. Clinical studies with molecularly targeted therapies have so far been disappointing, with little improvement in patient outcomes. Hence, there is an urgent need to search for new effective treatments for oesophageal cancer. Although preliminary characterization indicated the presence of (+)-catechin and gallocatechin, in-depth phytochemical identification is warranted in order to identify the AMPK modulator.

ACKNOWLEDGEMENTS

We thank the Global Young Academy (GYA), GYA Bio2bio working group, and GYA North-South grant (to V.N.B and A.K.), that allowed us to initiate this work. We thank the director and staff of Alteo Group, Médine Sugar Estate and Mauritius National Park Conservation Services for permission to collect endemic plant samples and the Mauritius Herbarium for plant identification. This study was supported by the Royal Society and Royal Society of Chemistry international exchange award, the Anne Forrest Fund for oesophageal cancer research, MRC Institute of Genetics and Molecular Medicine studentship, Mauritius Research Council under the National Research and Innovation Chair Program studentship, the Ministry of Education and Science of the Russian Federation (project no. 6.7997.2017/8.9), and Chancellor's Fellowship from the University of Edinburgh to Alexander Kagansky.

CONFLICT OF INTEREST

The authors declare the lack of any conflict of interest. ●

REFERENCES

1. Pennathur A., Gibson M.K., Jobe B.A., Luketich J.D. // Lancet. 2013. V. 381. № 9864. P. 400–412.
2. Napier K.J. // World J. Gastrointest. Oncol. 2014. V. 6. № 5. P. 112.
3. Willis K.J. State of the World's Plants 2017.
4. Graham J.G., Quinn M.L., Fabricant D.S., Farnsworth N.R. // J. Ethnopharmacol. 2000. V. 73. № 3. P. 347–377.
5. Rummun N., Neergheen-Bhujun V.S., Pynee K.B., Baider C., Bahorun T. // J. Ethnopharmacol. 2018. V. 213. № April 2017. P. 111–117.
6. Rummun N., Somanah J., Ramsaha S., Bahorun T., Neergheen-Bhujun V.S. // Int. J. Food Sci. 2013. V. 2013. P. 1–12.
7. Johnson-Ajinwo O.R., Richardson A., Li W.-W. // Phytomedicine. 2015. V. 22. № 1. P. 1–4.
8. Chu W.L., Lim Y.W., Radhakrishnan A.K., Lim P.E. // BMC Complement. Altern. Med. 2010. V. 10. № 53.
9. Macleod K.G., Serrels B., Carragher N.O. Proteomics for Drug Discovery. New York: Springer, 2017. P. 153–169.
10. Mathur S., Hoskins C. // Biomed. Reports. 2017. V. 6. № 6. P. 612–614.
11. Grzesik M., Naparło K., Bartosz G., Sadowska-Bartosz I. // Food Chem. 2018. V. 241. № June 2017. P. 480–492.
12. Bahorun T., Luximon-Ramma A., Crozier A., Aruoma O.I. // J. Sci. Food Agric. 2004. V. 84. № 12. P. 1553–1561.
13. Mersch-Sundermann V., Bahorun T., Stahl T., Neergheen V.S., Soobrattee M.A., Wohlfarth R., Sobel R., Brunn H.E., Schmeiser T., Lamy E., et al. // Toxicol. Vitr. 2006. V. 20. № 8. P. 1427–1434.
14. Luximon-Ramma A., Neergheen V.S., Bahorun T., Crozier A., Zbarsky V., Datla K.P., Dexter D.T., Aruoma O.I. // Biofactors. 2006. V. 27. № 1–4. P. 79–91.
15. Neergheen V.S., Bahorun T., Jen L.-S., Aruoma O.I. // Pharm. Biol. 2007. V. 45. № 1. P. 9–17.
16. Soobrattee M.A., Bahorun T., Thaunoo P. // Food Agric. Res. Counc. Réduit, Mauritius. 2005. P. 13–21.
17. Soobrattee M.A., Bahorun T., Neergheen V.S., Googoolye K., Aruoma O.I. // Toxicol. Vitr. 2008. V. 22. № 1. P. 45–56.

18. Neergheen V.S., Soobrattee M.A., Bahorun T., Aruoma O.I. // J. Plant Physiol. 2006. V. 163. № 8. P. 787–799.
19. Soobrattee M.A., Neergheen V.S., Luximon-Ramma A., Aruoma O.I., Bahorun T. // Mutat. Res. Mol. Mech. Mutagen. 2005. V. 579. № 1–2. P. 200–213.
20. San Miguel-Chávez R. In: Phenolic Compounds – Biological Activity. // InTechopen. 2017. P. 59–74
21. Cuvelier M.-E., Richard H., Berset C. // Biosci. Biotechnol. Biochem. 1992. V. 56. № 2. P. 324–325.
22. Procházková D., Boušová I., Wilhelmová N. // Fitoterapia. 2011. V. 82. № 4. P. 513–523.
23. Huang D., Ou B., Prior R.L. // J. Agric. Food Chem. 2005. V. 53. № 6. P. 1841–1856.
24. Ramful D., Tarnus E., Rondeau P., Da Silva C.R., Bahorun T., Bourdon E. // J. Agric. Food Chem. 2010. V. 58. № 20. P. 11119–11129.
25. Toyokuni S., Okamoto K., Yodoi J., Hiai H. // FEBS Lett. 1995. V. 358. № 1. P. 1–3.
26. Soobrattee M.A., Bahorun T., Aruoma O.I. // Biofactors. 2006. V. 27. № 1–4. P. 19–35.
27. Neergheen V., Bahorun T., Aruoma O.I. // Univ. Mauritius Res. J. 2011. V. 17. P. 240–255.
28. Ramos-Silva A., Tavares-Carreón F., Figueroa M., De la Torre-Zavala S., Gastelum-Arellanez A., Rodríguez-García A., Galán-Wong L.J., Avilés-Arnaut H. // BMC Complement. Altern. Med. 2017. V. 17. № 1. P. 241.
29. Sever R., Brugge J.S. // Cold Spring Harb. Perspect. Med. 2015. V. 5. № 4. P. a006098–a006098.
30. Li W., Saud S.M., Young M.R., Chen G., Hua B. // Oncotarget. 2015. V. 6. № 10. P. 7365–7378.
31. Cai X., Hu X., Tan X., Cheng W., Wang Q., Chen X., Guan Y., Chen C., Jing X. // PLoS One. 2015. V. 10. № 7. P. e0133349.
32. Wu P., Liu S., Su J., Chen J., Li L., Zhang R., Chen T. // Food Funct. 2017. V. 8. № 10. P. 3707–3722.
33. Xiao J., Niu G., Yin S., Xie S., Li Y., Nie D., Ma L., Wang X., Wu Y. // Acta Biochim. Biophys. Sin. (Shanghai). 2014. V. 46. № 5. P. 394–400.

GENERAL RULES

Acta Naturae publishes experimental articles and reviews, as well as articles on topical issues, short reviews, and reports on the subjects of basic and applied life sciences and biotechnology.

The journal *Acta Naturae* is on the list of the leading periodicals of the Higher Attestation Commission of the Russian Ministry of Education and Science. The journal Acta Naturae is indexed in PubMed, Web of Science, Scopus and RCSI databases.

The editors of *Acta Naturae* ask of the authors that they follow certain guidelines listed below. Articles which fail to conform to these guidelines will be rejected without review. The editors will not consider articles whose results have already been published or are being considered by other publications.

The maximum length of a review, together with tables and references, cannot exceed 60,000 characters with spaces (approximately 30 pages, A4 format, 1.5 spacing, Times New Roman font, size 12) and cannot contain more than 16 figures.

Experimental articles should not exceed 30,000 symbols (approximately 15 pages in A4 format, including tables and references). They should contain no more than ten figures.

A short report must include the study's rationale, experimental material, and conclusions. A short report should not exceed 12,000 symbols (8 pages in A4 format including no more than 12 references). It should contain no more than four figures.

The manuscript and the accompanying documents should be sent to the Editorial Board in electronic form:
1) text in Word 2003 for Windows format;
2) the figures in TIFF format;
3) the text of the article and figures in one pdf file;
4) the article's title, the names and initials of the authors, the full name of the organizations, the abstract, keywords, abbreviations, figure captions, and Russian references should be translated to English;
5) the cover letter stating that the submitted manuscript has not been published elsewhere and is not under consideration for publication;
6) the license agreement (the agreement form can be downloaded from the website www.actanaturae.ru).

MANUSCRIPT FORMATTING

The manuscript should be formatted in the following manner:

- Article title. Bold font. The title should not be too long or too short and must be informative. The title should not exceed 100 characters. It should reflect the major result, the essence, and uniqueness of the work, names and initials of the authors.
- The corresponding author, who will also be working with the proofs, should be marked with a footnote *.
- Full name of the scientific organization and its departmental affiliation. If there are two or more scientific organizations involved, they should be linked by digital superscripts with the authors' names. Abstract. The structure of the abstract should be very clear and must reflect the following: it should introduce the reader to the main issue and describe the experimental approach, the possibility of practical use, and the possibility of further research in the field. The average length of an abstract is 20 lines (1,500 characters).
- Keywords (3 – 6). These should include the field of research, methods, experimental subject, and the specifics of the work. List of abbreviations.
- INTRODUCTION
- EXPERIMENTAL PROCEDURES
- RESULTS AND DISCUSSION
- CONCLUSION

  The organizations that funded the work should be listed at the end of this section with grant numbers in parenthesis.
- REFERENCES

  The in-text references should be in brackets, such as [1].

RECOMMENDATIONS ON THE TYPING AND FORMATTING OF THE TEXT

- We recommend the use of Microsoft Word 2003 for Windows text editing software.
- The Times New Roman font should be used. Standard font size is 12.
- The space between the lines is 1.5.
- Using more than one whole space between words is not recommended.
- We do not accept articles with automatic referencing; automatic word hyphenation; or automatic prohibition of hyphenation, listing, automatic indentation, etc.
- We recommend that tables be created using Word software options (Table → Insert Table) or MS Excel. Tables that were created manually (using lots of spaces without boxes) cannot be accepted.
- Initials and last names should always be separated by a whole space; for example, A. A. Ivanov.
- Throughout the text, all dates should appear in the "day.month.year" format, for example 02.05.1991, 26.12.1874, etc.
- There should be no periods after the title of the article, the authors' names, headings and subheadings, figure captions, units (s – second, g – gram, min – minute, h – hour, d – day, deg – degree).
- Periods should be used after footnotes (including those in tables), table comments, abstracts, and abbreviations (mon. – months, y. – years, m. temp. – melting temperature); however, they should not be used in subscripted indexes (T_m – melting temperature; $T_{p.t}$ – temperature of phase transition). One exception is mln – million, which should be used without a period.
- Decimal numbers should always contain a period and not a comma (0.25 and not 0,25).
- The hyphen ("-") is surrounded by two whole spaces, while the "minus," "interval," or "chemical bond" symbols do not require a space.
- The only symbol used for multiplication is "×"; the "×" symbol can only be used if it has a number to its

right. The "·" symbol is used for denoting complex compounds in chemical formulas and also noncovalent complexes (such as DNA·RNA, etc.).
- Formulas must use the letter of the Latin and Greek alphabets.
- Latin genera and species' names should be in italics, while the taxa of higher orders should be in regular font.
- Gene names (except for yeast genes) should be italicized, while names of proteins should be in regular font.
- Names of nucleotides (A, T, G, C, U), amino acids (Arg, Ile, Val, etc.), and phosphonucleotides (ATP, AMP, etc.) should be written with Latin letters in regular font.
- Numeration of bases in nucleic acids and amino acid residues should not be hyphenated (T34, Ala89).
- When choosing units of measurement, SI units are to be used.
- Molecular mass should be in Daltons (Da, KDa, MDa).
- The number of nucleotide pairs should be abbreviated (bp, kbp).
- The number of amino acids should be abbreviated to aa.
- Biochemical terms, such as the names of enzymes, should conform to IUPAC standards.
- The number of term and name abbreviations in the text should be kept to a minimum.
- Repeating the same data in the text, tables, and graphs is not allowed.

GUIDENESS FOR ILLUSTRATIONS

- Figures should be supplied in separate files. Only TIFF is accepted.
- Figures should have a resolution of no less than 300 dpi for color and half-tone images and no less than 500 dpi.
- Files should not have any additional layers.

REVIEW AND PREPARATION OF THE MANUSCRIPT FOR PRINT AND PUBLICATION

Articles are published on a first-come, first-served basis. The members of the editorial board have the right to recommend the expedited publishing of articles which are deemed to be a priority and have received good reviews.

Articles which have been received by the editorial board are assessed by the board members and then sent for external review, if needed. The choice of reviewers is up to the editorial board. The manuscript is sent on to reviewers who are experts in this field of research, and the editorial board makes its decisions based on the reviews of these experts. The article may be accepted as is, sent back for improvements, or rejected.

The editorial board can decide to reject an article if it does not conform to the guidelines set above.

The return of an article to the authors for improvement does not mean that the article has been accepted for publication. After the revised text has been received, a decision is made by the editorial board. The author must return the improved text, together with the responses to all comments. The date of acceptance is the day on which the final version of the article was received by the publisher.

A revised manuscript must be sent back to the publisher a week after the authors have received the comments; if not, the article is considered a resubmission.

E-mail is used at all the stages of communication between the author, editors, publishers, and reviewers, so it is of vital importance that the authors monitor the address that they list in the article and inform the publisher of any changes in due time.

After the layout for the relevant issue of the journal is ready, the publisher sends out PDF files to the authors for a final review.

Changes other than simple corrections in the text, figures, or tables are not allowed at the final review stage. If this is necessary, the issue is resolved by the editorial board.

FORMAT OF REFERENCES

The journal uses a numeric reference system, which means that references are denoted as numbers in the text (in brackets) which refer to the number in the reference list.

For books: the last name and initials of the author, full title of the book, location of publisher, publisher, year in which the work was published, and the volume or issue and the number of pages in the book.

For periodicals: the last name and initials of the author, title of the journal, year in which the work was published, volume, issue, first and last page of the article. Must specify the name of the first 10 authors. Ross M.T., Grafham D.V., Coffey A.J., Scherer S., McLay K., Muzny D., Platzer M., Howell G.R., Burrows C., Bird C.P., et al. // Nature. 2005. V. 434. № 7031. P. 325–337.

References to books which have Russian translations should be accompanied with references to the original material listing the required data.

References to doctoral thesis abstracts must include the last name and initials of the author, the title of the thesis, the location in which the work was performed, and the year of completion.

References to patents must include the last names and initials of the authors, the type of the patent document (the author's rights or patent), the patent number, the name of the country that issued the document, the international invention classification index, and the year of patent issue.

The list of references should be on a separate page. The tables should be on a separate page, and figure captions should also be on a separate page.

The following e-mail addresses can be used to contact the editorial staff: vera.knorre@gmail.com, actanaturae@gmail.com,
tel.: (495) 727-38-60, (495) 930-87-07

ActaNaturae

Fluorescence of cells after staining with various proteins. The mean values for the three experiments ± mean error are given

Sample	Fluorescence intensity measured in the FL1 channel	
	SK-BR-3 cells	CHO cells
Unstained cells	3700 ± 400	3700 ± 900
+ β-LG-FITC	5700 ± 600	3300 ± 400
+ 4D5scFv-FITC	$2.7\times10^4 \pm 7\times10^3$	3200 ± 500
+ 4D5scFv-miniSOG	$2.3\times10^4 \pm 3\times10^3$	4600 ± 400
+ DARPin-miniSOG	$1.71\times10^4 \pm 1.6\times10^3$	3000 ± 400

Hence, it has been demonstrated that the targeted recombinant proteins 4D5scFv-miniSOG and DARPin-miniSOG are capable of highly specific binding to the HER2/neu receptor on the surface of human breast adenocarcinoma SK-BR-3 cells.

It was revealed that receptor-mediated internalization of proteins did not take place after the DARPin-miniSOG and 4D5scFv-miniSOG proteins were bound to the receptor on the surface of SK-BR-3 cells at +4°C. However, the receptor–protein complex undergoes internalization at +37°C, as evidenced by the reduction in the fluorescence intensity ΔMFI (the difference between the average fluorescence intensities of stained and unstained cells) (*Fig. 1*). The DARPin-miniSOG recombinant protein as part of its complex with the receptor is internalized faster than 4D5scFv-miniSOG, since ΔMFI for DARPin-miniSOG decreases twofold as compared to its baseline during the first 10 min, while ΔMFI for 4D5scFv-miniSOG is 40 min. These findings are consistent with the published data: 4D5scFv-miniSOG has a higher cytotoxicity than DARPin-miniSOG [5, 6], because 4D5scFv-miniSOG resides on the membrane for a longer time. Since necrosis is the predominant death mechanism of cells irradiated in the presence of these phototoxins, membrane damage makes a crucial contribution to the toxicity of targeted proteins. However, the decline in the fluorescence intensity of miniSOG can be indicative of reactions involving chromophore, which is also expected to affect its efficiency as a phototoxin.

In order to elucidate the reasons for the decline in the fluorescence intensity and toxicity of miniSOG-based proteins observed during their internalization, we evaluated the effect of various factors on the fluorescent properties of miniSOG. A hypothesis has been put forward that quenching of DARPin-miniSOG

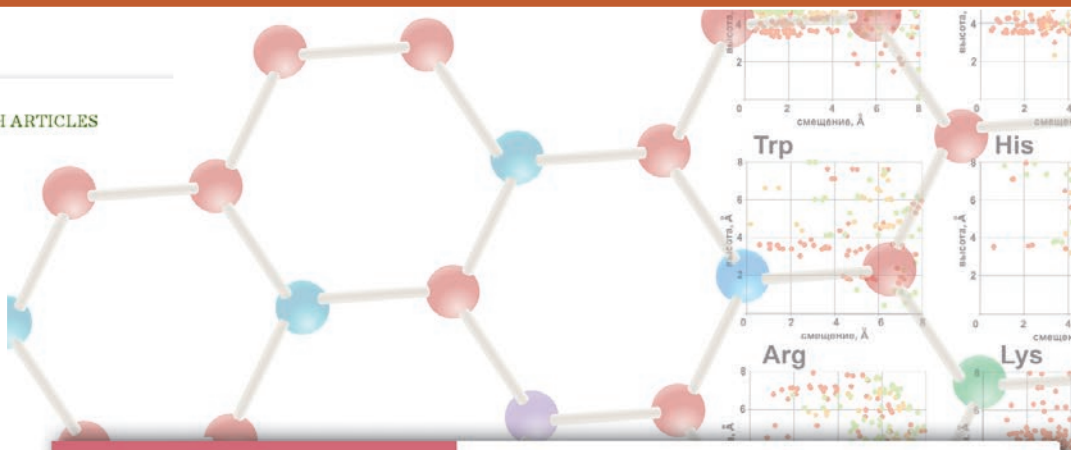

OCTOBER-DECEMBER 2018 VOL. 10 № 4 (39)
ISSN 2075-8251
ActaNaturae

The EIMB Hydrogel Microarray Technology: Thirty Years Later

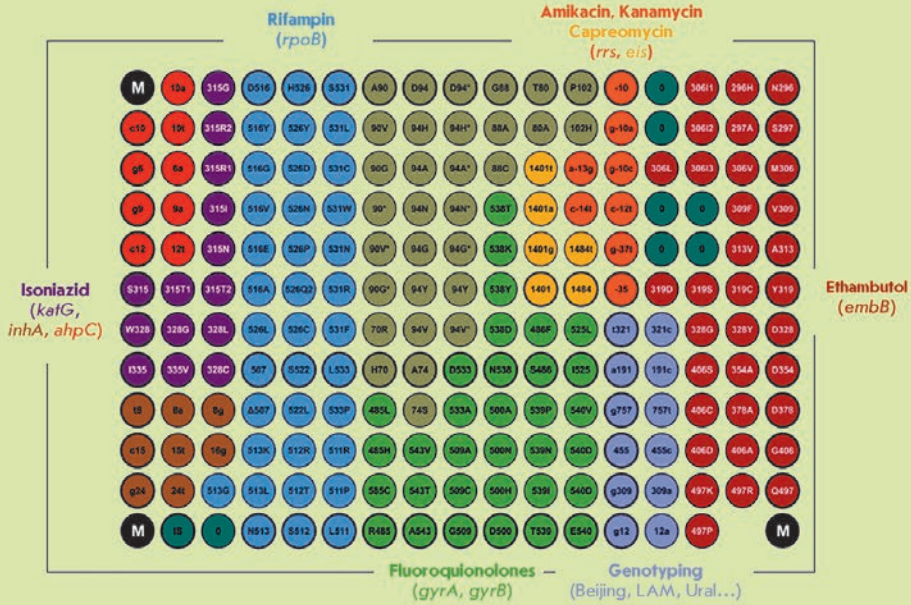

ActaNaturae

Journal “*Acta Naturae*” is a international journal on life sciences based in Moscow, Russia. Our goal is to present scientific work and discovery in molecular biology, biochemistry, biomedical disciplines and biotechnology. *Acta Naturae* is also a periodical for those who are curious in various aspects of biotechnological business, innovations in pharmaceutical areas, intellectual property protection and social consequences of scientific progress.

Being a totally unique publication in Russia, *Acta Naturae* will be useful to both representatives of fundamental research and experts in applied sciences.

Journal “*Acta Naturae*” is now available in open access in PubMed Central® and eLIBRARY.RU.

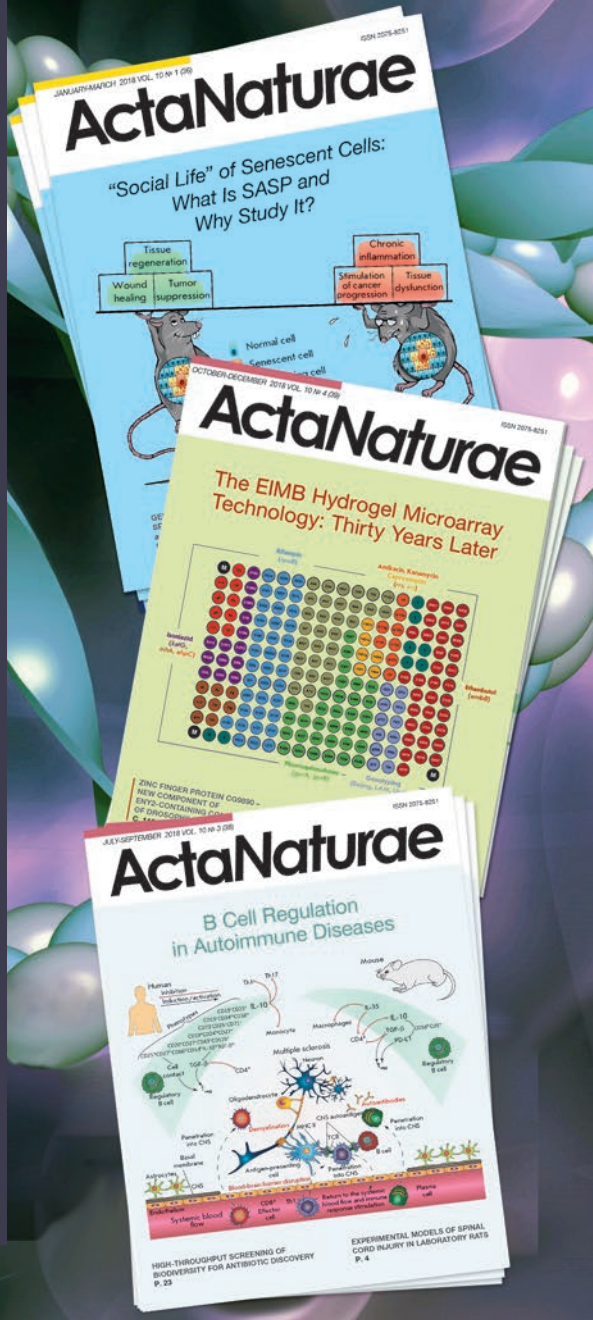

INFORMATION FOR AUTHORS:
if you want to publish in “Acta Naturae”, please contact us: actanaturae@gmail.com